UNIVERSITY OF BIRMINGHAM

NOVEL COMMUNICATION SYSTEM FOR BURIED WATER PIPE MONITORING USING ACOUSTIC SIGNAL PROPAGATION ALONG THE PIPE

By

Omotayo Oreoluwa Farai

A thesis submitted to

The University of Birmingham

For the degree of

Doctor of Philosophy

School of Civil Engineering

College of Engineering and

Physical Sciences

University of Birmingham

December 2020

ABSTRACT

This research presents the design and development of a novel wireless underground communication system for buried water pipe monitoring, using acoustic signal propagation along the pipe. One of the main challenges for wireless underground communication in buried water pipe monitoring is the limitation of reliable data communication range, between an underground transmitter and receiver, to less than 3 metres using radio signal propagation. In this work, an alternative means of enabling data communication within an underground soil environment was investigated by using the water pipe wall as an acoustic communication medium. With acoustic transducers carefully selected from an abundance of commercially available options, a digital communication transmitter was developed alongside a separate digital communication receiver according to the low cost (tens of pounds at most), low power supply requirement (in the order of 1 Watt-hour) and miniature (centimetre scale) size of a wireless communication node. Following the transmitter and receiver design, the developed system was tested in the laboratory along an above ground medium density polyethylene (MDPE) pipe as well as in the field along buried steel and MDPE pipes with reliable digital communication (i.e., 0% bit error rate) successfully achieved at 3.0 and 5.6 m along the buried steel and MDPE pipes respectively with these pipes buried in well or poorly graded SAND (SW or SP).

To analyse acoustic signal attenuation along the water pipes (a key requirement for predicting maximum data transmission range within the proposed communication system), three separate approaches were employed, i.e., analytical, numerical, and experimental (laboratory and field) approaches. While the analytical model was based on fundamental acoustic propagation equations, the numerical model was developed using Abaqus software to simulate acoustic propagation along the pipe; and the experimental approach directly measured acoustic signal

attenuation along the pipes in the laboratory and field experiments. The analytical model and experimental results were used to validate the acoustic attenuation predictions of the numerical model. For the above ground MDPE pipe, the numerical model and laboratory experiments predicted a maximum data communication range of 18-42 m while for the buried MDPE and steel pipes, the field measurements predicted a maximum data communication range of 14-17 m. The results for the buried water pipes are particularly important as they show the possibility of using low frequency (< 1 kHz) acoustic signal propagation along a buried water pipe for achieving reliable wireless underground communication in soil.

DEDICATION

To my parents and sisters

ACKNOWLEDGEMENTS

I would like to thank my supervisors, Prof. Nicole Metje, Prof. David Chapman, Dr. Carl Anthony for their constructive criticism and guidance throughout this research work. I would also like to thank the University of Birmingham for supporting me, through a part scholarship, during this research. I am also personally grateful to Dr. Ali Sadeghioon, not only for his interest in my research, but more importantly for being a constant mentor and friend throughout the course of this research. In addition, I would like to thank the laboratory technicians of the Civil Engineering department as well as the University of Birmingham Estates Services for their help in facilitating the laboratory and field aspects of my research. My deepest and most sincere gratitude goes to all my colleagues and friends in the Civil Engineering department and beyond, too numerous to mention, who have contributed in one way or the other to my life over the past years. I would finally, and most importantly, like to thank my parents and my sisters for their love, support, and kindness especially during the difficult times.

TABLE OF CONTENTS

LIST OF FIGURES

LIST OF TABLES

CHAPTER 1

INTRODUCTION

1.1 BACKGROUND AND MOTIVATION

Water is essential for human existence. Regular access to water supply can therefore be viewed as integral to the survival and proliferation of humankind (Piratla et al., 2015; Thornton et al., 2008). One of the main avenues for water delivery in many cities is the use of pipeline networks, which can cover large geographical areas. These pipeline networks provide water supply for domestic and industrial use as well as for fire protection within a community (Misiunas, 2008, 2005).

Water pipes, like any other civil infrastructure, are prone to failures which compromise their ability to provide regular service to a community. Water pipe failure can generally be described as the inability of a pipe to support internal fluid flow, resulting in a disruption of regular water supply through the pipe (Misiunas, 2008; Kokossalakis, 2006). A natural consequence of water pipe failure is therefore the unavoidable cost implication to a utility service owner. Such cost implications generally involve direct and indirect economic costs to the utility owner, as well as social and environmental costs to a community (Rajani & Kleiner, 2004; Makar & Kleiner, 2000). Some of the cost implications of water pipe failure are further illustrated by the example of a burst underground water main shown in Figure 1.1.

Figure 1.1: Flooding due to burst underground water main in Selly Oak area, Birmingham (Richardson, 2016)

As shown in Figure 1.1, a burst underground water main can result in severe road damage through flooding. In addition to the costs of pipe breakage as well as road damage repairs, there is also the risk of traffic disruption to commuter vehicles as well as health and safety risks to pedestrians. Water wastage within the supply network also represents another direct economic cost implication to a utility service owner. For example, between April 2019 and March 2020 in England and Wales, approximately 3 Gl of water was lost daily due to leaks in the water supply and distribution network (Water UK, 2020). With 1 cubic metre (1000 l) of water costing around £1.30 (Severn Trent, 2019), this translates to a daily loss of over £3.9 million potential revenue. Apart from direct economic cost implications, indirect economic costs of water pipe failure comprise the loss of production for third party entities (due to water outage) as well as road closure fees and costs. In addition to these economic costs, social costs of water pipe failure include the loss of public confidence and trust in a water supply provider as well as a negative environmental sustainability record and image on the part of the utility provider. Although it is possible to quantify direct economic costs in monetary terms, it is more difficult to estimate indirect and social costs of buried water pipe failure (Rajani & Kleiner, 2004; Makar & Kleiner,

2000). To prevent or mitigate water pipe failure occurrences, it is therefore necessary for utility owners to frequently monitor the physical and operational conditions of buried water pipes.

For buried water pipes, condition monitoring can be especially challenging due to the location of the water pipes within the underground environment (Makar & Kleiner, 2000). Condition monitoring techniques for buried water pipes therefore need to be deployable within an underground environment, in addition to being capable of relaying information pertaining to the buried pipe condition to a monitoring station. A plethora of buried water pipe monitoring technologies currently exists across the utility industry (e.g., Datta and Sarkar, 2016; Liu & Kleiner, 2012; Hao et al., 2012), with various benefits and drawbacks for their on-site deployment. Among the monitoring techniques, Wireless Sensor Networking (WSN) has emerged as a robust and cost-effective solution for the real-time condition monitoring of buried water pipes (BenSaleh et al., 2013; Whittle et al., 2013). This is largely due to the low power supply requirement (in the order of 1 Watt-hour), low cost (tens of pounds at most) and small size (centimetre scale) of wireless underground sensor nodes, which facilitate concealment, ease of deployment and long-term operation for pipeline monitoring operations (Sadeghioon et al., 2014; Akyildiz & Vuran 2010; Jahwar et al. 2007). Furthermore, the cost effectiveness of deploying individual wireless sensor nodes (due to modern advancements in integrated micro-electronic circuits costing only tens of pounds or less) implies that multiple wireless sensor nodes can be deployed over large coverage areas at relatively low costs compared to other buried water pipe inspection techniques (Yick et al., 2008; Stoianov et al., 2008).

One of the main challenges for WSN deployment, however, is the limited range of underground data communication between the wireless sensor nodes to less than 3 m (Sadeghioon, 2014; Silva & Vuran, 2010). The consequence of such limited communication range is an increase in the cost of deployment of the WSN for buried water pipe monitoring, by forcing a utility

operator to deploy multiple wireless underground sensors at relatively short spatial intervals (Akyildiz & Stuntebeck, 2006). A promising alternative for improving underground data communication range within a WSN is the use of acoustic signal propagation. Besides being wireless in nature, numerous studies on acoustic wave propagation along buried water pipes have shown the potential of acoustic waves to propagate at distances within tens to hundreds of metres in an underground soil environment (e.g., Muggleton & Yan, 2013; Long & Cawley, 2006; Long et al., 2003; Muggleton et al., 2002; Hunaidi et al., 2000). This fact introduces the possibility of using acoustic wave propagation within a WSN for wireless underground communication. In view of taking this idea forward, this project work investigates, with the aim of developing a working proof-of-concept, the use of acoustic signal propagation as a means of enabling wireless underground communication within the framework of potential integration into a WSN for buried water pipe monitoring.

1.2 AIM AND OBJECTIVES

The aim of this research is to design and develop a novel acoustic based digital communication system capable of enabling reliable data transmission along a pipe commensurate with buried water pipe monitoring systems. To achieve this aim, the following objectives were identified:

1. To conduct a critical review of wireless underground communication techniques, with emphasis on the physical communication medium, within a Wireless Sensor Network (WSN) for buried water pipe monitoring while discussing their limitations for practical deployment within the WSN.
2. To select the most appropriate commercially available components for an acoustic based digital communication system based on a thorough review and laboratory-based investigation.

3. To design and develop a working prototype of an acoustic based digital communication transmitter and receiver, with low power supply requirement (in the order of 1 Watt-hour), low cost (tens of pounds at most) and miniature (centimetre scale) hardware components.
4. To conduct laboratory and field experiments on acoustic based digital communication along exposed and buried water pipes to validate the possibility of achieving digital communication along a buried water pipe.
5. To analyse acoustic signal attenuation along exposed and buried water pipes within the communication system by conducting analytical and numerical based computations of acoustic wave propagation along the pipes.
6. To evaluate the novel communication system in terms of the maximum ranges at which reliable digital communication can be achieved and make recommendations about its suitability for practical applications in buried water pipe monitoring.

1.3 THESIS LAYOUT

This thesis comprises five chapters detailing the design and development of a novel, acoustic based digital communication system for buried water pipe monitoring.

Chapter 2 initially reviews the current state of the art in buried pipeline monitoring including the methods by which digital communication is enabled above and below the ground during pipeline monitoring operations. The chapter subsequently focuses on critically reviewing current wireless underground communication techniques for buried water pipe monitoring before reviewing acoustic signal propagation along a water pipe waveguide. It concludes by highlighting the main gaps in the literature.

Chapter 3 details the methodology for the design and development of the novel communication system. The chapter begins by outlining the operational stages needed for successful data

transmission between a digital communication transmitter and receiver. The processes by which each operational stage was achieved at both ends of the digital communication system, in addition to final testing of the finished product along exposed and buried water pipes, are further detailed in this chapter. The chapter also describes experimental, analytical, and numerical modelling approaches undertaken for the examination of acoustic signal attenuation along exposed and buried water pipes within the communication system.

Chapter 4 presents the results of data transmission within the communication system in addition to discussing its performance along exposed and buried water pipes using the experimental, analytical, and numerical modelling results for acoustic signal attenuation along the pipes.

The thesis is finally concluded in Chapter 5, with recommendations for further work.

CHAPTER 2

LITERATURE REVIEW

2.1 INTRODUCTION

This chapter begins by briefly describing the water supply network structure and common processes by which water pipes deteriorate. Following this discussion, the subject of buried pipeline monitoring is briefly discussed since this infrastructure is vital for the functioning of today's society by transporting vital assets to private and commercial premises. Often, these pipelines have been buried in the ground for decades and have subsequently deteriorated over time. Little is often therefore known about the condition of these buried assets as they are out of sight and monitoring can be challenging. Section 2.3 briefly reviews available monitoring strategies for these utility assets in terms of their sensor deployment strategies (i.e., either inspection based or continuous monitoring) before drawing out the usefulness of wireless sensor networking for continuous pipeline monitoring.

Considering its key role in enabling a remote operator to continuously monitor a buried pipe asset, Section 2.4 examines data communication strategies for continuous pipeline monitoring. The section critically reviews available data communication techniques for continuous pipeline monitoring while focusing on wireless underground to underground data communication. Within this section, current research into signal transmission techniques for wireless underground data communication is comprehensively reviewed while drawing out specific limitations within the framework of wireless sensor networking for buried pipeline monitoring.

Acoustic communication is introduced in Section 2.5 as a possible solution for enabling underground to underground data communication by using the buried pipeline waveguide as an acoustic propagation medium. Two possible communication channels exist within the physical structure of a water pipe waveguide, i.e., the internal fluid medium and the pipe wall. The

physical mechanisms of acoustic wave propagation along each channel are briefly discussed while reviewing currently available research into acoustic data communication along water pipes. The chapter is finally concluded in Section 2.6 by identifying knowledge gaps upon which this research will build on.

2.2 WATER SUPPLY NETWORK

Generally, pipeline systems play a vital role in the national economy as they are widely used in energy storage and transportation. Businesses in this industry transport natural gas, petroleum, slurry, water and other liquids within communities and over long-distance distribution grids within and outside national borders. For potable water supply, the pipeline network can be categorised into transmission and distribution systems (Misiunas, 2008, 2005). A water transmission system is responsible for conveying water from a source (such as a water treatment plant) to a storage facility or reservoir over several kilometres (Misiunas, 2008; Al-Barqawi & Zayed, 2006). A transmission system also typically consists of water pipes with diameters greater than 300 mm (Sadeghioon, 2014; Misiunas, 2005).

A water distribution system, on the other hand, conveys water from storage facilities to the end user located in residential and industrial areas. In contrast to water transmission pipes, water distribution pipe diameters are typically less than 300 mm (Al-Barqawi & Zayed, 2006; Misiunas, 2005). Water distribution systems can further be classified into distribution mains and service connections. Distribution mains are responsible for bridging the gap between water transmission systems and the end user while service connections enable water transportation from the distribution mains to private and commercial buildings (Misiunas, 2008, 2005). Water transmission and distribution systems, in terms of the materials which have been used for their construction, are briefly discussed next.

2.2.1 Water pipe materials

A variety of materials and technologies have historically been employed for constructing water supply pipes. The material used for the water pipe construction also varies according to when the pipes were installed as well as its diameter, with larger pipes (transmission mains) consisting of steel, mild steel cement lined (MSCL) or prestressed concrete cylinder pipes (PCCP) (Misiunas, 2005). Older water distribution mains also typically consist of cast iron or asbestos cement pipes while newer mains are typically made of ductile iron and polyvinyl chloride (PVC) pipes (Rajani & Kleiner, 2004). Pipe material distribution within a water supply network also depends on the country within which the network exists (Sadeghioon, 2014; Misiunas, 2005). In the UK, stricter regulations on the use of lead in pipes (Drinking Water Inspectorate, 2020) have led to the replacement or relining of existing lead or asbestos cement pipes. While pipe material distribution data for other countries also exist in the literature (e.g., Pelletier et al., 2003; Weimer, 2001), Saul et al. (2003) summarised the percentage distribution of different water pipe materials in the UK, based on asset management information provided by a utility service provider over a seven-year period while Rajani & Kleiner (2004) also published a study of pipe material distribution in 13 different European countries. These findings are summarised in Table 2.1 and Figure 2.1, respectively.

Table 2.1: Summary of pipe material distribution in the UK (Saul et al., 2003)

Material type	% of total pipe materials
Cast iron	43.5
Asbestos cement	30.3
Plastics	11.3
Unknown	11.5
Others	3.4

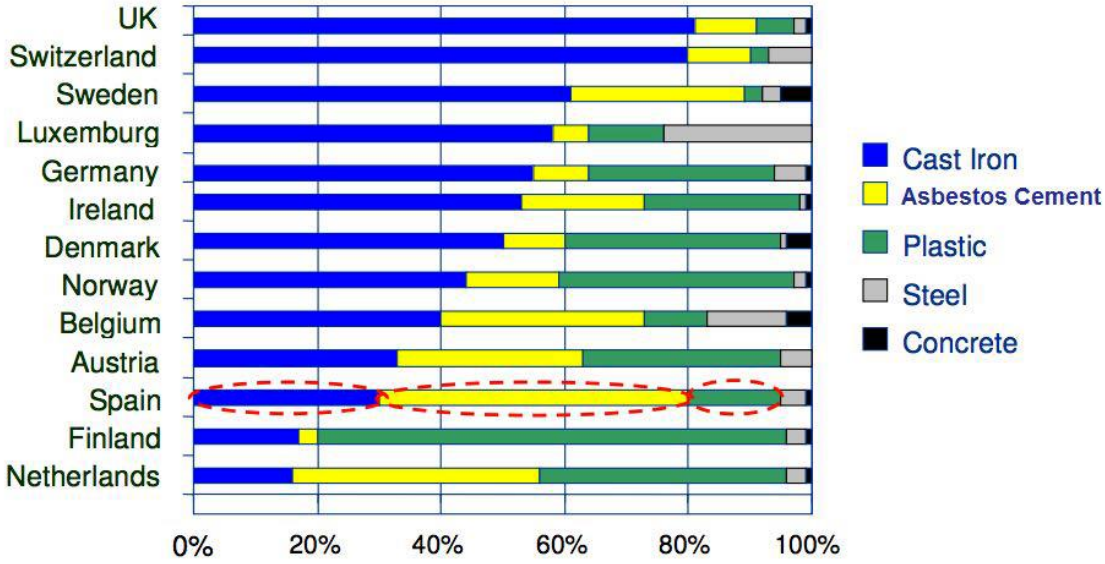

Figure 2.1: Pipe material distribution in selected European countries (Rajani & Kleiner)

From Table 2.1, cast iron constitutes the majority of pipe material distribution in the UK (with a known asset length of 43.5% of the total buried pipe network) based on analysis of a utility owner's asset management database by Saul et al. (2003). This proportion is even higher according to Rajani & Kleiner (2004) who estimated the proportion of cast iron pipes in the UK to be approximately 80%. The distribution of Figure 2.1 is nevertheless shifting to a more plastic based network as plastic pipes are nearly exclusively used for replacing and expanding existing water pipe networks (Sadeghioon, 2014).

Like any other civil infrastructure, water supply systems are subject to deterioration over time (Rogers & Grigg, 2009). This comes as no surprise especially when considering that the first urban water supply systems were built more than 500 years ago. In current water supply systems, the average pipe age is estimated to be around 50 years (Misiunas, 2005). The next section briefly discusses the processes by which such water pipes deteriorate and eventually fail.

2.2.2 Water pipe deterioration and failure

Pipe failure can be described as a multistep infrastructure deterioration process which compromises the structural integrity of the pipe. A partial failure features leak development along the pipe but the pipe remains in service while a complete failure means the pipe hydraulic balance is compromised to an extent where pipe repair or replacement is necessary (Misiunas, 2008, 2005). Pipe failure also constitutes exposure of potable water inside the buried pipe to contaminated ground water (ingress of water) due to pipe wall fracture. Both mechanisms (i.e., leak or ingress of water) constitute pipe failure. Pipe failure is therefore the consequence of deleterious processes which compromise the performance of a pipeline network. Such processes typically result in pipe deterioration which varies according to the pipe material as well as the environmental and operational conditions (Al-Barqawi & Zayed, 2006; Makar et al., 2001).

According to Rajani & Kleiner (2004), pipe deterioration can be divided into two categories, i.e., structural, and internal deterioration. Structural deterioration reduces the structural resiliency of pipes and their ability to withstand external stress while internal deterioration compromises the pipe internal structure which in turn affects the hydraulic capacity and water quality (Al- Barqawi & Zayed, 2006; Rajani & Kleiner, 2004).

The life cycle of a buried water pipe is also typically represented by a “bathtub” curve as shown in Figure 2.2 (Rajani & Kleiner, 2004).

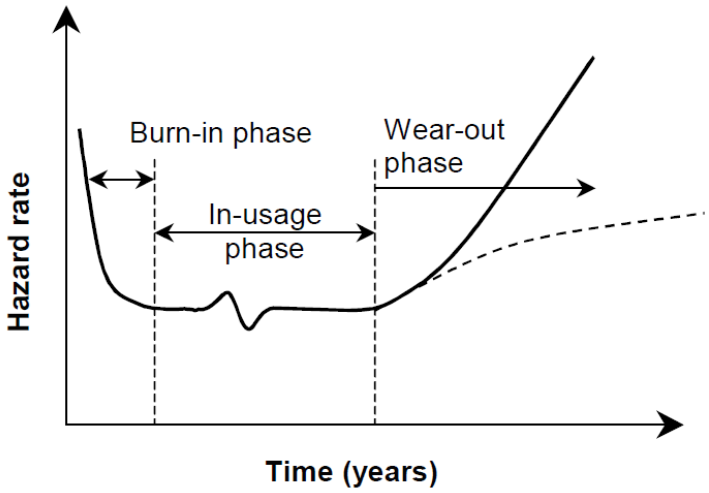

Figure 2.2: Life cycle of a buried water pipe (Rajani & Kleiner, 2004)

Figure 2.2 describes the hazard rate (risk of failure) with respect to time, for a buried water pipe over its operational lifetime. Three distinct phases can be readily observed from the figure. These are the "burn-in phase", "in-usage phase" and the "wear-out phase". The initial or "burn-in" phase represents the duration of the pipe life cycle within which the pipe is freshly installed underground. Failures which occur during this period are usually attributable to manufacturing and installation errors (Rogers & Grigg, 2009; Rajani & Kleiner, 2004). The "in-usage" phase represents the longest period in the pipe life cycle where the pipe enjoys the lowest risk of failure. Failures which occur during this phase typically arise due to random external loading conditions or third-party interference. The final or "wear out" phase is characterised by an increased failure risk as the pipe approaches the end of its life cycle. Such failures are therefore commonly attributable to the ageing and deterioration of the buried pipe (Rogers & Grigg, 2009; Rajani & Kleiner, 2004).

Pipe material and geometry are also known to affect the chronological order of a pipe deterioration process. Cast iron pipes, for instance, typically break prior to leakage while plastic pipes either break before leaking or vice versa (Misiunas, 2005). Plastic pipe degradation mechanisms over time, however, remain to be studied in greater detail since they are likely

slower compared to cast iron pipes and have not been in use for as long as their cast iron counterparts (Sadeghioon, 2014; Misiunas, 2008; Rajani & Kleiner, 2004).

The factors which contribute to pipe deterioration and eventual failure can also be categorised into static, dynamic and operational factors (Al-Barqawi & Zayed, 2006). Static factors are characterised by their unchanging nature with respect to time. Such factors include pipe geometry, material, and installation techniques. Dynamic factors, in contrast to static factors, change with time. Such factors include pipe age, soil moisture, soil electrochemical composition as well as temperature which represent dynamic influences that can contribute to pipe deterioration. Finally, operational factors refer to the contribution of regular pipeline operations such internal water pressure, pipeline replacement rate as well as pipe protection methods.

Other causes of pipe failure, as identified by Makar & Kleiner (2000), are failure due to manufacturing flaws, excessive forces, and human errors. Porosity has also been identified by the same authors as the most common type of manufacturing flaw in cast iron pipes. Porosity arises due to air being trapped inside the cast iron pipe material during manufacture. Other manufacturing flaws include variations in pipe wall thickness and inclusions such as the presence of iron phosphide compounds within the pipe structure (Misiunas, 2005; Makar & Kleiner, 2000). The action of excessive forces on the pipe by the surrounding environment is another possible cause of pipe failure. Excessive forces are often produced by ground movements around the pipe or, in some cases, incorrect installation methods which unduly stress the pipe (Makar & Kleiner, 2000). Human errors can also contribute to an eventual pipe failure. These include errors in the pipe design as well as installation errors.

In summary, pipe deterioration and failure can arise due to several factors which could be static, dynamic, or operational in nature. There are also other causes of pipe failure which do not

necessarily result from the gradual deterioration process, as noted in Makar & Kleiner (2000). As a result of the diversity of possible failure events, regular inspection of buried water pipes (especially during the wear out phase) is crucial to the maintenance of optimum pipe performance. Moreover, Misiunas (2005) noted the exponential increase of direct pipeline failure costs (which comprise pipeline repair costs, lost water, damaged infrastructure, and liabilities) with the time during which such failure is left unattended.

As buried water pipes are invisible and difficult to access, condition monitoring is challenging. Different options exist from remote sensing from the ground surface and in-pipe monitoring to discrete sensors around the pipe. The choice of the most appropriate buried pipeline monitoring technique is however influenced by the stage of the pipe deterioration process. Where pipeline monitoring is carried out prior to pipe failure, the pipeline monitoring technique is proactive. Reactive pipeline monitoring, on the other hand, is only carried out after the pipe failure to detect an ongoing leak (Misiunas, 2005). Proactive pipeline monitoring, due to its preventive nature, is therefore advantageous for buried pipeline monitoring as it avoids the potential cost implications of a complete pipe failure. For the water industry however, due to the relatively low costs of water (£1.30 per cubic metre), proactive failure management techniques need to be economically justifiable for buried pipeline monitoring as generally, the earlier the stage of pipe deterioration monitored, the more complex and expensive is the pipeline monitoring technique to be applied (Sadeghioon, 2014; Misiunas, 2008, 2005). A potentially cost-effective approach would therefore be to continuously monitor the pipe for indicators which arise from changes in the baseline data, i.e., at a time when the pipe has not shown any deterioration or at least no leaks. This can subsequently alert a utility asset owner on the presence of buried pipeline failure mechanisms thus potentially reducing pipeline failure costs by proactively monitoring the buried pipeline network.

Key to the effectiveness of any pipe monitoring technique is also the communication of relevant information pertaining to the buried pipe conditions, to a data processing unit where further examination of the pipe failure can be carried out in addition to providing necessary tools for decision making by the utility owner (Makar & Kleiner, 2000). Considering these points, the next section briefly discusses common pipeline condition assessment and failure monitoring technologies.

2.3 BURIED PIPELINE CONDITION ASSESSMENT AND FAILURE MONITORING

As societies develop and technologies advance, it is crucial for civil infrastructure which form the bedrock of goods and services delivery to be frequently monitored to ensure continuous and optimal operation. The field of civil infrastructure health monitoring is broad and quite diverse, incorporating the disciplines of electronic, communication and mechanical engineering, among others.

Buried utilities, with their complex and labyrinthine nature, have over the years played a significant role in the evolution of modern civilization. The proliferation of buried pipeline infrastructure has rapidly increased especially in the last century which has seen the advance of industrial technology (Costello et al, 2007). Effective location and health monitoring of this infrastructure however has more recently become a growing source of concern. This challenge has motivated extensive research and development with the aim of producing technological solutions which meet the need for increasingly effective solutions for buried pipeline location and condition assessment (Rogers et al., 2012; Hao et al., 2012; Costello et al., 2007).

It is understandable that to assess the condition of a buried pipeline, the location of such infrastructure must be known *a priori*. The generation of detailed maps of buried pipeline infrastructure, for example, is a massive problem in many urban cities across the world where

existing and newly installed infrastructure co-exist in an ever-increasing labyrinth (Rogers et al. 2012; Costello et al., 2007). Even after locating such infrastructure, there exists a persistent need to develop cost-effective condition monitoring technology especially since these infrastructures are invisible and difficult to access (Metje et al., 2012; Costello et al., 2007). Depending on the sensor deployment approach, buried pipeline condition monitoring techniques can further be categorised as inspection based and real-time monitoring techniques.

2.3.1 Buried pipeline inspection

Inspection techniques are based on the non-destructive evaluation (NDE) of buried infrastructure were failure or damage is suspected. A plethora of techniques for buried pipeline inspection can be found in the literature with extensive reviews of such techniques including Lee (2017), Datta and Sarkar (2016), Liu and Kleiner (2013), Hao et al. (2012), Marlow et al. (2007) and Costello et al. (2007). According to Misiunas (2005), inspection techniques for the condition assessment of buried water pipes can be categorised as direct and indirect methods. Direct methods of pipe inspection encompass all techniques where the condition of the buried pipe is directly monitored for signs of pipe deterioration and failure. Indirect methods of pipe inspection, on the other hand, rely on secondary indicators such as soil resistivity in order to assess the condition of the buried pipe (Liu & Kleiner, 2013; Misiunas, 2005). Direct methods of pipe inspection can further be classified into visual and non-visual methods, the most common of which are briefly discussed next.

2.3.1.1 Visual methods

Visual inspection techniques rely on the use of vision for detecting structural anomalies along buried infrastructure. One of the most widely deployed visual inspection techniques for buried pipeline monitoring is the use of Closed-Circuit Television (CCTV) technology (Kumar et al.,

2020; Selvakumar et al., 2014; Liu & Kleiner, 2013; Jo et al., 2010). Figure 2.3 shows the workflow of a typical CCTV inspection system.

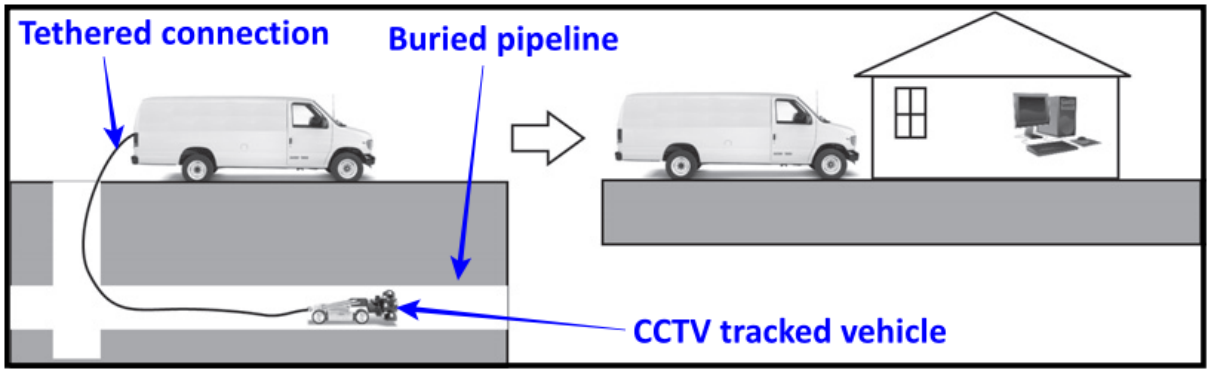

Figure 2.3: CCTV inspection workflow (Liu et al., 2012)

As shown in Figure 2.3, the CCTV inspection workflow features a tracked CCTV vehicle within a buried pipeline using a tethered connection to an above ground vehicle where acquired information is stored and later processed. CCTV for buried pipeline monitoring is however more frequently deployed for sewer as opposed to potable water pipes mainly due to the commonly larger diameters of sewer pipes as well as the relative ease in taking them out of service for inspection purposes (Liu & Kleiner, 2013). Jo et. al (2010) and Laven et. al (2008) however reported a CCTV technique which was adapted for the in-service inspection of potable water pipes. This technique, known as the Sahara® CCTV inspection tool features a tethered camera and lighting system located within a pressure resistant housing. Several limitations have however been identified with the CCTV technique. Hao et al. (2012), for example noted that the images of an interior pipe wall can only be acquired above the water surface in the case of water and sewer pipes. Unsteady camera movement as the equipment traverses the pipe is also considered to be a problem with this technique (Hao et al., 2012; Kirkham et al., 2000). Other system challenges include lack of detail in capturing the extent of a damage within the pipe wall, speed of data acquisition and the need for human expertise in data interpretation (Lee, 2017; Liu et al., 2012; Hao et al., 2012; Rajani & Kleiner, 2004; Duran et al., 2002; Misiunas,

2005). To improve the speed of data capture as well as level of data acquisition detail, scanning and laser profiling technologies such as those available from RapidView (2019) and Envirosight (2020) have been reported in the literature. These techniques however, and at potentially considerable expense to the utility owner, generally require the pipe to be emptied and cleaned before inspection operations can be carried out (Lee, 2017; Liu & Kleiner, 2013; Liu et al., 2012).

2.3.1.2 Non-visual methods

There are several non-visual methods for buried pipeline inspection, some of the most prolific including the electromagnetic (EM) as well as acoustic and ultrasonic methods (Liu & Kleiner, 2013; Liu et al., 2012). Among the EM techniques, Ground penetrating radar (GPR) is considered a proven method for buried utility inspection (Demirci et al., 2012; Hao et al., 2012; Misiunas, 2005; Duran et al.; 2002). With GPR, an electromagnetic pulse is transmitted from above the ground with the subsequent detection of the pulse reflection from various structural discontinuities providing pertinent information such as depth, location and condition of a buried utility asset (Metje et al., 2007; Maser, 1996). Two approaches employable for GPR sensing are the traditional and in-pipe methods (Hao et al., 2012; Duran et al., 2002). While the traditional GPR method involves both transmitter and receiver placed solely above the ground, the in-pipe method involves placing either the transmitter or both the transmitter and the receiver inside the buried pipe (e.g., Pennock et al., 2012; Pennock et al., 2007). Hao et al. (2012) also noted that in-pipe GPR techniques are advantageous to traditional methods as they enable a reduced path loss for the propagating EM wave in soil. GPR performance in general is however limited by signal attenuation in moist soils, especially those with high clay content (Liu et al., 2012; Metje et al., 2007). In addition, Liu et al., (2012) also noted that efficient use of this technology requires highly skilled operators especially for data interpretation.

The remote field eddy current (RFEC) technique is another common EM based inspection tool which uses exciter coils located within the pipe to generate a low frequency electromagnetic field subsequently detected by receiver coils also located within the pipe (Lee, 2017; Liu et al., 2012). The strength of this received magnetic field provides the basis on which the pipe wall thickness is assessed (Kumar et al., 2020; Liu & Kleiner, 2013; Misiunas, 2005). Commercially available technologies such as the PipeDiver® (Pure Technologies, 2020) and See Snake (Garrett & Shatat, 2012) inspection tools employ the RFEC technique for inspecting PCCP and ferromagnetic pipes. As noted by Rajani & Kleiner (2004) however, this technique is only suitable for metallic pipes or pipes with ferromagnetic material (such as PCCP) and so cannot be used for non-metallic (e.g., plastic) pipes.

Another inspection technique which can be applied to both metallic and non-metallic pipes is the acoustic or ultrasonic method for pipe inspection. Acoustic and ultrasonic methods rely on the use of sound waves for pipe inspection and several commercially available technologies based on this method have been reported in the literature (e.g., Kumar et al., 2020; Lee, 2017; Liu et al., 2012; Hao et al., 2012). Sonar technology, for example, relies on underwater sound propagation for inspecting the buried pipe interior by identifying pipe corrosion or debris using the time of flight between an excited sound wave at the sonar transmitter and the reflective target. Such information can be subsequently employed for constructing a sonar image of the pipe interior (White, 2020; Liu & Kleiner, 2013; Liu et al., 2012; Hao et al., 2012). The sonar technique can also operate in a high or low frequency mode with comparative advantages and disadvantages using either mode. With high sonic frequencies, more accurate detection of pipe defects is possible but at the expense of rapid signal attenuation along the pipe. Low frequencies, on the other hand enable greater penetration but lower image resolution of the pipe interior (Liu & Kleiner, 2013; Liu et al., 2012). Hao et al. (2012) also noted that the sonar technique can be operated in air or water but not simultaneously.

Compared to the sonar technique, a more portable, free-swimming acoustic device for buried pipeline inspection is the SmartBall® inspection tool (Figure 2.4a). During operation, the SmartBall® travels along the pipe, propelled by the internal pipe flow, while using on board acoustic sensors to identify leaks along the pipe (Pure Technologies, 2020; Ariaratnam & Chandrasekaran, 2010; Fletcher & Chandrasekaran, 2008). The SmartBall® device is deployed by insertion into an entry point such as a valve and subsequently retrieved at a separate valve downstream of the entry point. Acoustic data, acquired by the SmartBall® module as it travels within the pipe, is later analysed upon retrieval of the device for leak identification. In addition to the need for careful planning of the SmartBall® route along the pipe, Lee (2017) and Liu et al. (2012) also noted that the technique may not work in pipelines with water pressures above 400 PSI.

Another commercially available acoustic technique for the in-service inspection of buried pipelines is the Sahara® system which uses a tethered hydrophone moving along the pipe interior while recording leak noises (Figure 2.4b) (Liu & Kleiner, 2013; Costello et al., 2007; Bond et al., 2004). As described by Bond et al., (2004), the Sahara® system involves the insertion of a hydrophone (attached to a drogue) into the water pipe through a conventional 50 mm (or larger) tap. A secondary operator, equipped with an extremely low frequency (ELF) transmitter is located above the ground to track the hydrophone progress through the pipe, thus pinpointing the leak. Although the Sahara® system can be used in pipes as small as 150 mm in diameter, the Sahara® system, like other technologies such as the SmartBall® and sonar systems, needs to be deployed within the pipe (Lee, 2017; Liu et al., 2012). As Pal (2008) however noted, invasive sensor deployment within a potable water pipe, for example, introduces the risk of water contamination which can introduce further maintenance costs to the utility owner.

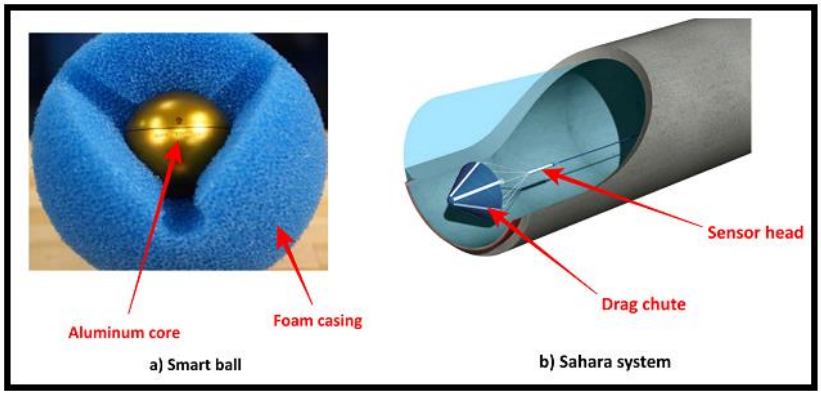

Figure 2.4a): Smart ball and b) Sahara inspection systems (Kumar et al., 2020)

Non-invasive acoustic techniques for buried pipeline inspection also exist in the literature and these include impact echo, Acoustic Pipe Wall Assessment (APWA), acoustic emission, leak noise detection and location as well as ultrasonic techniques. The impact echo technique uses impact generated stress waves (arising from a controlled impact such as a falling object or a pneumatic hammer) which propagate through and are reflected by the object under test (Liu & Kleiner, 2013; Hao et al., 2012; Markar & Chagnon, 1999). Based on the frequency, wave speed and penetration depth of the received acoustic wave, a mapping of this information to the buried pipe and surrounding soil conditions can subsequently be made. Markar & Chagnon (1999) however noted that at the time of writing, commercially available versions of this technology were manual in nature and required human entry into the pipe. To date, at least to the best of the author's knowledge, no commercially available improvement to this process with automated access to smaller pipelines exists in the literature.

A more recent technique using external acoustic impact for pipe condition assessment is the APWA. With APWA, acoustic signals are induced along a pipe (e.g., by striking a valve connection) and subsequently measuring the acoustic wave speed as it travels along various sections of the pipe using external sensors positioned along the pipe (Kumar et al., 2020; Echologics, 2020; Nestleroth et al., 2013). The average pipe wall thickness between adjacent sensors is further calculated by relating the acoustic wave speed to the pipe hoop stiffness, with

a weaker pipe wall showing greater flexing as the sound travels along the pipe (Kumar et al., 2020). A commercially available application of the APWA technique is the ePulse® pipeline condition assessment tool developed by Echologics for the condition assessment of metallic, AC and PCCP pipes. The ePulse® tool features the installation of acoustic sensors along two separate hydrants or valves while a third hydrant/valve is acoustically induced by tapping it for example. Each acoustic sensor subsequently captures the acoustic signal as it propagates along the pipeline before the data is collected and analysed on site. The range of pipe materials for which the ePulse® technique is applicable does not however cover plastic pipes and moreover, the other APWA tools described in Nestleroth et al. (2013) feature invasive sensor deployment within the buried pipeline.

An acoustic pipe inspection technique which does not require external pipe excitation is the acoustic emission technique. Acoustic emission is based on the detection of sound waves generated within the pipe wall during sudden events which compromise its structural integrity such as a leak or crack (Lee, 2017; Martini et al., 2017; Liu et al., 2012; Anastasopoulos et al., 2009). For buried pipeline inspection, Anastasopoulos et al. (2009), for example, performed several case studies (for both new and in-service buried pipelines) on leak detection and location using portable acoustic emission sensors (PAC5120 from Physical Acoustics). Anastasopoulos et al. (2009) subsequently reported the successful detection and location of suspected leaks along the buried pipelines using the acoustic emission technique. Additional measurement access points however needed to be dug on several occasions, to narrow down the suspected leak area along the buried pipeline to within a few metres. More recently, the use of acoustic emission for buried pipeline condition assessment has been directed towards a more long-term approach where the buried pipe is continuously monitored for signs of failure (e.g., Pure technologies, 2020; Paulson et al., 2014) and will be discussed in Section 2.3.2.

A similar technique to acoustic emission, but without the need for multiple excavations, is the leak noise detection and location technique. With this technique, acoustic sensors such as accelerometers are mounted along valves or fire hydrants to detect leak induced vibration along the buried pipeline (Liu & Kleiner, 2013; Liu et al., 2012). A commercially available tool, the LeakFinderST (formerly known as LeakFinderRT) from Echologics features the deployment of easily detachable acoustic sensors at convenient access points along the pipe (e.g., valves or fire hydrants) to monitor a segment of the buried pipe (Kumar et al., 2020; Anguiano et al., 2016; Echologics, 2020). The LeakFinderRT deployment set-up is shown in Figure 2.5.

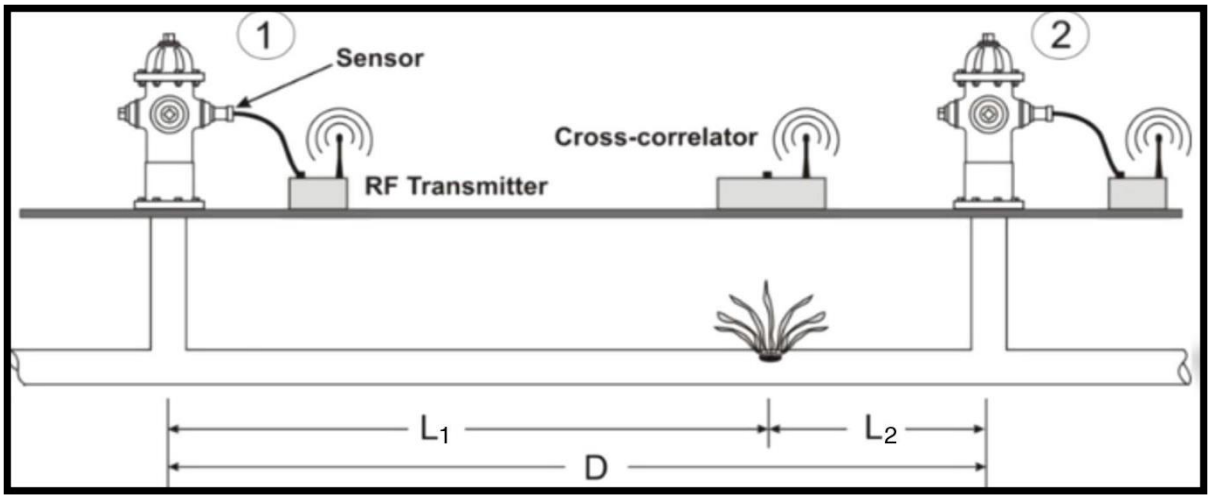

Figure 2.5: LeakFinderRT deployment along a buried water pipe (Kumar et al., 2020)

As shown in Figure 2.5, during operation a pair of acoustic sensors are installed either side of a suspected leak with each of the sensors connected to a wireless radio frequency (RF) transmitter via a cabled connection. The RF transmitters are linked wirelessly to a cross-correlator receiver where cross-correlation of the leak signal is performed on-site to locate the suspected leak. The main limitations of the LeakFinderRT include sensor spacing requirements (which are influenced by the pipe material and diameter due to acoustic signal attenuation along the pipe), need for the presence of pipe access points such as valves or fire hydrants (otherwise holes may need to be excavated to allow direct access to the pipe), limited information about

the leak size and susceptibility to low frequency vibrations from external sources such as pumps and vehicular traffic (Anguiano et al., 2016; Liu et al., 2012).

To overcome the challenge of low frequency interference, a high frequency approach to the acoustic condition assessment of buried pipelines is the ultrasonic method of pipe inspection. Ultrasonic techniques involve ultrasound transmission (>20 kHz) into a target object before analysing the received echo for the detection of structural defects along the object (Liu et al., 2012). Ultrasonic techniques for buried pipeline inspection include discrete and guided wave ultrasonic testing. Discrete ultrasonic testing for buried pipeline inspection involves ultrasonic transmission through a couplant into the pipe under test. The ultrasonic wave can be generated by piezoelectric ceramics, electromagnetic acoustic transducers, magnetostrictive transducers or laser and piezoelectric polymers (Liu & Kleiner, 2013; Liu et al., 2012). The transducer is placed normal to the pipe surface while inspection is carried out at discrete sections along the pipe. The ultrasonic wave travels through the pipe wall and is subsequently reflected along discontinuities within the wall. The reflections (echoes) of the ultrasonic wave, detected by the transducer, are further analysed to detect structural anomalies within the pipe wall (Liu & Kleiner, 2013; Liu et al., 2012). The external condition assessment tool (ECAT) from Advanced Engineering Solutions, Ltd. is an example of a pipeline inspection tool which was employed by Nestleroth et al. (2013) for testing short (1 m length) exposed sections of buried pipeline. With discrete ultrasonic testing however, the section of the pipeline under test needs to be exposed before testing can be carried out. This can become prohibitively expensive if long sections (e.g., several metres) of buried pipe need to be tested (Rose, 2014; Nestleroth et al., 2013).

Guided Wave Testing (GWT) is an alternative ultrasonic inspection approach which allows longer sections of buried pipeline to be inspected without the need to expose the entire pipe length. GWT is based on the ability of guided acoustic waves to propagate long distances (tens

to hundreds of metres) along a pipeline waveguide (Rose, 2014; Rose et al., 2008). In GWT, the ultrasonic waves are excited by a transducer ring clamped around the pipe circumference. These transducers generate either longitudinal, flexural, or torsional waves which propagate along the pipeline (Liu & Kleiner, 2013; Liu et al., 2012). When the guided waves encounter a structural defect along the pipe wall, a reflection occurs which can be detected by the transducer ring, thus enabling the identification and location of such a defect (Lowe et al., 1998). One major challenge with GWT is the excitation of multiple wave propagation modes (coherent noise) along the buried pipe during inspection which complicates the accurate interpretation of results obtained at the transducers (Cawley, 2002). GWT thus requires *a priori* knowledge of the acoustic dispersion characteristics of the pipe under test to systematically excite the pipe with minimal dispersive noise interference (Lowe & Cawley, 2006; Cawley, 2002).

A common drawback for pipeline inspection techniques in general, is the need for on-site technical personnel and equipment deployment to successfully run inspection operations. As noted by Liu et al. (2012), labour and equipment costs for the GWT technique, for example, can reach thousands of pounds for each inspection operation. Long-term continuous monitoring of the buried pipeline asset, without the need for constant personnel and equipment deployment is therefore an attractive proposition for potentially reducing pipeline monitoring costs. Some of the techniques currently deployed across the buried utility industry for real-time pipeline monitoring are reviewed next.

2.3.2 Buried water pipe real-time monitoring

Buried pipeline real-time monitoring techniques, in terms of sensor arrangement along the pipe, can be broadly categorized as discrete and continuous sensor techniques. While the discrete approach features sensor deployment at discrete points along the pipeline network, the continuous approach features the deployment of a continuous sensor stretching across the

network. A popular continuous sensor monitoring approach is the distributed fibre optic technique. A key feature of the distributed fibre optic technique is the ability to continuously monitor buried pipeline structures over large axial extents without the need for frequent access to the pipe (Rajeev et al., 2013; Frings, 2011; Inaudi & Glisic, 2010). A more extensive coverage of the pipeline is therefore made possible with fibre optic networks since every section of the pipe can potentially be monitored regardless of accessibility (Rajeev et al., 2013; Frings, 2011). Furthermore, fibre optic sensing offers the capacity for both sensing and communication within the same physical cable (Fernandez-Vallejo & Lopez-Amo, 2012). Figure 2.6 shows one method of fibre optic deployment within an in-service buried water pipe (Paulson et al., 2014).

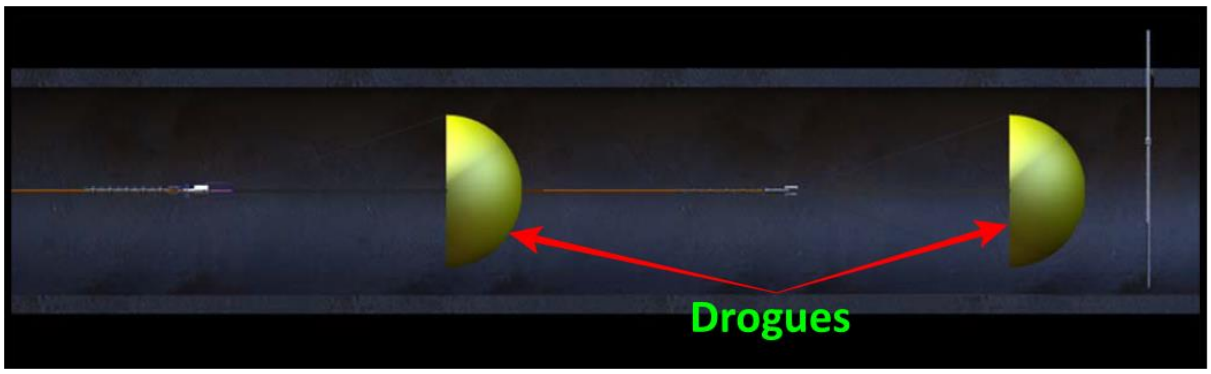

Figure 2.6: Live deployment representation of fibre optic cable within buried water pipe (Paulson et al., 2014)

As shown in Figure 2.6, a fibre optic cable can be deployed within a live water pipe by using drogues to tow a cord along the pipe. The drogues are then captured some miles downstream of the pipe before using the cord to pull in the fibre optic cable (Paulson et al., 2014). Pipe failure indicators resulting in temperature or strain anomalies along the pipe can subsequently be detected by the fibre optic cable before alerting a remote monitoring station above the ground. The SoundPrint® acoustic fibre optic (AFO) cable from Pure Technologies is an example of a commercially available fibre optic technology for the continuous monitoring of buried PCCP by sensing acoustic emission events along the pipe. One main limitation of distributed fibre optic sensors however, as noted by Sadeghioon (2014), is the inherent lack of

redundancy with this technique. For example, if a pipeline section needs to be replaced (due to damage or renewal) or the fibre optic sensor becomes damaged (due to third party interference), blind spots can be created in the distributed fibre optic network.

Discrete or quasi-distributed fibre optic sensors, where localised areas along the buried pipeline are continuously monitored, also exist in the literature (Sadeghioon, 2014; Rajeev et al., 2013; Liu et al., 2012). With discrete sensors, unlike the distributed system, redundancy is introduced into the fibre optic network as other sensors can serve as back up in the event of an individual sensor failure within the network. An example of the discrete fibre optic sensing is the fibre optic sensor for corrosion monitoring which measures pipe wall strain indicative of changes in the wall thickness (Liu & Kleiner, 2013; Liu et al., 2012). Discrete fibre optic sensors however require sections of the buried pipe to be exposed for sensor installation (Liu et al., 2012) which can further contribute to increased deployment costs.

Real-time monitoring techniques, where the sensors can be conveniently deployed at access points such as valves or fire hydrants (rather than digging holes), also exist in the literature where commercially available technologies include the Echowave® and EchoShore® systems (Echologics, 2020) as well as those listed in Anguiano et al. (2016) and Liu et al. (2012). These systems feature sensor installation at buried pipe access points before periodically transmitting acquired data to a remote monitoring station via a wireless (radio) communication network. Anguiano et al. (2016) however noted that capital equipment, maintenance, operational labour as well as contractor installation and set-up costs still need to be considered when deploying these techniques.

With the advent of low-cost integrated circuit (IC) technology, wireless sensor networks (WSN) have emerged as a cost-effective solution for real-time pipeline monitoring (Whittle et al., 2013; Akyildiz & Vuran 2010; Akyildiz et al., 2002). Wireless Sensor Networks (WSN) feature the

deployment of cost-effective integrated signal processing platforms which embody physical sensing elements or transducers for the purpose of information gathering and communication within any environment (Yick et al., 2008; Lewis, 2004). The ubiquitous nature of WSN enables the highly pervasive deployment of this technology across numerous industries such as the utility as well as oil and gas sectors (Owojaiye & Sun 2013).

A critical component of a WSN design is the choice of transmitter and receiver elements or nodes. In contrast to other networking paradigms, WSN involves the installation of nodes which have a distinctive feature of combining sensing, communication and signal processing on a single device or chip (Bulusu & Jha, 2005). Such devices are commonly known as "smart" sensors. A smart sensor, as defined by IEEE, is a physical sensor which incorporates functions beyond that of simply measuring a physical quantity. Such functions typically include signal processing, control, and communication (Frank, 2000).

One of the earliest deployments of a WSN for real-time monitoring of buried water pipes is the PipeNet monitoring system proposed by Stoianov et al. (2007). The PipeNet monitoring architecture, designed to obtain hydraulic and water quality measurements from a buried water pipe, is shown in Figure 2.7.

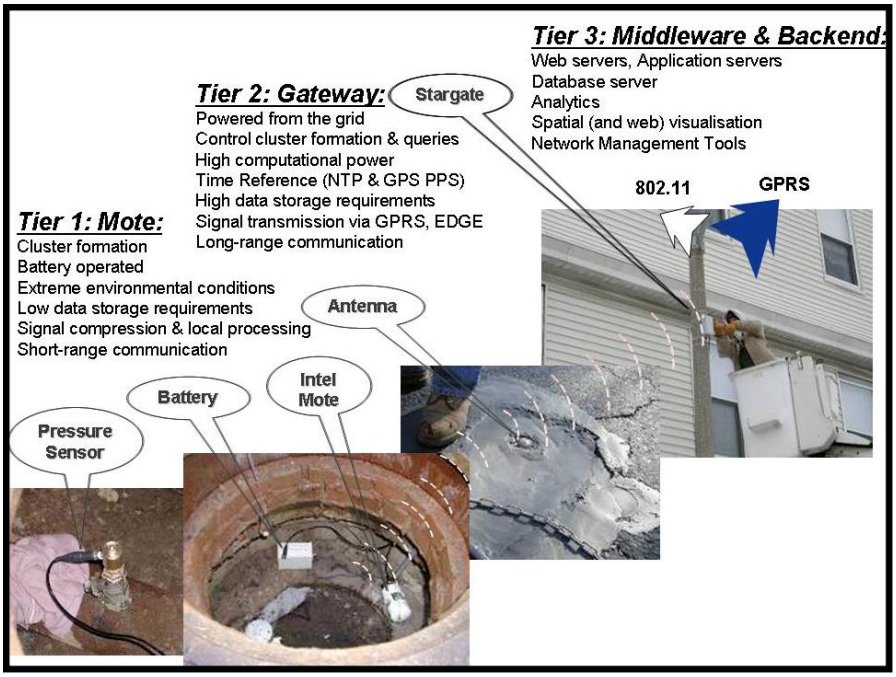

Figure 2.7: PipeNet deployment architecture (Stoianov et al., 2007)

As shown in Figure 2.7, the PipeNet deployment architecture consists of three monitoring tiers which represent the data flow path from the buried water pipe sensor to an above ground monitoring station. At the bottom tier (Tier 1), sensors are installed within the buried water pipe to collect pressure and pH data, respectively. Both sensors, which are battery operated, continuously record data at 100 samples per second (S/s) and at 5-minute intervals before transmitting the recorded data to a micro-computer (deployed on a nearby infrastructure such as a lamp post) located in the middle layer (Tier 2) of the PipeNet system. To transmit data from the in-pipe sensors to the above ground microcomputer (gateway), the in-pipe sensors are connected to a radio antenna which is embedded within the road surface (Figure 2.8) using underground cabling.

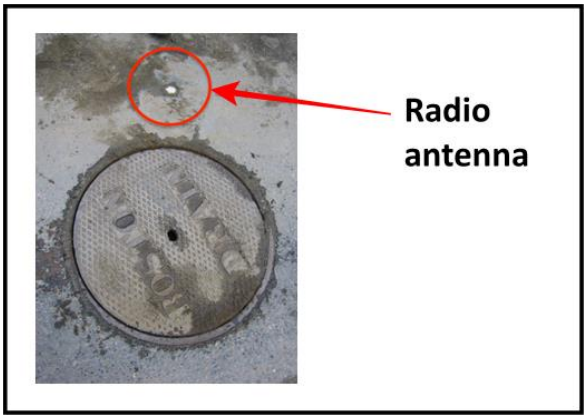

Figure 2.8: Antenna embedded within the road surface (Stoianov et al., 2008)

According to Stoianov et al. (2008), a clear line of sight (within 10-100 m) between the embedded radio antenna and the above ground gateway is required to ensure reliable data communication between Tiers 1 and 2 of the PipeNet system. Upon reception of the pressure and pH data from the Tier 1 sensors, the gateway further transmits the acquired data to above ground monitoring stations (or backend servers, according to Figure 2.7) located in Tier 3 of the PipeNet system, where further data analysis can be carried out.

A drawback for the PipeNet system is the need for a clear line of sight between the embedded radio antenna (Tier 1) and the above ground gateway (Tier 2) for reliable data communication. Since a clear line of sight may not always be possible in heavily built-up environments, this requirement can potentially pose a challenge for reliable data communication during system deployment. Another drawback with the PipeNet system is potential damage to the radio antenna embedded within the road surface. During the field trials conducted by Stoianov et al. (2008), it was discovered that a road re-surfacing operation destroyed the radio antenna, necessitating a relocation of the radio antenna to beneath a man-hole cover. Since this man-hole cover had a thickness of 4.5 cm, the overall data communication reliability was compromised (42% reduction) due to the influence of the man-hole cover in attenuating the transmitted radio signal (Stoianov et al., 2008).

A magnetic induction (MI)-based wireless underground sensor network (WSN) proposed by Sun et al. (2011), unlike the PipeNet system, can enable wireless underground communication between deployed sensors thus offering an alternative route for data communication (especially in the absence of a clear line of sight above the ground) within the WSN. This monitoring system, known as MISE-PIPE (Figure 2.9), features the deployment of both in-pipe and in-soil sensors which communicate with each other in an underground soil environment.

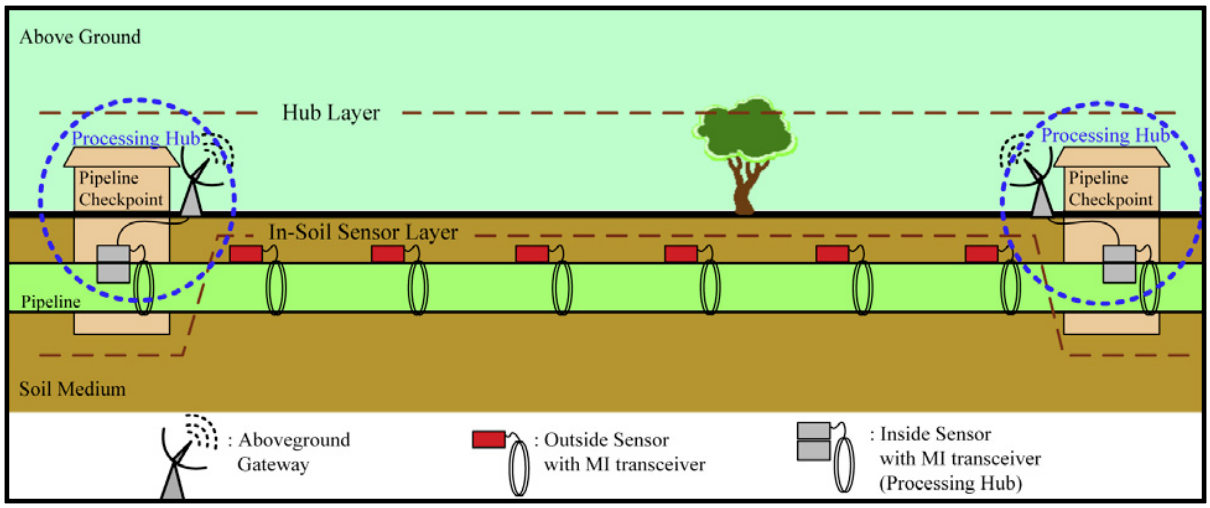

Figure 2.9: MISE-PIPE deployment architecture (Sun et al., 2011)

As shown in Figure 2.9, the MISE-PIPE system consists of a hub layer and an in-soil sensor layer. The hub layer comprises the in-pipe sensors which are deployed at specific access points (pipeline checkpoints) within the buried pipe network while the in-soil sensor layer consists of in-soil sensors which are deployed within the underground soil environment along the buried pipeline.

According to Sun et al., (2011), the MISE-PIPE architecture divides a buried water pipe network into separate sections, bordered by the pipeline checkpoints within which the pressure and acoustic sensors are installed. The in-soil sensors are further deployed along the buried pipe between two pipeline checkpoints, while communicating wirelessly with the pressure and acoustic sensors. The combination of the hub and in-soil layer sensors thus operates as a cluster

of heterogeneous sensors with the hub layer sensors acting as cluster heads and the in-soil sensors acting as cluster members. The cluster heads in the MISE-PIPE monitoring system are further responsible for gathering data from cluster members before transmitting this data (wired or wirelessly) to an above ground gateway located within the same pipeline checkpoint. Like the PipeNet monitoring system, the above ground gateway in the MISE-PIPE system is responsible for transmitting acquired data to an above ground monitoring station, via a wireless terrestrial network, where further data processing operations can be carried out (Sun et al., 2011).

The main challenge with the MISE-PIPE system concerns the establishment of a wireless underground communication link using magnetic induction signal transmission. As shown in Figure 2.9, each in-pipe and in-soil sensor requires a set of electrical coils to be wrapped around the buried water pipe, based on the magnetic induction signal transmission requirements for the MISE-PIPE system. To install the magnetic induction signal transceivers along existing water pipes, multiple sections of the buried water pipe would need to be excavated which can quickly increase deployment costs.

A separate WSN solution for buried water pipe monitoring, which does not require invasive pressure sensors or multiple electrical coils like the MISE-PIPE system, is the PipeTECT system proposed by Shinozuka et al. (2010) which employs micro-electromechanical (MEMS) sensors for acceleration measurements along a pipe surface. According to Mustafa & Chou (2012) and Shinozuka et al. (2010), a sharp change in the internal water pressure (caused by a leak event) along the pipe is always accompanied by a sharp change in pipe wall acceleration, hence MEMS acceleration sensors provide a more cost-effective solution (compared to invasive pressure sensors) for continuous pipe monitoring. For underground communication between the MEMS acceleration sensors, the PipeTECT system uses a Controller Area Network (CAN)

which, by definition, is a wired sensor network supporting data communication between sensors in a real-time monitoring application (Shinozuka et al., 2010). Although CAN enables underground data communication between the deployed sensors, the possibility of cable disconnections still presents a challenge for reliable data communication. Another challenge for wired underground communication is also the cost prohibitive nature of routing physical cables through a complex utility network (Sharma, 2012).

To eliminate the use of underground cables, a non-invasive wireless underground sensor network (WUSN) concept for buried water pipe monitoring was proposed by Sadeghioon et. al (2014). The general schematic of this WUSN architecture is shown in Figure 2.10.

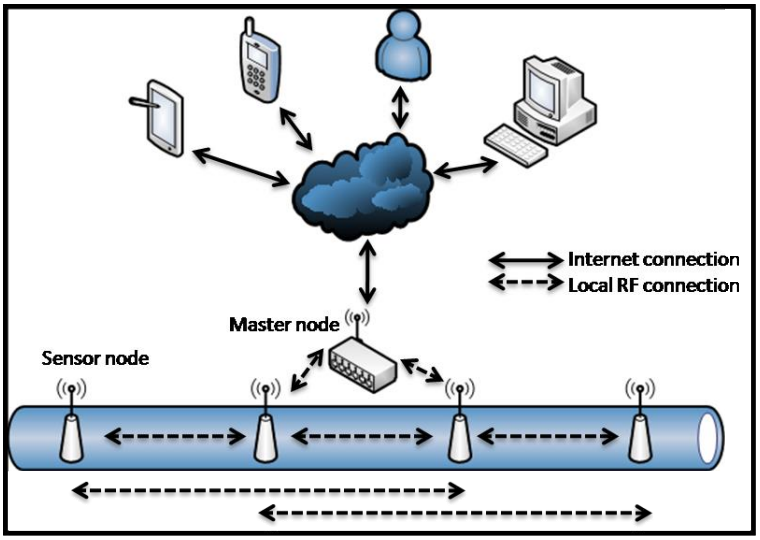

Figure 2.10: WUSN deployment concept proposed by Sadeghioon et al. (2014)

As shown in Figure 2.10, the WUSN concept proposed by Sadeghioon et al. (2014) features non-invasive sensor installation along the length of the buried water pipe. Each sensor node along the pipe communicates wirelessly with other sensor nodes in a multi-hop fashion via radio signal transmission within the underground soil environment. For every 4-5 sensor nodes (up to a maximum of 10 nodes), a master node operates as the wireless communication link between these underground sensors and an above ground monitoring station, using radio signal transmission both within the underground soil environment and above the ground (Sadeghioon

et al., 2014). Although this WUSN architecture was not specifically tested in the field, field trials were conducted by Sadeghioon (2014) on evaluating the performance of a non-invasive sensing technique (developed by the author) for integration within the proposed network. Data communication during the field trials was also implemented via radio signal transmission between a sensor node (to which the non-invasive sensors were connected) and a master node located in a nearby building. Like the PipeNet system however, the sensor node installations depended on the availability of a direct line-of-sight with an above ground master node. It is therefore apparent that key to successfully deploying a WSN for buried pipeline monitoring, is the availability of a reliable data communication link to facilitate the seamless operation of the WSN both above and below the ground. Three possible data communication channels therefore exist within a WSN, i.e., the above ground, underground to above ground as well as the underground-to-underground data communication channels. The next section briefly discusses above ground and underground to above ground data communication, before focusing on underground-to-underground data communication.

2.4 DATA COMMUNICATION FOR BURIED WATER PIPE MONITORING

2.4.1 Above ground communication

With above ground digital communication, the communication channel exists solely above the ground. Radio waves possess the ability to propagate over large distances in space thus inspiring widespread application for numerous above ground communication applications including terrestrial and satellite communication (Molisch, 2011). For buried pipeline monitoring, radio waves are typically employed for above ground communication due to the low path loss (total attenuation) they experience as they propagate through the air (Raorane & Patil, 2014). Data communication between the gateway and backend server in the PipeNet system for example, is an example of above ground data communication. For buried pipeline monitoring however,

above ground communication is only useful once data has been collected below the ground and successfully transmitted to the gateway.

2.4.2 Underground to above ground communication

In this scenario, the communication channel cuts across the ground surface thus linking underground sensors to the above ground communication network through a gateway transceiver located above the ground (Silva, 2010). For real-time monitoring, underground to above ground communication can be wired or wireless. The PipeNet and MISE-PIPE systems for example, use a wired link for establishing digital communication between in-pipe sensors and an above ground transceiver (Sun et al., 2011; Stoianov et al., 2008). As previously mentioned however, wired communication systems introduce cabling problems (such as routing costs) for buried pipeline monitoring compared to their wireless counterparts.

For wireless communication, Lin et al. (2008) proposed a technique for underground to above ground communication using radio signal propagation. With this approach, the radio transceiver is installed within a fire hydrant (FH) chamber (typically made of concrete and cast iron) below the ground as shown in Figure 2.11a. Figure 2.11b also shows the wireless communication path between the underground radio transmitter and the rest of the wireless communication network above the ground.

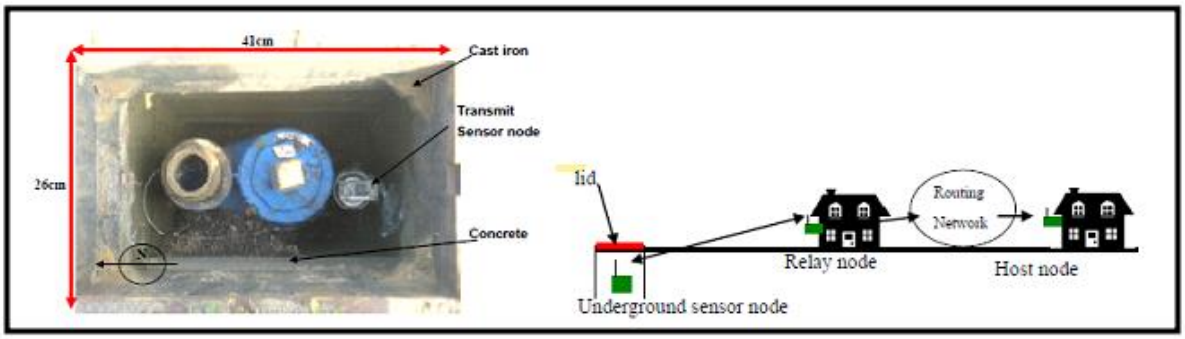

Figure 2.11a: Radio transmitter installed within fire hydrant chamber and b) radio communication path from below the ground (Lin et al., 2008)

As shown in Figure 2.11b, the radio communication path from the below ground sensor crosses the chamber lid (made of cast or ductile iron) before reaching an above ground relay node and the rest of the communication network. From their field trials, Lin et al. (2008) reported signal propagation distances of 39-80 m between the underground radio transmitter and an above ground receiver. It is however important to note here that the radio communication path was still predominantly through air (within and outside the FH chamber) even with the presence of the chamber lid (which also had air gaps and spacings through which the radio waves could propagate).

2.4.3 Underground to underground communication

For underground-to-underground data communication, the communication channel exists entirely below the ground. An underground communication link must therefore be established between individual sensors located along the buried pipeline. Like the underground to above ground case, underground-to-underground data communication can also be wired or wireless. The PipeTECT system for example, uses wired communication in the form of an underground CAN for enabling pipe monitoring (Shinozuka et al., 2010). Again, network routing using wired systems (especially underground) can be cost prohibitive for buried pipeline monitoring applications.

Wireless underground-to-underground communication using radio waves can exist through air (e.g., communication through tunnels) or through the soil (Akyildiz et al., 2009; Z. Sun & Akyildiz, 2010). For buried utility assets, the "hostile" nature of the underground soil environment poses a challenge for radio signal propagation (Akyldiz & Vuran, 2010; Akyildiz & Stuntebeck 2006). The term "hostile" in this context refers to the tendency of the underground soil environment to impede radio signal propagation. Since wireless communication (especially through air) is typically enabled by radio wave propagation, existing research for wireless

underground communication through soil has naturally focused on investigating radio signal performance in soil. Wireless communication through soil however presents a new set of challenges for radio waves. Radio waves, which are a class of electromagnetic (EM) waves tend to attenuate quickly in certain soil types due to path losses experienced by the radio wave in soil (Vuran & Akyildiz, 2008; Li et al., 2007; Akyildiz & Stuntebeck, 2006). Other causes of EM attenuation in soil include reflections at soil-air boundaries, multipath fading as well as diminished propagation velocities in the soil dielectric medium (Li et al., 2007; Akyildiz & Stuntebeck 2006).

To experimentally investigate radio signal propagation in soil, Vuran & Silva (2009) first reported field trials conducted at the University of Nebraska-Lincoln city campus in Lincoln Nebraska, using MICA2 wireless sensor nodes, operating at 433 MHz. A soil analysis report of the field test site is shown in Table 2.2.

Table 2.2: Soil analysis report of a field test site (Vuran & Silva, 2009)

Sample depth (m)	Texture	%Sand	%Silt	%Clay
0 – 0.15	Loam	27	45	28
0.15 – 0.30	Clay loam	31	40	29
0.30 – 0.45	Clay loam	35	35	30

For the field experiments, the burial depths of the radio signal transmitter and receiver were fixed at 0.4 m, while the horizontal distance between the transmitter and receiver (horizontal inter-node distance) was varied between 0.1 and 1.0 m (Vuran & Silva, 2009). The results of the received signal strength (dBm) for different radio transmit powers (dBm), as the horizontal inter-node distance was increased, are shown in Figure 2.12.

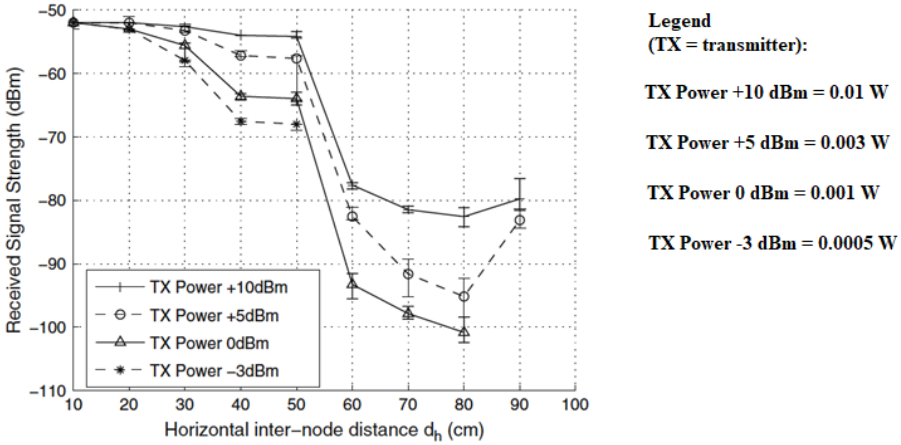

Figure 2.12: Received radio signal strength against horizontal internode distance between a radio transmitter and receiver buried in soil (Vuran & Silva, 2009)

A downward trend in received radio signal strength at increasing inter-node distances can be observed in Figure 2.12. The slight increase in received signal strength between 0.8 and 0.9 m was noted by Vuran & Silva (2009) to be likely due to radio signal reflections at the ground surface. Figure 2.13 also shows the radio signal strength to increase with radio transmitter power between 0.5 and 10.0 mW leading Vuran & Silva (2009) to suggest the use of radio transmit powers of at least 10 mW for wireless underground communication in soil. It should be noted here that although higher transmit powers will improve the receiver signal strength, there is still the constraint of limited radio transmit power available within a commercially available WSN node (e.g., the MICA2 wireless nodes used by Vuran & Silva (2009) were limited to 0.01 W). Figure 2.13 therefore suggests that the practical range of wireless underground communication with a commercially available WSN node is limited to less than 1 m.

Using a time domain reflectometry (TDR) method for measuring soil permittivity, (Sadeghioon, 2014) also conducted separate field trials for radio signal propagation in soil at a test site adjacent to an agricultural farm in the Leighton Buzzard area (Location A) and in an open area of the Severn Trent Water, Lake house facility (Location B) both in the United Kingdom. The

soil permittivity and conductivity for both sites (measured with the TDR) along with the soil classification (BSI, 1990), are shown in Tables 2.3 and 2.4.

Table 2.3: Soil properties for location "A" (Sadeghioon, 2014)

Location	Soil classification	GWC	ϵ' (F/m)	ϵ'' (F/m)	σ (mS/m)
A	Gravelly SAND (C_u = 2.00, C_k = 0.99)	12.97%	7.14	1.31	2.32

Table 2.4: Soil properties for location "B" (Sadeghioon, 2014)

Location	Soil classification	GWC	ϵ' (F/m)	ϵ'' (F/m)	σ (mS/m)
A (0.5 m depth)	Gravelly SAND (C_u = 9.43, C_k = 0.42)	17.02%	11.78	1.96	3.74
B (0.9 m depth)	Gravelly SAND (C_u = 7.87, C_k = 0.51)	20.18%	19.30	4.33	7.61

Using an ultra-low power wireless sensor node with an average power consumption of 1.31-5.25 µW, Sadeghioon (2014), like Vuran & Silva (2009), also transmitted radio signals at a maximum power of 0.01 W within the underground soil during the field trials. For location A, two separate sets of experiments involving radio signal transmission at 433 and 868 MHz were conducted by Sadeghioon (2014). During the experiments, the radio signal transmitter was placed (on separate occasions) at the bottom of three 300 mm diameter holes at depths of 200, 400 and 600 mm. The holes were subsequently backfilled with the excavated soil before a handheld radio spectrum analyser was placed at the top of each backfilled hole prior to final covering by topsoil and grass (Sadeghioon, 2014). The results of the radio signal transmission experiments for each hole are shown in Figure 2.13.

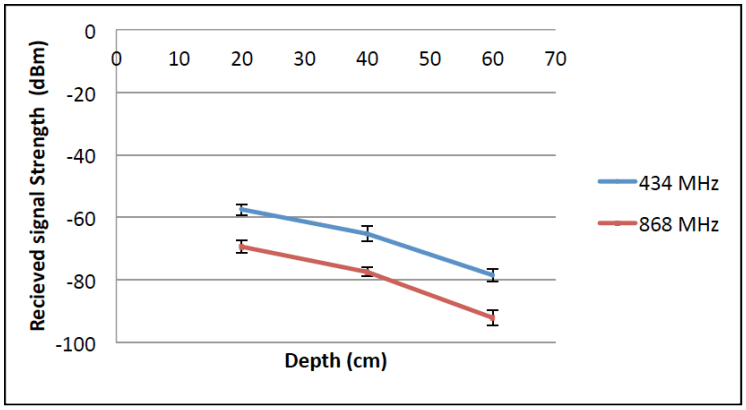

Figure 2.13: Received signal strengths at increasing soil depths from the radio transmitter at Location A (Sadeghioon, 2014)

According to Sadeghioon (2014), the radio signal transmit power at 434 and 868 MHz were 0 dBm (1 mW) and +10 dBm (10 mW) respectively. The signal strength offset in Figure 2.14, between each transmission frequency, was therefore a result of the difference in the radio signal transmission powers at each frequency. Using a noise floor threshold of – 80 dBm (1×10^{-11} W), below which a received wireless signal will be indistinguishable from background noise (Sun et al., 2011), Figure 2.13 implies a maximum radio signal transmission range of less than 0.7 m.

For location B, Table 2.4 shows the gravimetric water content (GWC), complex dielectric permittivity and electrical conductivity of the soil to increase at 90 cm depth compared to 50 cm depth within the soil. The reason for this can be seen in the lower coefficient of uniformity (C_u) and higher coefficient of gradation (C_k) of the soil at 90 cm depth compared to the soil at 50 cm depth meaning that the soil sample at 90 cm depth consisted of a higher cumulative percentage of finer particles compared to the soil at 50 cm depth. These values, according to Sadeghioon (2014), were responsible for a higher GWC as well as complex permittivity and electrical conductivity of the soil at 90 cm depth. For the location B field trials, two separate sets of experiments involving the radio signal transmitter and receiver installed at depths of 50 and 90 cm were also conducted by Sadeghioon (2014). For each radio signal transmission

experiment at each depth, the radio signal receiver was transferred between six different holes (at 60 cm spacing) which were horizontally separated from the radio signal transmitter. The results of the radio signal transmission experiments for each depth at location B is shown in Figure 2.14.

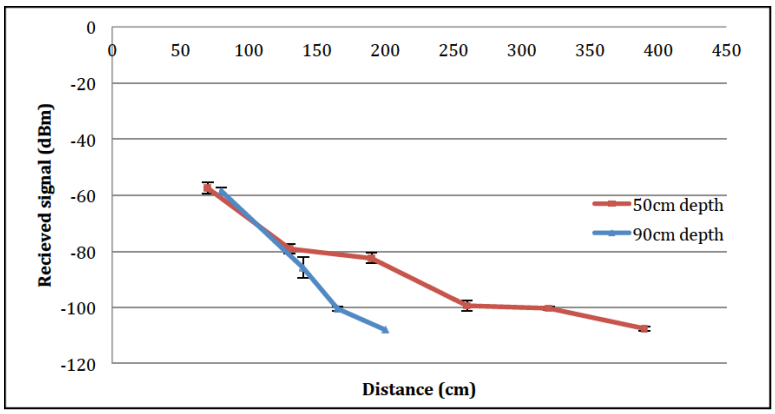

Figure 2.14: Received signal strengths at increasing distances between the radio transmitter and receiver for different soil depths at Location B (Sadeghioon, 2014)

From Figure 2.14, the received signal strengths at the radio receiver for 90 cm depth was significantly lower than the received signal strengths for 50 cm depth. As noted by Sadeghioon (2014), this was due to the increased soil GWC and higher permittivity values at 90 cm depth. Using the same – 80 dBm threshold previously discussed, Figure 2.14 shows a maximum radio signal transmission range of less than 2 m for either receiver depth. Results of the field trials by Sadeghioon (2014) at both locations therefore showed that, based on the available radio transmit power from the wireless sensor nodes, reliable radio signal transmission was less than 2 m even at a relatively shallow (50 cm) transmitter and receiver depth. For the radio transmitter at 90 cm, the reliable digital communication distance was predicted to be even shorter at less than 1.5 m. Since buried water pipes are typically located within the subsoil region at depths between 50-100 cm, reliable digital communication between wireless underground sensors at such depths, using radio signal transmission, is limited to less than 2 m.

Further investigation into radio signal transmission for variable soil mixtures, through controlled laboratory experiments, were conducted by Abdorahimi (2014). For the laboratory tests, the radio signal was transmitted at 434 MHz using the same wireless sensor nodes designed by Sadeghioon (2014). Both the radio transmitter and receiver antennas were placed in the soil contained within an aluminium container (60 cm length and 10 cm diameter) which was perforated at 10 cm intervals to allow variable positioning of the receiver antenna at increasing distances from the radio transmitter. Radio signal attenuation was subsequently measured using five different soil compositions and three different moisture contents shown in Table 2.5.

Table 2.5: Soil compositions for laboratory-based radio propagation experiments in Abdorahimi (2014)

Sand (%)	Clay (%)
10	90
30	70
50	50
70	30
90	10

Laboratory results of radio signal transmission, conducted by Abdorahimi (2014), for the different soil mixtures in Table 2.5 and at 20% GWC and +10 dBm (10 mW) radio transmit power, are shown in Figure 2.15.

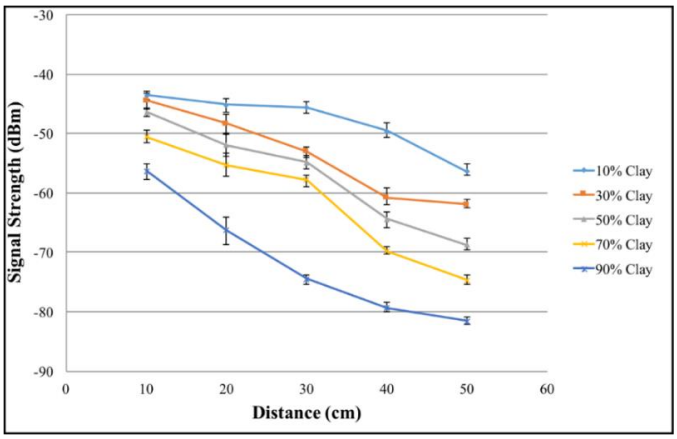

Figure 2.15: Received signal strengths at increasing distances between the radio transmitter and receiver for different soil compositions (Abdorahimi, 2014)

Figure 2.15 shows, as expected, a reduction in the received signal strength at increasing distances of the radio receiver from the transmitter. The signal attenuation also increases with increasing clay content due to higher complex permittivity with increasing clay content (Abdorahimi, 2014). Using the – 80 dBm threshold for the 90% clay soil sample, the maximum radio transmission distance, as shown in the figure, is less than 0.5 m which further illustrates the limited radio propagation range in a soil sample with high clay content.

The results presented in Vuran & Silva (2009), Sadeghioon (2014) and Abdorahimi (2014) show that for a buried pipeline monitoring application, the expected wireless underground communication range using radio signal propagation with commercially available wireless sensor nodes does not exceed 3 m (even in the best of cases). For pipelines where individual lengths of buried water pipes can extend for several kilometres, the cost of installing wireless sensor nodes at these short distances along the buried water pipe can quickly become prohibitive for a utility owner.

In response to the challenge of limited radio signal propagation range within an underground soil environment, an alternative technique for wireless signal transmission was proposed by Sun & Akyldiz (2010) and Akyldiz et al., (2009). This wireless signal transmission technique relies on the principle of mutual magnetic induction between two electrical coils, for signal transmission within an underground soil environment. According to Sun & Akyldiz (2010) and Akyldiz et al., (2009), magnetic induction (MI)-based signal transmission presented a promising alternative to radio-based signal transmission because, unlike an electromagnetic field, a magnetic field shows little variation in air, water, or soil (due to the similar magnetic permeabilities of air, water, and most types of soil). It was therefore argued that MI-based signal transmission would be largely unaffected by the presence of soil or water within an underground soil environment (Sun & Akyldiz, 2010; Akyldiz et al., 2009).

As acknowledged by Sun et al. (2011) however, the performance of the MI signal transmission technique using field trials along buried water pipes, remains to be evaluated. At the time of conducting this review, there was still no evidence in the literature concerning the field development of the MI signal transmission technique. Furthermore, based on the fundamental equations for the MI signal transmission technique (Sun & Akyldiz, 2010; Akyldiz et al., 2009), MI signal path loss within an underground soil environment is affected by changes in the radius of electrical coils which need to be wrapped around the pipe to facilitate MI signal transmission. The implication of this requirement is that an electrical coil of specific parameters (such as coil resistance and capacitance) is only useful for a buried water pipe of specific diameter if a signal transmission range within tens of metres is to be achieved. Deploying the MI communication system along a complex buried pipeline network featuring multiple pipes of different diameters will therefore require the frequent re-design of the MI relay coils, which would inevitably result in increased deployment costs for a utility owner.

A separate (non-EM or MI-based) approach for enabling wireless underground communication through soil, which has been considered in the literature (although to a comparatively limited extent), is by using the buried water pipe as an acoustic waveguide. The next section further discusses this possibility by reviewing previous research efforts which have been undertaken to achieve this purpose.

2.5 ACOUSTIC COMMUNICATION ALONG A WATER PIPE WAVEGUIDE

Unlike radio and MI signal transmission, acoustic signal transmission requires the presence of a material medium for wave propagation between a communication transmitter and receiver. An acoustic waveguide in the form of a water pipe consists of two channels through which acoustic communication is possible, i.e., the internal fluid medium of the pipe and the pipe wall.

Acoustic communication within the internal fluid medium of a water pipe is further reviewed next.

2.5.1 Underwater acoustic communication within a pipe

The earliest comprehensive study of acoustic based digital communication within a water pipe was conducted by Kokossalakis (2006). According to Kokossalakis (2006) and Kondis (2005), the general equation of motion for acoustic wave propagation within the internal fluid medium of a water pipe waveguide can be expressed as

$$\nabla^2 \emptyset = \frac{1}{c^2}\frac{\partial^2 \emptyset}{\partial t^2} \tag{2.1}$$

Where $\emptyset$ (m^2/s) is the acoustic velocity potential, c (m/s) is the acoustic wave velocity in the internal fluid medium and t (s) is time. The solution to Equation (2.1) for an acoustic signal propagating outward from an internally located acoustic signal source within the water pipe, as derived from Kausel (2006), can be expressed as

$$\emptyset(r, \theta, z) = (c_1 \cos(n\theta) + c_2 \sin(n\theta)) J_n(k_a r) e^{-ik_z z} \tag{2.2}$$

Where r (m), θ (m) and z (m) are the radial, circumferential and axial displacements respectively of the propagating acoustic wave, J_n is a Bessel function of order n, k_a and k_z are radial and axial wavenumbers along the water pipe respectively and c_1 and c_2 are constants.

Kokossalakis (2006), using numerical simulations, further investigated acoustic signal propagation along a cast iron pipe during excitation from an acoustic source located within the pipe. The main objective of the simulations was to examine acoustic dispersion along the pipe initially for the simplified case of a perfectly rigid pipe surrounded by vacuum and then for a flexible pipe buried in soil. Acoustic dispersion, for the purpose of definition, refers to the time, frequency, and phase changes of a transmitted acoustic signal along a water pipe waveguide,

due to the influence of the waveguide in distorting the spatial form of acoustic signal during propagation along the pipe (Kokossalakis, 2006).

For the rigid pipe approximation, the water pipe radius was set as $R = 0.5$ m, while the acoustic wave velocity, density and material damping of the internal fluid medium were set as 1500 m/s, 1000 kg/m^3 and 0.1% respectively. For acoustic excitation at 5 kHz, Figure 2.16 shows the simulation results at 10 m, 100 m and 500 m along the pipe (Kokossalakis, 2006).

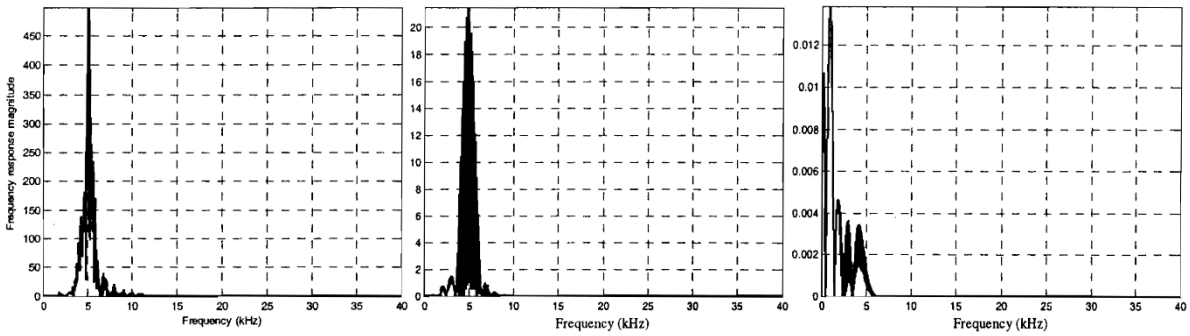

Figure 2.16: Frequency response spectrum for acoustic signal propagation at a) 10 m, b) 100 m and c) 500 m (Kokossalakis, 2006)

As shown in Figures 2.16a and b, the frequency response magnitude of the transmitted acoustic signal at 10 m and 100 m along the water pipe waveguide, peaked at 5 kHz. Figure 2.16c however showed a shift in the peak acoustic signal frequency at 500 m along the pipe towards frequencies less than 5 kHz. As noted by Kokossalakis (2006), acoustic signal reverberation within the water pipe waveguide results in the rapid decay of high frequency acoustic waves exemplified by the low-pass filter behaviour of the pipe at increasing distances.

For the same pipeline waveguide and at a transmitter-receiver distance of 10 m, the author also observed that for increasing acoustic excitation frequencies (1 kHz, 5 kHz, and 10 kHz), an increasing number of acoustic propagation modes (which contributed to increased reverberation along the pipe) was excited along the pipe. Furthermore, increasing the pipe diameter also

showed increased reverberation within the pipe due to the excitation of more acoustic propagation modes for the larger pipes.

Kokossalakis (2006) further investigated the effect of pipe wall flexibility and surrounding soil properties on acoustic signal propagation along a buried water pipe. As noted by the author, a buried flexible water pipe will transmit acoustic energy through the pipe wall into the surrounding soil, further contributing to acoustic signal attenuation (through radiation damping) along the pipe. The simulation results for separate acoustic signal propagation distances of 10 and 100 metres along a buried cast iron pipe and for a signal transmission frequency of 1 kHz, pipe wall thickness of 2 cm and surrounding soil acoustic wave velocity of 200 m/s, are shown in Figure 2.17.

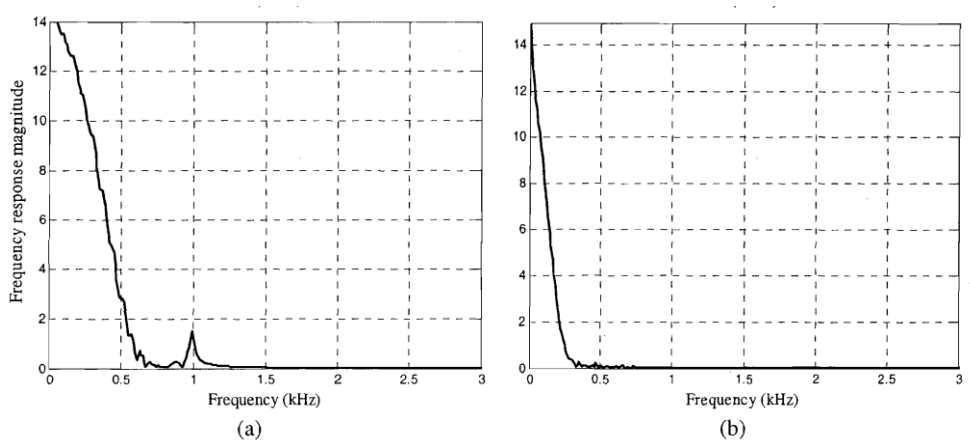

Figure 2.17: Simulation results for acoustic signal propagation along a buried water pipe at a) 10 m and b) 100 m (Kokossalakis, 2006)

From Figure 2.17a, for single squared pulse excitation of 1 kHz at the acoustic signal transmitter, most of the acoustic signal energy at 10 m along the buried water pipe was concentrated below 500 Hz. This low pass filter behaviour of the buried water pipe was significantly more prominent at 100 m (Figure 2.18b), where most of the acoustic signal energy was concentrated below 250 Hz. The key observation from these results, as noted by Kokossalakis (2006), was therefore the increased low-pass filtering of high frequency acoustic

signals (due to radiation into the surrounding soil) compared to the rigid pipe in space. The author also interestingly observed that this low-pass filtering effect was more pronounced for larger pipes due to a reduced pipe wall stiffness with increasing radius which allowed more high frequency acoustic waves to radiate into the surrounding soil. For increasing pipe wall thickness between 10 mm and 10 cm, the author also noted a reduction in acoustic wave radiation into the surrounding soil for thicker pipes due to a correspondingly increased pipe wall stiffness which prevented the acoustic waves from escaping into the soil.

The influence on surrounding soil stiffness on acoustic wave propagation along the buried pipe was also examined by considering two extreme cases of soil acoustic wave velocities of 0 m/s (corresponding to no surrounding medium) and 2000 m/s (corresponding to soil with high mechanical stiffness, i.e., "stiff" soil) in addition to the default case of 200 m/s (corresponding to soil with low mechanical stiffness, i.e., "soft" soil). The results showed that while (as expected) no acoustic radiation occurred for the case of the pipe with no surrounding medium, less radiation occurred from the pipe into the hard soil compared to the soft soil indicating the contribution of the hard soil in increasing the pipe wall stiffness thus reducing acoustic radiation into the soil (Kokossalakis, 2006). The influence of pipe material on acoustic signal propagation was also examined by the author with the results showing an increased low-pass filter behaviour as well as signal attenuation (due to radiation into the surrounding soil) for a polyvinyl chloride (PVC) pipe compared to the cast iron pipe.

To experimentally examine acoustic communication along a water pipe, Kokossalakis (2006) further designed the laboratory set-up shown in Figure 2.18.

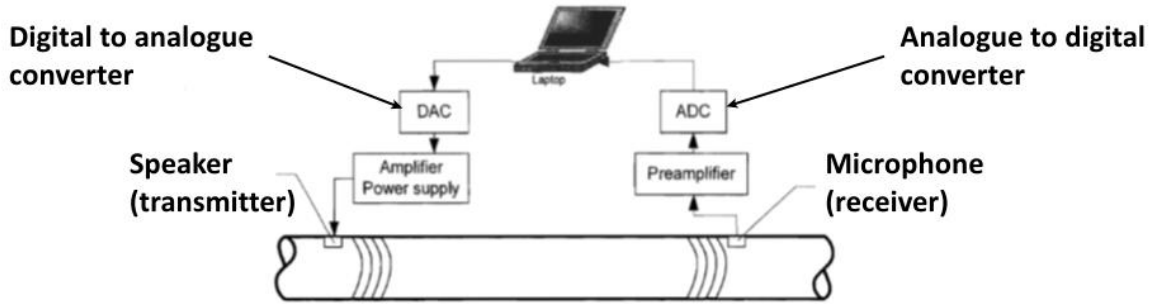

Figure 2.18: Experimental set-up for an acoustic communication system (Kokossalakis, 2006)

As shown in Figure 2.18, the laboratory set-up comprised an in-pipe speaker (acoustic transmitter) and microphone (acoustic receiver) installed at either end of the pipe for acoustic wave generation and detection, respectively. The pipeline waveguide employed by the author was an empty polyvinyl chloride (PVC) pipe of 100 mm diameter and 9 m length. Both the speaker and the microphone were connected to a laptop station which was responsible for signal processing of the acoustic signal. To enable digital communication, the speaker was connected to the laptop via a digital to analogue converter (DAC) and power amplifier while the microphone was connected to the laptop via a signal pre-amplifier and analogue to digital converter (ADC). While the DAC was responsible for converting digital information into a continuous signal at the communication system transmitter, the ADC was responsible for converting the continuous signal (detected by the microphone) back into a digital format (Kokossalakis, 2006).

To examine the performance of the digital communication system, Kokossalakis (2006) investigated three separate digital modulation techniques for data transmission at 1-7 kilobits per second (kbps) along the pipe. These modulation techniques were the frequency shift keying (FSK), amplitude shift keying (ASK) and quadrature amplitude modulation (QAM) methods. With FSK modulation, very high bit error rates (BER) of 32%, 30% and 34% at 1, 4 and 7 kbps

respectively were recorded along the pipe (Kokossalakis, 2006). As observed by the author, this high BER was mainly due to the dispersive nature of the pipe waveguide. Such dispersion resulted in the time spreading and frequency shifting (multipath propagation) of the acoustic signal causing erroneous digital information recovery at the receiver. Like FSK modulation, ASK modulation also showed very high BER of 36%, 35% and 38% 1, 4 and 7 kbps, respectively. Digital communication performance was even worse with the QAM technique with recorded BER of 76%, 80% and 68% at 1, 4 and 7 kbps, respectively. As noted by the author, these poor performances were mainly due to channel-imposed corruption of the transmitted digital information due to acoustic dispersion along the pipe.

It was therefore concluded by Kokossalakis (2006) that, to achieve reliable digital communication along the water pipe structure, additional signal processing components were needed to complement the already existing signal processing components of the digital communication system. The additional components included channel encoding, stacking and equalisation. Following their implementation, the author reported a BER performance of 0% at 1, 4 and 7 kbps. Although digital communication was completely reliable in this case (BER of 0%), two challenges arise for practical deployment within a WSN for buried water pipe monitoring. Firstly, an increase in signal processing complexity inevitably results in increased power demands at the digital communication transmitter and receiver (Kokossalakis, 2006). Such power consumption requirements may therefore result in the need to regularly replace the power sources of the digital communication system which is likely to become costly for long term buried water pipe monitoring. Secondly, increased signal processing complexity often necessitates a corresponding increase in size of the circuit hardware responsible for conducting the signal processing functions (for example, where more than one acoustic signal receiver was needed within the water pipe to improve data communication reliability in Kokossalakis (2006)). For buried water pipe monitoring where access to the pipe is limited, this hardware

increase be challenging since access to the entire circumference of the pipe is often needed especially for receiver installation. It should also be noted here that the Kokossalakis (2006) experiments were limited to an exposed, empty pipe in the laboratory without further practical examination of digital communication in fluid filled pipes (either in the lab or in the field). Another attempt at in-pipe acoustic communication was also conducted by Kantaris & Makris (2015) using FSK digital modulation along a water filled pipe 5 m length. For the system, digital communication was achieved along the pipe at 21 bps using 6.25 W at the digital communication nodes. Like Kokossalakis (2006) however, these experiments were also limited to laboratory tests with no further validation in the field.

A common drawback for in-pipe acoustic communication is the invasive nature of the acoustic transducers, i.e., the transducers need to be installed within the pipe. As previously mentioned in Section 2.3, invasive transducer deployment (particularly for potable water pipes) can pose health and safety risks customers (due to potential water contamination) in addition to the potential costs of creating access points within the pipe. To eliminate the need for invasive acoustic transducer deployment, a non-invasive acoustic communication system was proposed by Joseph et al. (2017). In this work, a pair of piezoelectric transducers was employed for acoustic signal transmission along a buried water pipe as shown in Figure 2.19.

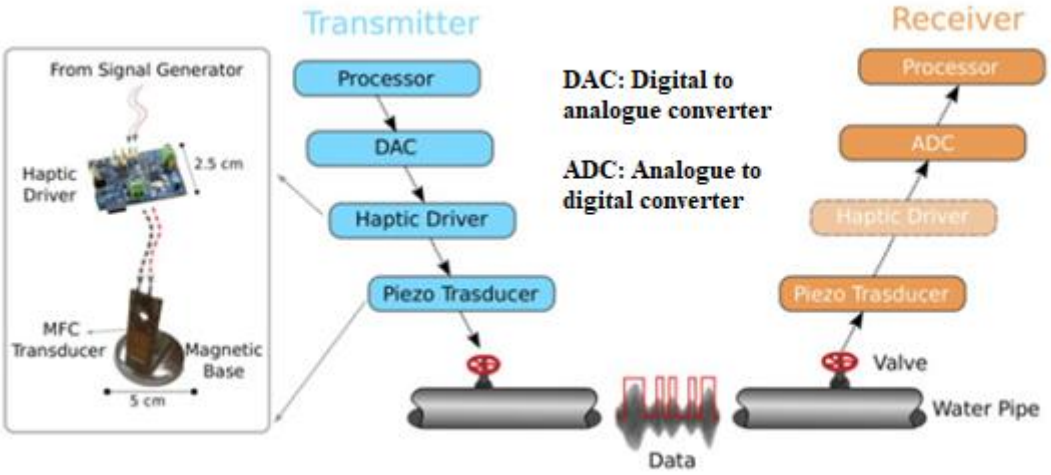

Figure 2.19: Acoustic communication system design for a buried potable water pipe (Joseph et al., 2017)

As shown in Figure 2.19, the acoustic communication system designed by Joseph et al. (2017) featured the installation of separate piezoelectric transducers along a metallic (mild steel) pipe using magnetic resonators to couple acoustic energy between the transducers and the pipe. The piezoelectric transducers employed for the system design were macro fibre composite (MFC) transducers developed by Smart Materials (2015). The choice of piezoelectric transducers and installation method enabled quick and convenient deployment of the acoustic transducers along the pipe, a necessary requirement for long-term wireless underground communication in buried water pipe monitoring (Joseph et al., 2017).

With the digital communication transmitter and receiver placed 40 m apart, digital information was transmitted using an acoustic wave propagating at 500 Hz within the internal fluid medium of the pipe (Joseph et al., 2017). Although the BER results for the digital communication experiments were not explicitly stated, a data transmission success rate of 70% was reported using amplitude and frequency modulation (AM and FM) for data transmission at 100 kbps along the pipe. This corresponded to a BER of 30% which is still relatively high considering that 0% BER was achieved by Kokossalakis (2006) albeit only in the laboratory. Although the experiment reported by Joseph et al. (2017) was the only practical investigation into acoustic

communication along a buried water pipe, the experiment relied on a potable water pipe of metallic nature where the acoustic communication channel was the internal fluid medium. It is still therefore unclear if reliable wireless underground digital communication is possible at similar distances using acoustic wave propagation along not only buried non-metallic pipes but also along empty or partially filled water pipes.

As previously mentioned at the beginning of this section, acoustic communication along the pipe wall represents another approach to enabling data communication along a pipe. The next section further reviews previous research efforts into acoustic based data communication along the pipe wall.

2.5.2 Acoustic communication along the pipe wall

Acoustic communication along a pipe wall is based on three-dimensional elastic wave propagation along the pipe, the fundamental equation of which can be expressed as (Rose, 2014)

$$\mu\nabla^2\vec{U} + (\lambda + \mu)\nabla\nabla.\vec{U} = \rho\left[\partial^2\vec{U}/_{\partial t^2}\right] \qquad (2.5)$$

Where $\vec{U}$ is the displacement field, which is a function of the three cylindrical coordinates (axial, radial and circumferential) t (s) is time, ρ (Kg/m^3) is the pipe material density and λ and μ are the Lamé constants. Based on the theory of elasticity and by applying traction free boundary conditions to the pipe inner and outer surfaces, the general solutions to Equation (2.5) lead to a set of eigenvalues which produce dispersion curves (i.e., graphs of acoustic phase velocity against frequency) such as that shown in Figure 2.20 for an empty plastic pipe.

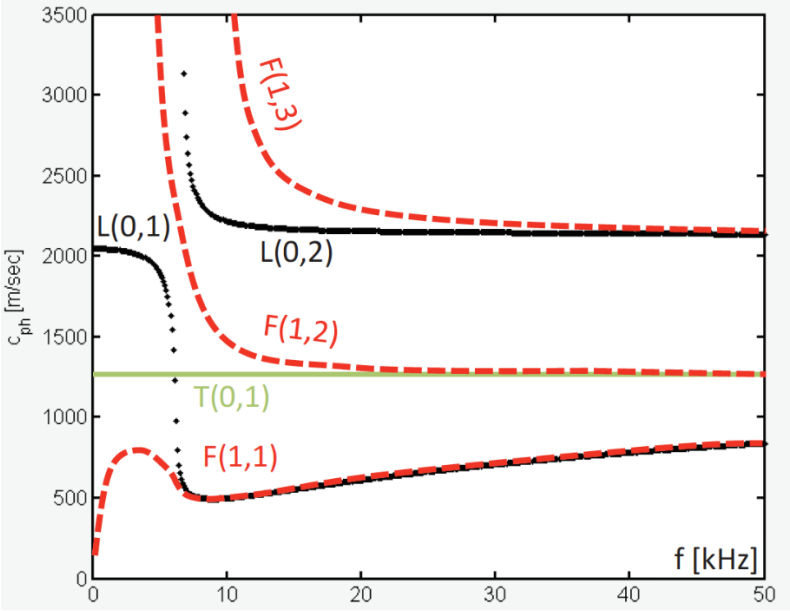

Figure 2.20: Sample dispersion curves for an empty plastic pipe at 0-50 kHz acoustic excitation (Wockel et al., 2015)

From Figure 2.20, the sample dispersion curves for an empty plastic pipe within the frequency range of 0-50 kHz consist of multiple acoustic wave propagation modes of separate phase velocity (c_{ph}) per unit frequency. The acoustic propagation modes can further be categorised as longitudinal (L), flexural (F) and torsional (T) acoustic wave modes. While the longitudinal wave modes have dominant particle motions in either the axial or radial directions, the torsional wave modes have dominant particle motions in the circumferential direction. The flexural wave modes, on the other hand, have negligible particle motion in the axial direction (Wockel et al., 2015).

Furthermore, each acoustic wave mode can be characterised as either axisymmetric or non-axisymmetric. For an axisymmetric acoustic wave mode, there is no circumferential variation around the pipe circumference while the opposite is the case for a non-axisymmetric mode. For convenience, each propagating acoustic wave mode along the pipe is nominally represented as either L, T or F (m, n). According to this notational convention, *m* represents the circumferential order (where 0 denotes an axisymmetric wave) of the acoustic wave mode while *n* represents

the group order (i.e., a number which classifies the wave modes according to their group velocities) of the same acoustic wave mode. Using this knowledge, Figure 2.20 therefore shows that the longitudinal and torsional wave modes are axially symmetric along the water pipe waveguide while the flexural wave modes are non-axisymmetric.

For acoustic communication along a pipe wall, the most notable attempt (at least to the best of the author's knowledge) in the literature was reported by Jin et al. (2013). In this work, a time reversal pulse position modulation (TR-PPM) technique was proposed in view of minimizing the signal processing requirements which, as previously argued by Kokossalakis (2006), is needed for ensuring reliable digital communication along a water pipe. With the TR-PPM technique, an acoustic pulse of 250 kHz centre frequency was initially transmitted along the pipe to record the dispersive influence of the pipe on the pulse. This information was subsequently employed for mitigating acoustic dispersion along the pipe by time reversing the received pulse before re-transmitting it back to the acoustic transmitter, thus eliminating the dispersive effects of the pipe on the pulse (evidenced by a sharp peak of the re-transmitted signal, with a high signal to noise ratio at the acoustic transmitter). The time reversed pulse was subsequently modulated (using PPM) at the acoustic transmitter before re-transmitting it along the pipe for final digital information recovery at the acoustic receiver.

Two sets of experiments were conducted along exposed water pipes of different materials and lengths to examine this communication system's performance. The first set of experiments were conducted along a carbon steel pipe of 1833 mm length and 70 mm diameter, while the second set of experiments were conducted along a stainless-steel pipe of 1500 mm length and 115 mm outside diameter. The physical layout for each experiment is shown in Figure 2.21.

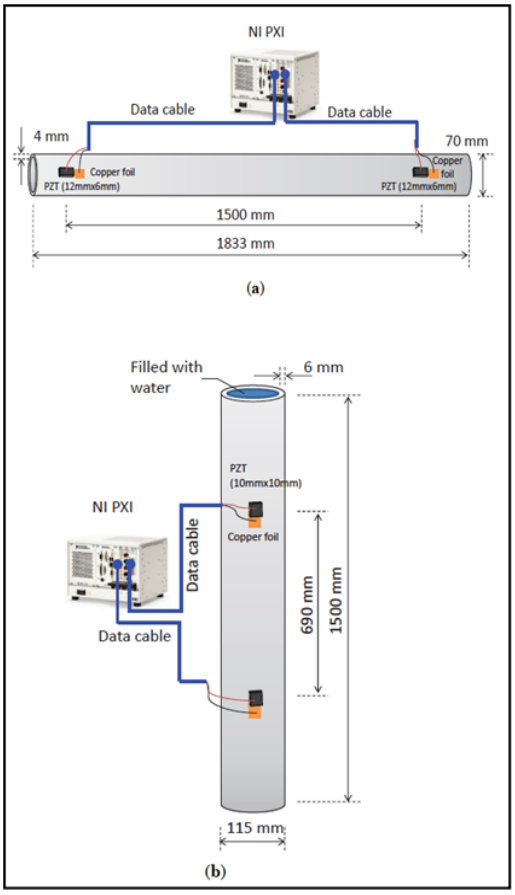

Figure 2.21: Experimental set-up for acoustic communication along a) carbon steel pipe b) stainless steel pipe (Jin et al., 2013)

As shown in Figure 2.21a, a pair of piezoelectric zirconate titanate (PZT) transducers (PSI-5A4E, Piezo Systems, Inc.) were installed along a carbon steel pipe (70 mm outer diameter and 4 mm wall thickness) at 1.5 m apart. Each PZT transducer, 12 m long and 6 mm wide, was installed along the pipe using cyanoacrylate adhesive (Jin et al., 2013). The transducers were further connected to signal National Instruments (NI PXI) system, which consisted of an arbitrary waveform generator, digital oscilloscope, and an internal controller. A similar arrangement was also employed along the stainless-steel pipe (Figure 2.21b) where the PZT transducers (10 mm long and 10 mm wide) were installed at 690 mm apart. The stainless-steel pipe was further filled with water and installed in a vertical arrangement to allow the pipe to hold the water (Jin et al., 2013). For each experiment, the waveform generator (in combination with one of the PZT transducers) was employed for transmitting digitally encoded information

(using TR-PPM) along the exposed water pipe. The digital oscilloscope (in combination with the other PZT transducer) was employed at the other end of the pipe for receiving the digitally encoded information. The results of the digital communication experiments along the carbon steel pipe are summarized in Table 2.6 (Jin et al., 2013).

Table 2.6: Results of digital communication experiments along carbon steel pipe (Jin et al., 2013)

Data rate (kbps)	Average bit error rate (%)
10	0
20	0.06
50	1.10
100	5.01

Table 2.6 shows the average BER recorded along the carbon steel pipe for data rates between 10 and 100 kbps. As shown in the results, the BER gradually increased with increasing data rate which, according to Jin et al. (2013) was due to inter-symbol interference at the digital communication receiver (which became more pronounced at shorter time intervals, i.e., higher data rates, between each digital information pulse. Similarly, the digital communication results along the stainless-steel pipe are summarized in Table 2.7.

Table 2.7: Results of digital communication experiments along stainless-steel pipe (Jin et al., 2013)

Data rate (kbps)	Average bit error rate for empty pipe (%)	Average bit error rate for water-filled pipe (%)
10	1.195	0.290
20	4.202	3.890
50	13.700	7.212
100	19.000	12.900

From Table 2.7, the average BER recorded along the stainless-steel pipe was higher for the empty pipe, compared to the water-filled pipe. These results suggested the influence of the internal water medium in dampening the propagating acoustic wave modes which, for an empty pipe, would have presented a noisier medium (i.e., coherent noise) for acoustic wave

propagation thus increasing the measured BER (Jin et al., 2013). Nevertheless, as with the carbon steel pipe, the BER for the stainless-steel pipe also increased with increasing data communication rate.

Although acoustic communication along the pipe wall was reported by Jin et al. (2013), the digital communication distance along the exposed water pipes was limited to less than 2 m. Moreover, the digital communication experiments were only conducted along exposed water pipes (of metallic nature) within a laboratory environment without further examination along buried water pipes. Furthermore, the increased BER for the exposed stainless-steel pipe implied increased acoustic dispersion along the water pipe for which the time reversal algorithm could not adequately compensate (Jin et al., 2013). For plastic pipes, which have been shown to be significantly more dispersive compared to metallic pipes (e.g., Muggleton et al., 2002), the digital communication performance may be unreliable even at less than 2 metres.

Chakraborty & Saulnier (2015) also examined ultrasonic based acoustic communication along a 4.8 m metallic pipe (0.25 m diameter and 17.78 mm wall thickness) both in air and submerged in water within the laboratory, using a chirp on-off-keying OOK digital modulation technique to successfully transmit data along the pipe at 100 bps with less than 10 mW transmit power. Like Jin et al. (2013) however, the success of these experiments relied on the relatively lower acoustic dispersion along metallic compared to plastic pipes which allowed successful demodulation of the transmitted digital information at a limited distance of 4.8 m along the exposed pipe. There is therefore currently no evidence of the validity of this approach along buried and especially plastic pipes which are prone to higher acoustic dispersion compared to metallic pipes.

One option for minimising acoustic dispersion along a pipe is through selective excitation of specific acoustic propagation modes along the pipe, which are non-dispersive at certain

excitation frequencies. This is the method employed by the GWT inspection technique previously discussed in Section 2.3.1.2. As noted in the section however, buried pipe access limitations along with personnel and equipment deployment costs make this technique challenging for a continuous monitoring application. Another option for minimising acoustic dispersion along the pipe is to reduce the acoustic excitation frequency. As previously shown in Figure 2.20, the number of excited acoustic propagation modes along the pipe is less at lower acoustic frequencies with only three acoustic modes present below 1 kHz. The distinction between low and high frequencies along a water pipe, as noted by Pan et al. (2009), is typically defined by the ring frequency of the pipe which can be expressed as

$$f_{ring} = \frac{c_l}{2\pi a} \tag{2.9}$$

Where f_{ring} (Hz) is the pipe ring frequency, c_l (m/s) is the longitudinal acoustic wave speed along the pipe and a (m) is the pipe diameter. For most buried water pipes where diameters are less than 1 metre, the ring frequencies would generally exist above 1 kHz (Finnveden, 1997; Pinnington & Briscoe, 1994). This implies that low frequency acoustic wave propagation along a pipe can be classified as frequencies which exist below 1 kHz for most buried water pipes. At such low frequencies (where the pipe dimensions are small compared to the acoustic wavelength), acoustic wave propagation (in the form of a longitudinal acoustic wave along the pipe wall) can be modelled in one dimensional (1D) form, the governing equation which can be expressed as (Santamarina, 2001; Kinsler et al., 1999)

$$\frac{\partial^2 u}{\partial x^2} = \frac{1}{c^2}\frac{\partial^2 u}{\partial t^2} \tag{2.10}$$

Where u (m) is the particle displacement in the axial (x) direction of the pipe, c (m/s) is the acoustic wave speed and t (s) is time. The solution to Equation (2.10) can further be expressed as

$$u(x,t) = Ae^{j(\omega t - kx)} + Be^{j(\omega t + kx)} \tag{2.11}$$

Where A and B are complex amplitude constants of travelling acoustic waves along the pipe, ω (rads/s) is the acoustic angular frequency and $k = \omega/c$ is the acoustic wavenumber along the pipe. Considering material losses along an infinitely long pipe, a solution to longitudinal wave motion along the pipe is (Santamarina, 2001)

$$u(x,t) = Ae^{j(\omega t - \gamma^* x)} = Ae^{-\alpha x}e^{j(\omega t - kx)} \tag{2.12}$$

Where $\gamma^* = k - j\alpha$ is the complex propagation constant with the real part (k) representing the acoustic wavenumber and the imaginary part (α) representing the attenuation coefficient (i.e., decay in acoustic amplitude with increasing axial distance (x) along the pipe as shown in Figure 2.22).

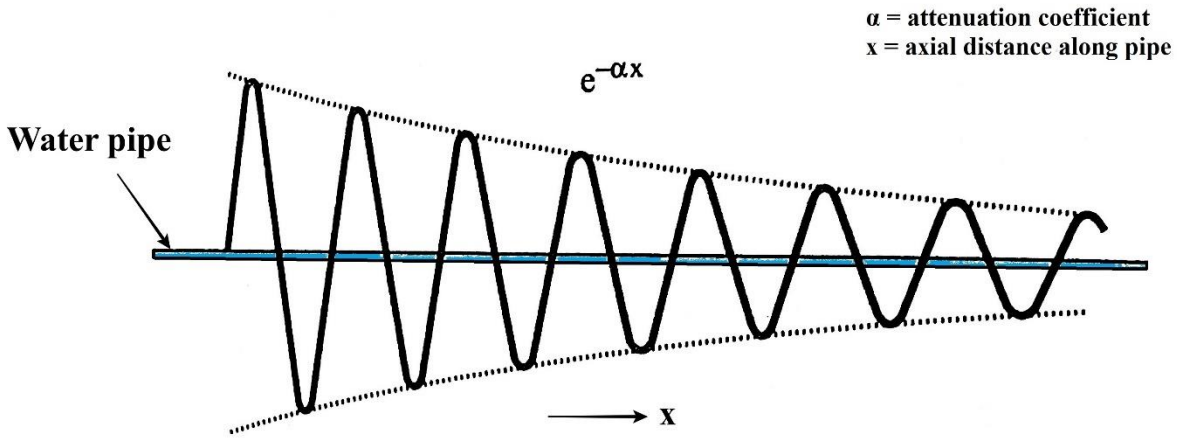

Figure 2.22: Acoustic signal attenuation along an infinitely long pipe

Within a buried water pipe network however, the presence of pipe wall discontinuities at pipe junctions and bends creates interfaces at which the travelling acoustic waves reflect and

subsequently superpose on travelling incident waves along the pipe. As the incident travelling wave along the pipe is reflected at the pipe wall discontinuity, a right-going travelling wave is superposed on a left-going reflected wave resulting in a standing wave which neither moves right or left but oscillates up and down along the pipe. Points on the pipe that do not move (where the amplitude is zero) are called nodes and points where the standing wave pattern has a maximum amplitude are called anti-nodes (Kinsler et al., 1999).

An example of a standing acoustic wave is along a finite length pipe which is mounted on fixed supports but free at each end (i.e., free-free). The standing acoustic wave generated along the pipe can be expressed as (Kinsler et al., 1999)

$$u_n(x,t) = 2A_n e^{j\omega_n t} cosk_n x \qquad (2.13)$$

Where u_n (m) is the complex displacement corresponding to an nth vibration mode (where n is a positive integer), A_n is the amplitude constant for the nth vibration mode, ω_n (rads/s) is the angular frequency of the nth vibration mode and k_n is the acoustic wavenumber of the nth vibration mode. A full wavelength standing acoustic wave profile for the second vibration mode (n=2) along a finite length pipe is shown in Figure 2.23.

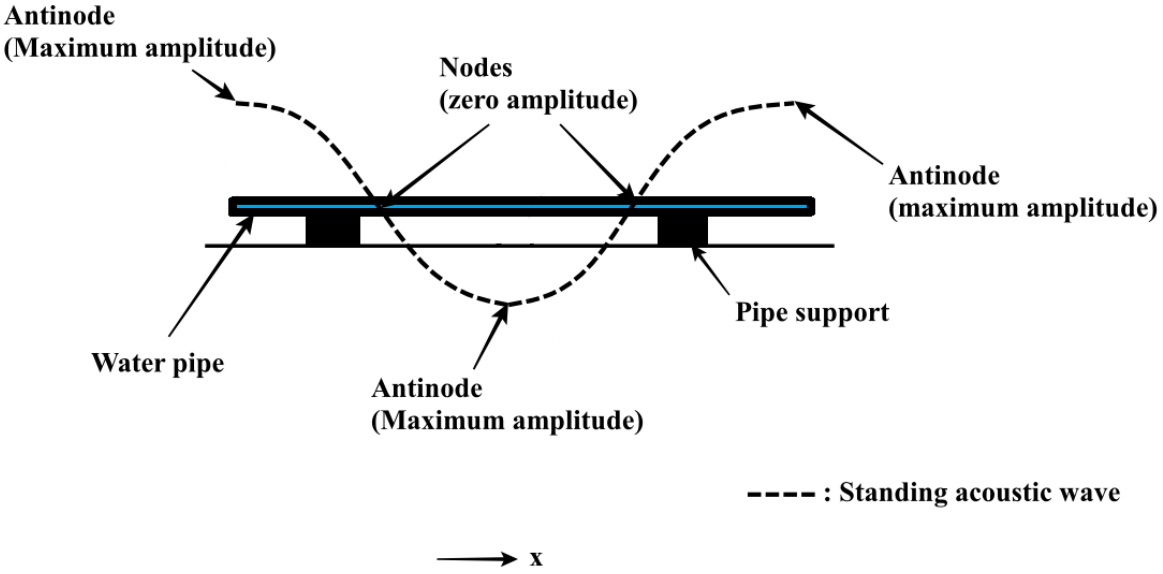

Figure 2.23: Standing acoustic wave profile along a finite length pipe mounted on fixed supports and with both ends free

Low frequency acoustic wave propagation along a pipe wall is also modal in nature (as previously shown by the dispersion curves in Figure 2.20), consisting of longitudinal, flexural, and torsional acoustic wave modes. At increasing acoustic excitation frequencies, an increasing number of acoustic wave modes are also excited along the pipe. The lower the acoustic excitation frequency however, the smaller the number of modes is excited and in such cases the modes corresponding to higher acoustic frequencies generate acoustic wave fields (near-field evanescent waves) which exponentially decay at increasing axial distances from the acoustic source (Kokossalakis, 2006).

For practical application in buried water pipe monitoring, Long et al. (2003) showed the possibility of generating a low frequency longitudinal acoustic wave along a buried ductile iron pipe of 150 mm diameter a test site with the soil properties in Table 2.8.

Table 2.8: Soil material properties measured at a test site in Long et al. (2003)

Soil density (kg/m^3)	Soil longitudinal acoustic wave speed (m/s)	Soil shear acoustic wave speed (m/s)
1950	900	80

In the work by Long et al. (2003), it was observed that during acoustic excitation of the buried pipe (using a solenoid activated tapper with a steel tip) between 0-5 kHz, the fundamental longitudinal acoustic wave mode L(0,1) was detected at approximately 10 m along the buried ductile iron pipe. The flexural acoustic wave mode, by comparison, was undetectable at this distance due to acoustic dispersion experienced by this wave mode along the pipe. Furthermore, there was no evidence of a torsional acoustic wave due to the nature of acoustic excitation along the pipe (i.e., mechanically tapping the pipe at a single location) since torsional acoustic waves require an acoustic transducer ring to be installed around a pipe circumference (Jackson, 2019; Bareille, 2012) which is impractical for implementation within a wireless sensor network for continuous pipeline monitoring. In addition to only conducting field experiments along a buried metallic pipe, the experiments conducted by Long et al. (2003) were however focused the applicability of low frequency acoustic wave propagation along the buried pipe for condition assessment purposes. The possibility of enabling reliable wireless underground communication using low frequency longitudinal acoustic wave propagation along a buried water pipe therefore remained unexplored.

2.6 SUMMARY AND IDENTIFICATION OF KEY GAPS IN KNOWLEDGE

Buried pipeline monitoring, depending on the sensor deployment approach, can be categorised as either inspection-based or real-time monitoring. While the inspection-based approach also requires the presence of on-site technical personnel and equipment deployment for pipe monitoring operations (thus contributing to increased inspection costs), the real-time monitoring approach offers a more cost-effective solution to buried water pipe monitoring by affording real-time and long-term buried water pipe monitoring capabilities using permanently deployed sensors. With the rise of low-cost integrated circuit technology, WSNs have presented an avenue for further reducing the costs of buried water pipe monitoring while delivering the

real-time objective for continuous pipeline monitoring. One of the main challenges for WSN deployment in buried water pipe monitoring is however the establishment of a reliable wireless communication link within the underground soil environment. Traditionally, radio waves have proven successful for wireless communication through air (above the ground and below the ground within tunnels) but research has shown that within an underground soil environment, radio signal transmission is limited to less than 3 m (and even as low as a few centimetres in soils with high clay content) using commercially available wireless sensor nodes. Another approach which has been investigated in the literature is the use of magnetic induction communication. In addition to no field trials of this technique reported in the literature, multiple electrical coils of specific parameters (such as coil resistance and capacitance) which vary according to the pipe diameter would need to be wrapped around the buried pipe to improve signal transmission range to within tens of metres.

A separate approach for enabling wireless underground communication through soil is by using the buried water pipe as an acoustic waveguide. Although acoustic signal propagation along buried water pipes has been used for pipe inspection and condition assessment (e.g., leak detection and location), relatively limited research has been conducted on using this technique for enabling reliable digital communication within an underground soil environment. The earliest study of acoustic based digital communication along a water pipe by Kokossalakis (2006) showed the possibility of achieving acoustic data communication along a PVC pipe (albeit empty and exposed in the laboratory) at 9 m along the pipe. The study focused on using the internal fluid medium of the pipe for acoustic communication using acoustic transducers deployed inside the pipe. Rather than use invasive acoustic transducers (which can potentially contaminate water inside the pipe), another approach to acoustic data communication along the pipe is by using the pipe wall as the acoustic propagation medium. The most notable study of this approach was by Jin et al. (2013) but, due to acoustic signal dispersion along the pipe, the

results showed very limited acoustic communication range (less than 2 m) along exposed metallic pipes in the laboratory (with no field tests conducted for the communication system).

Although the problem of acoustic dispersion along a pipe can be tackled by selectively exciting acoustic propagation modes along the pipe (such as is done with the guided wave technique), this technique requires costly and bulky equipment as well as trained personnel deployment which is not feasible for a real-time monitoring solution. Another approach to tackling acoustic dispersion along the pipe is by reducing the acoustic excitation frequency below 1 kHz (for water distribution pipes) where only a few acoustic propagation modes can propagate along the pipe. Field tests using this technique, such as that conducted by Long et al. (2003) have however only focused on low frequency acoustic propagation along a buried water pipe for condition assessment purposes.

Finally, regarding their feasibility for enabling reliable wireless underground communication within a real-time buried water pipe monitoring application, the data communication range and bit error rates (BER) as well as cost, size, and power supply requirements of individual data communication nodes within the wireless underground communication techniques reviewed in this chapter are summarised in Table 2.9. Deployment limitations, specific to each data communication system are also included in the table.

Table 2.9: Comparison of wireless underground communication techniques applicable for real-time buried water pipe monitoring

Data communication technique	Data transmission range (m)	Bit error rate (%)	Typical hardware cost per data communication node (£)	Typical physical dimensions per data communication node (mm)	Typical power supply requirement (Watt-hour)	Deployment limitations for the communication technique
Radio-based communication (Sadeghioon, 2014; Vuran & Silva, 2010; Silva & Vuran, 2009; Johnson et al., 2009)	1-3	0-100	100	Length: 57 Width:32 Height: 6	< 10	Reliable communication depends on antenna orientation and burial depth of the communication nodes. Data communication is also limited to less than 1 m in soils with high clay content.
Magnetic induction-based communication (Sun et al., 2011; Akyildiz & Sun, 2010; Akyildiz & Sun, 2009)	10 (inter-coil distance along a non-metallic pipe)	0-50	N/A	Dependent on pipe diameter since the coils need to be wrapped around the pipe	N/A	Multiple relay coils need to be installed along non-metallic pipes (typically at 3 metre intervals) to ensure reliable underground communication. To install these coils, access is also needed around the entire circumference of the buried water pipe, which may not be feasible.
Underwater acoustic communication along a pipe	3-9	0-80	> 300	*Length: 30 *Width: 30 *Height: 2	N/A	Acoustic transducers for digital communication are invasive (i.e., inside

(Kokossalakis, 2006)						the pipe) which can pose health and safety risks for implementation along water distribution pipes.
Underwater acoustic communication along a pipe (Joseph et al., 2017)	40	30	70	*Length: 37 *Width: 18	< 10	This technique also relies on underwater acoustic propagation within metallic pipes. There is currently no evidence of the applicability of this technique to buried non-metallic pipes.
Acoustic (ultrasonic) communication along a pipe wall (Jin et al., 2013)	< 2	0-5	> 1000	*Length: 10-12 *Width: 6-10	N/A	Communication distance is limited to less than 2 metres along exposed metallic pipes. No evidence of this technique along buried water pipes in soil.
Acoustic (ultrasonic) communication along a pipe wall Chakraborty & Saulnier (2015)	< 5	0	40	*Length: 15 *Width: 15 *Height: 1	N/A	Communication distance is limited to less than 5 metres along metallic pipe submerged in water. No evidence of this technique along buried water pipes in soil.

*Acoustic transducer dimensions

The key research gaps identified in the literature review are therefore:

I. Radio signal propagation, which is traditionally employed for digital communication in WSN for continuous pipeline monitoring, has a limited signal propagation range (less than 3 m) in an underground soil environment. Such limited radio communication range can render the WSN deployment costly due to the need to deploy sensors at very short distances. There is therefore the need to research new techniques for enabling reliable wireless underground communication within the framework of potential integration into a WSN for buried water pipe monitoring.

II. Acoustic signal transmission has the potential to enable wireless underground communication by using the buried water pipe as an acoustic waveguide. There is however comparatively little research on using acoustic data communication along a buried water pipe especially using wireless sensors which can be installed non-invasively along the pipe. Research is also required to better understand the impact of different pipe materials, wall thicknesses, pipe diameters and surrounding soil condition on acoustic signal propagation along the pipe.

III. Ultrasonic wave propagation for non-invasive acoustic communication along the pipe wall has been investigated in the literature (Chackraborty & Saulnier, 2014; Jin et al., 2013). With this technique however, digital communication is limited to less than 5 metres along exposed and metallic pipes. There remains therefore, the opportunity for further research into acoustic data communication along water pipes (of metallic and non-metallic material) at distances of greater than 5 m especially in an underground soil environment.

IV. Low frequency (< 1 kHz) acoustic wave propagation along the pipe wall, as opposed to its ultrasonic counterpart, is less prone to acoustic signal dispersion along the pipe due to the limited number of acoustic propagation modes which are excited along the pipe for

this bandwidth. Field tests reported in the literature have however only focused on low frequency acoustic propagation along buried water pipe for condition assessment purposes and so there still exists the opportunity for researching low frequency acoustic propagation along a buried water pipe for enabling reliable wireless underground communication.

CHAPTER 3

METHODOLOGY

3.1 INTRODUCTION

A key gap identified from the literature review is the absence of long range (at least 3 m) and reliable wireless underground communication in soil for the real-time condition monitoring of buried water pipes. It was shown in the later part of the review that the use of acoustic wave propagation (specifically the longitudinal acoustic wave mode) along the pipe wall at frequencies below 1 kHz can potentially fill this gap. The longitudinal acoustic wave, compared to other possible acoustic wave propagation modes along the pipe wall, as shown by Long et al. (2003) for example, can be generated at a single location along a buried cast iron pipe (using a non-invasive acoustic transducer) and detected along the same pipe beyond 3 m. Within the context of real-time buried water pipe monitoring and based on the possibility of using the pipe wall acoustic channel for non-invasive acoustic data communication, this chapter therefore proposes a solution for reliable wireless underground communication in buried water pipe monitoring using longitudinal acoustic wave propagation along the pipe. Based on the literature review outcome and to address the issue of cost-effective and real-time buried water pipe monitoring, such a solution must be able to:

I. Operate at a data communication range beyond 3 m to reduce deployment costs for individual data communication nodes (at approximately £100 per node), compared to a traditional radio-based alternative, for distributed monitoring across a buried water pipe network;

II. Enable reliable (0% BER) wireless underground data communication with a data transmission rate of at least 1 bit per second (bps) which is the minimum requirement for real-time data communication.

III. Operate with a maximum power supply requirement of less than 10 Watt-hour such as is available from an off-the-shelf single cell battery with maximum physical dimensions in tens of millimetres. As noted by Sadeghioon (2014), power availability is one of the main issues for continuous buried pipeline monitoring due to the large scale and long operational life of buried pipe networks as well as the lack of long-term and easily accessible power sources below the ground. Besides possible energy harvesting solutions such as vibration, thermal or fluid flow (within the buried pipe) energy harvesting (e.g., Shukla et al., 2018; Keddis & Schwesinger, 2016; Walton et al., 2011; Kokossalakis, 2006), a single cell battery of millimetre dimensions can be integrated within the wireless underground communication node for continuous pipeline monitoring. Compared to energy harvesting solutions, the battery cell approach is more flexible in terms of node installation location along the buried pipeline network (especially in cases where wireless underground communication nodes are retrofitted to existing pipes), non-invasive and can also enable long-term buried pipeline monitoring through efficient power management (Metje et al., 2012; Walton et al., 2011). For example, using a 9 V commercially available Lithium battery with a typical power supply capacity of 7 Watt-hour (Battery Station, 2021) a single data transmission every 24 hours can potentially enable continuous system operation beyond 1 year (before replacing the battery) if the power consumption is less than 0.02 W per data transmission. It is therefore advantageous for the proposed communication system to prioritise power conservation over data transmission capacity to prolong battery lifetime.

Based on the outlined system requirements, the design and performance testing of a prototype low cost, low power miniaturized digital communication system using low frequency (less than 1 kHz) acoustic wave propagation along exposed and buried water pipes is presented in this

chapter. The chapter begins by presenting the stepwise operational stages of the prototype system, with minimal signal processing requirements, in Section 3.2 while Section 3.3 further describes the hardware layout to achieve the step-by-step functions of each stage of the communication system.

Section 3.4 reports the basis of selection of acoustic transducers for acoustic wave generation and detection within the communication system while Sections 3.5 and 3.6 describe the coupling of the component hardware units as well as the embedded system design to achieve a functional digital communication transmitter and receiver. The system deployment for performance tests along exposed pipes in the laboratory and buried water pipes in the field is reported in Section 3.7. Following the communication system deployment, acoustic signal attenuation is examined along exposed and buried water pipes using analytical and numerical modelling in addition to conducting laboratory and field trials along exposed and buried water pipes, respectively. A short summary of the chapter is presented in Section 3.9.

3.2 OPERATIONAL STAGES OF THE PROPOSED COMMUNICATION SYSTEM

The prototype communication system proposed in this work is digital in nature due to the unique advantage of the possibility of transmitting digitally compressed information which can potentially minimise power consumption at a digital communication node. The prototype system, which can be divided into the digital transmitter and receiver sections, involves the core elements of a standard digital communication system, i.e., message generation, message encoding, digital modulation, signal transmission (in this case acoustic wave transmission along a pipe), digital demodulation, message decoding and message reception. These stages are shown in the block diagram in Figure 3.1, which also shows the stages that must be synchronized. Each of these stages, with respect to the communication transmitter and receiver

development, will be described in further detail in Sections 3.5 and 3.6. Even though additional elements representing higher complexity signal processing techniques can be added to the core communication components in Figure 3.1, the proposed system (at the expense of achievable bit rate) uses a more fundamental and robust approach which guarantees reliable data transmission while avoiding the inevitable rise in power consumption associated with increased signal processing complexity.

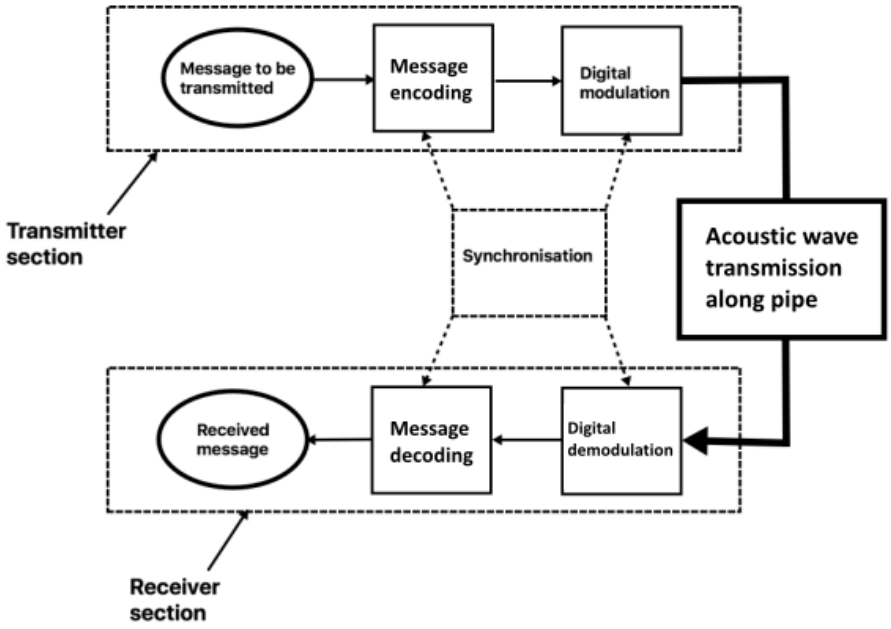

Figure 3.1: Operational stages of the digital communication system

3.3 HARDWARE LAYOUT OF THE PROPOSED COMMUNICATION SYSTEM

As already reviewed in Chapter 2, many underground water pipeline monitoring sensors have evolved over time, each one offering its own unique advantage especially in terms of cost, size, and power requirements. The communication system developed in this work was therefore designed and constructed based on minimising the overall cost, physical size, and power implications of each node within a pipeline monitoring network.

The costing criterion was based on the guideline set by Akyildiz & Vuran (2010), that a distributed and wireless underground sensor network can only be economically viable for buried water pipe monitoring if the cost of deploying the individual wireless underground nodes is cheaper than the alternative of deploying traditional pipe inspection and monitoring sensors. From Table 2.9, the typical hardware cost per data communication node of a radio based wireless underground communication system (with data communication range of less than 3 m) is approximately £100. To enable a more cost-effective solution for buried pipeline monitoring using the proposed communication system (where the data communication range is at least 3 m thus reducing the spatial density of distributed communication nodes along the buried pipe network), a design criterion stipulating a maximum cost of £100 per digital communication node was adopted and targeted for this work.

The eventual size of the finished product was guided by the criterion that each digital communication node should be small enough to be easily deployed along a buried water pipe with minimal intrusion to the pipeline network. Considering the typical dimensions of ground access points (such as valve covers which are either 300-1200 mm in length and 300-1200 mm in breadth for rectangular access points or 450-600 mm in diameter for circular access points) to buried water distribution pipes, conservative upper limits of 200 mm length, 100 mm breadth and 50 mm height were chosen as the maximum dimensions for the proposed digital communication node. These dimensions were also chosen to ensure convenient installation of the digital communication nodes directly along buried water distribution pipes (with outer diameters as low as 90 mm) without any significant change to the mechanical integrity of such pipes.

According to Akyildiz & Stuntebeck (2006), a distributed wireless underground sensor network for continuous pipe monitoring should also be able to last several years with minimal routine

maintenance costs including change of power source. The lifetime of the power source must therefore be long enough to meet this requirement and its size must be easily integrable within each communication system node described in this work. Therefore, a commercially available, off-the-shelf power supply (such as the 9 V Lithium battery previously described in Section 3.1) was employed as a power source within the proposed communication system. The system specifications for each digital communication node are summarised in Table 3.1.

Table 3.1: System specifications for each digital communication node within the proposed communication system

Maximum cost (£)	Maximum physical dimensions (mm)	Power supply requirement (Watt-hour)
100	Length: 200 Width: 100 Height: 50	< 10

Based on the cost, physical size and power supply requirements targeted for this hardware design, an embedded systems design approach was adopted for the communication system development. An embedded system can be defined as an electronic system consisting of one or more microcontrollers configured to perform a specific task within a given physical environment. A microcontroller in turn is a programmable integrated circuit (IC) which allows the embedded system to interact with its physical environment through the microcontroller input and output ports (Valvano, 2012). At the heart of any embedded system design is therefore a microcontroller responsible for executing a software algorithm aimed at achieving a predetermined objective within a given physical environment. To develop the embedded system design for the proposed communication system in the laboratory, the hardware layout to achieve the stepwise functions outlined in Figure 3.1 is presented in Figure 3.2.

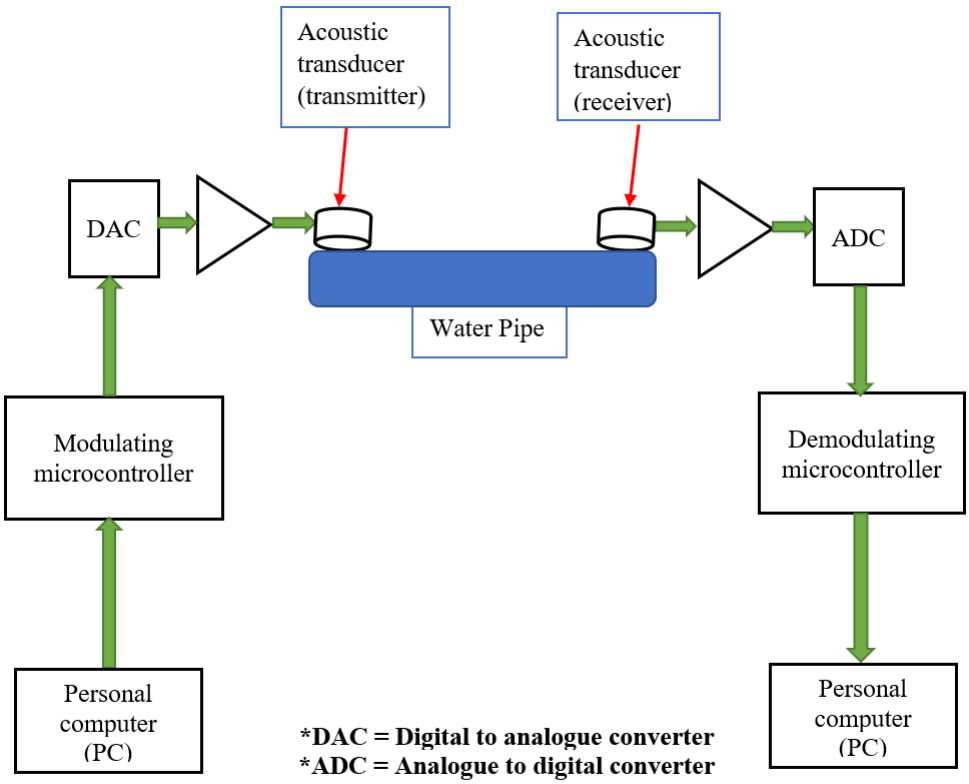

Figure 3.2: Hardware layout of the proposed communication system

Figure 3.2 shows a generalised schematic of the hardware layout of the proposed communication system, with the presence of the power supplies implied but not shown. As shown in Figure 3.2, the first hardware stage is a personal computer (PC) where the message to be transmitted is input and encoded. The second hardware stage, as shown in Figure 3.2, is the modulating microcontroller within which the digital modulation algorithm is executed. Following this microcontroller stage is the digital to analogue converter (DAC) which transforms the discrete-time digitally modulated signal into a continuous signal. This signal is further amplified and transmitted along the water pipe waveguide by a signal amplifier and transmitting acoustic transducer, respectively.

At the receiver section, the receiving acoustic transducer captures the transmitted signal before the signal pre-amplification stage. As noted by Kokossalakis (2006), a signal pre-amplification

stage is necessary in a communication system to adjust the amplitude of a received signal to match the input power threshold of an analogue to digital converter (ADC) present at the digital communication receiver. The ADC of Figure 3.2 subsequently converts the amplified signal into a discrete-time signal before the demodulating microcontroller extracts the digital information from the signal in the same sequence with which it was transmitted. The extracted digital information is subsequently fed into a separate PC which decodes and presents the originally transmitted message to an observer.

From the perspective of an embedded system design, Figure 3.2 can be functionally described as a microcontroller module, external interface circuit and acoustic transducers. In Figure 3.2, although it is obvious that the modulating/demodulating microcontroller fulfils the role of the microcontroller module, the PC can also be regarded as an extension of this microcontroller module as it is itself a collection of multiple microcontrollers connected, through the output/input ports of the PC, to the modulating/demodulating microcontroller. The DAC/ADC and signal amplifiers of Figure 3.2 can further be regarded as external interface circuits between the microcontroller modules and the acoustic transducers. This embedded system design is summarised in Figure 3.3.

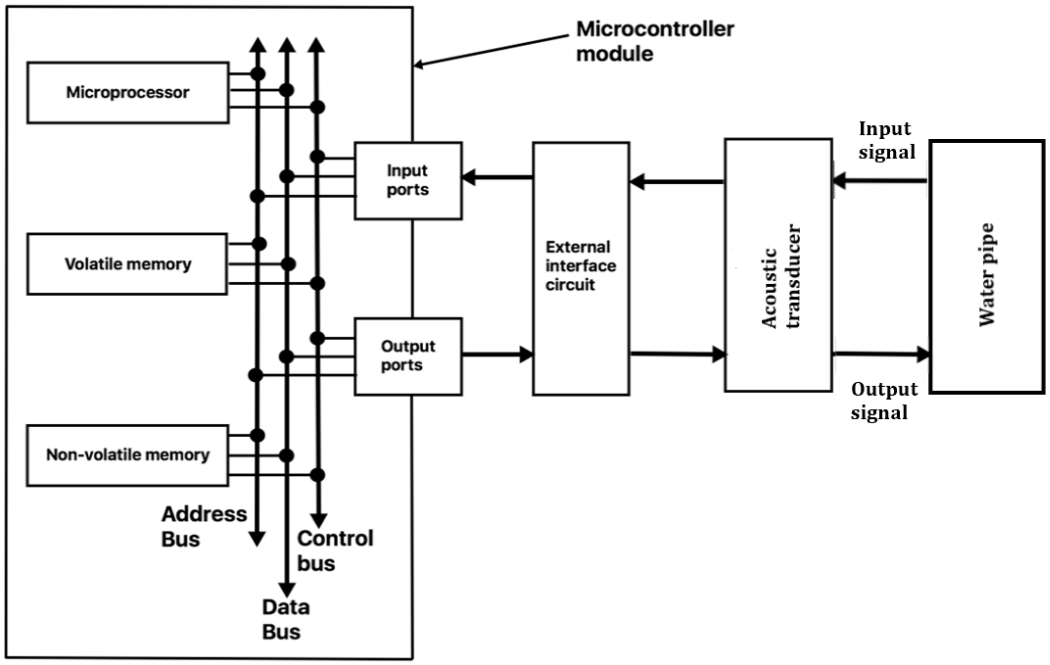

Figure 3.3: Hardware layout of the proposed communication system in terms of an embedded system design

As shown in Figure 3.3, the embedded system design at the digital communication transmitter or receiver comprises a microcontroller module, an external interface circuit as well as the acoustic transducer which converts electrical into acoustic energy (and vice versa). Among the plethora of potential candidates for the role of acoustic transducer, a choice needed to be made for the best-fit option which satisfies the design objectives introduced at the beginning of this section. Section 3.4 reports the method by which this choice was made.

3.4 SELECTION OF ACOUSTIC TRANSDUCERS FOR INTEGRATION WITHIN THE COMMUNICATION SYSTEM

In this section, the process by which the best-fit choices of acoustic transducers, for integration within the proposed communication system, were selected from an abundance of commercially available options (at the time of conducting this research) is described. A qualitative comparison of the acoustic transducers was initially undertaken to filter out a selection of commercially

available options which were later compared in the laboratory before making a final choice for implementation within the communication system.

3.4.1 Qualitative comparison of acoustic transducers

An acoustic transducer, for the purpose of definition, is an acoustic actuator or sensor which can be employed for generating or detecting acoustic waves. Before comparing acoustic transducers, it is necessary to note that among the plethora of acoustic transducer technologies which can potentially be employed for generating or detecting acoustic waves along a pipe (e.g., Pons, 2005), transducers featuring electrical to mechanical energy conversion (and vice versa) present two key advantages:

I. Most vibration motion control systems are designed using integrated electronic circuits. This is due to the high pervasion of digital logic circuit design in vibration actuation and sensing systems (Lee, 2011; Pons, 2005). The opportunity for digital logic circuit design also presents an important avenue for reducing the physical size of an electronic circuit featuring an acoustic transducer, which ties in with the small (in tens of millimetres) size requirement of the digital communication nodes within the proposed communication system.

II. Due to the high pervasion of digital logic circuitry, the availability of electronic components is greater for electrical to mechanical energy conversion (and vice versa) in acoustic transducer circuits, than it is for other types of acoustic transducer circuits featuring non-electrical to mechanical energy conversion. This is largely due to the relatively cheaper costs of transducer fabrication and readily available off-the shelf electronic components which can be integrated within such an acoustic transducer circuit (Pons, 2005).

Considering these advantages, Table 3.2 presents a qualitative summary of all the electromechanical transducers which were considered for this project. The transducer list of Table 3.2 was achieved by filtering out key acoustic transducers from the multitude of commercially available options using the following requirements:

I. Only acoustic transducers with operational frequencies below 1 kHz were considered.
II. Only acoustic transducers which cost less than £100 were considered.
III. Only acoustic transducers with physical dimensions which were a fraction of the maximum size of a digital communication node (based on the requirements of Section 3.3) were considered.
IV. Only acoustic transducers designed for directly coupling acoustic energy into solids (i.e., vibration transducers) were considered. Thus, acoustic transducers designed for directly coupling acoustic energy into fluids such as air or water (e.g., traditional acoustic speakers) were not considered.
V. The power requirement of each acoustic transducer must be low enough to be supplied by a power source which is compact enough to be integrated within the digital communication nodes. In other words, only acoustic transducers with potential power sources of dimensions within tens of millimetres were considered.

It should also be noted that only "active" acoustic sensors (i.e., sensors which, by themselves, do not require an external power supply to operate) were considered. An active sensor as opposed to its passive (i.e., requiring an external power supply to operate) counterpart presented a more attractive choice for the communication system since it could potentially reduce the overall power demand at the digital communication receiver by allowing limited power resources to be diverted to other signal processing operations at the receiver.

Table 3.2: Comparison of state of the art, commercially available acoustic transducers considered for the proposed communication system

Manufacturer	Transducer Type	Typical Cost (£)	Typical Physical Dimension (mm)	Typical power input (W)
Stem Inc.	Mini piezo stack	26	Length: 2.0 Width: 2.0 Thickness: 2.0	1.1
	Stack piezo	30	Length; 3.0 Width: 3.0 Thickness: 5.0	8.5
	Piezo bimorph	7	Length: 25.0 Width: 7.1 Thickness: 0.5	1.1
	Piezo round bimorph	5	Outer Diameter: 27.0 Thickness: 0.5	3.3
	Piezo ceramic bimorph	15	Length: 32 Width: 2.2 Thickness: 0.7	1.1
Piezodrive	Piezoelectric bender (BA4902)	10	Length: 49.0 Width: 2.1 Thickness: 0.75	0.2
	Piezoelectric bender (BA43502)	10	Length: 3.5 Width: 2.1 Thickness: 0.6	0.2
	Piezoelectric bender (BA6020)	35	Length: 60.0 Width: 20.0 Thickness: 0.8	0.7
	Piezoelectric bender (BA4510)	15	Length: 45.0 Width: 10.0 Thickness: 0.5	2.8
	Piezo stack (SB050510)	30	Length: 5.0 Width: 5.0 Thickness: 10	11.3
	Piezo stack (SB050520)	63	Length: 5.0 Width: 5.0 Thickness: 20.0	22.6
	Piezo tube (TB1005)	42	Length: 10.0 Diameter: 5.0 Thickness: 0.7	0.1
	Piezo tube (TB2005)	68	Length: 20.0 Diameter: 5.0 Thickness: 0.7	0.6
	Brass reinforced Piezoelectric bending actuators	69 – 83	Length: 31.8-63.5 Width: 3.2-31.8 Thickness: 0.4-0.7	2.4
	High performance benders	8 – 54	Length: 31.8-63.5 Width: 3.2-31.8 Thickness: 0.4-0.9	5.2

Piezo Systems	High performance benders	9 – 55	Length: 31.8-63.5 Width: 3.2-31.8 Thickness: 0.4-0.7	10.4
	Piezo bending discs	90	Outer Diameter: 3.2-63.5 Thickness: 0.4	25.3
	Standard brass reinforced extension sensors	69 – 83	Length: 31.8 – 63.5 Width: 3.2 – 31.8 Thickness: 0.4	Details not available
	Brass reinforced piezoelectric bending sensors	69 – 83	Length: 31.8-63.5 Width: 3.2-31.8 Thickness: 0.4	Details not available
Physik Instrumente (PI)	Dura-act patch transducer	60 – 97	Length: 16.0-61.0 Width: 13.0-35.0 Thickness: 0.4-0.8	1.3
Measurement Specialties	PVDF film transducers	3 – 4	Length: 25.0-40.0 Width: 13.0-35.0 Thickness: 0.04-0.23	6
Smart Material	Macro fibre composite transducers (MFC P1/F1)	30 – 243	Length: 38.0-160.0 Width: 10.0-64.0 Thickness: 0.3	0.5
	Macro fibre composite transducers (MFC P2/P3)	35 – 111	Length: 16.0-186.0 Width: 8.0-88.0 Thickness: 0.3	0.9
Sparkun Electronics	Rectangular and circular type surface transducers	7 – 15	Length: 215.0 Width: 14.5 Thickness: 7.9 Outer Diameter: 28.0-50.0 Height: 27.0 – 30.0	1.0-3.0
Precision Microdrives	Linear resonant actuators (LRA)	6 – 9	Body Diameter: 8.0-10.0 Body Length: 2.6-3.7	0.03-0.14
	Internal eccentric rotating mass (ERM) vibration motors	4 – 6	Body Diameter: 7.0-10.0 Body Length: 2.1-4.0	0.06-0.20
	External eccentric rotating mass (ERM) vibration motors	4 – 15	Body Diameter: 3.2-34.0 Body Length: 3.4-32.3	0.03-3.00

Table 3.2 is a qualitative comparison of over 130 individual acoustic transducers which can be broadly categorised as piezoelectric and electromagnetic transducers. While an electromagnetic transducer uses the force from a current carrying conductor within a magnetic field to operate

(Lee, 2011), a piezoelectric transducer uses the "piezoelectric effect" for its operation (Physik Instrumente, 2016). In Table 3.2, the transducers from Sparkfun Electronics and Precision Microdrives are electromagnetic in nature while the transducers from the other manufacturers are piezoelectric. The next sections further describe the process of selecting specific acoustic transducers from Table 3.2, which represent the best-fit compromise of cost, power, and size, for integration within the communication system.

3.4.1.1 Selection of best-fit electromagnetic transducer

Using cost as a selection criterion, the survey of the electromagnetic transducers from Precision Microdrives (Table 3.2) yielded the specific transducer models listed in Table 3.3 as two of the cheapest options which were commercially available.

Table 3.3: Qualitative summary of the selected vibration motors

Vibration motor	Manufacturer model	Physical size and form factor	Typical power supply requirement (W)	Cost (£)
Internal eccentric rotating mass motor	308-100 (Precision Microdrives, 2015)	Coin type vibration motor with 8mm diameter	0.2	4
External eccentric rotating mass motor	308-103 (Precision Microdrives, 2015)	Cylindrical vibration motor with 8mm diameter and 20mm length	0.7	4

As shown in Table 3.3, the vibration motors considered for further examination were the 308-100 and the 308-103 vibration motors manufactured by Precision Microdrives. The 308-100 vibration motor is a coin type vibration motor with 8 mm diameter, the schematic of which is shown in Figure 3.4a (Precision Microdrives, 2015a).

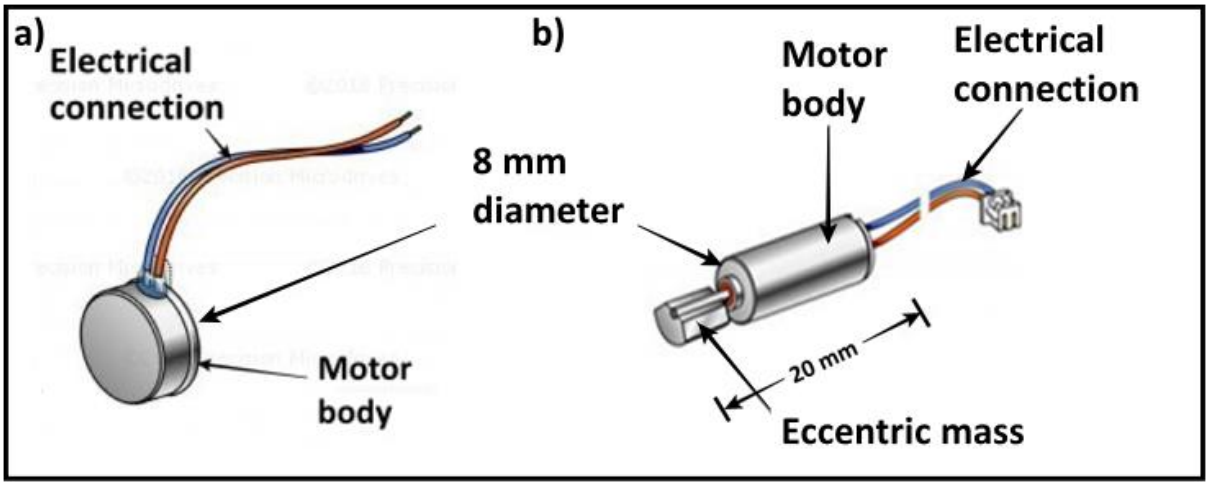

Figure 3.4: 308-100 vibration motor (Precision Microdrives, 2015 and b) 308-103 vibration motor (Precision Microdrives, 2015

As shown in Figure 3.4a, the coin type (308-100) vibration motor consists of a motor body (8 mm diameter) attached to a pair of electrical cables for power supply. The motor body encapsulates an eccentric rotating mass (ERM), which is responsible for the vibrational motion of the motor during operation. Another key quality of the coin vibration motor is the typical power consumption requirement of 0.21 W (Precision Microdrives, 2015a), which is well within the supply range of off-the-shelf power sources that can be conveniently integrated at the digital communication nodes of the proposed communication system.

The cylindrical (308-103) vibration motor, on the other hand, is an external ERM vibration motor with 8 mm diameter and 20 mm length, the schematic of which is shown in Figure 3.4b. As shown in the figure, this external ERM vibration motor consists of a motor body attached to a pair of electrical cables for power supply. The motor body, in this case, is separately attached to the ERM (through a rotating shaft), which is responsible for the vibrational motion of the motor. Another key feature of the external ERM motor is the typical power consumption of 0.72 W (Precision Microdrives, 2015b). Although the power consumption of the external ERM motor is slightly higher than that of the coin motor, this value is still well within the supply range of typical off-the-shelf batteries.

For the Sparkfun Electronics transducers, only two models were commercially available at the time of this research, i.e., the rectangular and circular surface transducers. The rectangular surface transducer, shown in Figure 3.5a, consists of electrical coil windings located within a rectangular metallic housing of 21.5 mm length, 14.5 mm width and 7.9 mm height. The circular surface transducer on the other hand, shown in Figure 3.5b, consists of electrical coil windings located within a circular metallic housing of base diameter and height of 30 mm 20 mm respectively. Like the vibration motors, power supply requirements of the surface transducers (1-3 W) are well within the supply range of typical off-the-shelf batteries.

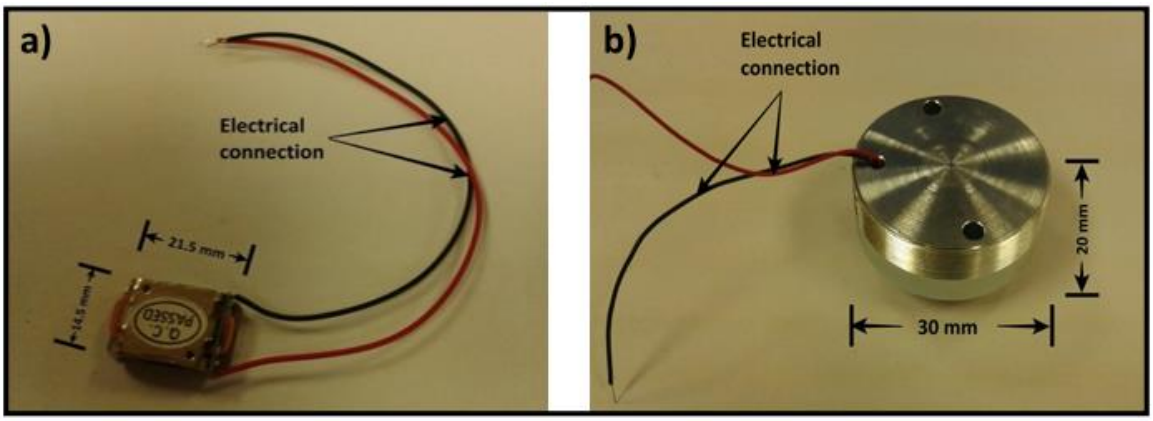

Figure 3.5: Figure 3.5: Rectangular type surface transducer and b) circular type surface transducer

The selected electromagnetic transducers described in this section were further compared in the laboratory, the procedure for which will be described in Section 3.4.3.

3.4.1.2 Selection of best-fit piezoelectric transducer

The piezoelectric transducers in Table 3.2 can be broadly categorised as single layer, multilayer, or fibre composite transducers. A special category of single or multilayer transducer considered for this research was the piezoelectric bender. A piezoelectric bender consists of either one ("unimorph") or two ("bimorph") piezoelectric layers which are bonded to a non-piezoelectric substrate (Wang et al. 1999). In the case of a unimorph arrangement for electrical to mechanical

energy conversion for example, the single piezoelectric material is polarised such that the application of an electric field results in a contraction of the material. This contraction movement is opposed by the non-piezoelectric substrate, resulting in a bending motion of the actuator. For a bimorph arrangement, both piezoelectric materials are oppositely polarised resulting in a contraction movement in one material and an expansion movement in the other. This separate contraction and expansion of each piezoelectric material also results in the bending motion of the bimorph actuator (Wang et al. 1999). The main disadvantage of the piezoelectric bender however, compared to other piezoelectric transducers, is its poor electromechanical coupling which result in a weaker power output for such transducers (Wang et al. 1999). In addition, Wang et al. (1999) also noted that the presence of internal stresses within the actuator resulting from the bending motion also contributes to internal energy losses within the transducer.

Another category of multilayer transducer considered for this research was the piezoelectric stack. Unlike the piezoelectric benders, piezoelectric stacks are physically rigid in nature and thus immune to the bending stresses which contribute to mechanical energy losses within the actuator. The rigid nature of the piezoelectric stacks however presented a disadvantage for integration within the communication system as the desired structural flexibility for efficient installation along a water pipe was lost in this case. Yet another category of piezoelectric actuators, which offered a useful compromise between structural flexibility and electromechanical conversion efficiency was the piezoelectric patch, an example of which is shown in Figure 3.6 (Physik Instrumente, 2016).

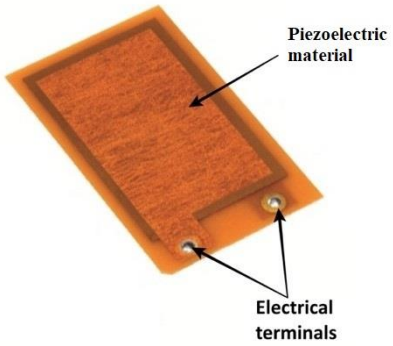

Figure 3.6: Piezoelectric patch transducer (Physik Instrumente, 2016)

As shown in Figure 3.6, the piezoelectric patch consists of a rectangular surface to which a pair of electrical terminals can be connected for power supply. Within the active area of the rectangular surface there are piezo ceramic plates responsible for the conversion of electrical to mechanical energy or vice versa (Physik Instrumente, 2016). The flexibility of the piezoelectric patch presented a key advantage over the piezoelectric bender or stack, as it provided a more flexible and energy efficient installation option. Despite this advantage, however, the minimum cost of commercially available piezoelectric patches, at the time of conducting this research, was £60 which was considerably higher than the minimum cost of the piezoelectric bender, for example, at £10.

A cheaper alternative to the piezoelectric patch, discovered during the research, was the piezoelectric fibre composite. The specific brand of piezoelectric fibre composite considered was the macro fibre composite (MFC). The MFC consists of multiple rectangular piezo ceramic fibres sandwiched between layers of adhesive epoxy and polyimide material as illustrated schematically in Figure 3.7.

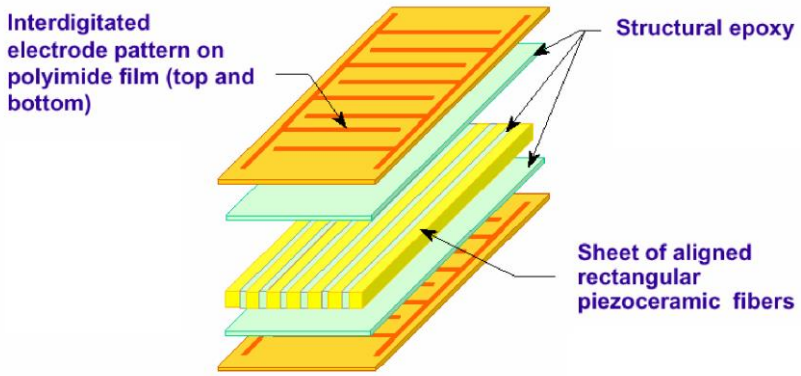

Figure 3.7: Macro-Fibre-Composite (Smart-Material, 2015)

As shown in Figure 3.7, the main components of the MFC are the interdigitated electrodes, structural epoxy, and the rectangular piezo ceramic fibres. This interdigitated electrode pattern of the MFC improves the electromechanical conversion efficiency of the transducer compared to traditional monolithic (such as the piezoelectric patch or bender) options (Sodano 2003; Williams et al. 2002). The structural epoxy material of the MFC further enables effective bonding of the piezo ceramic fibres to the protective polyimide film. In addition to high efficiency, the piezo ceramic fibre structure of the MFC also provides better crack resistance to its monolithic counterparts due to its fibrous nature. For these advantages, the MFC was selected in preference to the other commercially available piezoelectric transducers listed in Table 3.2. The specific brand of MFC transducer from Smart Material (M-2814-P2), offering good compromise of cost, size and power requirement, is shown in Figure 3.8.

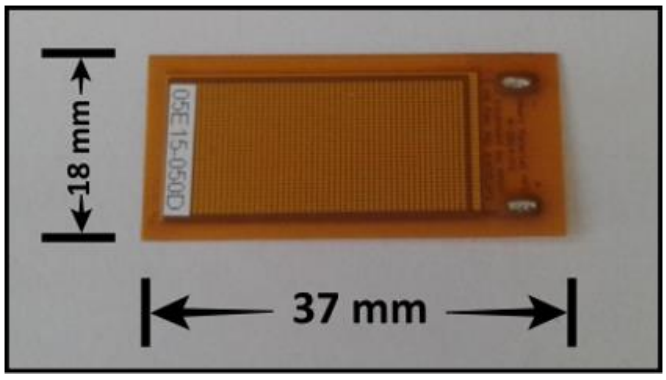

Figure 3.8: M-2814-P2 piezoelectric transducer

For acoustic signal generation along the pipe, the M-2814-P2 was further compared with the vibration motors and surface transducers within a laboratory environment (Section 3.4.3). For acoustic sensing on the other hand, the M-2814-P2 automatically qualified as the best-fit choice since the electromagnetic transducers, by nature of their construction, could not be used for acoustic sensing along the pipe. Before comparing the acoustic transducers, these transducers first needed to be installed along the pipe surface. The next section justifies the methodology by which the acoustic transducers were installed along a pipe in the laboratory.

3.4.2 Acoustic transducer installation along the pipe

A transmission line analogy, as shown in Figure 3.9, can be employed for modelling the acoustic energy flow between an installed acoustic transducer and the water pipe.

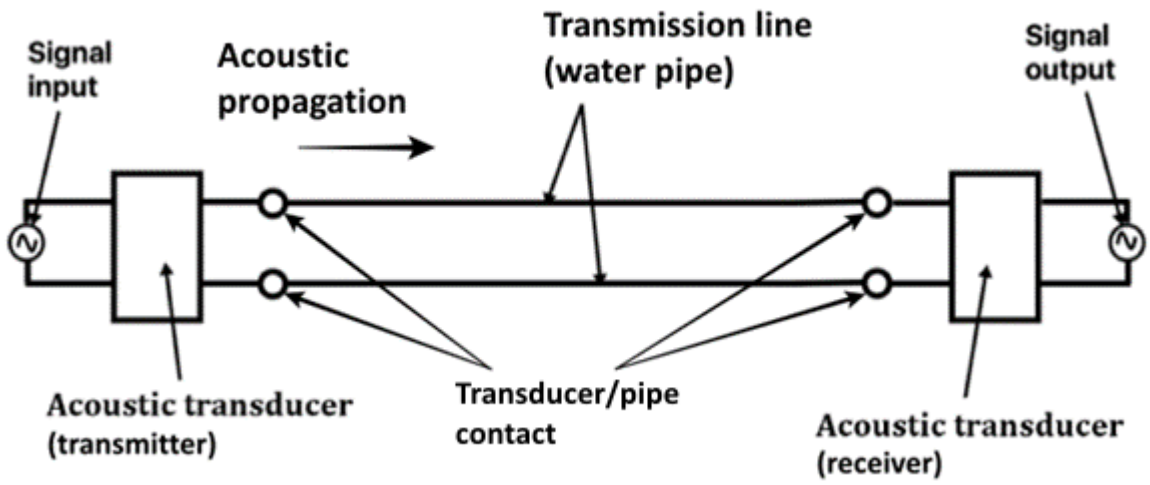

Figure 3.9: Transmission line analogy for installing the acoustic transducers

From Figure 3.9, the seamless flow of acoustic energy between the transmitting and receiving acoustic transducers depends on the path continuity (ideally an impedance match between the acoustic transducer and water pipe) enabled by the connectors. To ensure this continuity, the acoustic transducers and the water pipe need to be maintained in constant contact during transducer operation for which there exists two main techniques which can potentially be

employed for fulfilling this purpose. These techniques are the adhesive and non-adhesive contact methods.

While adhesive contact methods feature the use of an adhesive material for bonding the acoustic transducer to the pipe, non-adhesive contact methods do not involve the use of an adhesive layer. An example of a non-adhesive contact method for acoustic transducer installation was described by Joseph et al., (2018), where a magnetic contact method was employed for installing acoustic transducers along a buried water pipe. The magnetic installation technique, however, is only appropriate for metallic water pipes. Since the communication system described in this thesis was designed to operate on both metallic and non-metallic pipes, the magnetic contact method was inadequate as a means of acoustic transducer installation.

Another option for non-adhesive contact installation is the use of mechanical fasteners such as Jubilee clips or cable ties. However, in addition to requiring access to the entire pipe circumference (which may not always be possible for a buried water pipe), the mechanical fastening method requires precise tightening of the fastening mechanism to ensure rigidity of the transducer installation without over-dampening the generated acoustic wave. Such precision setting procedures, which will vary according to the material properties of the mechanical fastener as well as the water pipe, would be time consuming and difficult to control in the field.

In contrast to the non-adhesive contact methods, the adhesive contact method presents the advantages of quick installation as well as versatility for buried pipes of different materials and dimensions. For example, a commercially available cyanoacrylate adhesive can be easily applied along the pipe surface for quick and convenient bonding of the acoustic transducers, over an area equal to the base area if the transducer. For these reasons, the adhesive contact method was subsequently chosen, in preference to the non-adhesive option, for installing the acoustic transducers. The next section further describes the process by which installed acoustic

transducers (from the selection in Section 3.4.1) were compared along a water pipe, for final implementation within the communication system.

3.4.3 Laboratory comparison of the acoustic transducers

The objective of the laboratory experiments described in this section was to select the best-fit acoustic transducer for generating an acoustic wave within the proposed communication system. For acoustic wave sensing on the other hand, as previously mentioned in Section 3.4.1.2, the M-2814-P2 was already selected at this point to fulfil that purpose.

Since a key objective of the communication system design was to achieve acoustic signal transmission along a buried water pipe at a distance of at least 3 metres, the selection of the most appropriate acoustic transducer depended on which transducer produced the highest acoustic amplitude along the pipe. The laboratory methodology described in this section thus compared the relative acoustic amplitudes of the vibration motors, the surface transducers and the MFC (also the M-2814-P2 model but as an actuator) during operation along the pipe.

3.4.3.1 Pipe set-up in the laboratory

Besides the acoustic transducers, the laboratory apparatus featured a medium density polyethylene (MDPE) pipe of 90.6 mm diameter pipe and an overall length of 6 m, as shown schematically in Figure 3.10.

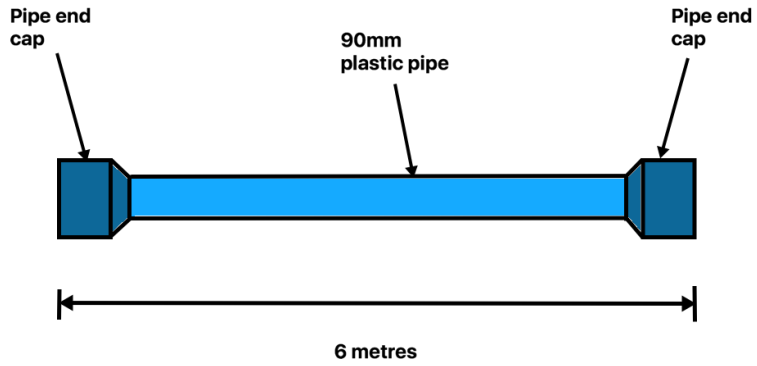

Figure 3.10: Schematic of the plastic (MDPE) pipe

For the first set of laboratory experiments, the external ERM vibration motor was installed along the plastic pipe by attaching steel blocks between the base of the vibration motor and the surface of the pipe using a commercially available cyanoacrylate adhesive. This set-up was chosen to elevate the vibration motor's external rotating mass above the pipe surface (thus ensuring free rotation of the mass), while providing a stable support for the vibration motor during its operation.

To generate the longitudinal acoustic wave along the pipe wall, the external ERM vibration motor was aligned with its motor shaft parallel to the MDPE pipe axis with another possible orientation being with the motor shaft perpendicular to the pipe axis (both methods of vibration motor alignment are further discussed in Section 3.8.3.3). The internal ERM vibration motor was also aligned in a similar manner (with its internal motor shaft parallel to the MDPE pipe axis) while the surface acoustic transducers did not require any specific orientation for installation along the pipe. The MFC piezoelectric sensor (M-2814-P2) on the other hand, for acoustic sensing, was directly bonded to the pipe at 5.6 m from the vibration motor as shown in Figure 3.11. The M-2814-P2, according to Smart-Material (2015), operates by generating an electrical signal through longitudinal mechanical contraction of the piezoelectric material and so the M-2814-P2 was aligned with its longitudinal axis parallel to the MDPE pipe axis for longitudinal acoustic wave detection along the pipe. The same MFC orientation was also employed for longitudinal acoustic wave generation (using the reverse piezoelectric effect) along the pipe during comparison with the other vibration actuators.

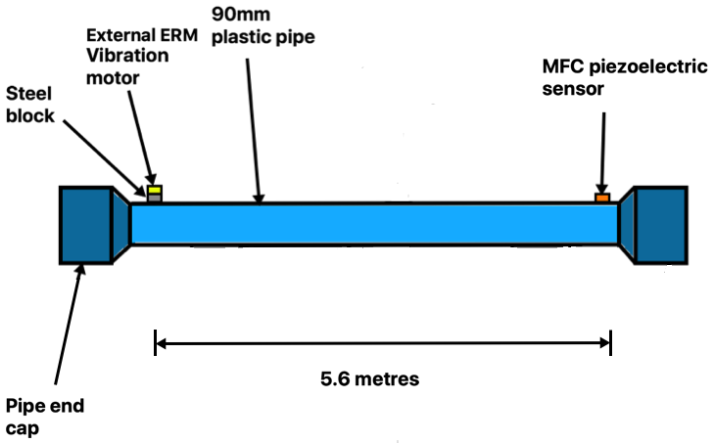

Figure 3.11: Schematic of the external ERM vibration motor and MFC sensor installations along the plastic pipe

Following the installation of the external ERM vibration motor and the MFC sensor, the experimental arrangement was set-up in the laboratory as shown in Figure 3.12.

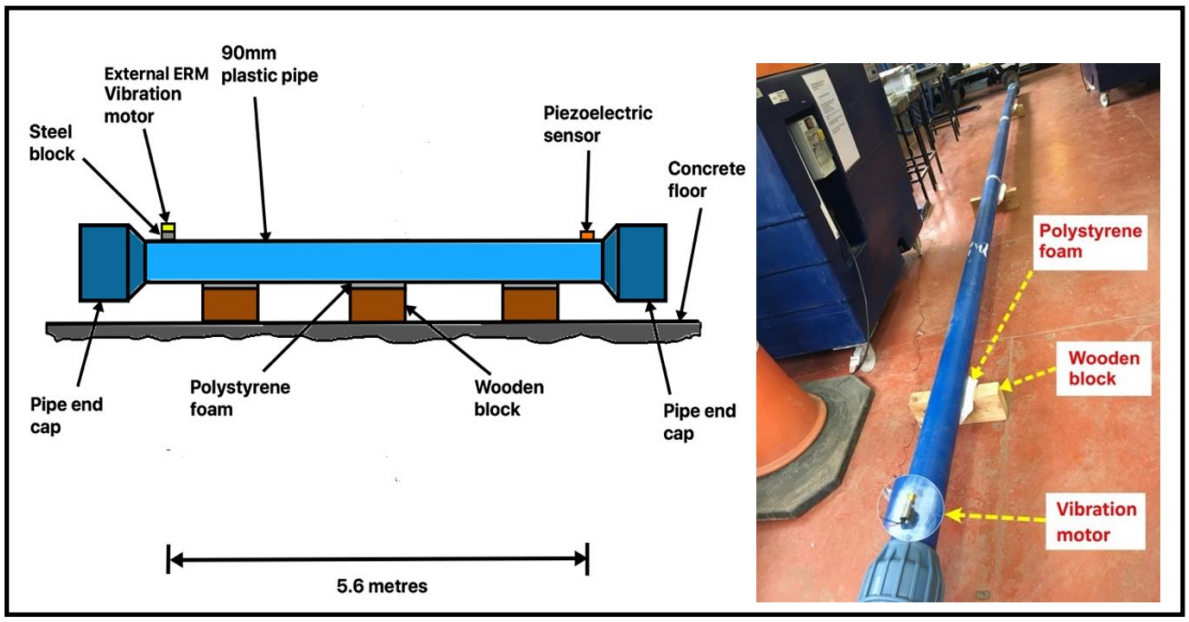

Figure 3.12: Laboratory arrangement of the plastic pipe showing wooden block support with sound insulating material (polystyrene foam)

As shown in Figure 3.12, the plastic pipe was supported above the laboratory floor by three wooden blocks with a 10 mm layer of polystyrene foam between the wooden blocks and the pipe. The wooden blocks were employed for preventing direct contact between the pipe and the laboratory floor which could otherwise create a path for unwanted acoustic noise from the

laboratory surroundings. The polystyrene foams were further employed for creating an additional sound buffer between the wooden blocks and the pipe. The wooden blocks chosen for the pipe supports were also constructed with V-shaped cuts to constrain the pipe while minimising acoustic radiation from the pipe into the wood. As shown in Figure 3.13, compared to a circular cut for example, the V-shaped cut minimised contact area between the pipe and the wood which was beneficial for reducing acoustic signal leakage into the wood.

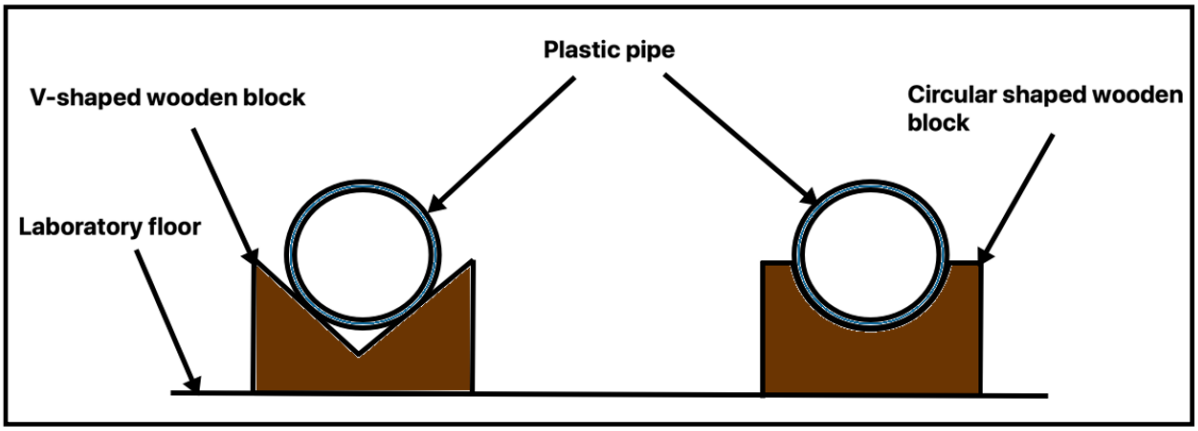

Figure 3.13: Cross-sectional diagrams of plastic pipe illustrating the difference between V-shaped and circular cut wooden block supports

It is important to also note the possibility of generating a standing acoustic wave (previously described in Section 2.5.2) along the pipe set-up in Figure 3.12 due to the finite pipe length in addition to the pipe boundary conditions (i.e., free at both ends). The resonant frequencies of this standing acoustic wave can be expressed as (Kinsler et al., 1999)

$$f_n = (n/2)(c/L) \tag{3.1}$$

Where f_n (Hz) is the frequency of the nth vibration mode, c (m/s) is the acoustic wave speed along the pipe and L is the pipe length. For an MDPE pipe material with acoustic wave speed of 1455 m/s (Muggleton & Yan, 2013) and pipe length of 6 m, the resonant frequencies below 1 kHz are summarised in Table 3.4. Knowledge of the pipe resonant frequencies in Table 3.4 was useful (as will be shown in Section 3.4.3.3) in understanding the degree to which the

presence of standing acoustic waves along the exposed MDPE pipes may have influenced the quality of results obtained from the acoustic transducer comparison experiments.

Table 3.4: Resonant frequencies below 1 kHz for the 6 m MDPE pipe

Vibration mode number	Frequency (Hz)
1	121
2	243
3	364
4	485
5	606
6	728
7	849
8	970

3.4.3.2 Instrumentation for the transducer comparison experiments

This section describes the instrumentation necessary for executing the acoustic transducer comparison experiments in the laboratory. For signal transmission, a microcontroller based acoustic signal transmitter was designed to control the acoustic actuators during operation along the pipe. With a microcontroller based acoustic transmitter, being consistent with the overall methodology for the communication system design, the acoustic transmitter circuit could later be upgraded into a full digital communication transmitter (Section 3.5) while saving design costs. The microcontroller employed at the acoustic transmitter was the LPC1768 microcontroller manufactured by NXP semiconductors (NXP, 2016; NXP, 2009) which was chosen for its low cost (less than £50), small size (55 mm length and 26 mm width) and low power (0.46 W).

For the ERM vibration motor, the acoustic transmitter circuit consisted of the microcontroller and an n-channel metal oxide field effect transistor (MOSFET) for interfacing the vibration motor and the microcontroller as shown in Figure 3.14.

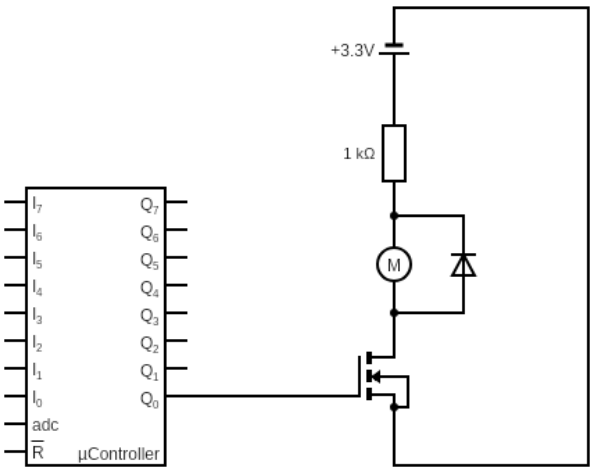

Figure 3.14: Acoustic transmitter circuit using the vibration motor

Figure 3.14 shows the circuit schematic for controlling the ERM vibration motor during the acoustic transmission experiments. As shown in the figure, the microcontroller was connected to the n-channel MOSFET through the transistor gate thereby switching the vibration motor (labelled M in the diagram) according to a binary information signal from the microcontroller. A fly back diode was also connected to the vibration motor to prevent sudden voltage spikes across the motor during switching operations. The microcontroller was further programmed to sequentially transmit repeated binary pulses (of 1 s duration) according to the flowchart in Figure 3.15.

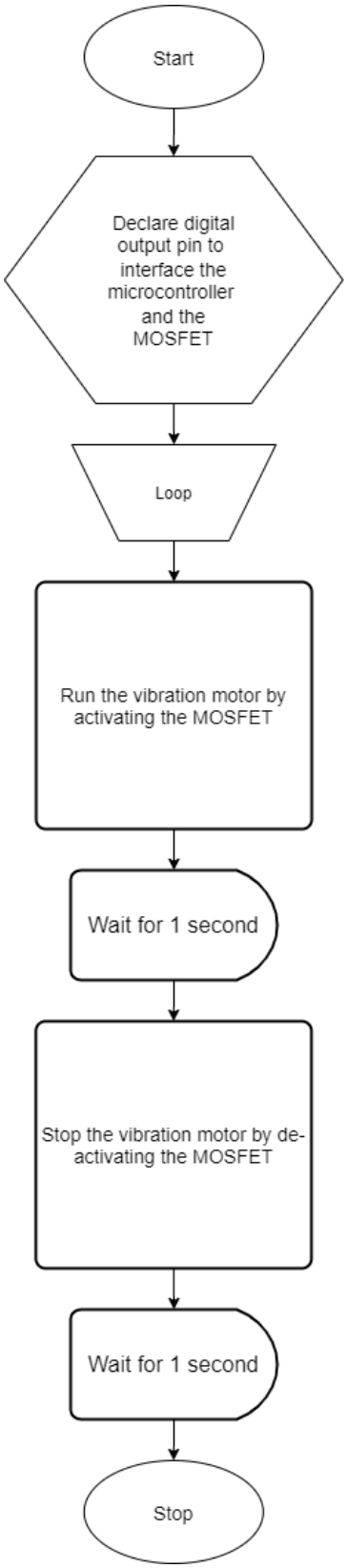

Figure 3.15: Flowchart for controlling the ERM vibration motor

From Figure 3.15, the algorithm for controlling the ERM vibration motor began with a digital output pin assignment to interface the microcontroller and the MOSFET. Following this procedure, the MOSFET was activated for 1 s before subsequent de-activation thereby allowing the transmission of 1 s acoustic pulse by the vibration motor. A pulse duration of 1 s was chosen for the acoustic transmission experiments to maximise the transmitted acoustic power while maintaining the objective of real-time data communication of at least 1 bit per second along the pipe.

To operate the surface transducers, the microcontroller was directly connected to the surface transducers while activating them at a desired excitation frequency using pulse width modulation (PWM). The programme flowchart for this process is shown in Figure 3.16.

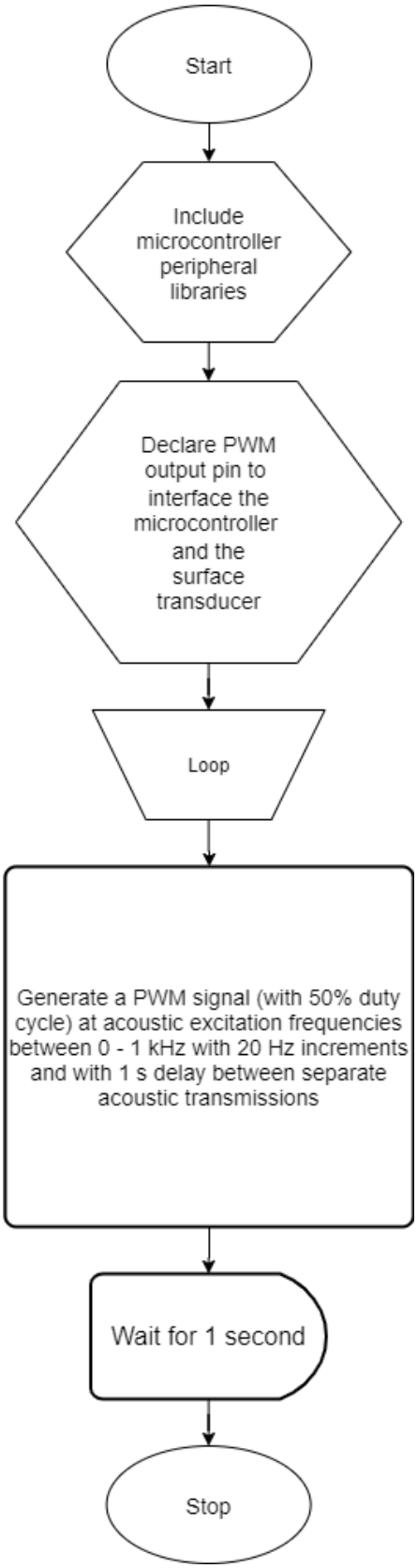

Figure 3.16: Flowchart for controlling the surface transducer

From Figure 3.16, the algorithm for controlling the surface transducer began with an inclusion of the necessary microcontroller libraries for executing the PWM command. A PWM output pin was further assigned to interface the microcontroller and the surface transducer. Following this pin assignment, separate PWM pulses (each of 1 s duration) at increasing frequencies between 0 and 1 kHz were generated at the microcontroller with a 1 s spacing between each pulse. With this method, the water pipe was therefore repeatedly excited between 0 and 1 kHz to cover the communication channel bandwidth.

Regarding the flowchart of Figure 3.16, the MFC transducer was also activated in a similar manner to the surface transducers. For the hardware design however, a piezoelectric transducer interface was introduced between the microcontroller and the MFC. This transducer interface, the DRV 8662 evaluation board from Texas Instruments, is shown in Figure 3.17.

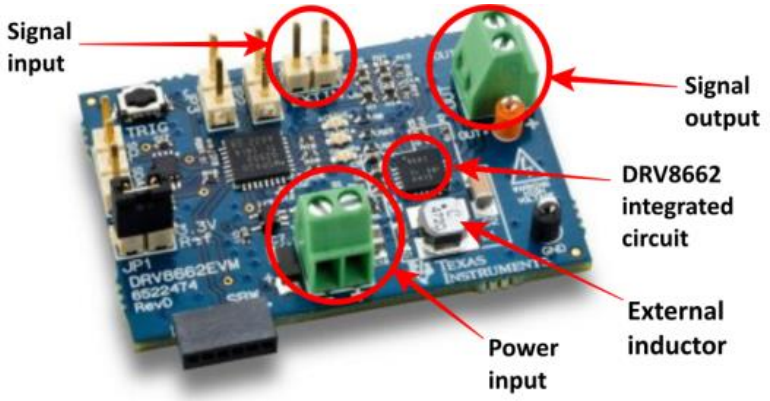

Figure 3.17: DRV 8662 Evaluation board (Texas Instruments, 2016) for driving the MFC

From Figure 3.17, the main components of the DRV 8662 evaluation board for driving the MFC were the signal input terminal (from the microcontroller), the signal output terminal (connected to the MFC), a power input terminal (3.3 V), the DRV 8662 integrated circuit (IC) and an external inductor. The DRV 8662 IC is a high voltage piezoelectric driver with an integrated boost converter and voltage amplifier, located within a single package of 4.15mm x 4.15mm surface area (Texas Instruments, 2014). With the help of the external inductor, the DRV 8662

IC provided the necessary amplification of the input PWM signal for driving the MFC transducer.

Following the acoustic transmitter set-up, a National Instruments (NI-USB 6211) digital acquisition device (DAQ) was connected to a separate MFC (M-2814-P2) sensor (which was installed along the pipe) before connecting the DAQ to a PC. The complete laboratory set-up for the acoustic signal transmission experiments is shown in Figure 3.18.

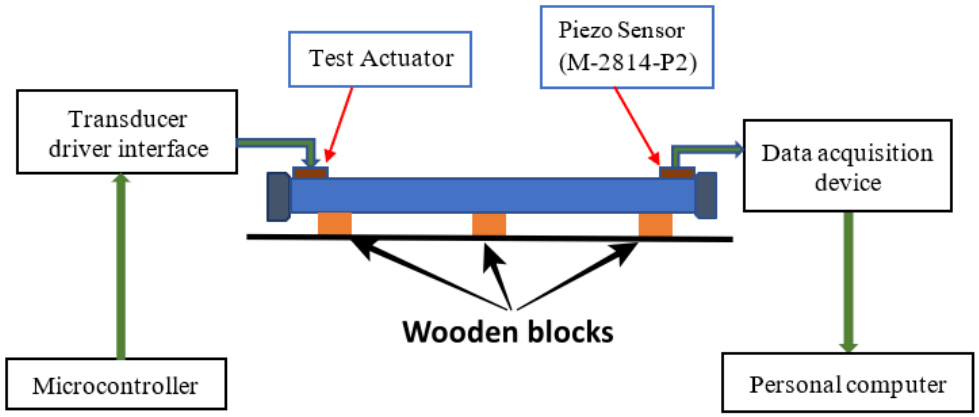

Figure 3.18: Laboratory set-up for comparing the acoustic transducers

Figure 3.18 shows the laboratory set-up for the acoustic signal transmission experiments featuring the test actuator installed along the MDPE pipe. The signal flow path from the microcontroller to the transducer driver interface and from the piezoelectric (MFC) sensor to the data acquisition device and PC is also shown in the diagram.

To capture the transmitted acoustic signal along the pipe, the MFC converted the mechanical vibrations along the pipe into corresponding electrical signals which were digitally sampled by the DAQ at a rate of at least twice the acoustic bandwidth (i.e., at least 2 kHz for the experiments) to obtain an accurate copy of the transmitted acoustic signal according to the Nyquist sampling criterion. Once the acoustic signals were recorded at the PC, a single side band (SSB) fast Fourier transform (FFT) technique was applied to the recorded waveforms to

convert the signals from the time into the frequency domain. The x-axis of the FFT spectrum was further created according to Equation (3.1)

$$f = {}^{f_s}/_{N} \tag{3.1}$$

Where f (Hz) represents each frequency point along the x-axis, f_s (Hz) is the DAQ sampling frequency and N is the total number of samples (FFT points) collected at the DAQ. To enhance the frequency resolution of the FFT, a 50000-point FFT with a sampling frequency of 10 kHz was used for creating each frequency bin along the x-axis. The FFT amplitude per unit sample of the acquired acoustic signal was subsequently plotted against frequency with the results presented in the next section while the Matlab code for implementing the FFT is provided in Appendix B.

3.4.3.3 Acoustic signal transmission results

For the acoustic signal generated by the external ERM vibration motor, the FFT spectrum is shown in Figure 3.19.

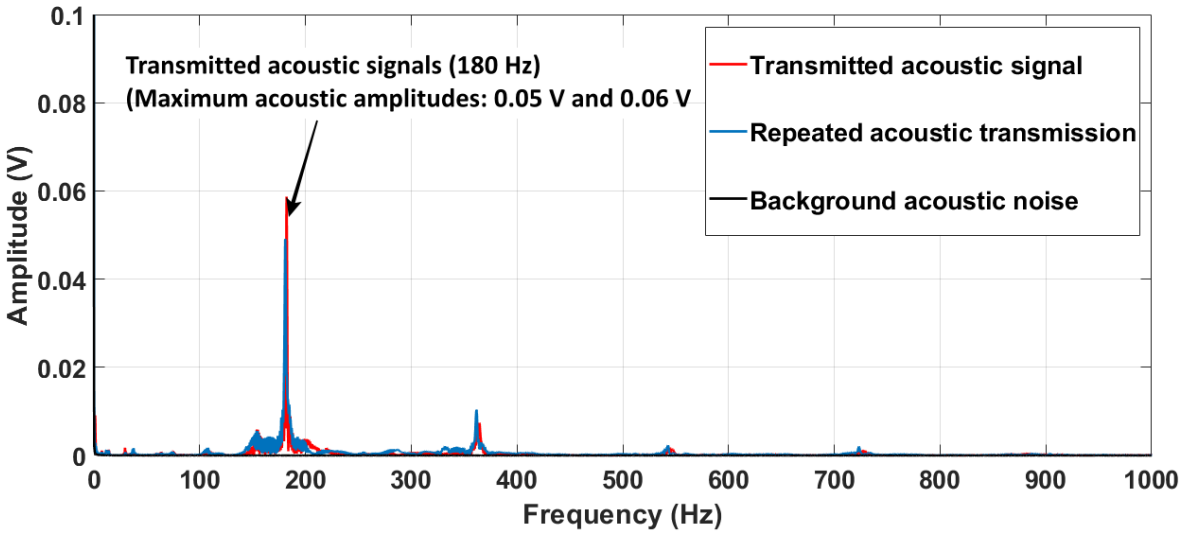

Figure 3.19: Acoustic signal spectra for external ERM vibration motor operation along the MDPE pipe

As shown in Figure 3.19, acoustic signal peaks between 0.04 and 0.06 V can be observed around 180 Hz for separate acoustic transmissions by the external ERM vibration motor. The external ERM vibration motor was subsequently replaced by the internal ERM vibration motor with the experiment repeated and results shown in Figure 3.20.

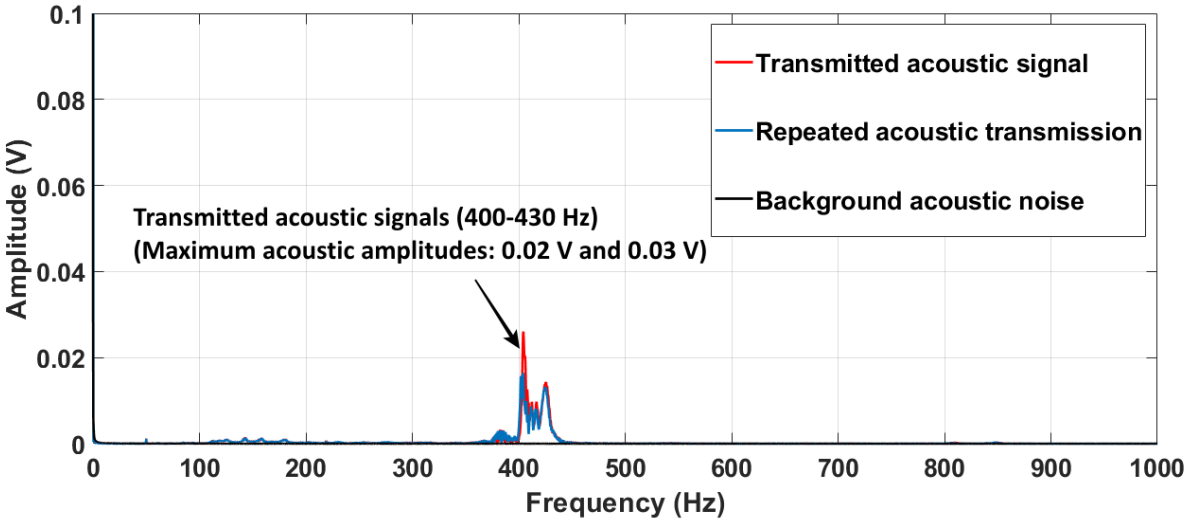

Figure 3.20: Acoustic spectra for internal ERM vibration motor operation along the MDPE pipe

From Figure 3.20, the acoustic signal peak amplitudes for the internal ERM vibration motor generated acoustic signals are between 0.01 and 0.03 V. Figures 3.19 and 3.20 therefore show that the external ERM vibration motor was a better option for acoustic signal generation due to its higher acoustic amplitude (approximately twice the amplitude of the coin motor).

Furthermore, in Figures 3.19 and 3.20, the peak acoustic signal amplitudes (indicating the operating frequencies of the vibration motors) measured along the pipe were located at 180 Hz and 400 Hz, respectively. These frequencies are outside the pipe resonant frequencies listed in Table 3.4 thus confirming the measurement of travelling as opposed to standing acoustic waves along the pipe set-up in Figure 3.12. The external ERM vibration motor also showed a relatively stable steady state frequency (indicated by the narrow band acoustic signal peak in Figure 3.19

compared to Figure 3.20) which was also advantageous for digital communication reliability within the proposed communication system.

The acoustic transmission experiments were further repeated by replacing the vibration motors initially with the surface transducers followed by the MFC transducer, while exciting the acoustic transducers at 180 Hz (to directly compare with the external ERM vibration motor). While the acoustic signals generated by the surface acoustic transducers were undetectable along the MDPE pipe, the acoustic signals detected for the MFC transducer are shown in Figure 3.21.

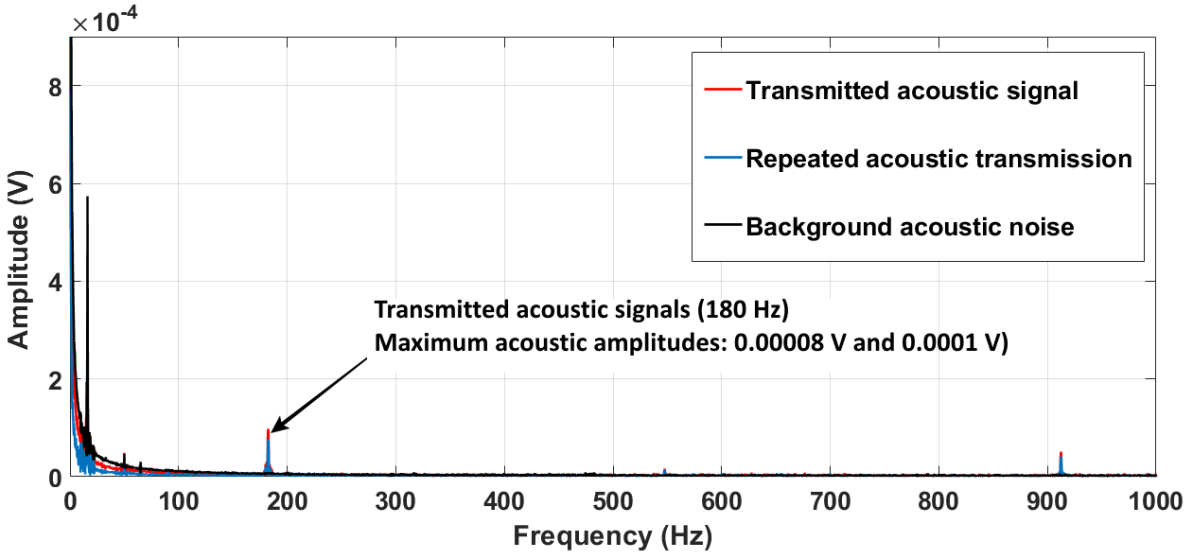

Figure 3.21: Acoustic spectra for MFC operation along the MDPE pipe

As shown in Figure 3.21, the transmitted acoustic signal amplitude for the MFC operating along the exposed MDPE pipe is significantly lower (by two orders of magnitude) than the acoustic amplitude using the external ERM vibration motor along the pipe. The external ERM vibration motor was therefore selected as the final choice for acoustic signal generation while the MFC, as previously discussed in Section 3.4.1.2, remained the acoustic sensor of choice. The procedure for integrating the vibration motor and MFC sensor at the digital communication

transmitter and receiver respectively, along with the methodology by which these communication nodes were designed, are further described in Sections 3.5 and 3.6.

3.5 DEVELOPMENT OF THE DIGITAL COMMUNICATION TRANSMITTER

Figure 3.1 outlined the operational stages at the digital communication transmitter as the message to be transmitted, message encoding, digital modulation as well as the message synchronisation (with the digital communication receiver) processes.

3.5.1 Message encoding

The first operational stage of the digital communication transmitter was the message encoding process. Message encoding transforms an acquired message at the input of a digital communication system into its corresponding binary format for further transmission across the communication system (Mutagi, 2013; Proakis & Salehi, 2008; Kokossalakis, 2006). If the message to be transmitted is analogue in nature, the message must be initially sampled at a rate which obeys the Nyquist sampling criterion to obtain an accurate copy of an analogue message in digital format (Nguyen & Shwedyk, 2009). On the other hand, for a message which is already digital in nature, the digital to analogue conversion process is not required. Such information however needs to be formatted according to some specified standard (e.g., American Standard for Information Interchange (ASCII), Binary Coded Decimal, Morse code, etc.) before further transmission across the digital communication system (Kokossalakis, 2006; Sklar, 2001). For the proposed communication system, the ASCII encoding format was employed for transforming a digital message at the PC in Figure 3.2 into binary form.

3.5.2 Digital modulation

Following the message encoding stage in Figure 3.1 was the digital modulation stage. Digital modulation refers to the process of manipulating the physical characteristics of a signal according to a pre-defined set of data symbols representing the message to be transmitted

(Mutagi, 2012; Kokossalakis, 2006; Sklar, 2001). The need to modulate a digital information signal becomes apparent, with the presence of an external medium (such as air, water, electrical cables etc.) representing a physical discontinuity between the digital communication transmitter and receiver. Such an external medium (which can extend in range from a few millimetres to several kilometres) typically poses challenges, in terms of power and bandwidth limitations, to the transmission of digital information across the digital communication system (Mutagi, 2012). Digital modulation therefore serves the specific purpose of mapping digital information to a waveform (digital information carrier) with the appropriate power and bandwidth characteristics to enable propagation across the external medium (Sklar, 2001). When this mapping process is undertaken with the constraint that a transmitted waveform depends on one or more previously transmitted waveforms, the digital modulator is said to have memory. On the other hand, when a transmitted waveform does not depend on previously transmitted waveforms (only depending on the data sequence under consideration), the modulator is said to be memoryless (Kokossalakis, 2006). With a memoryless modulator therefore, potential errors from previously transmitted waveforms are not carried forward to subsequent digital transmissions and so for digital communication reliability, this choice of digital modulation technique was advantageous.

In general, two categories of digital modulation techniques exist, i.e., baseband and passband modulation. With digital baseband modulation, a sequence of discrete pulse signals is responsible for digital information transmission. In contrast, digital passband modulation features the variation of the amplitude, frequency, or phase of a sinusoidal signal (carrier wave) to transmit digital information (Mutagi, 2012; Nguyen & Shwedyk, 2009). Since the ERM vibration motor was chosen for acoustic signal generation at the digital communication transmitter, the resonant frequency of the ERM during operation (i.e., the maximum acoustic peaks in Figure 3.19) represented the carrier wave which was to be modulated according to the

digital information to be transmitted. This carrier wave can further be expressed mathematically as

$$s(t) = a(t)\cos\left[\omega_c(t) + \emptyset_c(t)\right] \qquad (3.2)$$

Where $s(t)$ is the carrier wave function, t (s) is time, $a(t)$ is the carrier wave amplitude, ω_c (rads/s) is the angular frequency of the carrier wave and $\emptyset_c$ (rads) is the carrier wave phase. Depending on the property of the carrier wave (i.e., $a(t)$, ω_c or $\emptyset_c$) to be modulated, passband modulation can be fundamentally categorised as amplitude shift keying (ASK), frequency shift keying (FSK) and phase shift keying (PSK). With ASK, the amplitude of the carrier wave is modulated while with FSK and PSK, the frequency and phase of the carrier wave are modulated respectively (Proakis, 2001).

Other digital modulation techniques applicable across the digital communications industry generally include (but are not limited to) quadrature amplitude modulation (QAM), differential phase shift keying (DPSK) and pulse amplitude modulation (PAM). Variations of these digital modulation techniques also exist based on the number of discrete symbols, *M*, which can be mapped on to a carrier wave. Such modulation techniques include 64 QAM (M = 64), 16 QAM (M = 16), 4 PSK (M = 4) and so forth. These techniques however, compared to a binary modulation approach, require increasingly complex signal processing circuitry within the digital communication system to reduce ambiguity of symbol detection at the digital communication receiver (Kokossalakis, 2006). A binary modulation technique was therefore considered advantageous for the proposed communication system due to its inherent reliability (compared to other *M-ary* modulation techniques) with minimal signal processing complexity.

The eventual choice of binary modulation technique was further based on a compromise between power and bandwidth considerations for the communication system. While on the one hand modulation techniques such as amplitude shift keying (ASK) and phase shift keying (PSK)

are more suitable for bandwidth limited channels (such as that presented by the ERM motor operating between 0 and 200 Hz), the frequency shift keying (FSK) technique is more suitable for power limited channels (e.g., in an underground environment where power sources are limited). The FSK technique is however disadvantageous for bandwidth limited channels due to its poor bandwidth efficiency (Kokossalakis, 2006; Proakis, 2001). Considering these challenges (i.e., limited bandwidth and power supply), a specialised form of ASK known as on-off-keying (OOK) which combined the benefits of bandwidth efficiency (1 bit/Hz) and power conservation (through data transmission by intermittently activating and de-activating the digital communication transmitter) was adopted for the communication system design.

For the modulating microcontroller role in Figure 3.2, the same LPC1768 microcontroller introduced in Section 3.4.3.2 was employed due to (as previously mentioned in the section) its low cost, small size, and low power. Furthermore, to implement the OOK modulation algorithm, the microcontroller needed to be interfaced with the vibration motor. An external interface circuit which comprised the electronic hardware responsible for interfacing the microcontroller to the vibration motor was subsequently designed with OOK modulation in mind. This external interface circuit was thus designed to systematically switch the vibration motor between full power ("on" state) and no power ("off" state) during digital transmission. To achieve this objective, an L293D integrated circuit (IC) from Texas Instruments was integrated at the communication transmitter. This L293D is a low cost (less than £5), small size (38 mm length and 17 mm width) and low power (as low as 0.04 W) electronic device capable of driving a direct current (DC) motor with currents approaching 600mA in both forward and reverse directions (Texas Instruments, 2016). Furthermore, as shown in Figure 3.22, the L293D consists of four separate amplifiers (numerically labelled in the figure) each of which could drive the DC rotor of the vibration motor in either forward or reverse direction.

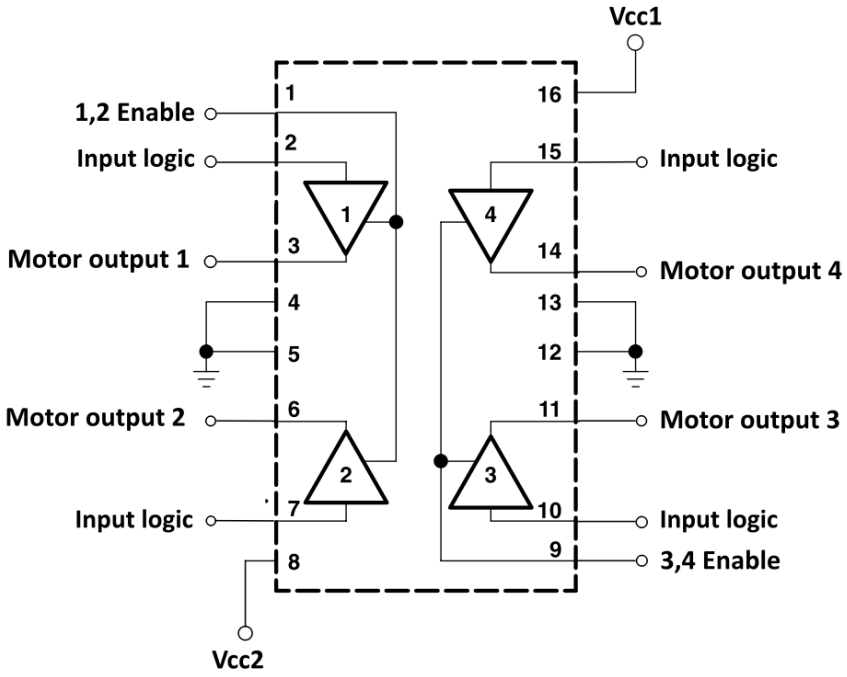

Figure 3.22: Schematic diagram of the L293D integrated circuit showing separate amplifiers (numerically labelled in the figure) for driving the vibration motor

Also shown in Figure 3.22 are the input logic and motor output pins, connected to each amplifier within the L293D. Depending on the amplifier in use, the input logic pin connected the amplifier to the microcontroller while the motor output pin connected the same amplifier to the vibration motor. During operation, binary signals representing the digitally modulated signal at the microcontroller determined the state (i.e., logic HIGH or LOW) of an input logic pin at the L293D. Depending on this input logic state, the vibration motor connected to the corresponding output of the input logic pin was subsequently activated or de-activated. A logic HIGH thus activated the motor while a logic LOW de-activated the motor. In this manner, the OOK modulation algorithm was employed for digitally modulating the acoustic signal generated by the vibration motor.

Although each amplifier in Figure 3.22 could individually be employed for driving the vibration motor, two amplifiers were combined for driving the vibration motor. The reason for this was the difference in performance between two modes of motor control, i.e., non-active and active

braking techniques. With non-active braking the DC rotor of the vibration motor was operated according to the logic input of one amplifier (i.e., HIGH, or LOW logic input), allowing the rotor to either rotate or come to rest. Due to the rotational inertia of the DC rotor however, the rotor did not immediately come to rest during a logic LOW input thus resulting in a slightly extended period of motor activity. This delay in motor response was overcome by employing the active braking technique according to Table 3.5.

Table 3.5: Logic control for actively braking the vibration motor

Logic inputs at separate amplifiers	DC rotor movement
LOW & LOW	Off
LOW & HIGH	Either forward or reverse direction
HIGH & LOW	Either forward or reverse direction
HIGH & HIGH	Motor stop

As shown in Table 3.5, four input logic combinations were possible for controlling the DC rotor of the vibration motor with the active braking technique. The key difference between the active and non-active braking technique was in the method by which the DC rotor was stopped. In the last row of Table 3.5, a simultaneous input HIGH logic at both amplifiers de-activated the DC rotor by attempting to rotate the rotor simultaneously in the forward and reverse directions. Equal and opposite forces were thus generated within the DC rotor thus preventing rotor movement and eliminating inertial effects during motor de-activation. In such a way, a quicker response time was achieved at the vibration motor by replacing the LOW command of the non-active braking technique with the simultaneous HIGH-HIGH command of the active braking technique. The algorithm flowchart for implementing the active and non – active braking techniques at the digital communication transmitter is shown in Figure 3.23.

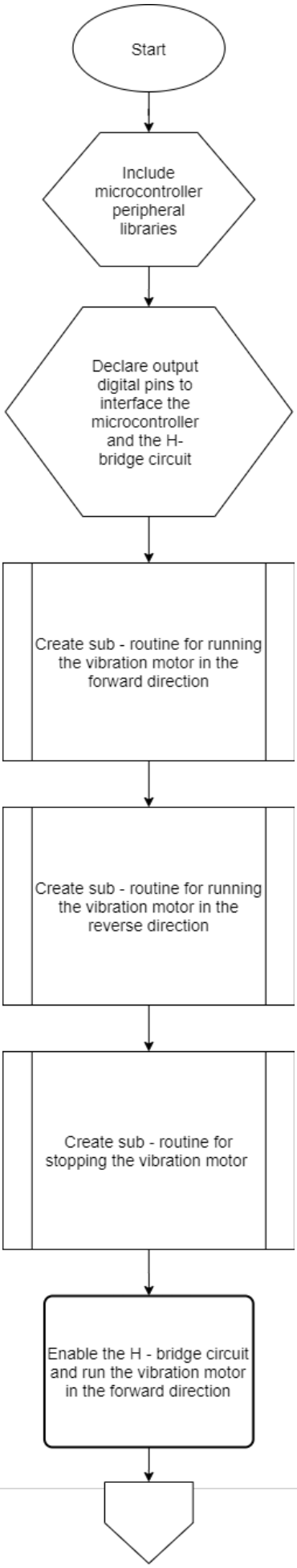
Start
Include microcontroller peripheral libraries
Declare output digital pins to interface the microcontroller and the H-bridge circuit
Create sub - routine for running the vibration motor in the forward direction
Create sub - routine for running the vibration motor in the reverse direction
Create sub - routine for stopping the vibration motor
Enable the H - bridge circuit and run the vibration motor in the forward direction

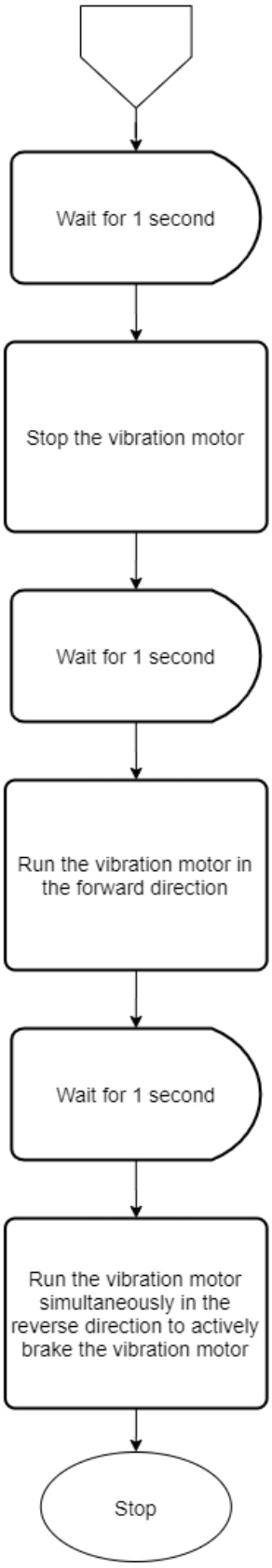

Figure 3.23: Flowchart for active and non-active braking at the digital communication transmitter

As shown in Figure 3.23, the algorithm for implementing non-active and active braking techniques at the digital communication transmitter began with the inclusion of the necessary software libraries for interfacing the microcontroller with an external peripheral device (in this case the H-bridge circuit) as well as declaration of the output digital pins to interface the microcontroller and the H-bridge circuit. Following this initialization, separate programme sub-routines were written to run the vibration motor in the forward and reverse directions as well as for stopping the vibration motor. The remaining stages of the algorithm further implemented these sub-routines procedurally by running the vibration motor and stopping it using non-active braking before re-activating the vibration motor and subsequently stopping it with the active braking technique.

The results of separate digital transmissions with the non-active and active braking techniques along the exposed MDPE pipe (Figure 3.10) are shown by the time domain plots of Figures 3.24a and b. An illustration of the difference between active and non-active braking is also shown in Figure 3.25.

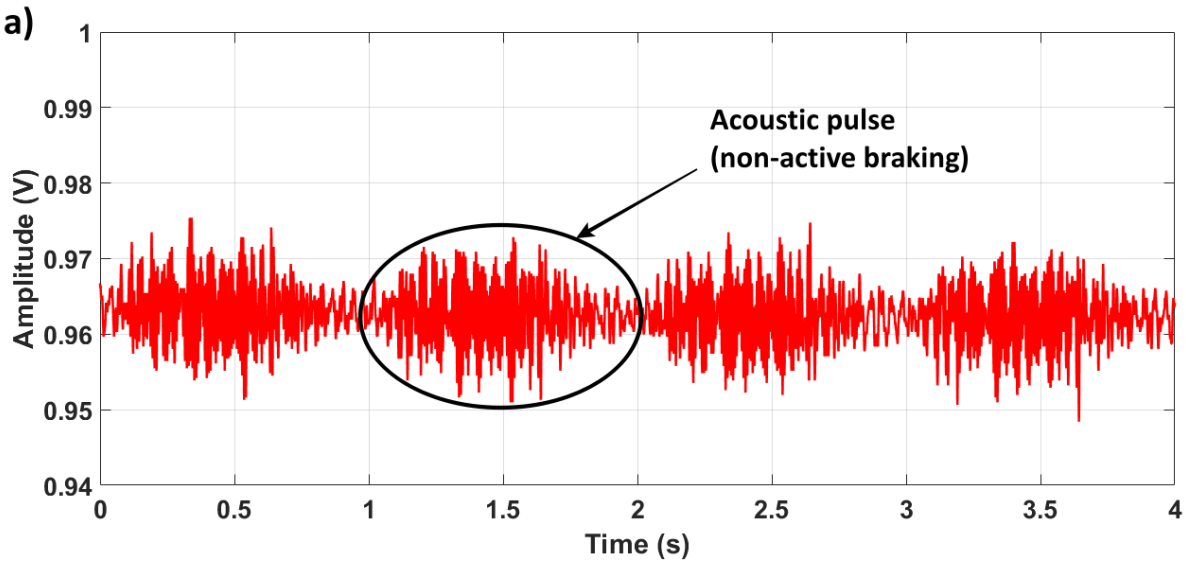

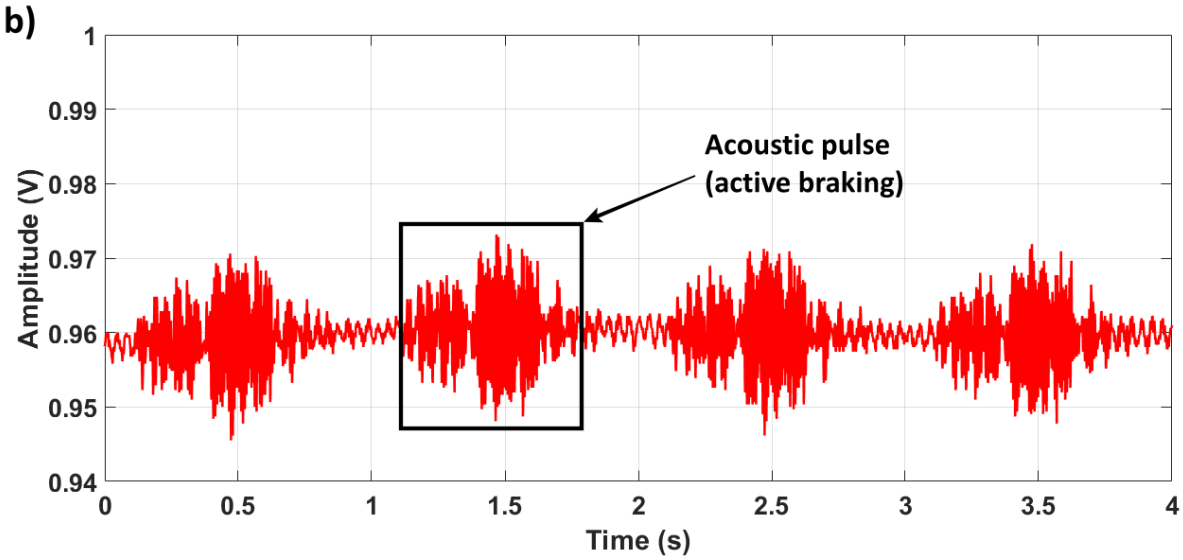

Figure 3.24a: Non-active and b) active braking with the ERM vibration motor

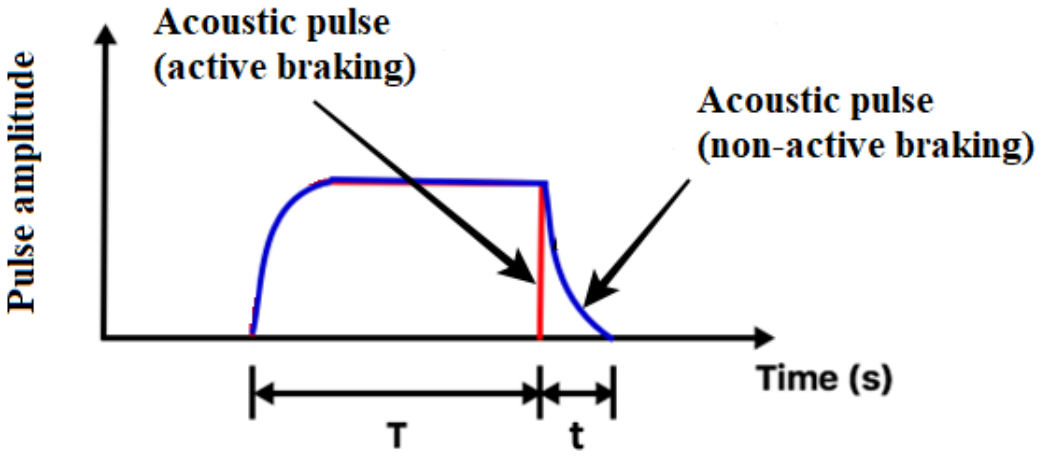

Figure 3.25: Pulse shapes for non-active and active braking with the vibration motor

As shown in Figures 3.24 and 3.25, an acoustic pulse generated with active braking decayed relatively instantaneously compared to a pulse generated with the non-active braking technique (which decayed gradually). This was crucial for maximizing the digital communication bandwidth since the presence (or absence) of an acoustic pulse within an allocated time window, T, signified one bit of digital information. With the non-active braking technique, the acoustic pulse extended beyond T (Figure 3.25), with a time window of T + t thus implying a

potentially lower data transmission rate compared to a pulse generated using the active braking technique. The active braking technique was therefore selected in preference to the non-active braking option for digital modulation at the communication transmitter.

3.5.3 Message synchronisation

Common to both transmitter and receiver sections in Figure 3.1 is the synchronisation component (shown in dashed lines). To ensure reliable digital communication, the message encoding and digital modulation stages must be synchronised with the message decoding and digital demodulation stages respectively thus ensuring the sequential flow of digital information across the communication system. Message synchronisation can generally be categorised into carrier, symbol, and frame synchronisation (Proakis & Salehi, 2008; Kokossalakis, 2006; Proakis, 2001; Sklar, 2001). With carrier synchronisation, the digital communication transmitter notifies the receiver of an incoming digital information signal, by initially transmitting a separate carrier wave pulse (pilot signal) before the digital demodulation process (otherwise known as coherent demodulation) can begin. With symbol synchronisation, the digital communication transmitter provides information of the start and end times of each digital symbol (in addition to the digital information itself) to ensure reliable demodulation at the receiver. To ensure accurate symbol detection, a clock timing signal is therefore required at the digital communication receiver (Kokossalakis, 2006; Sklar, 2001; Proakis, 2001). Lastly frame synchronisation involves the addition of an extra length of digital information to a block of codes during transmission across the digital communication system. This extra length of digital information must however be known *a priori* by the digital communication receiver to ensure successful synchronisation of digital information within the communication system (Kokossalakis, 2006; Sklar, 2001; Proakis, 2001).

Considering the three options for message synchronisation within the proposed communication system, the carrier synchronisation method involved the least signal processing complexity (which, importantly, reduces the power and physical size requirements of the digital communication node) as it only required the separate transmission of a carrier wave pulse to notify the digital communication receiver of an incoming digital transmission. The carrier wave synchronisation method was therefore employed for message synchronisation between the digital communication transmitter and receiver. The next section further describes the procedure for digital information transmission which incorporates all the transmitter operational stages.

3.5.4 Procedure for digital information transmission

For digital information transmission, the PC was first connected, through a serial port, to the modulating microcontroller within which the transmitter operational stages (bar message encoding) were executed. The serial connection between the PC and the microcontroller was programmed to transmit information at 300 bauds/second which was well above the data rate requirement of the digital communication system (thus avoiding the risk of any data communication bottleneck between the PC and the digital communication transmitter). Furthermore, the PC at the digital communication transmitter enabled message input (via the PC keyboard) and encoding before the transmitting the encoded message (via the serial connection) to the modulating microcontroller for OOK modulation.

Following the serial connection set-up, the modulating microcontroller was connected to the ERM vibration motor (which was already installed along the exposed MDPE pipe) via the H-bridge circuit. For the first digital transmission experiments, a digitally modulated binary information stream was programmed at the modulating microcontroller, the flowchart of which is shown in Figure 3.26 while the C programme is provided in Appendix A.

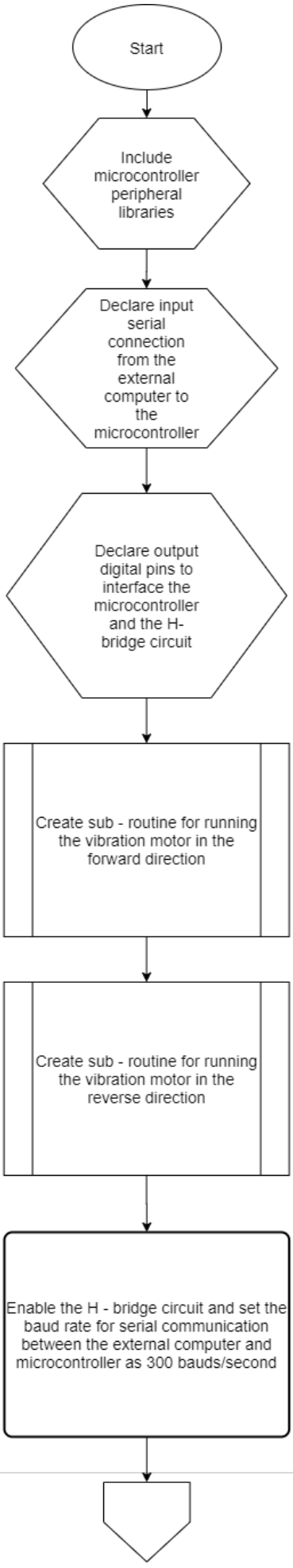
Start
Include microcontroller peripheral libraries
Declare input serial connection from the external computer to the microcontroller
Declare output digital pins to interface the microcontroller and the H-bridge circuit
Create sub - routine for running the vibration motor in the forward direction
Create sub - routine for running the vibration motor in the reverse direction
Enable the H - bridge circuit and set the baud rate for serial communication between the external computer and microcontroller as 300 bauds/second

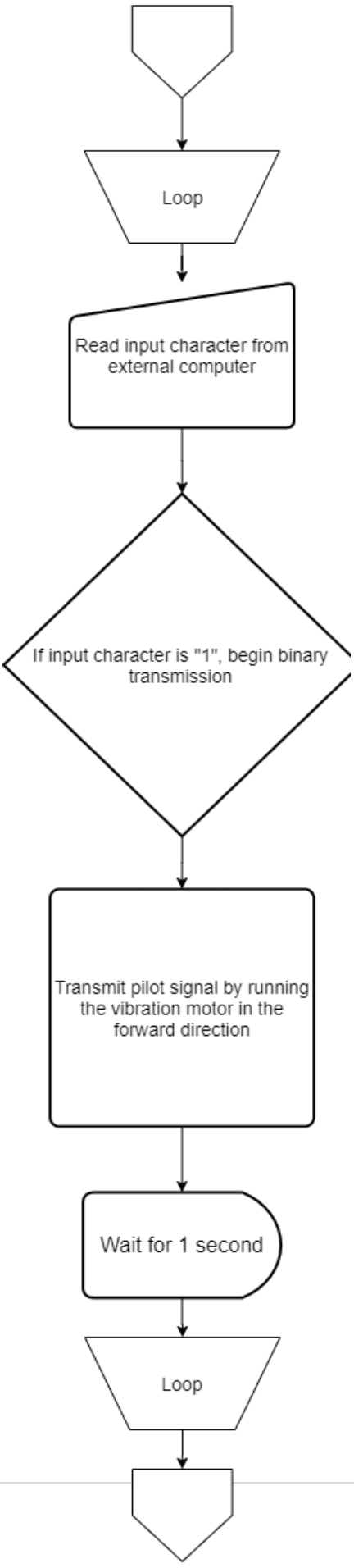
Loop
Read input character from external computer
If input character is "1", begin binary transmission
Transmit pilot signal by running the vibration motor in the forward direction
Wait for 1 second
Loop

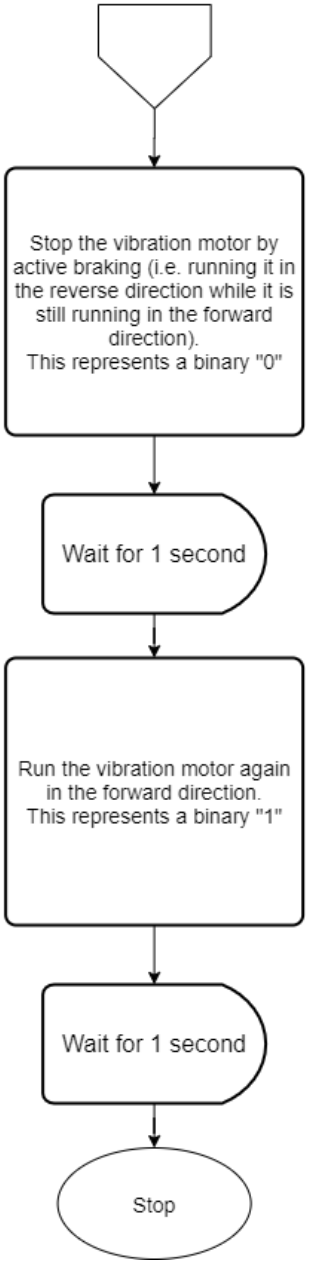

Figure 3.26: Flowchart for binary transmission at the digital communication transmitter

After the start of the algorithm, the first three programme elements of Figure 3.26 included standard programme initialization and declaration steps which prepared the microcontroller for serial interfacing with the PC as well as peripheral interfacing with the H-bridge circuit. Following programme initialization, separate sub-routines were written to rotate the ERM motor in the forward and reverse directions before setting a baud rate of 300 bauds/second. The

microcontroller was subsequently programmed to read an input character from the PC with the condition of running the vibration motor for 1 s in the forward direction if the input character was “1”. With this technique, a pilot signal of 1 s was initially transmitted by the ERM vibration motor before it was de-activated (for 1 s) using active braking. This de-activated period (which represented a binary “0”) was followed by activating the vibration motor again in the forward direction (representing a binary “1”) with the process repeating itself until manually stopped. With this procedure, a binary information stream (representing an alternating sequence of zeros and ones) was successfully generated at the digital communication transmitter.

The generation of a more complex sequence of digital information, such as the ASCII representation of an alphabetic character, was also implemented at the digital communication transmitter with the flowchart for this process shown in Figure 3.27 (the corresponding C programme is also provided in Appendix A).

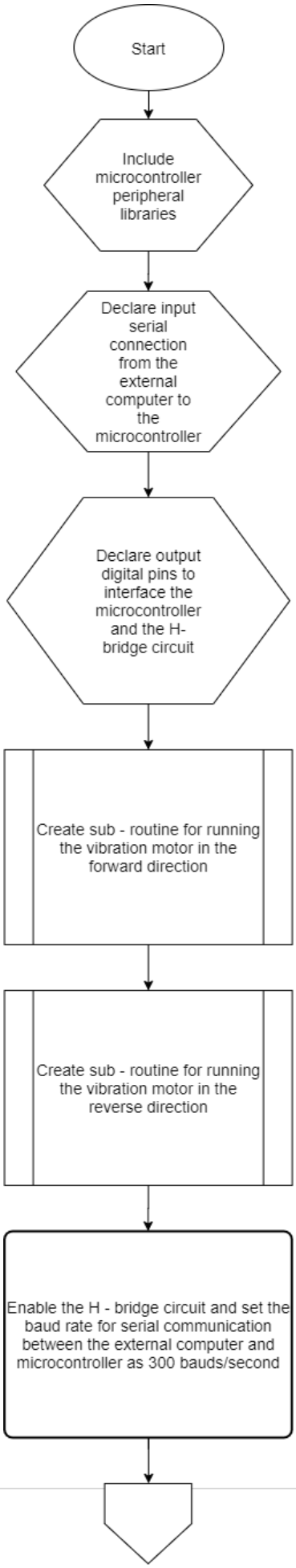
Start
Include microcontroller peripheral libraries
Declare input serial connection from the external computer to the microcontroller
Declare output digital pins to interface the microcontroller and the H-bridge circuit
Create sub - routine for running the vibration motor in the forward direction
Create sub - routine for running the vibration motor in the reverse direction
Enable the H - bridge circuit and set the baud rate for serial communication between the external computer and microcontroller as 300 bauds/second

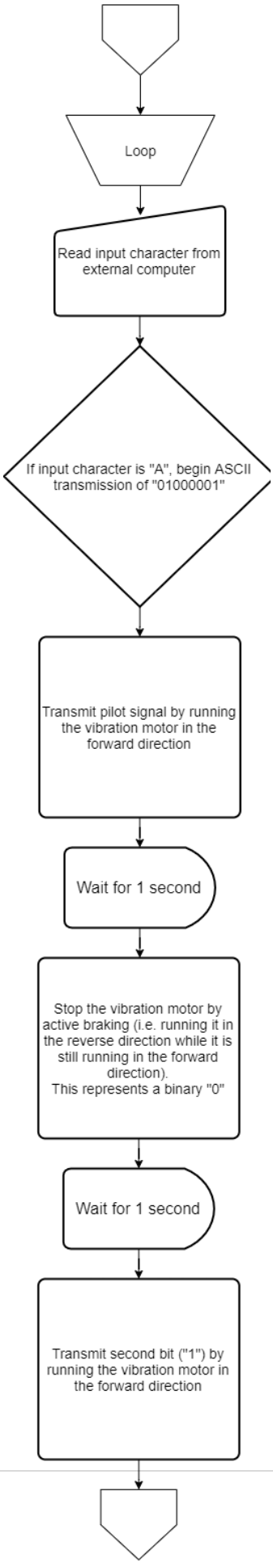
Loop
Read input character from external computer
If input character is "A", begin ASCII transmission of "01000001"
Transmit pilot signal by running the vibration motor in the forward direction
Wait for 1 second
Stop the vibration motor by active braking (i.e. running it in the reverse direction while it is still running in the forward direction).
This represents a binary "0"
Wait for 1 second
Transmit second bit ("1") by running the vibration motor in the forward direction

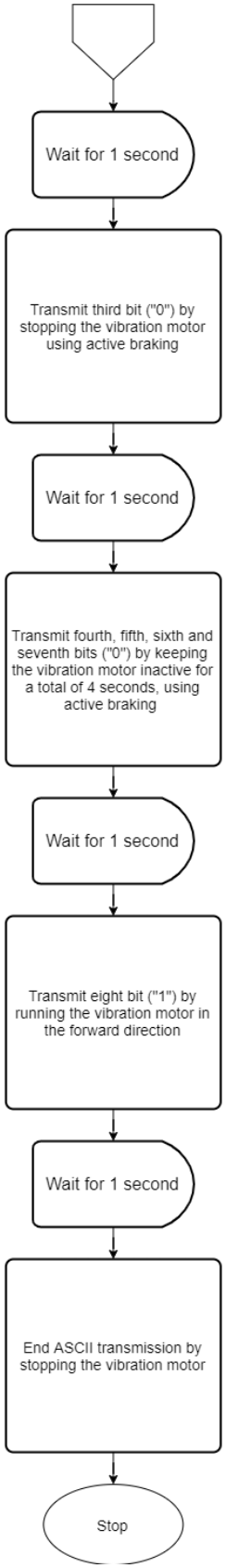

Figure 3.27: Flowchart for ASCII encoded data transmission at the digital communication transmitter

For ASCII transmission, the first seven blocks of Figure 3.27 are the same as the corresponding blocks in Figure 3.26 for binary transmission. The main difference between the ASCII and binary transmission was the nature of the input character to be read by the microcontroller from the PC. For the ASCII transmission example in Figure 3.27, the ASCII code for an alphabetic character "A" (i.e., "01000001") was to be generated at the digital communication transmitter. Once the symbol entered at the PC was recognized by the microcontroller as its binary equivalent, a pilot signal was generated at the ERM vibration motor before individual bits of the ASCII character were generated by sequentially activating and de-activating the vibration motor to represent "1" and "0" respectively.

3.5.5 Printed circuit board design of the digital communication transmitter

The final hardware design of the digital communication transmitter was in the form of a printed circuit board (PCB) (Figure 3.28), the circuit layout for which was designed using the DipTrace software package. The circuit schematic of the digital communication transmitter (provided in Appendix C) was printed on a PCB layout with FR4 substrate using a commercially available PCB manufacturer (PCBWay Ltd). Figure 3.28 shows the final product complete with microcontroller, serial port (for PC communication) and H-bridge (L293D) circuit for interfacing with the ERM vibration motor.

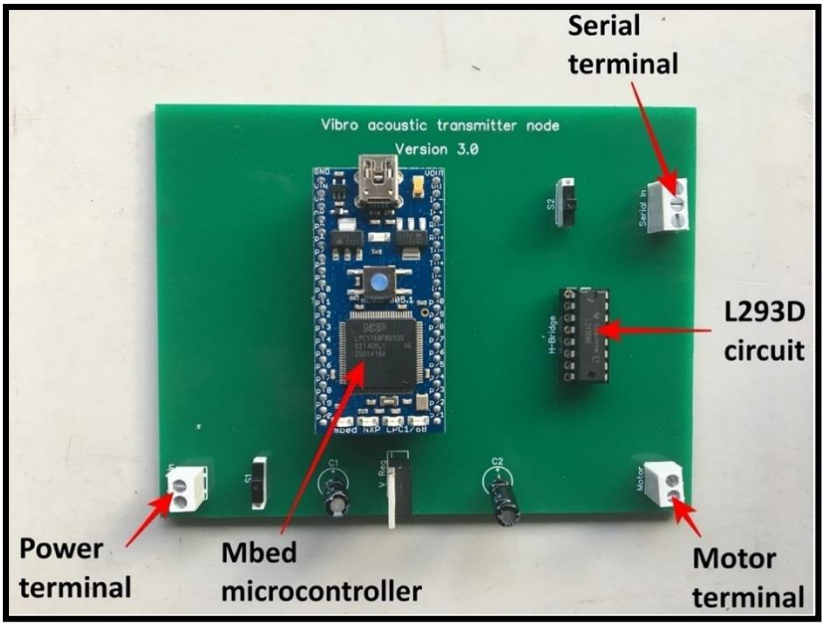

Figure 3.28: Printed circuit board of the digital communication transmitter

The digital communication transmitter development described in this section represented one half of the proposed communication system. At this stage, digitally modulated information could be generated at the communication transmitter. The second half of the communication system development comprised a digital communication receiver designed to successfully demodulate and extract this information, which was transmitted along the exposed MDPE pipe. The method by which this was achieved is described next.

3.6 DEVELOPMENT OF THE DIGITAL COMMUNICATION RECEIVER

Based on Figure 3.1, the operational stages at the digital communication receiver after the acoustic propagation channel (i.e., the water pipe waveguide) are digital demodulation, message decoding (as well as synchronisation with the transmitter) and message presentation to an observer. These stages, within the context of developing the digital communication receiver, are described next.

3.6.1 Digital demodulation

As discussed in Section 3.4.1.2, the MFC transducer was selected as the best-fit choice for acoustic sensing at the digital communication receiver. Once the acoustic signal was therefore detected along the pipe by the MFC sensor and before digital demodulation could take place, the standard practice of amplifying the detected signal (which, like in any wireless communication system, was expected to have experienced some degree of attenuation between the transmitter and receiver) was initially implemented. A signal pre-amplifier circuit, shown in Figure 3.29, was therefore designed to interface the MFC sensor with the rest of the digital communication receiver.

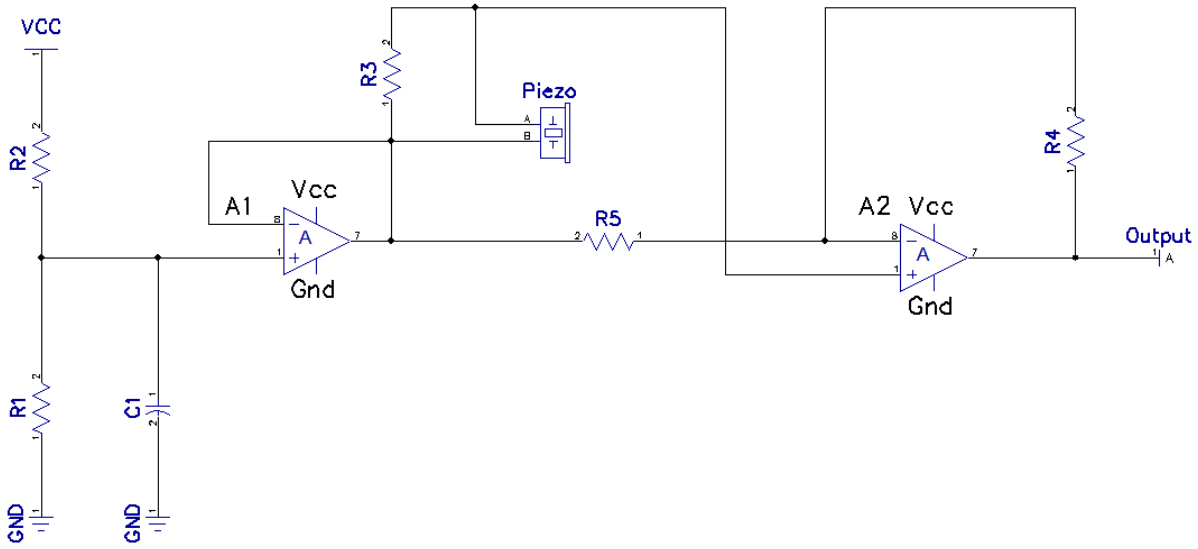

Figure 3.29: Signal pre-amplifier circuit at the front-end of the digital communication receiver

As shown in Figure 3.29, a two-stage amplifier was designed where the inverting (negative) input of amplifier A1 was connected to terminal B of the MFC (labelled “Piezo”), while the non-inverting (positive) input of amplifier A2 was connected to terminal A of the MFC. A1 was further isolated from the ground (GND) terminal of the signal pre-amplifier circuit through

a voltage divider network (V_{cc}, R1 and R2). Amplifier A1 thus served as a buffer network for protecting the MFC from GND noise.

The second amplifier (A2) on the other hand (which was key to the amplifier design), amplified the MFC acquired signal according to Equation (3.3) (Horowitz & Hill, 2016).

$$\frac{V_{out}}{V_{in}} = 1 + \frac{R_4}{R_5} \tag{3.3}$$

Where V_{in} and V_{out} (V) are the input and output voltages respectively of amplifier A2, R_4 (Ω) is the feedback resistor of amplifier A2 while R_5 (Ω) is the input resistor of amplifier A2. For signal amplification, operational amplifiers are generally preferable to single transistor amplifiers due to their relatively higher power gains (Horowitz & Hill, 2016). Low cost (£5), small size (10 mm length and 7 mm width) and low power (tens of milliwatts) operational amplifiers (LT1001 from Linear Technology, 1983) were subsequently employed for amplifiers A1 and A2. Since the maximum voltage output of the LT1001 amplifier is 4 V (with a 5 V supply) (Linear Technology, 1983), R4 and R5 were chosen so as not to saturate A2. Using the average voltage detected at the MFC sensor for the external ERM vibration motor test along the exposed MDPE pipe (i.e., 0.05 V in Figure 3.19) as V_{in} and with $V_{out} = 4$ V, R4 and R5 were subsequently chosen, using Equation (3.3), as 79 kΩ and 1 kΩ respectively.

Following signal amplification at the front-end of the digital communication receiver, a non-coherent demodulation approach was adopted as opposed to a coherent demodulation alternative. A receiver is said to be coherent if it requires knowledge of the absolute phase of an incoming carrier signal whereas the opposite is the case for a non-coherent receiver (Proakis & Salehi, 2008; Kokossalakis, 2006). Coherent receivers therefore possess copies of all possible waveforms expected at the receiver before matching them with the incoming signal, a requirement which consequently increases the signal processing complexity of the receiver

compared to a non-coherent alternative. Due to the reduced signal processing complexity offered by non-coherent demodulation therefore, this research employed non-coherent demodulation for the digital communication receiver design. To further guarantee digital communication reliability with the non-coherent demodulator, a phase locked loop (PLL) was implemented as part of the digital communication receiver. With a PLL, the digital communication receiver was synchronised with the digital communication transmitter using the pilot signal approach previously described in Section 3.5.3. Once the receiver detected a pilot signal (in the form of an incoming acoustic wave) therefore, it was phase locked to this signal while the rest of the digital demodulation process was carried out at the digital communication receiver thus guaranteeing reliable digital communication.

To demodulate the amplified signal, the PLL circuit was designed as the first step in the digital demodulation process. The internal block diagram of the PLL integrated circuit (IC) implemented at this stage is shown in Figure 3.30.

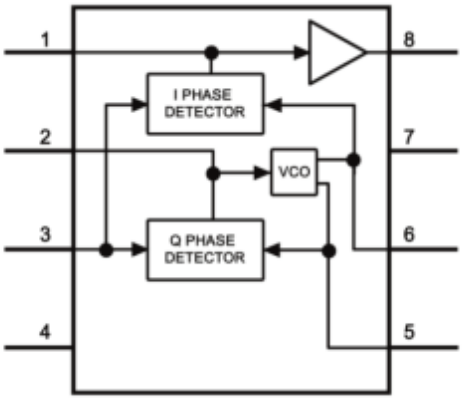

Figure 3.30: Internal block diagram of the PLL IC (Texas Instruments, 2014)

The PLL IC in Figure 3.30 (LM567 from Texas Instruments) is a low cost (£1), small size (9.8 mm length and 6.4 mm width) and low power (0.1 W) device consisting of two separate phase detectors (in-phase and quadrature-phase detectors), a voltage-controlled oscillator (VCO) and a signal comparator (connected to pin 8 of the PLL IC in the figure). Furthermore, the phase detectors and the VCO operate within a feedback loop as shown in Figure 3.31.

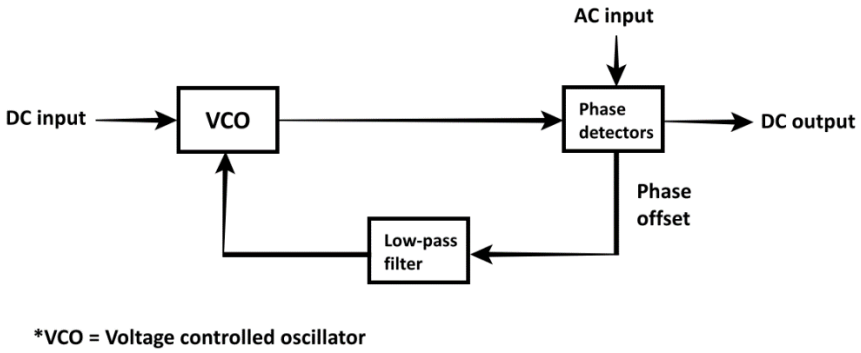

Figure 3.31: Feedback loop showing the phase detectors and the voltage-controlled oscillator of the PLL

As shown in Figure 3.31, the LM567 feedback loop comprises the phase detectors, the VCO and a low-pass filter. During operation, the phase detectors compared the AC input from the signal pre-amplifier with a VCO generated signal. The phase offset between these signals was subsequently fed through a low-pass filter back into the VCO to adjust its frequency. The VCO frequency was thus continuously adjusted through this feedback loop until a constant phase offset was generated, resulting in the "phase locking" of the loop. Once phase locking was achieved, a DC signal was produced at the output of the phase detectors, signifying a lock condition of the PLL where the VCO frequency matched the frequency of the input AC signal. For the non-coherent demodulator, achievement of this lock condition was a crucial step in recovering the transmitted digital information signal.

The initial VCO frequency was configured using an external resistor and capacitor combination according to Equation (3.4) (Texas Instruments, 2014).

$$f = \frac{1.1}{RC} \tag{3.4}$$

Where f (Hz) is the VCO frequency, R (kΩ) is the external resistor value and C is the external capacitor value (μF). Since the acoustic carrier signal (represented by the resonant frequency of the ERM vibration motor) detected by the MFC sensor was between 100 and 200 Hz, a

capacitance of 1µF and variable resistance between 5 kΩ and 11 kΩ were implemented at the PLL to set the VCO to operate within this bandwidth. Furthermore, the low-pass filter was implemented according to Equation (3.5) (Texas Instruments, 2014).

$$BW = f \times C \tag{3.5}$$

Where BW (% of VCO frequency) is the bandwidth sensitivity of the PLL, f (Hz) is the VCO frequency and C (µF) is the low-pass filter capacitance. By setting the low-pass filter capacitance to 1µF, the bandwidth sensitivity of the VCO was set to within 14% of the VCO frequency. Thus, if the VCO frequency was set as 150 Hz for example, the PLL could detect and lock on to an incoming carrier signal within ± 21 Hz of this frequency.

Once the incoming acoustic signal was locked by the PLL, a DC output signal was subsequently generated by the PLL. To visually confirm this phase locking, a light emitting diode (LED) which activated upon phase locking was incorporated at the digital communication receiver and is shown in Figure 3.32.

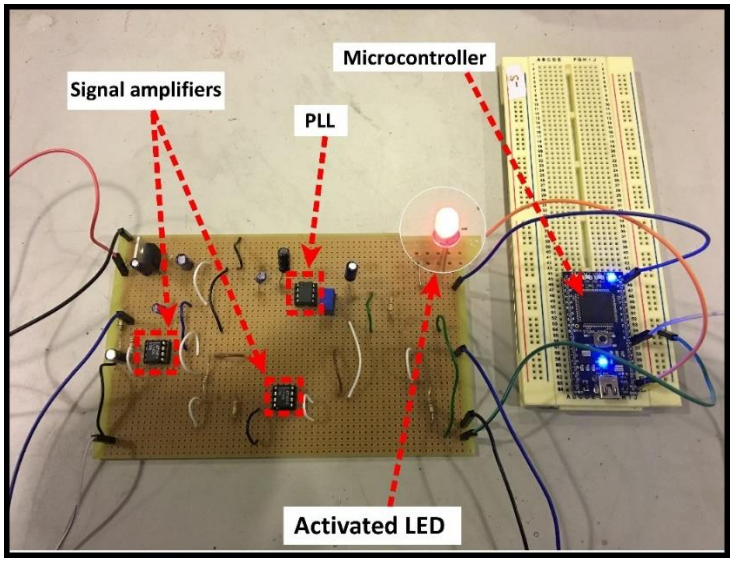

Figure 3.32: Digital communication receiver showing activated LED (signifying phase locking)

As shown in Figure 3.32, a LED was activated at the digital communication receiver upon phase locking while the opposite was the case, i.e., the LED was de-activated, outside of phase locking. Two possibilities therefore existed at the output of the PLL, i.e., the presence (logic HIGH state) or absence (logic LOW state) of a DC signal which corresponded to the "on" and "off" states of OOK demodulation at the digital communication receiver. It is also important to note here that this output DC signal was an "active low" signal meaning that a 0 V output at the PLL IC (pin 8 in Figure 3.30) corresponded to a logic HIGH state while conversely, a 5 V output corresponded to a logic LOW state. This information, as will be shown in Section 3.6.3, was key to successful message synchronisation and subsequent recovery at the demodulating microcontroller.

3.6.2 Message decoding

For message decoding, the same ASCII encoding/decoding scheme employed at the digital communication transmitter was also employed at the digital communication receiver to correctly decode the originally transmitted message.

3.6.3 Message synchronisation

Key to synchronising the operational stages of the digital communication receiver (using carrier synchronisation) with the digital communication transmitter was the creation of an interrupt service routine (interrupt handler) which was triggered at the demodulating microcontroller upon the arrival of an incoming pilot signal. Two types of interrupt handlers were programmed at the digital communication receiver:

I. Binary message interrupt handler;

II. ASCII message interrupt handler

The flowchart for the binary message interrupt handler is shown in Figure 3.33.

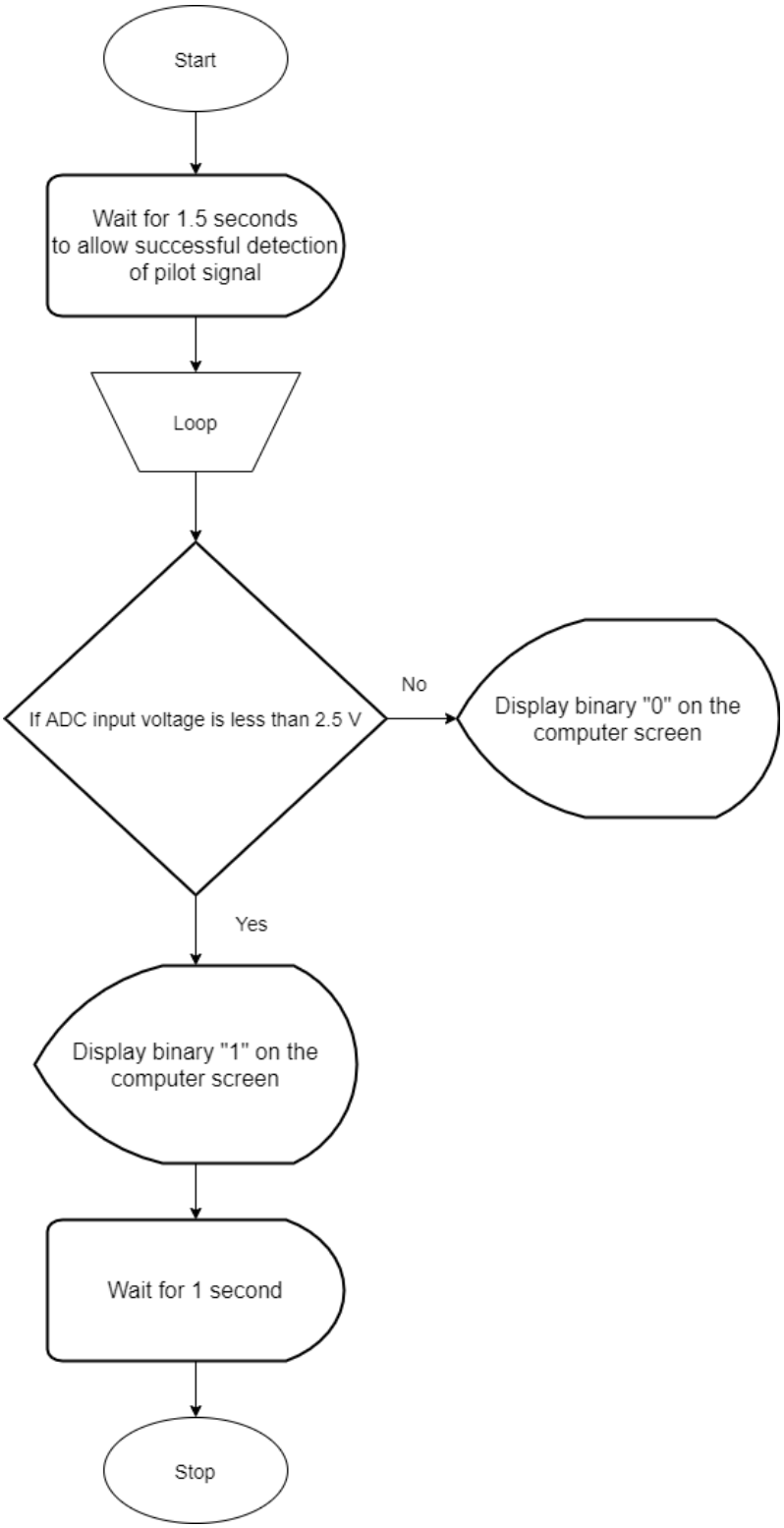

Figure 3.33: Flow chart for the binary message interrupt handler at the digital communication receiver

At the start of the flowchart in Figure 3.33 was an initial 1.5 s delay at the demodulating microcontroller once it was triggered by the arrival of the pilot signal. The importance of this time delay is further illustrated in Figure 3.34.

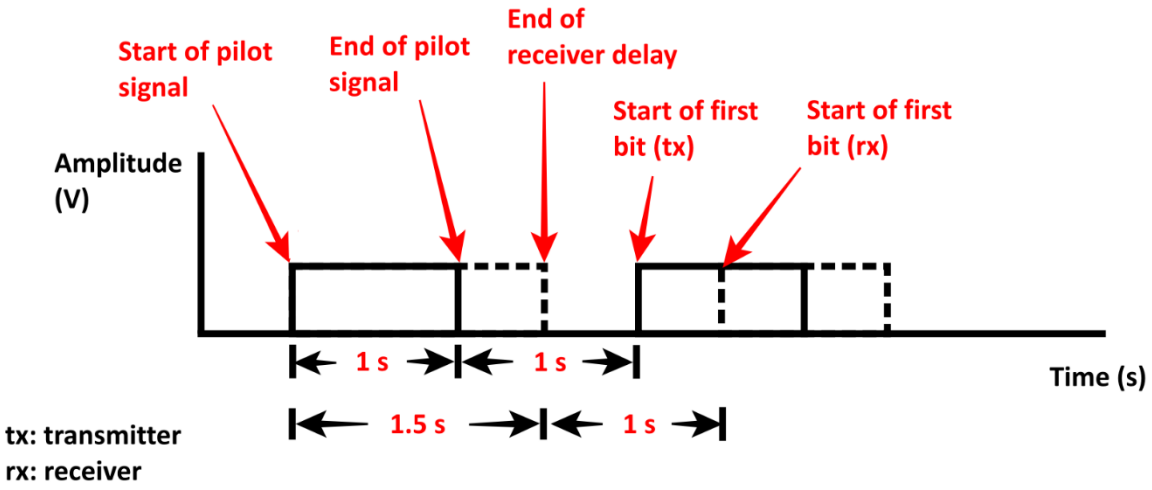

Figure 3.34: Time delay technique for synchronising the digital communication transmitter and receiver

As shown in Figure 3.34, although the pilot signal duration was 1 s, the receiver was delayed by a further 0.5 s after the end of the pilot signal. With this delay, the receiver clock constantly lagged the transmitter clock by 0.5 s for subsequent digital transmissions between the transmitter and receiver. The benefit of this approach was to set the time at which the receiver detected a transmitted pulse to the pulse midpoint (as shown in Figure 3.34) rather than at the pulse edge thus further guaranteeing reliable pulse detection at the receiver.

Following the pilot signal delay in the flowchart of Figure 3.33, a decision was repeatedly made (every 1 s) at the input ADC of the demodulating microcontroller on the voltage level of the incoming DC signal which was output from the PLL as described in Section 3.6.1. With this ADC, the input voltage range for detecting a binary "1" was set as < 2.5 V while the voltage range for a binary "0" was set as ≥ 2.5 V based on the active LOW nature of the incoming DC signal. This 2.5 V threshold was incorporated to further reduce the possibility of random noise

interference with the correct recovery of the transmitted binary information at the digital communication receiver. DC signals below 2.5 V were thus classified as binary “1” while those at 2.5 V and above were classified as binary “0”.

For the ASCII message interrupt handler, the flowchart is shown in Figure 3.35.

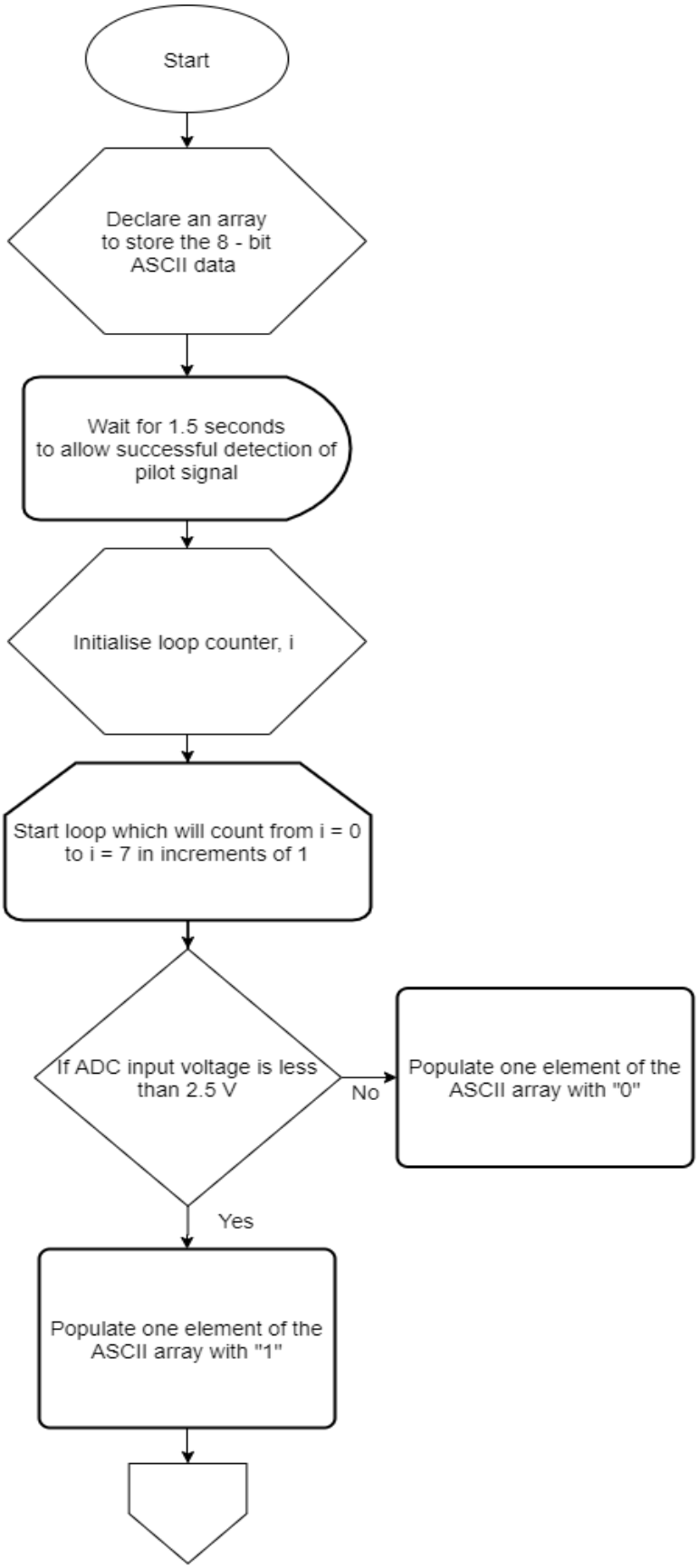
Start
Declare an array to store the 8 - bit ASCII data
Wait for 1.5 seconds to allow successful detection of pilot signal
Initialise loop counter, i
Start loop which will count from i = 0 to i = 7 in increments of 1
If ADC input voltage is less than 2.5 V
No
Populate one element of the ASCII array with "0"
Yes
Populate one element of the ASCII array with "1"

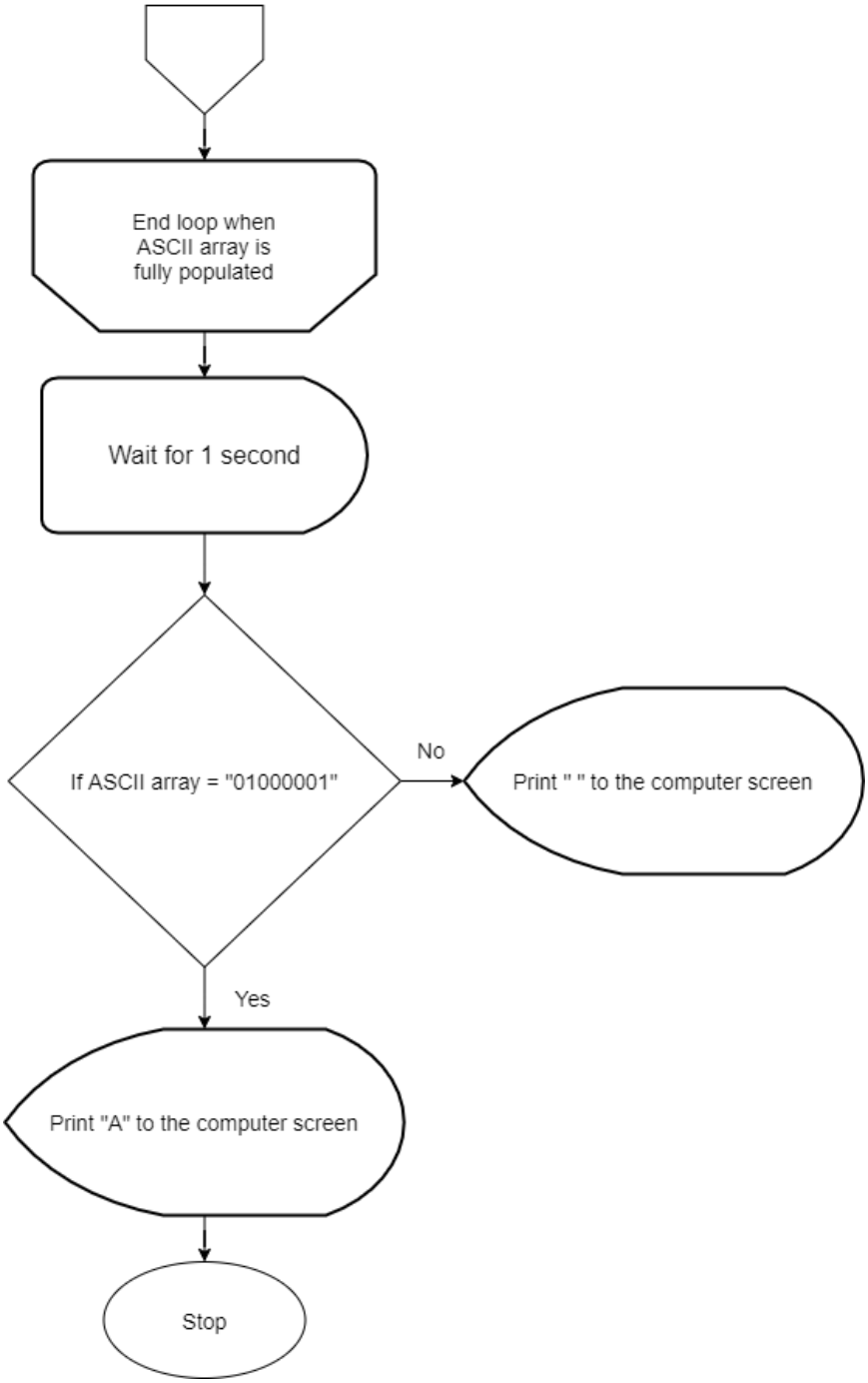

Figure 3.35: Flow chart for the ASCII message interrupt handler at the digital communication receiver

For the ASCII interrupt handler, an 8-element array was initially declared to store the 8-bit ASCII message before presentation at the PC monitor. Following the pilot signal detection, a loop counter, which successively populated each array element based on the input signal at the ADC, was implemented. Once the 8-element array was fully populated, the array value was

compared to an already existing copy of the message to be decoded (in this case “01000001” which represents “A” according to the ASCII encoding scheme). If both copies matched, the decoded message was subsequently presented at the PC monitor.

3.6.4 Procedure for digital information recovery

The general procedure for digital information recovery, incorporating the interrupt handlers described in the previous section, is presented in this section. For digital information recovery, the PC was first connected, through a serial port, to the demodulating microcontroller. Like the digital communication transmitter, the serial connection between the PC and the microcontroller was programmed to transmit information at 300 bauds/second. Following the serial connection set-up, the microcontroller was connected to the signal pre-amplifier and PLL circuits with the signal pre-amplifier circuit further connected to the MFC sensor which was already installed along the exposed MDPE pipe. The detailed circuit schematic of the digital communication receiver is provided in Appendix C of this thesis.

For the first digital communication experiments, the digital communication receiver was tested for its ability to reliably recover the binary information stream previously described in Section 3.5.4 while the second set of experiments tested the digital communication receiver for ASCII message recovery. The flowchart for both procedures, which were the same (except for their individual interrupt handlers), is shown in Figure 3.36.

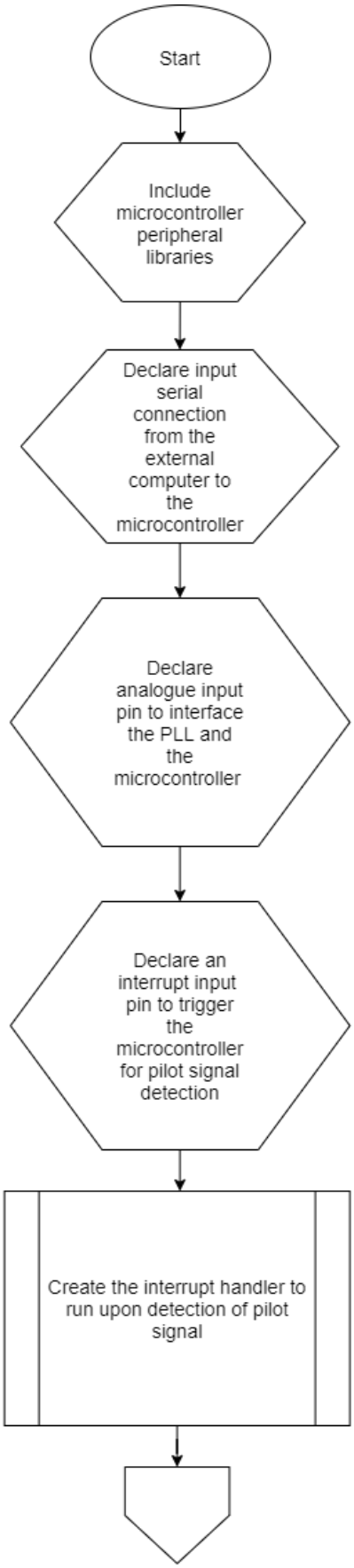
Start
Include microcontroller peripheral libraries
Declare input serial connection from the external computer to the microcontroller
Declare analogue input pin to interface the PLL and the microcontroller
Declare an interrupt input pin to trigger the microcontroller for pilot signal detection
Create the interrupt handler to run upon detection of pilot signal

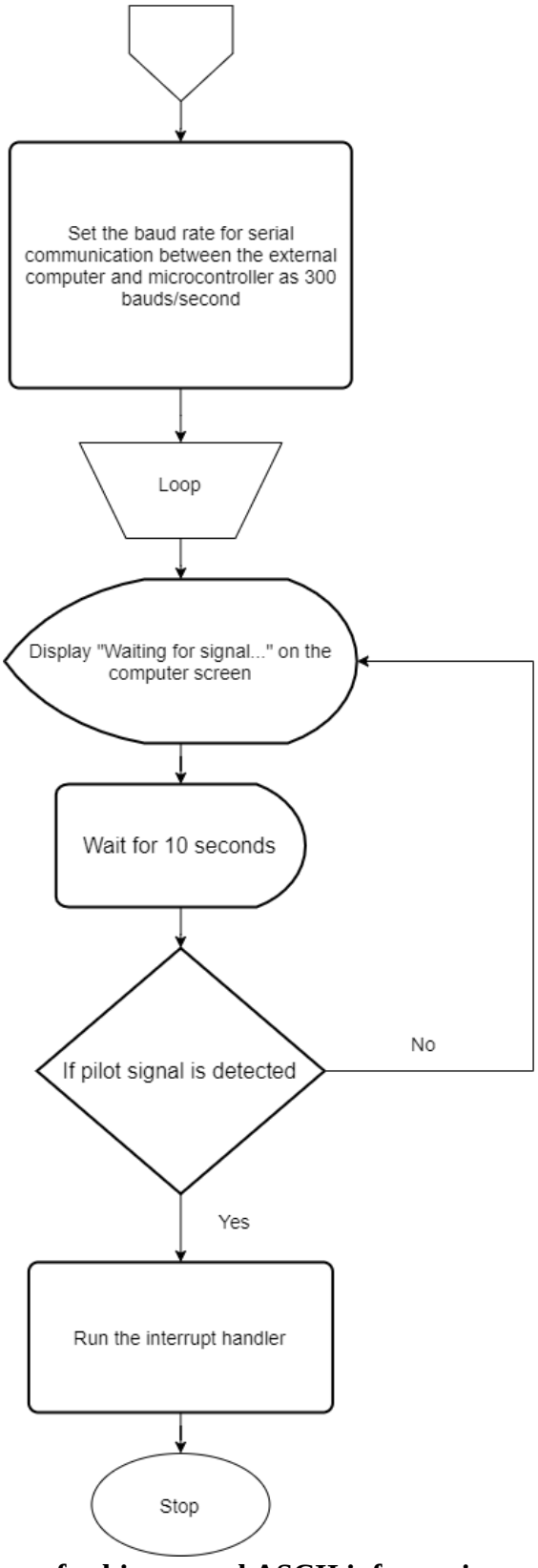

Figure 3.36: Flowchart for binary and ASCII information recovery at the digital communication receiver

As shown in Figure 3.36, after the start of the algorithm, the first four elements of the flowchart consisted of initialisation procedures which included the declaration of a serial communication link between the PC and demodulating microcontroller, declaration of an analogue input pin to interface the PLL and microcontroller as well as the declaration of a separate interrupt pin to trigger the microcontroller upon arrival of an incoming pilot signal. Following the initialisation steps, an interrupt handler was created for either binary or ASCII message recovery at the receiver. The baud rate for serial communication between the microcontroller and PC was subsequently set before a status message ("Waiting for signal…") was programmed to repeatedly display at the PC monitor to signify the idle state of the digital communication receiver. Once a pilot signal was detected however, the digital communication receiver was removed from this idle state by running either of the interrupt handlers previously described in Section 3.6.3.

3.6.5 Printed circuit board implementation of the digital communication receiver

Like the digital communication transmitter, the final hardware design of the digital communication receiver was also in the form of a printed circuit board (PCB), the circuit layout for which was also designed using the DipTrace software package. The circuit schematic of the digital communication receiver was also printed on a PCB layout with FR4 substrate using a commercially available PCB manufacturer (PCBWay Ltd). Figure 3.37 shows the final product complete with microcontroller, serial port (for PC communication), PLL circuit, LED indicator as well as the signal pre-amplifiers which interfaced the MFC with the rest of the digital communication receiver.

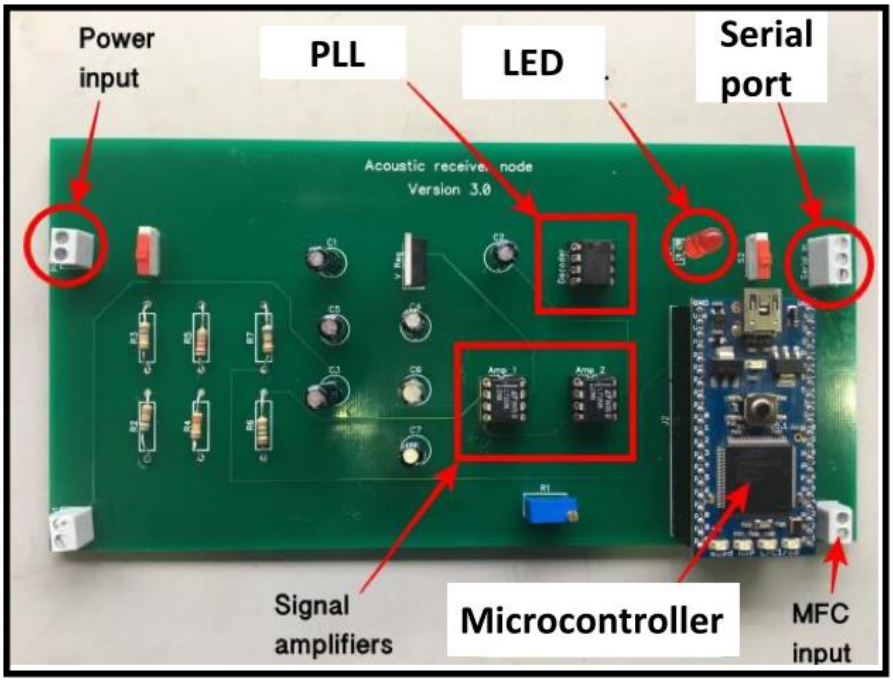

Figure 3.37: PCB design of the digital communication receiver

3.7 COMMMUNICATION SYSTEM DEPLOYMENT

Following the communication transmitter and receiver development, the communication system was further tested along exposed and buried water pipes within the laboratory and field, respectively. Figure 3.38 shows the communication transmitter and receiver deployed along the exposed MDPE pipe previously described in Section 3.4.3.

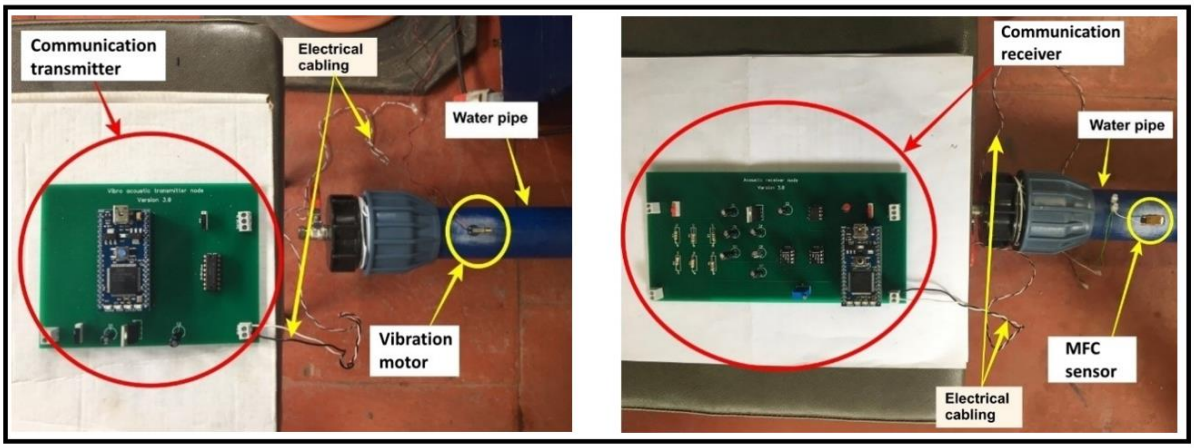

Figure 3.38: Digital communication transmitter and receiver deployed along exposed MDPE pipe

For the field trials, two separate opportunities for deploying the communication system within the University of Birmingham main campus were exploited. The first opportunity was to deploy the communication system along a 150 mm diameter buried steel pipe along which a leak repair was being conducted. Figure 3.39 shows the schematic of the communication system deployment.

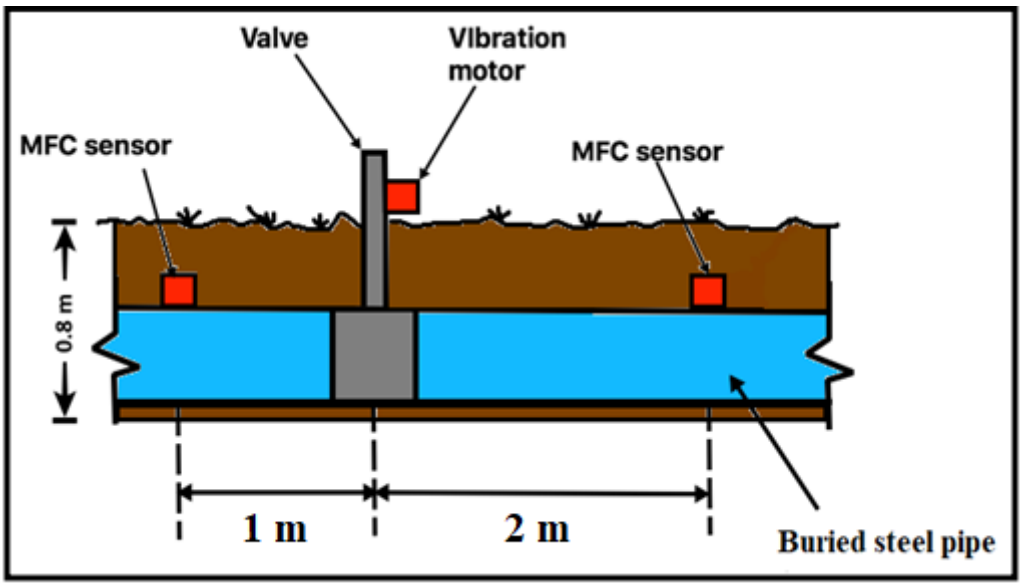

Figure 3.39: Schematic of the communication system deployment

As shown in Figure 3.39, the vibration motor was installed along the pipe valve while the MFC sensors were installed directly along the pipe surface. Although it would have been preferable to install the vibration motor directly along the buried pipe, the timing of the transducer installations with the pipe burial only allowed the MFC sensors to be installed directly along the pipe while the vibration motor had to be installed along the connecting valve as shown in Figure 3.40.

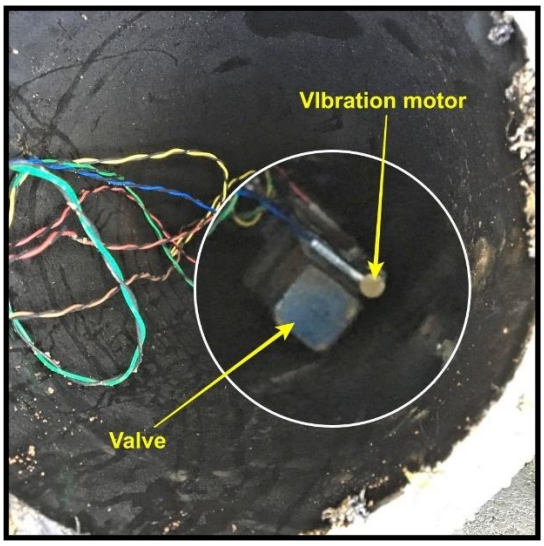

Figure 3.40: Vibration motor installation along the pipe valve

Figure 3.41 shows the final deployment of the communication system along the buried steel pipe.

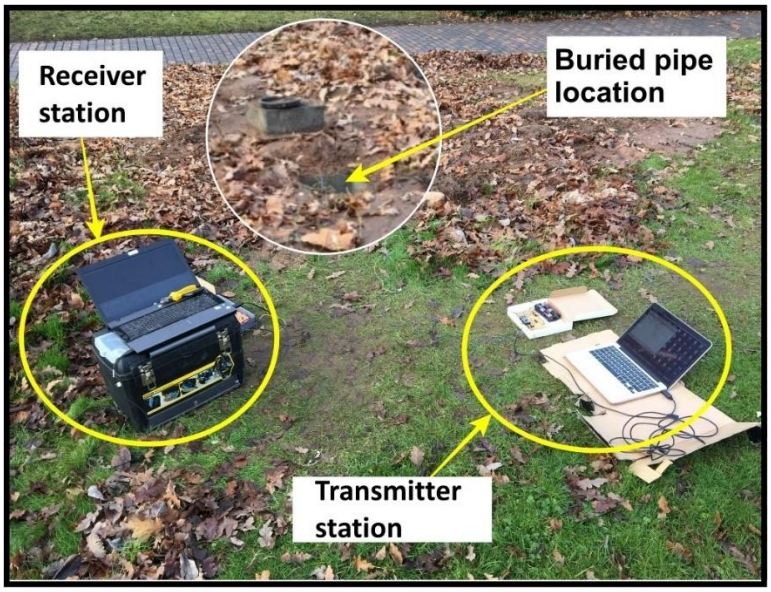

Figure 3.41: Communication system deployed along a buried steel pipe

The second opportunity for field trials arose as part of a separate multidisciplinary project on buried infrastructure condition assessment at the University of Birmingham main campus. For these trials, two trenches (nominally identified as Trench 1 and Trench 2) each of 8 m length and 0.8 m depth were dug before an MDPE pipe (6 m length and 90 mm outer diameter), filled

with water prior to deployment, was deployed in each trench. For Trench 1, the soil backfill around the buried plastic pipe was un-compacted, while for Trench 2, the soil backfill around the buried plastic pipe was compacted. Further details of the soil composition for each trench are provided in Section 3.8.2. One vibration motor and two MFC sensors were also installed along each pipe as shown in Figure 3.42.

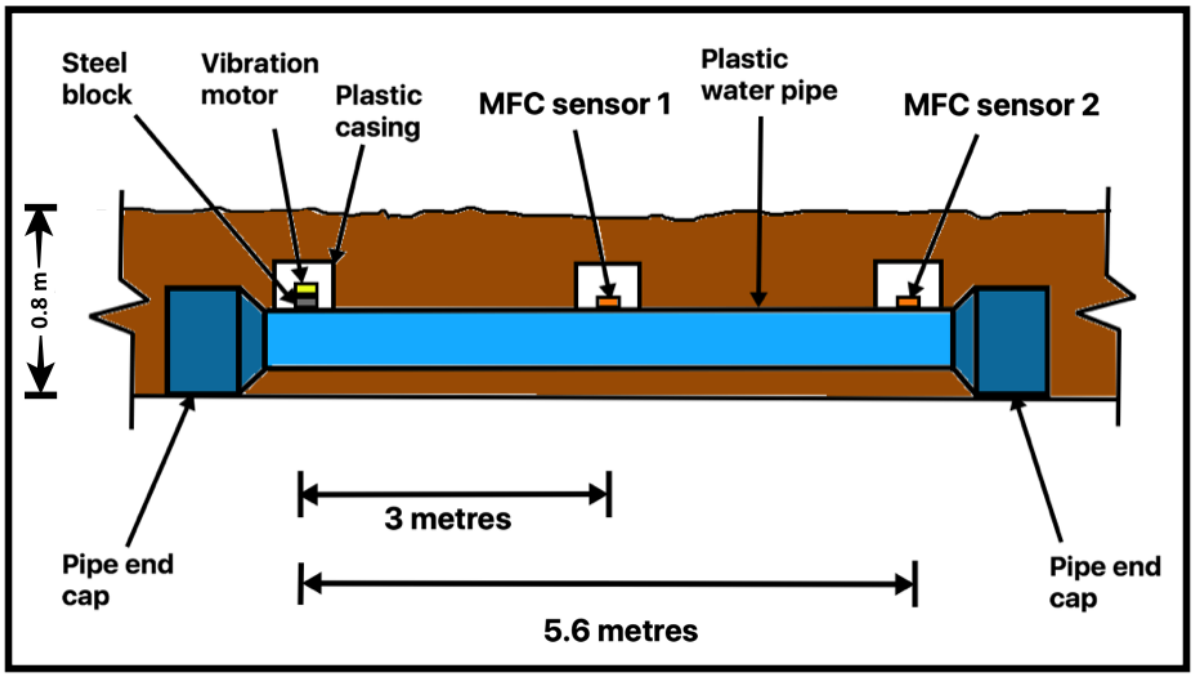

Figure 3.42: Schematic of the communication system deployment for a buried plastic pipe

While the installation distance of MFC sensor 1 was chosen to reflect the minimum distance threshold (3 m) of wireless underground communication for the tests, MFC sensor 2 was installed at the other extreme end of the pipe to test data communication at the maximum available distance along the pipe. Both the vibration motor and sensors were further enclosed within plastic casings to ensure protection against soil debris and are shown along one of the buried plastic pipes, before soil backfilling, in Figure 3.43.

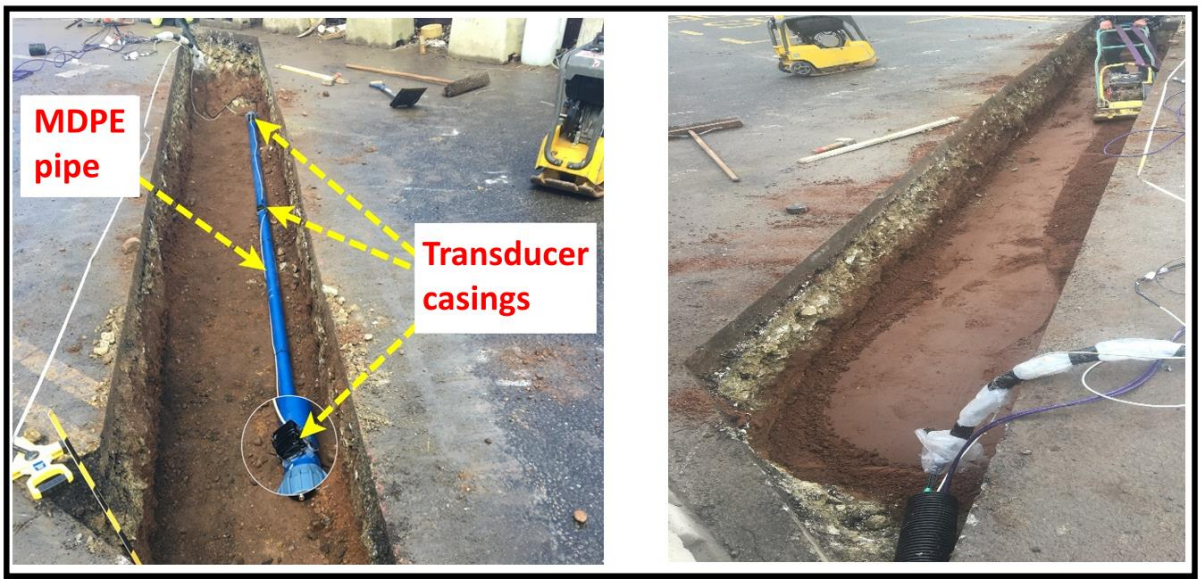

Figure 3.43: Buried plastic pipe before and after soil backfilling

Results of digital communication along the exposed and buried water pipes will be presented in Chapter 4. It was however evident from the tests that successful operation of the digital communication system depended on the acoustic signal strength upon arrival at the digital communication receiver. Furthermore, this acoustic signal strength was expected to vary based on the pipe material as well as its surrounding media (e.g., soil) properties due to acoustic signal attenuation along the pipe. The reliability of digital communication at increasing distances between the communication transmitter and receiver therefore depended on knowledge of acoustic signal attenuation along the water pipe. It was thus important to examine acoustic signal attenuation along the exposed and buried water pipes, the methodology of which is presented next.

3.8 EXAMINATION OF ACOUSTIC SIGNAL ATTENUATION ALONG A WATER PIPE

This section describes the methodology by which acoustic signal attenuation was examined along exposed and buried water pipes. Three separate approaches were employed for the analysis, i.e., analytical, experimental, and numerical methods.

3.8.1 Analytical examination of acoustic attenuation along the water pipe

The analytical examination of acoustic attenuation along an exposed water pipe is first discussed in this section before treating the case of a buried water pipe.

3.8.1.1 Analytical examination of acoustic attenuation along an exposed water pipe

According to Muggleton & Yan (2013), Muggleton et al (2004), Muggleton et al. (2002) and Pinnington & Briscoe (1994), low frequency (< 1 kHz) acoustic wave propagation along a water pipe structure can be described in terms of an axisymmetric wave propagating along the pipe wall material, as well as within the internal fluid medium of the pipe. For an exposed water pipe, the pipe wall propagating acoustic wavenumber can theoretically be expressed as (Muggleton & Yan, 2013; Muggleton et al., 2004; Muggleton et al., 2002)

$$k_2^2 = k_L^2\left(1 + \frac{\nu_p^2}{1-\nu_p^2}\frac{E_p(1+i\eta)h/a^2}{\left(E_p(1+i\eta)h/a^2\right)+\left(2B_f/a\right)-\omega^2 h\rho_p}\right) \tag{3.6}$$

Where k_2 is the pipe wall propagating acoustic wavenumber, k_L is the wavenumber of a compressional wave in a plate, B_f (N/m^2) is the bulk modulus of the internal fluid, E_p (N/m^2) is the elastic modulus of the pipe wall material, ρ_p (kg/m^3) is the density of the pipe wall material, ν_p is the Poisson's ratio of the pipe wall material, η is the material loss factor of the pipe wall and a (m) and h (m) are the water pipe inner radius and wall thickness respectively.

According to Muggleton & Yan (2013), the pipe wall acoustic wavenumber is a complex number, the real part of which represents acoustic wave speed along the pipe while the imaginary part represents acoustic wave attenuation along the pipe. For the digital communication system described in this thesis, the imaginary part of the acoustic wavenumber forms the theoretical basis of predicting acoustic signal attenuation along the pipe. The acoustic signal attenuation, in decibels/metre (dB/m), is further expressed as (Muggleton & Yan, 2013; Muggleton et al., 2004; Muggleton et al., 2002)

$$Loss = 20\frac{Im\{ka\}}{\ln(10)} \quad (3.7)$$

Where $Loss$ (dB/m) is the acoustic attenuation, $Im\{ka\}$ is the imaginary part of the pipe wall acoustic wavenumber and a is the water pipe inner radius. Results of acoustic attenuation prediction using the analytical model (for the exposed MDPE pipe with material and geometric properties listed in Table 3.4) are further presented and discussed in Chapter 4. The MDPE pipe material properties shown in Table 3.6 were obtained from a similar pipe in Muggleton & Yan (2013).

Table 3.6: Geometric and material properties of the MDPE pipe

Pipe inner radius (m)	0.0361
Pipe wall thickness (m)	0.0092
Elastic modulus (N/m^2)	1.6×10^9
Poisson's ratio	0.4
Density (kg/m^3)	900
Material loss factor	0.06
Longitudinal wave speed (m/s)	1455
Bulk modulus of water (N/m^2)	2.25×10^9

Parametric analyses of acoustic signal attenuation along the exposed MDPE pipe, with respect to changes in the pipe inner radius, wall thickness, elastic modulus and Poisson's ratio were also conducted using the analytical model with the results presented in Chapter 4. Acoustic signal attenuation along other pipe materials (Table 3.7), with the same geometric dimensions as the exposed MDPE pipe, was also computed using the analytical model with the results (and how they compare with MDPE pipe results) also presented in Chapter 4. The Matlab programme for executing the analytical computations of acoustic attenuation along the exposed MDPE pipe is also provided in Appendix B.

Table 3.7: Material properties of PVC, cast iron and steel pipes

Properties	PVC	Cast iron	Steel
Density (kg/m^3)	2000	7100	7800
Elastic modulus (N/m^2)	5.00×10^9	1.00×10^{11}	0.21×10^{11}
Poisson's ratio	0.400	0.290	0.310
Material loss factor	0.065	0.001	0.002

3.8.1.2 Analytical examination of acoustic attenuation along a buried water pipe

For low frequency acoustic excitation of a buried water pipe, the pipe wall acoustic wavenumber can be expressed as (Muggleton et al., 2004; Muggleton et al., 2002)

$$k_2^2 = k_L^2\left(1 + \frac{\nu_p^2}{1-\nu_p^2}\frac{E_p(1+i\eta)h/a^2}{(E_p h/a^2)+(2B_f/a)-\omega^2 h\rho_p+i\omega(Z_{d2}+Z_{r2})}\right) \quad (3.8)$$

The additional terms in Equation (3.8), compared to Equation (3.6), are Z_{d2} and Z_{r2} which represent bulk and shear acoustic wave impedances in the surrounding soil medium. These acoustic wave impedances can further be expressed, in terms of Hankel functions of the second kind, as (Muggleton et al., 2004; Muggleton et al., 2002)

$$Z_{d2} \approx -i\rho_m c_d \frac{H_0(k_d a)}{H_0'(k_d a)} \quad (3.9a)$$

$$Z_{r2} \approx -i\rho_m c_r \frac{H_0(k_r a)}{H_0'(k_r a)} \quad (3.9b)$$

Where ρ_m (kg/m^3) is the surrounding soil density, k_d and k_r are the wavenumbers of the soil bulk and shear acoustic waves respectively, c_d and c_r (m/s) are the acoustic wave speeds of the soil bulk and shear acoustic waves and a (m) is the water pipe inner radius. The general relationship between acoustic wavenumber and wave speed can also be expressed as (Pal, 2008; Santamarina et al., 2001)

$$k = \frac{c}{\omega} \quad (3.10)$$

Where *c* (m/s) is the acoustic wave speed of the bulk or shear acoustic wave propagating within the surrounding soil. It is evident so far, that knowledge of the acoustic wave speed in the surrounding soil is essential to the prediction of acoustic wave attenuation along the buried pipe in soil. To obtain this information, a general description of the surrounding soil within which the pipes described in Section 3.7 (for the communication system field deployment) were buried was necessary. Soil samples surrounding the buried pipes were therefore collected and classified according to British Standards Institution (1990). The soil classification results for the soil surrounding the buried steel pipe are summarised in Figure 3.44 as well as in Tables 3.8 and 3.9.

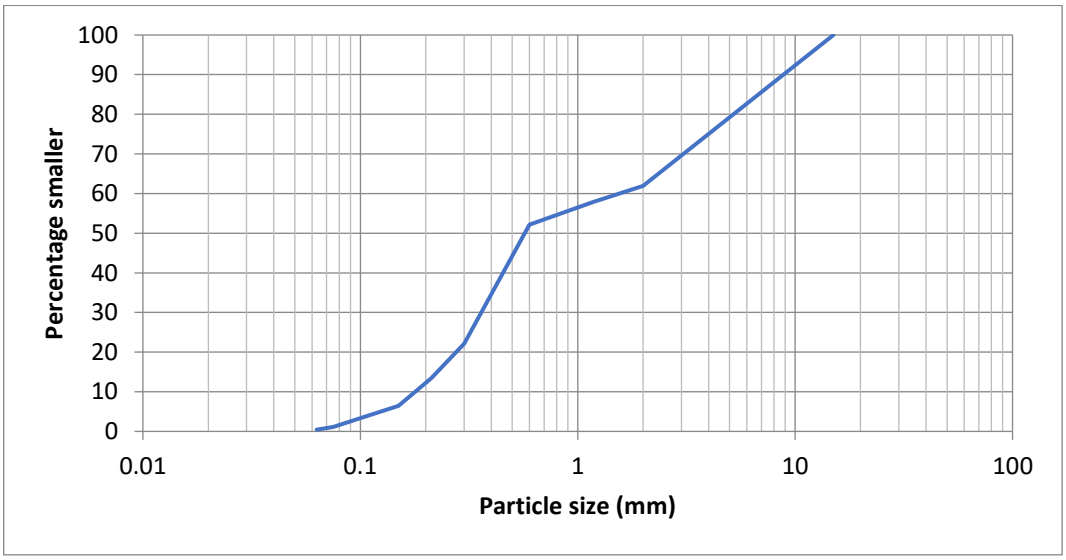

Figure 3.44: Particle size distribution curve for the soil surrounding the buried steel pipe

Table 3.8: Approximate proportions of particle sizes within the soil surrounding the buried steel pipe

% Gravel	% Sand	% Fines	% < 425 microns	Depth (m)
38.1	61.5	0.4	22.1	0.6

Table 3.9: Material properties of the soil surrounding the buried steel pipe

Sample	Depth (m)	Gravimetric water content (%)	Bulk density (kg/m^3)
1	0.6	12.2	1680
2	0.6	13.6	1650
3	0.6	13.0	1660
		Average: 12.9	**Average:** 1663

The coefficients of uniformity and curvature of the soil were further calculated according to Equations (3.11) & (3.12).

$$C_u = D_{60}/D_{10} \tag{3.11}$$

$$C_c = \frac{D_{30}^2}{D_{10} \times D_{60}} \tag{3.12}$$

Where C_u and C_c are the coefficients of uniformity and curvature respectively, D_{10} is the maximum size of the smallest 10% of the sample, D_{30} is the maximum size of the smallest 30% of the sample and D_{60} is the maximum size of the smallest 60% of the sample. Based on C_u and C_c (7.9 and 0.5 respectively) as well as Table 3.9, the soil surrounding the buried steel pipe was classified as poorly graded SAND (SP). For the buried plastic pipe, the soil classification results Trench 1 is summarised in Figure 3.45, Tables 3.10 and 3.11 while the results for Trench 2 are summarised in Figure 3.46, Tables 3.12 and 3.13.

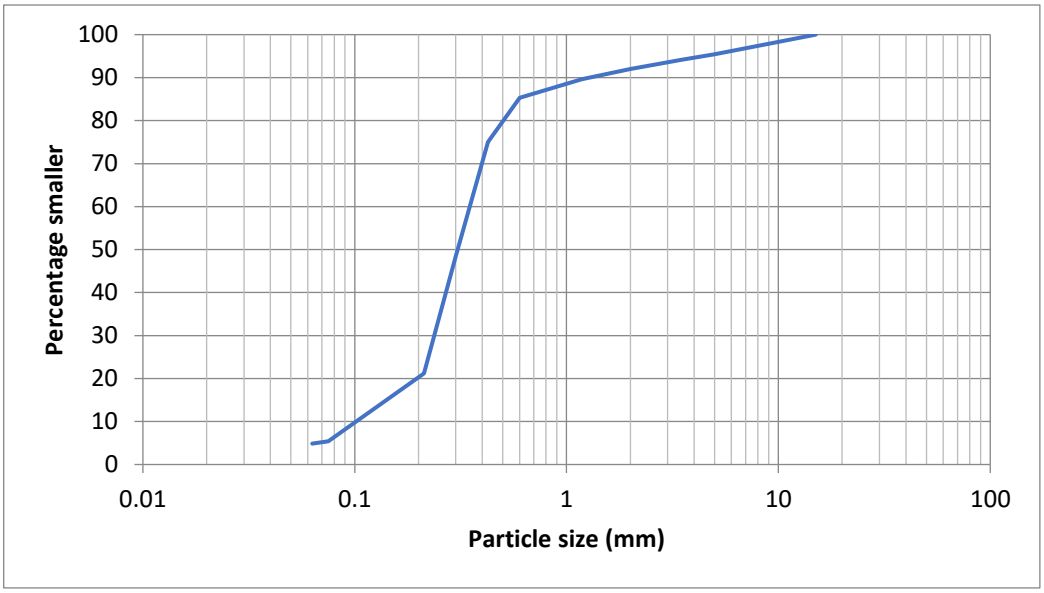

Figure 3.45: Particle size distribution curve for the soil surrounding the buried MDPE pipe (Trench 1)

Table 3.10: Approximate proportions of particle sizes within the soil surrounding the buried MDPE pipe (Trench 1)

% Gravel	% Sand	% Fines	% < 425 microns	Depth (m)
8	87	5	75	0.6

Table 3.11: Material properties of the soil surrounding the buried MDPE pipe (Trench 1)

Sample	Depth (m)	Gravimetric water content (%)	Bulk density (kg/m^3)
1	0.6	4.8	1750
2	0.6	5.8	1740
3	0.6	5.3	1700
		Average: 5.3	**Average:** 1730

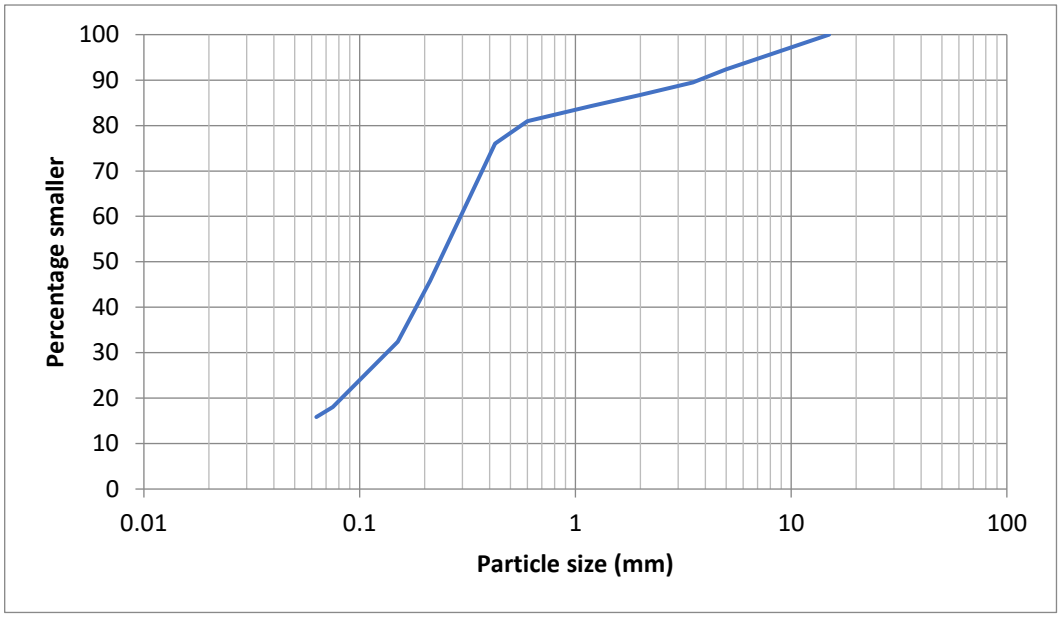

Figure 3.46: Particle size distribution curve for the soil surrounding the buried MDPE pipe (Trench 2)

Table 3.12: Approximate proportions of particle sizes within the soil surrounding the buried MDPE pipe (Trench 2)

% Gravel	% Sand	% Fines	% < 425 microns	Depth (m)
13	71	16	16	0.6

Table 3.13: Material properties of the soil surrounding the buried MDPE pipe (Trench 2)

Sample	Depth (m)	Gravimetric water content (%)	Bulk density (kg/m^3)
1	0.6	3.5	2400
2	0.6	4.5	2000
3	0.6	4.4	1970
		Average: 4.1	**Average:** 2123

For Trench 1, C_u and C_c were calculated as 4 and 2 respectively while the same coefficients for Trench 2 were calculated as 3.4 and 0.4, respectively. Based on these uniformity and curvature coefficients, as well as the information provided in Tables 3.11 and 3.13, the soil in Trench 1 was classified as well graded SAND (SW) while the soil in Trench 2 was classified as poorly graded SAND (SW). Further discussion on the influence of acoustic wave speed

within these soil types on the analytical prediction of acoustic signal attenuation within the soil is presented in Chapter 4. The Matlab programme for executing the analytical computations of acoustic signal attenuation along the buried pipes are also provided in Appendix B. For now, the next section describes laboratory and field experiments for validating the analytical model predictions by measuring acoustic signal attenuation along exposed and buried water pipes.

3.8.2 Measurement of acoustic signal attenuation along water pipes

The laboratory and field experiments for measuring acoustic signal attenuation along exposed and buried water pipes respectively are described in this section.

3.8.2.1 Laboratory experiments along an exposed water pipe

The laboratory set-up for acoustic attenuation measurements along an exposed water pipe comprised an MDPE pipe with the same cross-sectional dimensions as the pipe described in Section 3.4.3 but of 40 m length. This length was chosen to accommodate only single path acoustic propagation along the pipe (i.e., without acoustic signal reflection at the pipe ends) according to Equation (3.13).

$$distance\ (m) = velocity\ (m/s) \times time\ (s) \qquad (3.13)$$

With an acoustic velocity of 1455 m/s (Muggleton & Yan, 2013) and by installing the acoustic transmitter (ERM vibration motor) mid-way along the pipe (and at 90 degrees according to the circumferential configuration of Figure 3.47), an acoustic pulse of 0.01 s was chosen to excite the pipe as it was short enough to only allow single path acoustic propagation along the pipe. The vibration motor frequency is however time dependent, only achieving a relatively stable frequency within 100-200 Hz after 0.08 s (Precision Microdrives, 2015b). The detected acoustic signals along the pipe, during acoustic excitation, were therefore expected to be outside the

100-200 Hz bandwidth as will be shown by the corresponding results in Chapter 4. The schematic layout and picture of the experimental set-up are shown in Figures 3.48 and 3.49.

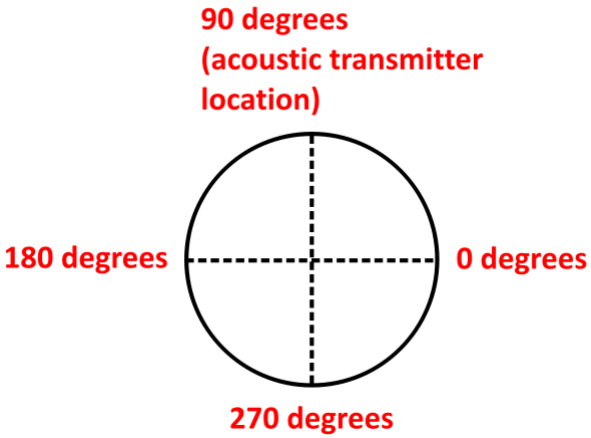

Figure 3.47: Pipe cross-section showing the acoustic transmitter location

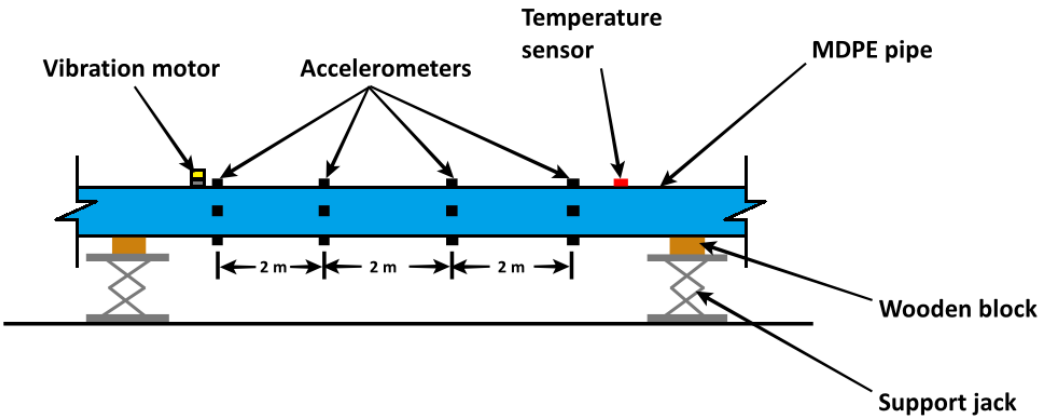

Figure 3.48: Schematic of the exposed MDPE pipe set-up

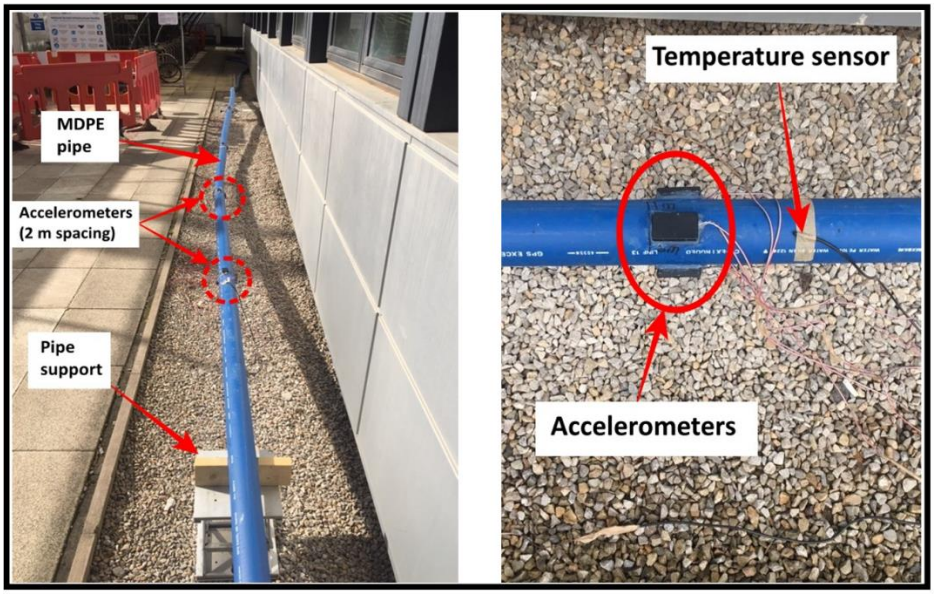

Figure 3.49: Experimental set-up of the exposed MDPE pipe outside the laboratory

As shown in Figures 3.48 and 3.49, the pipe was supported by a combination of 2 separate wooden blocks and support jacks to elevate the pipe above the ground (thus preventing any contact with the ground). The support mechanisms were also placed greater than 6 metres apart, allowing the section of the pipe along which the acoustic transducers were installed to be supported without any need for extra supports which could have presented a path for acoustic signal leakage from the pipe. Unlike the experiments described in Section 3.4.3, the choice of wooden block and insulating material was irrelevant in this case as the support mechanisms in Figures 3.48 and 3.49 were intentionally placed outside the pipe section along which acoustic signal measurements were taken.

For acoustic excitation, the ERM vibration motor (which was driven at 12 V using the acoustic transmitter circuit in Figure 3.28) was programmed to repeatedly transmit a single pulse of 0.01 s along the pipe. The choice of 12 V was made to maximise acoustic power input into the pipe. To capture the axial motion of the propagating acoustic wave, small (3 mm length, 3 mm width and 1.5 mm thickness), low power (0.9 mW) and low cost (£8) triaxial accelerometers (ADXL 337 from Analog Devices) were installed at 0, 90, 180 and 270 degrees around the pipe (according to the configuration in Figure 3.47) by adhering them to a plastic casing before

placing the sensors in direct contact with the pipe. Four sets of these accelerometers were further installed at 0, 2, 4 and 6 m from the ERM vibration motor. The accelerometers were subsequently connected to a digital acquisition device (NI USB 6211 from National Instruments) which was also connected to a PC to store the acoustic signals acquired during the experiments. The acoustic signals were subsequently captured by repeatedly exciting the pipe with the ERM vibration motor once every five seconds thus allowing adequate time spacing between each acoustic pulse transmission.

To record the pipe wall temperature, a DS18B20 temperature sensor from Maxim Integrated was also taped directly to the pipe surface. Temperature measurements were taken along the pipe to adjust any temperature dependent pipe wall parameters within the analytical model when comparing with the experiment results.

The acoustic attenuation experiments were also repeated along a water-filled pipe by filling the MDPE pipe with water (as shown in Figure 3.50) using a hosepipe connected to a tap inside the laboratory, before repeating the experiments.

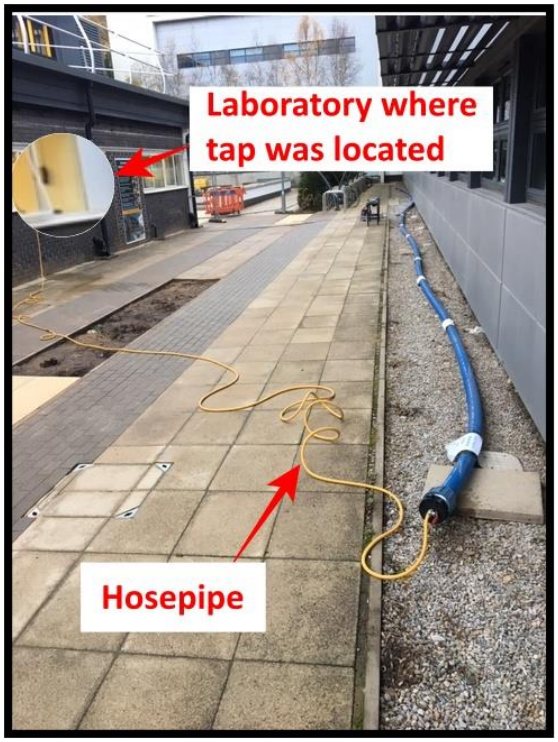

Figure 3.50: Exposed MDPE pipe being filled with water

3.8.2.2 Field trials along buried water pipes

For the field trials, the same buried pipes employed for the communication system deployment were also used for measuring acoustic signal attenuation along the pipes. For the buried steel pipe, the acoustic signal amplitude was measured at the two separate sensor locations either side of the valve (Figure 3.39) before calculating the attenuation. A similar procedure was also employed for the buried MDPE pipes where the acoustic signal amplitude was measured at the two MFC sensor locations (Figure 3.42). As with the laboratory experiments, the results of the field trials along the buried water pipes will be presented in Chapter 4.

3.8.3 Numerical examination of acoustic attenuation along the water pipe

A key difference between the analytical model and the laboratory and field experiments is the nature of acoustic excitation along the pipe. While the analytical model assumes a centralised acoustic source within the pipe, with axisymmetric distribution of acoustic energy, the experiments featured a non-axisymmetric acoustic source (the ERM vibration motor) located

at the pipe crown (or 90 degrees according to Figure 3.47). To incorporate this feature into the acoustic attenuation prediction, a numerical model was developed.

For the numerical modelling, a finite element analysis (FEA) approach was chosen as it offered a computationally efficient approach for numerically computing the amplitude distribution of a propagating acoustic wave along a water pipe waveguide due to external excitation of the pipe. Furthermore, the FEA method is a widely used numerical solution approach for solving wave propagation and structural vibration problems (Rose, 2014). Since acoustic wave propagation is a dynamic problem, the governing equation of motion for an FEA model involving guided acoustic wave propagation along a hollow cylinder is (Rose, 2014; Drozdz, 2008):

$$[M]\ddot{u} + [C]\dot{u} + [k]u = [F] \tag{3.14}$$

Where $[M]$ is a diagonal lumped mass matrix whose values are determined by the material density of the cylinder, $[k]$ is the static stiffness matrix whose values are determined by the Young's modulus and Poisson's ratio of the cylinder, $[C]$ is the viscous damping matrix which is determined by the Rayleigh damping of the cylinder, $[F]$ is the external acoustic excitation force applied to the hollow cylinder and $\ddot{u}$, $\dot{u}$ and u are the cylinder acceleration (m/s), velocity (m/s) and displacement (m) respectively.

For the FEA model, wave propagation occurs along the cylinder when the initial equilibrium condition is disturbed by the application of force or displacement constraints. To solve Equation (3.14), thereby computing the dynamic response of the cylinder, numerical calculations in the time domain are needed. A popular technique for calculating this dynamic response is the direct integration method, i.e., a finite difference method which obtains a derivation of time, t from Taylor's polynomial (Rose, 2014). For this research, an explicit dynamic analysis technique using direct integration method in the form of a central difference operator, was employed for

modelling acoustic wave propagation along the cylindrical hollow cylinder. The main reason for adopting the explicit dynamic analysis approach was the advantage of computational efficiency offered by this approach (Drodz, 2008), over other techniques for computing the dynamic response of a physical structure.

For the explicit dynamic analysis, a commercially available FEA package was employed. According to Drozdz (2008), a commercially available FEA package not only offers a robust and memory efficient solver but also reduces the highly complex and time-consuming necessity of developing and maintaining specialist FE code. Commercially available FE packages also offer user-friendly interfaces for pre- and post-processing operations, which significantly increases their flexibility and ease of use. The commercially available FE package chosen for the explicit dynamic analysis was the ABAQUS/Explicit (Dassault Systemes, 2011) software package, which remains a widely available and well supported software choice for FEA within the academia and engineering industry. The procedure for modelling acoustic wave propagation along the MDPE water pipe waveguide, using ABAQUS/Explicit, is further described next.

3.8.3.1 Pipe geometry and material set-up

To begin the FEA, a two-dimensional (2-D) cross-section of the water pipe waveguide, with outer diameter of 90.6 mm and wall thickness of 9.2 mm was constructed and subsequently extruded into a three-dimensional (3-D) cylinder. Following the geometry extrusion, the material properties for the MDPE water pipe (Table 3.6) were applied to the FEA model.

Following the material property definitions, boundary conditions stipulating no rotational degree of freedom while keeping the boundaries fixed (i.e., no translational motion) were also applied at the pipe edges. The pipe was subsequently meshed into finite elements using first order hexahedral elements with reduced integration (C3D8R). Infinite element (CIN3D8) meshing was also applied to the pipe edges to prevent acoustic wave reflections at the edges.

To determine the optimum mesh density for the model which minimised computational time while maintaining modelling accuracy, a convergence analysis was performed.

3.8.3.2 Convergence analysis

For the convergence analysis, the pipe was excited at 200 Hz in the axial direction (as shown in Figure 3.51) while measuring the pipe wall acceleration at four separate locations at 90 degrees around the pipe circumference. To measure the pipe wall acceleration at the acoustic excitation frequency, the time domain acoustic signal in the numerical results was converted into frequency domain using the SSB-FFT approach previously described in Section 3.4.3.2. This same FFT procedure was also employed for analysing the numerical modelling results for the exposed and buried water pipes which will be presented in Chapter 4.

During the convergence analysis, the first acoustic measurement location was at the point of acoustic excitation while the other three locations were 1, 2 and 3 m away from the acoustic transmitter. Tables 3.14-3.17 show the results of the convergence analysis.

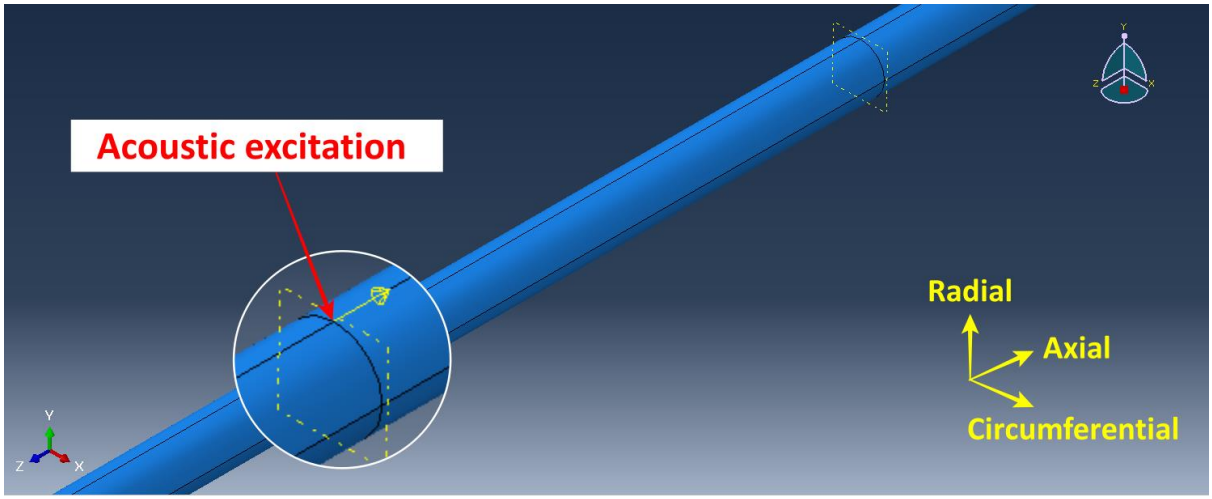

Figure 3.51: Pipe numerical model showing the acoustic excitation direction

Table 3.14: Convergence analysis at 0 m from the acoustic transmitter

Mesh length (m)	Number of elements	Computational time (hrs)	Pipe wall acceleration (m/s^2)
1.500	116	0.18	0.41
1.000	168	0.18	0.36
0.500	656	0.18	0.26
0.100	3200	0.18	0.30
0.020	32000	0.21	0.43
0.010	96000	0.52	0.61
0.008	140028	0.79	0.66
0.007	205704	1.12	0.79

Table 3.15: Convergence analysis at 1 m from the acoustic transmitter

Mesh length (m)	Number of elements	Computational time (hrs)	Pipe wall acceleration (m/s^2)
1.500	116	0.18	0.34
1.00	168	0.18	0.32
0.500	656	0.18	0.23
0.100	3200	0.18	0.22
0.020	32000	0.21	0.22
0.010	96000	0.52	0.22
0.008	140028	0.79	0.22
0.007	205704	1.12	0.22

Table 3.16: Convergence analysis results at 2 m from the acoustic transmitter

Mesh length (m)	Number of elements	Computational time (hrs)	Pipe wall acceleration (m/s^2)
1.500	116	0.18	0.34
1.000	168	0.18	0.32
0.500	656	0.18	0.22
0.100	3200	0.18	0.20
0.020	32000	0.21	0.18
0.010	96000	0.52	0.18
0.008	140028	0.79	0.18
0.007	205704	1.12	0.18

Table 3.17: Convergence analysis results at 3 m from the acoustic transmitter

Mesh length (m)	Number of elements	Computational time (hrs)	Pipe wall acceleration (m/s^2)
1.500	116	0.18	0.34
1.000	168	0.18	0.29
0.500	656	0.18	0.21
0.100	3200	0.18	0.21
0.020	32000	0.21	0.17
0.010	96000	0.52	0.17
0.008	140028	0.79	0.17
0.007	205704	1.12	0.17

While the results in Tables 3.15-3.17 show convergence in the pipe wall acceleration for mesh sizes of 0.02 m and below, the results in Table 3.14 did not. It was therefore decided to separately re-mesh this region (i.e., 0-1 m from the acoustic transmitter) while keeping the mesh density along the rest of the pipe constant. The results of the repeated analysis are shown in Table 3.18.

Table 3.18: Repeated convergence analysis at 0 m from the acoustic transmitter

Mesh length (m)	Number of elements	Computational time (hrs)	Pipe wall acceleration (m/s^2)
1.500	3152	0.18	0.28
0.100	3200	0.18	0.30
0.020	7040	0.18	0.32
0.010	13720	0.18	0.34
0.009	16032	0.20	0.35
0.008	18540	0.23	0.35
0.007	21320	0.28	0.35
0.006	26736	0.50	0.35

In Table 3.18, the results indeed converged for mesh sizes of 0.009 m and below showing that the pipe needed to be finely meshed between 0 and 1 m from the acoustic transmitter while the region beyond 1 m could be more coarsely meshed as shown in Figure 3.52.

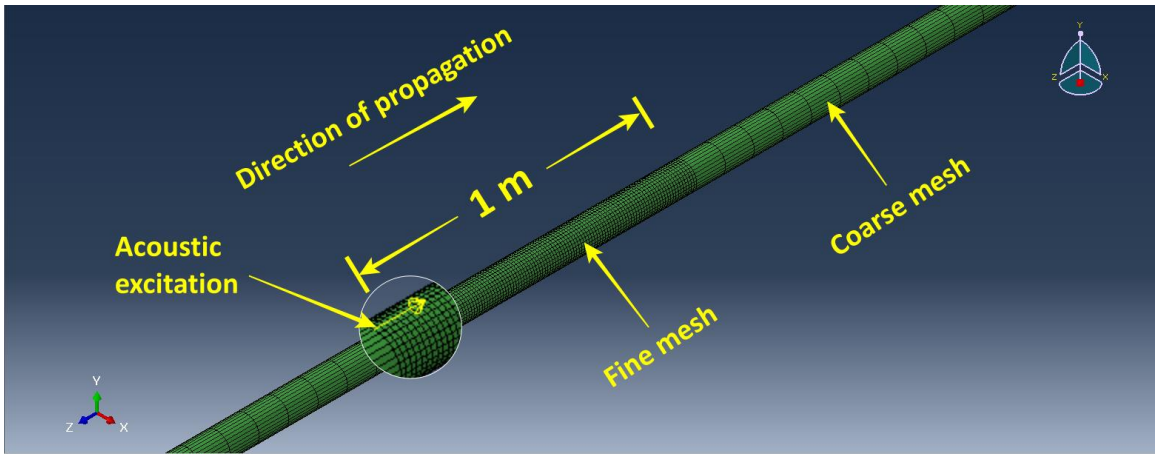

Figure 3.52: Pipe section showing the finely and coarsely meshed regions

Following the convergence analysis, further acoustic measurement points were positioned around the pipe circumference (at 0, 90, 180 and 270 degrees) between 0 m and 10 m from the acoustic transmitter with 1 m axial spacing between the measurement points before separately modelling acoustic signal propagation along exposed and buried water pipes as described next.

3.8.3.3 Numerical model for acoustic signal attenuation along an exposed water pipe

To model the exposed MDPE pipe in Section 3.8.2.1, the acoustic excitation direction due to the positioning of the ERM vibration motor needed to be incorporated within the model. The ERM vibration motor, during its operation, is characterised by oscillatory motion in two primary directions as shown in Figure 3.53 (Precision Microdrives, n.d.).

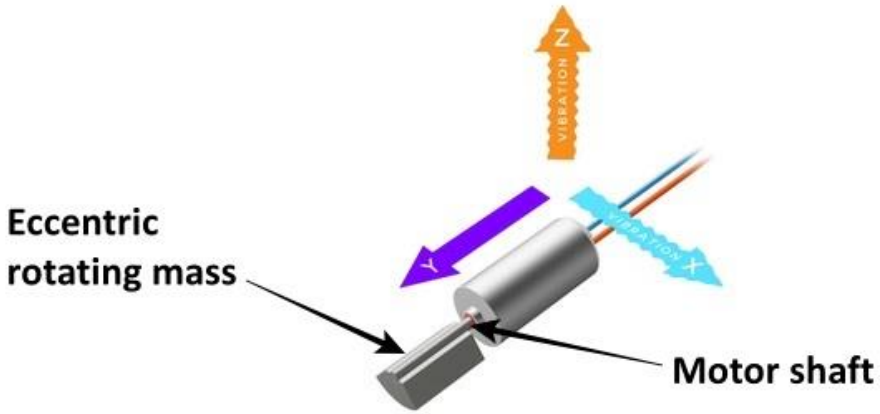

Figure 3.53: Vibration directions of the ERM vibration motor (from Precision Microdrives, n.d.)

As shown in Figure 3.53, the vibration motor, during operation, vibrates in two directions which are orthogonal to the motor shaft. Two types of geometric orientations were therefore possible with the ERM vibration motor for installation along the pipe. The first orientation featured the vibration motor shaft parallel to the pipe axis, with the subsequent acoustic excitation directions shown, within the numerical model, in Figure 3.54.

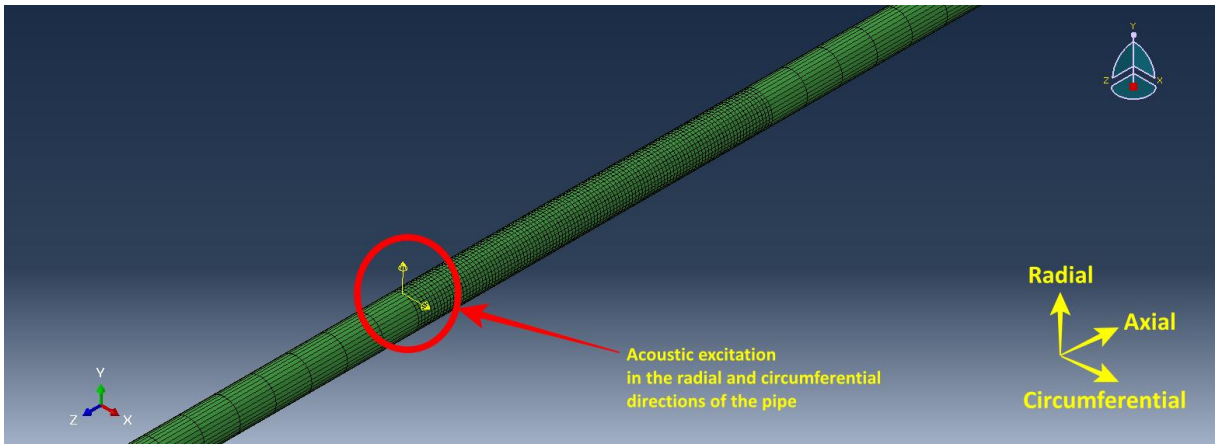

Figure 3.54: Acoustic excitation of the exposed MDPE pipe in the radial and circumferential directions

In Figure 3.54, acoustic excitation along the pipe (for the vibration motor installed with its shaft parallel to the pipe axis) was in the radial and circumferential directions of the pipe. The second orientation method of the vibration motor featured the vibration motor shaft installed perpendicular to the pipe axis, with the subsequent acoustic excitation directions shown in the numerical model in Figure 3.55.

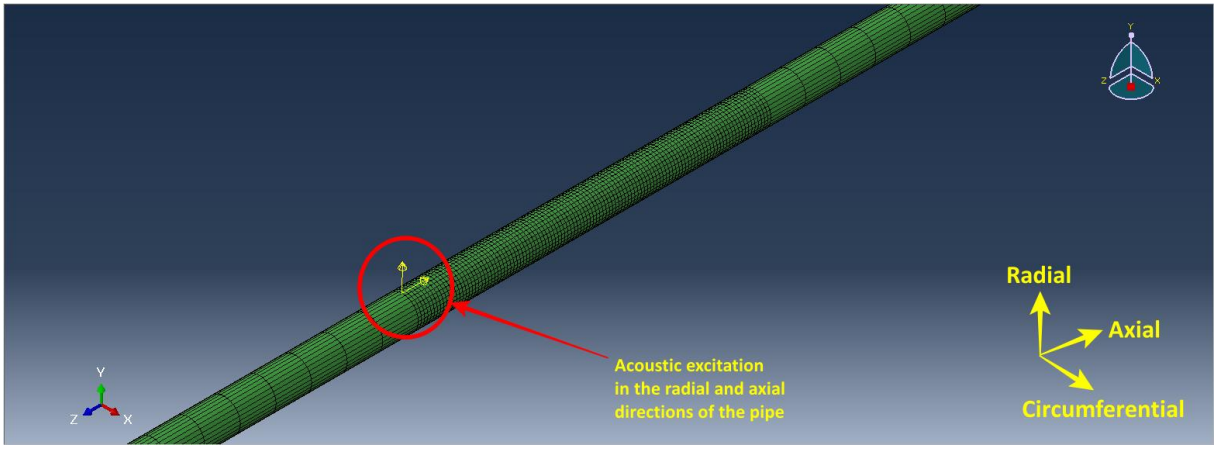

Figure 3.55: Acoustic excitation of the exposed MDPE pipe in the radial and axial directions

In Figure 3.55, acoustic excitation along the pipe (for the vibration motor installed with its shaft perpendicular to the pipe axis) was in the radial and axial directions of the pipe. The ERM vibration motor in the experiments described in Section 3.8.2.1 was however installed with its shaft parallel to the pipe axis and so the numerical model was initially run with acoustic excitation in the radial and circumferential directions before comparing the results with acoustic excitation in the radial and axial directions.

For the water-filled pipe in Section 3.8.2.1, an acoustic medium with bulk modulus and density of 2.25×10^9 N/m^2 and 997 Kg/m^3 respectively was incorporated within the pipe before meshing this medium with the AC3D8R (8-node linear acoustic brick) element. The model was subsequently run with acoustic excitation in the radial and circumferential directions (to replicate the experiments) before comparing the results with those of the empty pipe numerical model. Both numerical modelling predictions and laboratory experiment results for the exposed MDPE pipe will be presented and discussed in Chapter 4. Like the analytical model, parametric analysis of acoustic signal attenuation along the exposed MDPE pipe, with respect to the pipe inner radius, wall thickness, elastic modulus and Poisson's ratio were also conducted with the results also presented in Chapter 4.

3.8.3.4 Numerical model for acoustic signal attenuation along a buried water pipe

For the buried water pipe, a surrounding soil medium was added to the pipe model as shown in Figure 3.56.

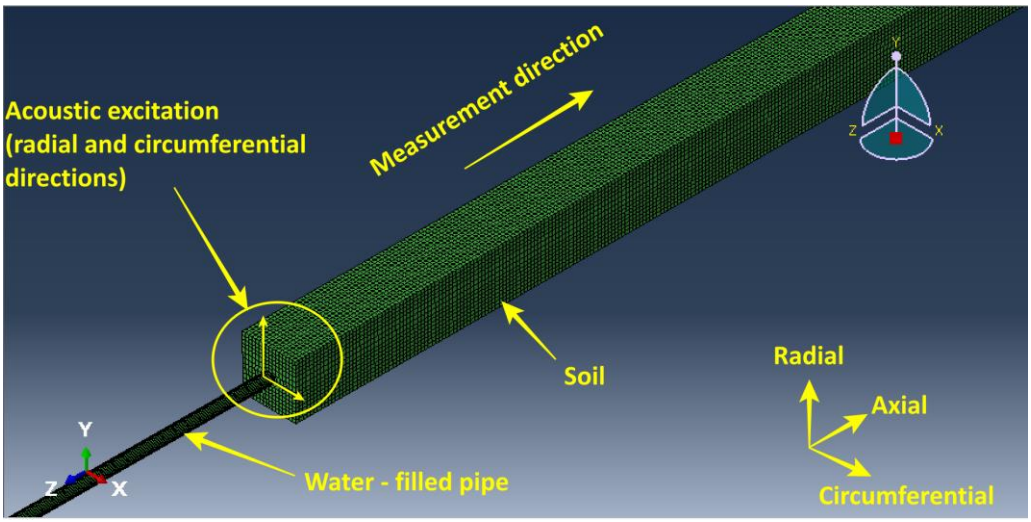

Figure 3.56: Numerical model for buried water-filled pipe

Figure 3.56 shows a surrounding soil medium around the section of the exposed pipe where acoustic measurements were to be taken in the numerical model. The soil medium, which was meshed using the AC3D8R (8-node linear acoustic brick) element, was only added to the relevant section of the pipe model (where acoustic measurements were to be taken) to save computational resources during the FEA.

To directly compare the numerical model predictions with the field trials, soil material properties were assigned to the buried pipe model according to the soil properties sampled from the field trials. Separate numerical models were therefore conducted for:

I. The buried steel pipe with steel pipe material properties (Table 3.7) assigned to the pipe while soil properties from the buried steel pipe field trials (Table 3.9) were assigned to the surrounding soil.

II. The buried MDPE pipe in Trench 1 with the MDPE material properties (Table 3.6) assigned to the pipe while soil properties from the buried MDPE pipe field trials (Table 3.11) were assigned to the surrounding soil.

III. The buried MDPE pipe in Trench 2 with the MDPE material properties (Table 3.6) assigned to the pipe while soil properties from the buried MDPE pipe field trials (Table 3.13) were assigned to the surrounding soil.

Since the pipe length employed for the buried MDPE pipe field trial was 6 m (rather than an infinitely long pipe), a separate numerical model, using this shorter pipe length, was also developed for the buried MDPE pipe before comparing the results with the field trials.

3.9 SUMMARY

This chapter presented the methodology by which the proposed communication system described in this thesis was developed. An outline of the operational stages of the communication system was initially laid out before the system hardware arrangement was described. Following the description of the hardware layout, the method by which commercially available acoustic signal transducers were selected and evaluated for integration at the digital communication nodes was presented. The acoustic transducer selection process, which also included laboratory testing, yielded the selection of the external ERM vibration motor and MFC piezoelectric sensor for acoustic transmission and detection respectively along a water pipe. The development of the digital communication transmitter and receiver, including the algorithms for enabling reliable digital communication using the selected acoustic transducers, was also discussed in the chapter.

To be able to predict the communication system performance, an understanding of the physical mechanisms by which an acoustic signal attenuated along an exposed or buried pipe needed to be achieved. To this end, analytical and numerical models in addition to laboratory and field trials were conducted to evaluate acoustic signal attenuation along exposed and buried water pipes.

CHAPTER 4

RESULTS AND DISCUSSION

4.1 INTRODUCTION

Results of acoustic signal attenuation along exposed and buried water pipes as well as their implications for reliable data communication along the pipes are presented and discussed in this chapter. Section 4.2 initially presents the results of data communication trials along exposed and buried water pipes using the communication system developed in Chapter 3. It was also put forward in the chapter that key to predicting data communication reliability along a water pipe is the quantification of acoustic signal attenuation along the pipe. Sections 4.3 and 4.4 present the results of three separate approaches, i.e., analytical, numerical, and experimental, for examining acoustic signal attenuation along exposed and buried water pipes and how these results compare with each another. Section 4.5 further uses the acoustic attenuation predictions to evaluate data communication reliability along the pipes while Section 4.6 discusses a possible application of the proposed communication system for buried water pipe monitoring. A short summary of the chapter is presented in Section 4.7.

4.2 DIGITAL COMMUNICATION RESULTS ALONG EXPOSED AND BURIED WATER PIPES

This section presents digital communication results along the exposed and buried water pipes described in Chapter 3 using the system developed in the same chapter. Figure 4.1 shows the idle status message programmed at the digital communication receiver (Section 3.6.4) and subsequently displayed at the output monitor of the receiver PC prior to data transmission along the pipe.

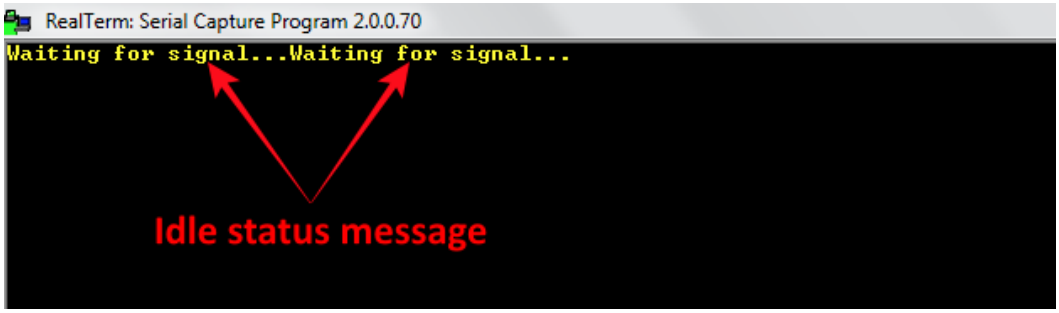

Figure 4.1: Idle status message at digital communication receiver before data transmission

Following successful pilot signal detection (which, as described in Section 3.6.3, synchronised the digital communication transmitter and receiver), Figures 4.2a and b show the digital communication results along the exposed and buried water pipes.

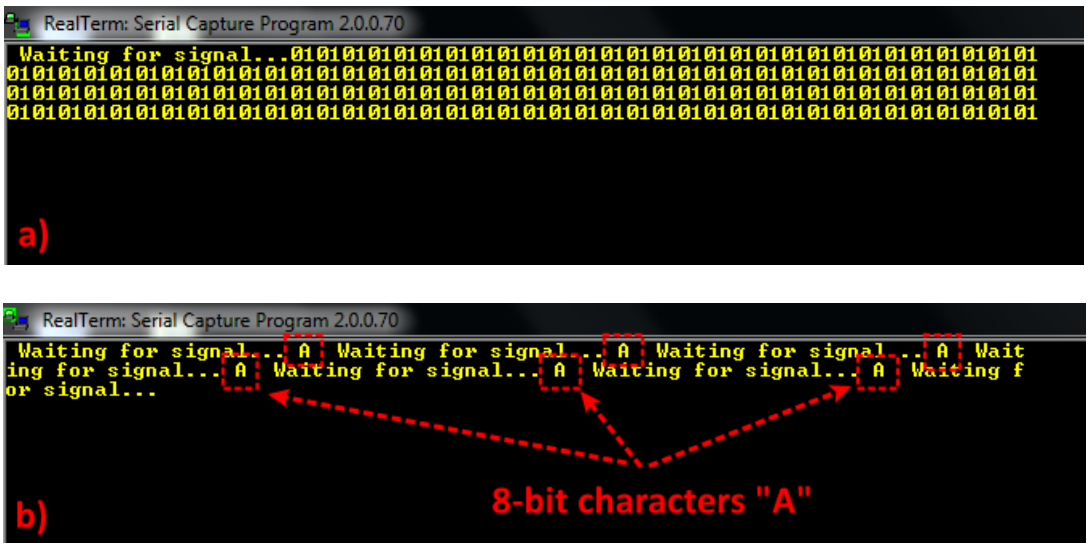

Figure 4.2: Binary and b) ASCII data transmission along exposed and buried water pipes

Shown in Figures 4.2a and b is the repeated transmission of binary as well as ASCII encoded digital information, without any bit error, using the digital communication transmitter and receiver described in Chapter 3. The results of Figure 4.2 a and b are therefore evidence of the successful deployment of the proposed communication system, for repeated data transmission (without any bit error) especially along a buried water pipe. To the best of the author's knowledge, this is the first time the pipe wall of either a metallic or non-metallic pipe has been

successfully employed for enabling reliable, non-invasive digital communication along an exposed or buried water pipe. Using the communication system, with a data transmission rate of 2 bps for example, a 2-bit number would require 1 s for data transmission while 4 and 8-bit numbers/characters would require 2 and 4 s respectively (and so on). For a non-data intensive pipeline monitoring application (where less emphasis is on real-time data throughput), this latency may be tolerated if, as is the objective of the communication system, longer ranges of wireless underground data communication can be achieved compared to existing solutions based on radio signal propagation (which, as discussed in Section 2.4.3 are currently limited to less than 3 m). The results presented so far show that reliable digital communication is possible along an exposed or buried water pipe (especially of non-metallic material) using acoustic signal propagation along the pipe wall. To predict the ranges at which such communication is possible using the system developed in Chapter 3, the next sections present the results of analytical and numerical models as well as experimental trials designed to evaluate acoustic signal attenuation along the exposed and buried water pipes.

4.3 ACOUSTIC SIGNAL ATTENUATION ALONG AN EXPOSED WATER PIPE

4.3.1 Analytical model predictions for an exposed pipe

It was shown in Section 3.8.1 that acoustic signal attenuation (dB/m) along a pipe wall, using analytical computations, depends on certain pipe geometric (pipe inner radius and wall thickness) and mechanical (pipe wall elastic modulus and Poisson's ratio) properties. For the MDPE pipe described in Section 3.4.3 and with the material properties in Table 3.4, Figure 4.3 shows the frequency dependency of acoustic attenuation along the pipe, within the bandwidth of the proposed communication system, using analytical computations.

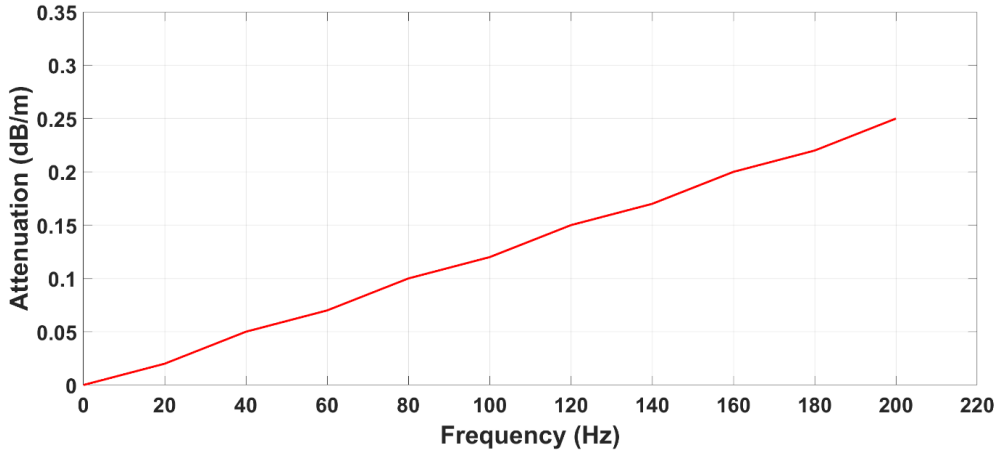

Figure 4.3: Analytical predictions of the frequency dependency of acoustic signal attenuation along an exposed MDPE pipe

According to Figure 4.3, acoustic attenuation along an exposed MDPE pipe increases with acoustic excitation frequency, which is in line with Equation (3.4) (which shows that acoustic wavenumber along the pipe is directly proportional to the acoustic excitation frequency) and Equation (3.5) which shows that acoustic attenuation is also directly proportional to the imaginary part of the acoustic wavenumber. For a water-filled pipe, Figure 4.4 also shows the frequency dependency of acoustic attenuation compared to an empty pipe.

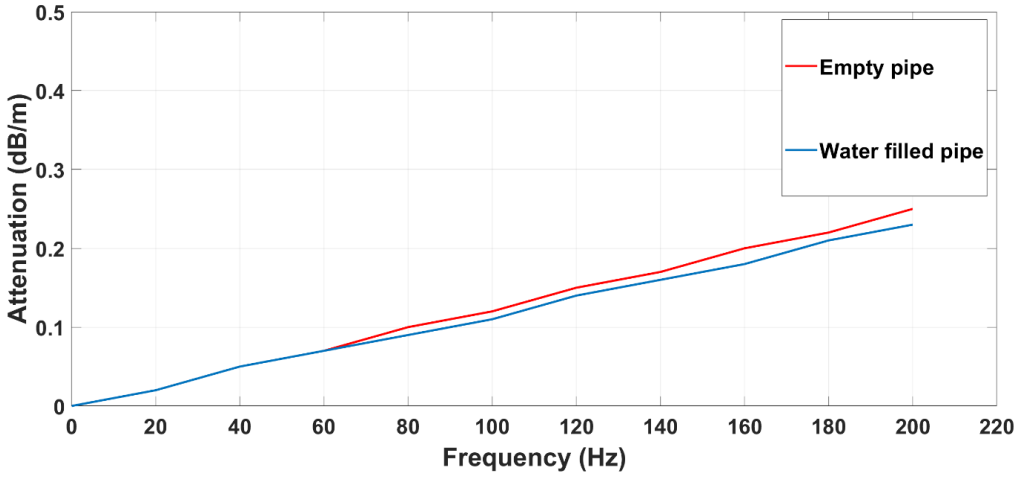

Figure 4.4: Analytical predictions of the frequency dependency of acoustic attenuation along (exposed) water-filled and empty MDPE pipes

As shown in Figure 4.4, a slight reduction (maximum of 0.02 dB/m) in acoustic attenuation occurs along the pipe at excitation frequencies above 60 Hz. This is understandable when, as

noted by Muggleton et al. (2002), considering the effect of water within the pipe in stiffening the pipe wall (especially at higher frequencies) thus slightly reducing acoustic attenuation (by reducing the acoustic wave number) along the pipe wall.

Using the pipe inner radius, wall thickness, elastic modulus and Poisson's ratio as independent variables, parametric analysis of acoustic signal attenuation along the exposed MDPE pipe, based on the analytical calculations, is further discussed. The base case, around which the parametric analyses are implemented, are the geometric and material properties of the MDPE pipe in Table 3.4. The parametric analysis also focuses on acoustic excitation frequencies between 100 and 200 Hz since it is advantageous for the digital communication system, in practice, to operate within this bandwidth as it avoids background acoustic noise interference which, in the field, is typically concentrated below 100 Hz (e.g., Hunaidi & Chu, 1999).

To examine the influence of pipe inner radius on acoustic attenuation, Table 4.1 shows the predicted acoustic attenuation (at 150 Hz acoustic excitation) for a range of pipe inner radii typical of water distribution pipes.

Table 4.1: Analytically predicted acoustic attenuation along exposed MDPE pipe with respect to change in pipe inner radius

Pipe inner radius (mm)	Acoustic attenuation (dB)
15.8	0.18
36.1	0.18
140.8	0.18

Table 4.1 shows that the analytically predicted acoustic attenuation along the exposed MDPE pipe is independent of the pipe inner radius. With the analytical model therefore, changes in the pipe inner radius (at least within the limits of typical water distribution pipes) do not influence acoustic signal attenuation along the pipe.

For pipe wall thickness variation, Table 4.2 shows the acoustic attenuation predictions for separate pipe wall thicknesses.

Table 4.2: Analytically predicted acoustic attenuation along exposed MDPE pipe with respect to change in pipe wall thickness

Pipe wall thickness (mm)	Acoustic attenuation (dB)
9.2	0.18
14.0	0.18
17.0	0.18

Again, like Table 4.1, acoustic attenuation along the exposed MDPE pipe is insensitive to pipe wall thickness variation according to the analytical model. The results presented so far have thus shown that based on the analytical model predictions, acoustic attenuation along the MDPE pipe is insensitive to the pipe geometric properties. This insensitivity can be traced to the low frequency approximations (Muggleton et al., 2004; Muggleton et al., 2002; Pinnington and Briscoe, 1994) for acoustic wave motion along a thin cylindrical shell, inherent in the analytical derivations for acoustic wave attenuation along a water pipe waveguide.

Regarding the pipe mechanical properties, Bilgin et al. (2007) noted that the mechanical properties of polyethylene do not remain constant within the range of temperatures typically found in civil engineering applications. For the pipe wall elastic modulus, this functional relationship with temperature can be expressed as (Bilgin et al., 2007)

$$E = 1050e^{-0.018T} \tag{4.1}$$

Where E (MPa) and T (°C) are the pipe wall elastic modulus and temperature, respectively. For temperatures between -25 and 50 °C (which encompasses the maximum expected temperature range for water distribution pipes), the corresponding elastic modulus of the MPDE pipe was calculated using Equation (4.1) before analytically predicting acoustic attenuation along the pipe (for separate pipe wall elastic moduli in N/m^2) as shown in Table 4.3.

Table 4.3: Analytically predicted acoustic attenuation along exposed MDPE pipe with respect to change in pipe wall elastic modulus

Pipe wall elastic modulus (N/m^2)	Acoustic attenuation (dB)
1.6×10^9	0.18
8.8×10^8	0.25
4.3×10^8	0.36

Table 4.3 shows the analytically predicted acoustic attenuation along the exposed MDPE pipe to increase with decreasing pipe wall elastic modulus. It is therefore clear from the table that unlike Tables 4.1 and 4.2, the analytical prediction of acoustic attenuation along the MDPE pipe is sensitive to changes in the pipe wall elastic modulus. Using the MDPE pipe wall elastic modulus in Table 3.6 as a base value, accurate analytical prediction (to within 2 decimal places) of acoustic attenuation along the exposed MDPE pipe (based on a 14.9×10^{-11} dB/m increase in acoustic attenuation per N/m^2 decrease in pipe wall elastic modulus) would require a choice of pipe wall elastic modulus within $\pm 2\%$ of the base value of the MDPE pipe wall elastic modulus in Table 3.6.

Like the elastic modulus, the functional relationship between the pipe wall Poisson's ratio and temperature can also be expressed as (Bilgin et al., 2007)

$$\upsilon = 0.433 + 10.73 \times 10^{-4} T \qquad (4.2)$$

Where υ is the pipe wall Poisson's ratio. For the same temperature range previously described (i.e., between -25 and 50 °C), the corresponding Poisson's ratio of the MPDE pipe was calculated using Equation (4.2) before predicting acoustic signal attenuation along the pipe as shown in Table 4.4.

Table 4.4: Analytically predicted acoustic attenuation along exposed MDPE pipe with respect to change in pipe wall Poisson's ratio

Pipe wall Poisson's ratio	Acoustic attenuation (dB)
0.16	0.18
0.43	0.18
0.97	0.18

Like Tables 4.1 and 4.2, analytical predictions of acoustic attenuation along the exposed MDPE pipe for varying Poisson's ratio is constant. According to the analytical model therefore, acoustic attenuation along the MDPE pipe is only sensitive to changes in the pipe wall elastic modulus.

Acoustic attenuation predictions for other pipe materials (Table 3.7) of the same physical dimensions as the MDPE pipe (Table 3.6) are also shown in Figure 4.5 and Table 4.5.

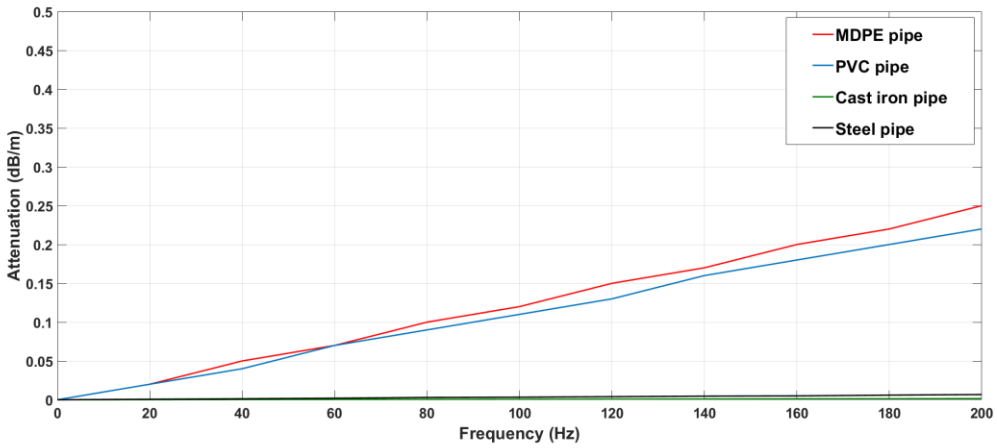

Figure 4.5: Analytical predictions of the frequency dependence of acoustic attenuation along exposed MDPE, PVC, cast iron and steel pipes

Table 4.5: Acoustic attenuation predictions (analytical model) along exposed MDPE, PVC, cast iron and steel pipes

Frequency (Hz)	MDPE attenuation (dB/m)	PVC attenuation (dB/m)	Cast iron attenuation (dB/m)	Steel attenuation (dB/m)
0	0	0	0	0
20	0.02	0.02	1.45×10^{-4}	6.65×10^{-4}
40	0.05	0.04	2.91×10^{-4}	1.30×10^{-3}
60	0.07	0.07	4.36×10^{-4}	2.00×10^{-3}
80	0.10	0.09	5.82×10^{-4}	3.00×10^{-3}
100	0.12	0.11	7.27×10^{-4}	3.30×10^{-3}
120	0.15	0.13	8.73×10^{-4}	4.00×10^{-3}
140	0.17	0.16	1.00×10^{-3}	4.70×10^{-3}
160	0.20	0.18	1.20×10^{-3}	5.00×10^{-3}
180	0.22	0.20	1.30×10^{-3}	6.00×10^{-3}
200	0.25	0.22	1.50×10^{-3}	6.70×10^{-3}

From Table 4.5, acoustic attenuation along the non-metallic pipes is significantly greater (by 2 orders of magnitude) than for the metallic pipes. This is understandable as the metallic pipe elastic moduli in Table 3.7 are significantly higher (also 2 orders of magnitude) than the elastic moduli of the non-metallic pipes. Further validation of the analytical model predictions using the results of the experiments conducted along the bespoke laboratory set-up described in Section 3.8.2.1 is presented next.

4.3.2 Results of acoustic attenuation experiments along an exposed pipe

Results of the experiments described in Section 3.8.2.1 are presented in this section. To directly compare with the analytical model results, these results focus on axial particle motion along the pipe wall. Furthermore, predominantly axial particle motion at less than 1 kHz, as previously discussed in Section 2.5.2, is indicative of longitudinal acoustic wave propagation along the pipe wall. For the accelerometers located at 0 degrees around the pipe circumference for example, Figures 4.6 and 4.7 show the acoustic signals in the time and frequency domains when separate acoustic measurements were taken at 0, 2, 4 and 6 m along the pipe. It should be noted that the acoustic measurements at each distance were taken independently, hence the acoustic

pulse locations (within the 5 s window of each plot) are not dependent on the measurement distances.

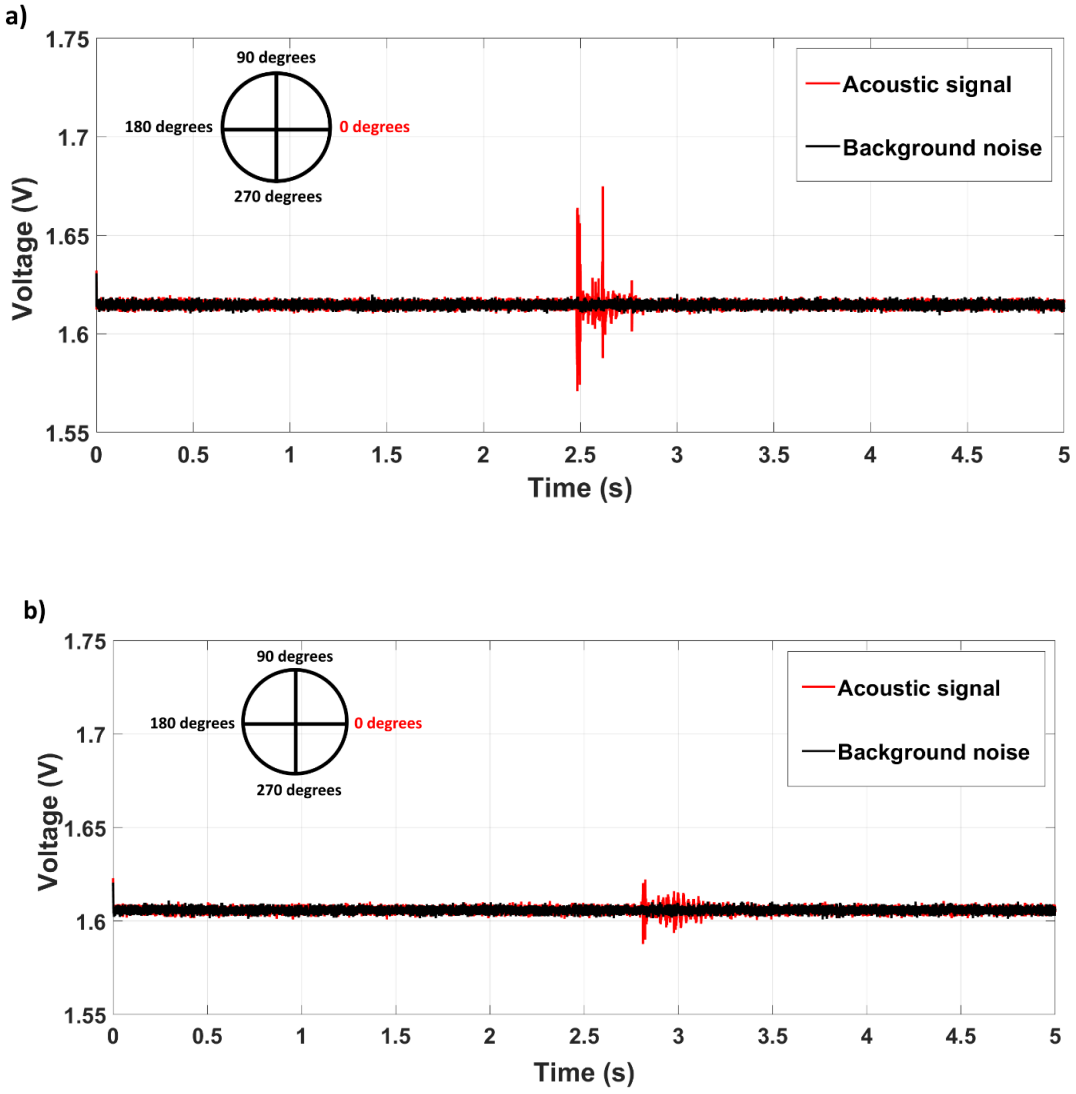

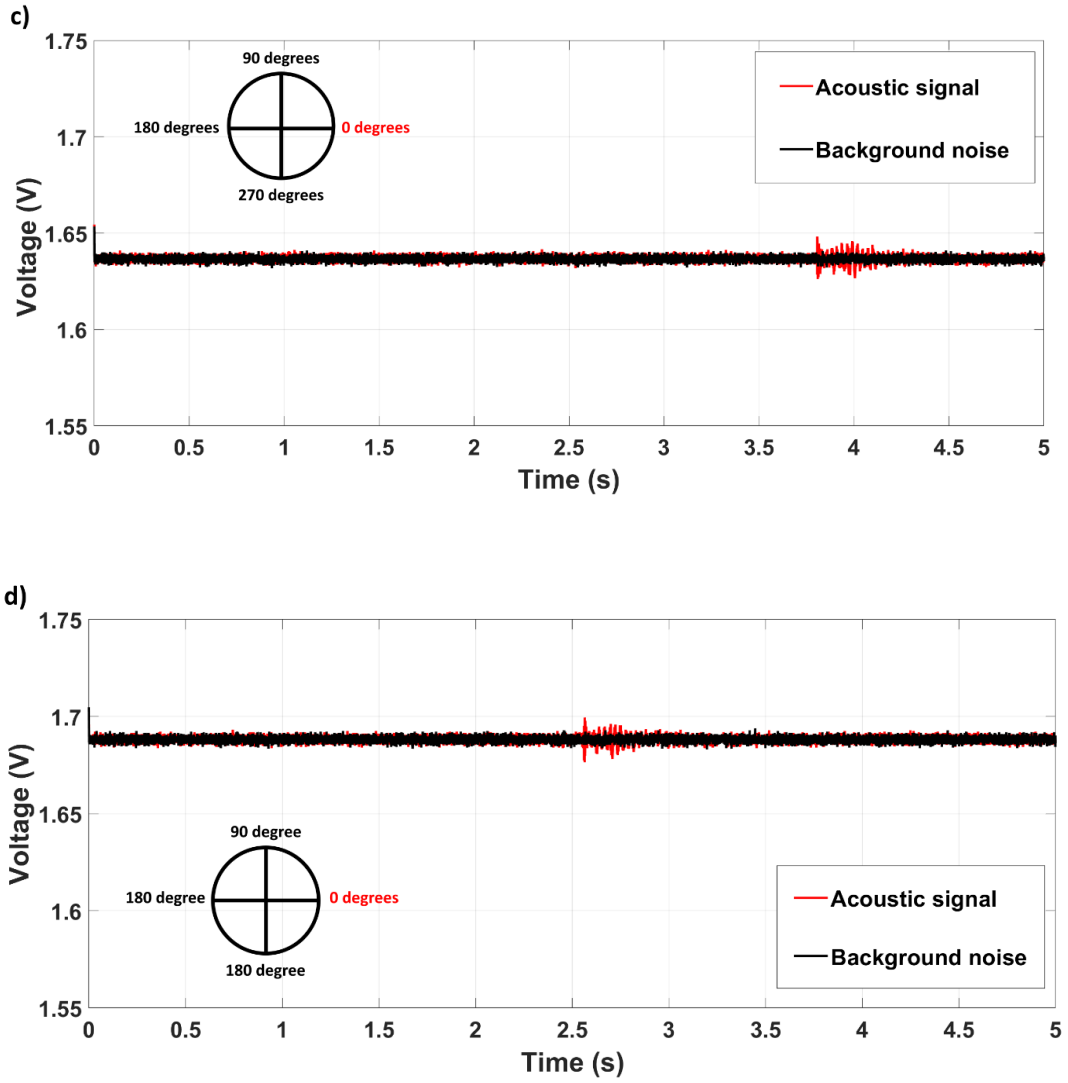

Figure 4.6: Acoustic signals (time domain) measured along the exposed (empty) MDPE pipe at 0 degrees around the pipe and at a) 0 b) 2 c) 4 and d) 6 m from the acoustic transmitter

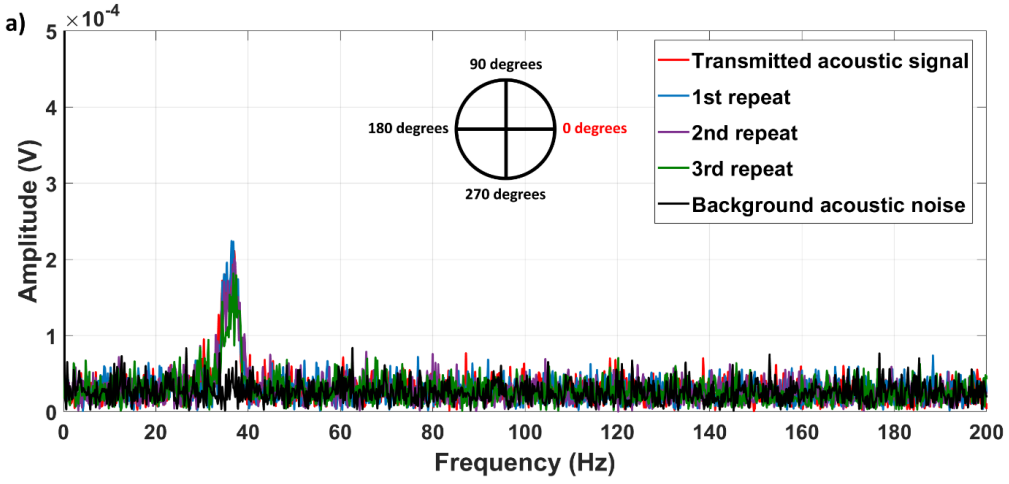

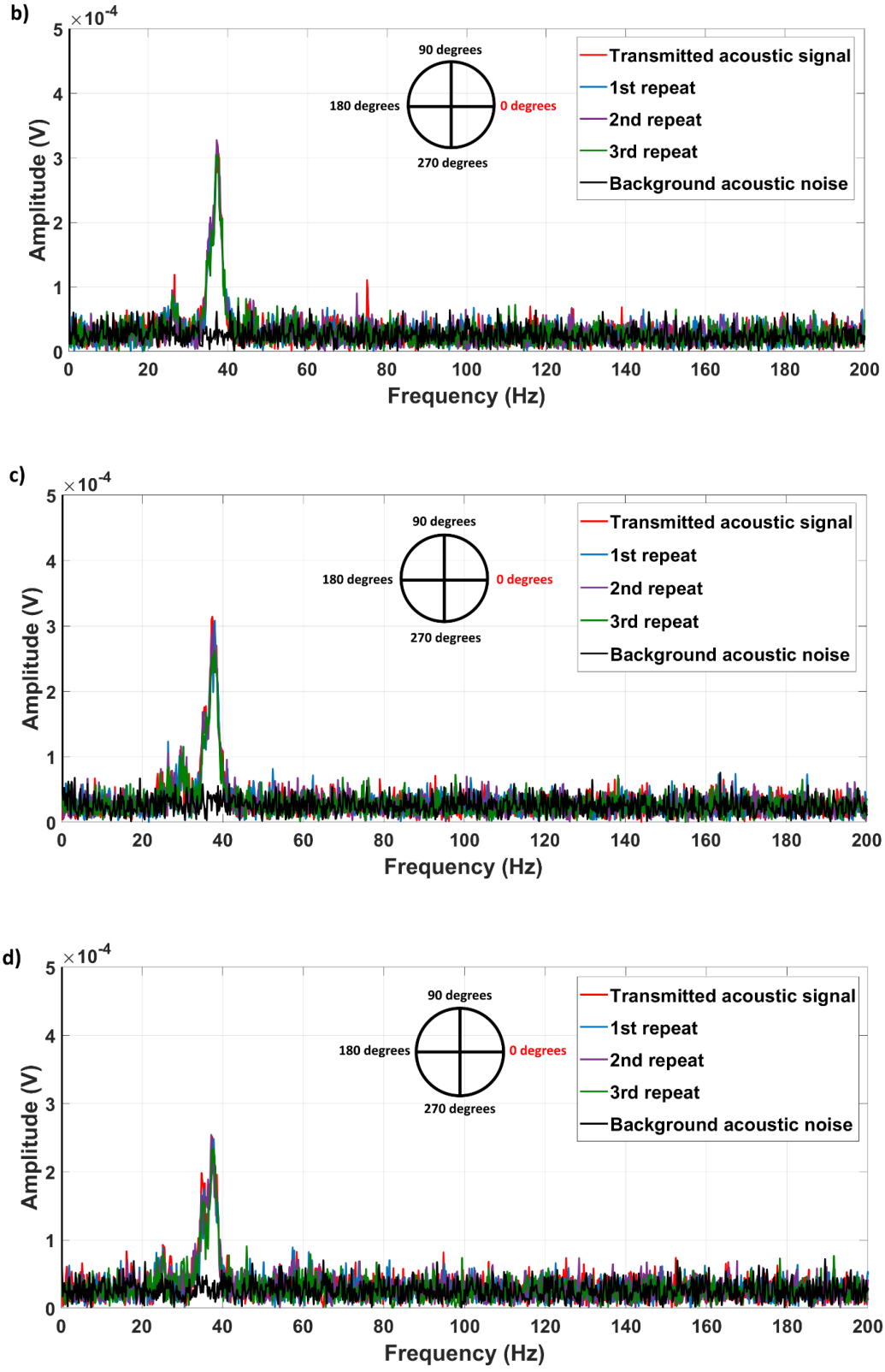

Figure 4.7: Acoustic signals (frequency domain) measured along the exposed (empty) MDPE pipe at 0 degrees around the pipe and at a) 0 b) 2 c) 4 and d) 6 m from the acoustic transmitter

From Figure 4.7, as expected due to the reasons previously described in Section 3.8.2.1, the acoustic signals measured along the pipe (during acoustic excitation of the pipe) were outside the 100-200 Hz bandwidth (as shown by the peak acoustic signal amplitudes at approximately 38 Hz in Figure 4.7). Figure 4.6a also shows more prominent acoustic signal peaks closest to the actuator but the corresponding frequency domain signal (Figure 4.7a) shows a lower acoustic amplitude at 38 Hz compared to the rest of the pipe. A significant portion of the acoustic energy closest to the actuator therefore constitutes coherent noise representing higher order acoustic wave modes (as noted, for example, in Rose (2014)) generated at the point of acoustic excitation. As shown in Figure 4.6b, these high frequency peaks significantly diminish in amplitude between at 2 m also validating the pipe response as a low-pass acoustic filter as also reported separately by Kokossalakis (2006) and Jin et al. (2013). Table 4.6 and Figure 4.8 further summarise the average peak acoustic amplitudes (in terms of measured voltages at the accelerometers) for repeated acoustic transmissions at the other circumferential positions of the pipe and at increasing distances from the acoustic transmitter.

Table 4.6: Average peak acoustic signal amplitudes at each circumferential location along the exposed (empty) MDPE pipe

Axial distance from acoustic transmitter (m)	Average peak acoustic amplitude at 0 degrees around pipe (V)	Average peak acoustic amplitude at 90 degrees around pipe (V)	Average peak acoustic amplitude at 180 degrees around pipe (V)	Average peak acoustic amplitude at 270 degrees around pipe (V)
0	2.04×10^{-4}	2.26×10^{-4}	2.42×10^{-4}	2.37×10^{-4}
2	3.13×10^{-4}	2.55×10^{-4}	2.90×10^{-4}	3.32×10^{-4}
4	2.96×10^{-4}	2.31×10^{-4}	2.50×10^{-4}	2.83×10^{-4}
6	2.47×10^{-4}	2.37×10^{-4}	2.65×10^{-4}	2.05×10^{-4}

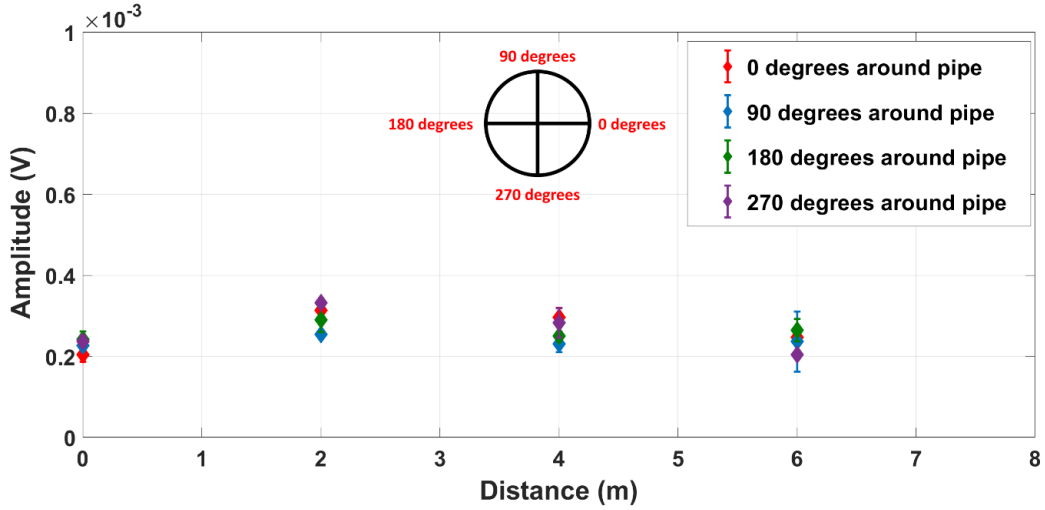

Figure 4.8: Acoustic amplitudes at the four circumferential locations and at increasing distances along the exposed (empty) MDPE pipe

The error bars in Figure 4.8 indicate the variability in vibration motor speed during repeated acoustic transmission along the pipe. As shown in Table 4.6 and Figure 4.8, the acoustic amplitude closest to the transmitter (not only for the acoustic receivers at 0 degrees but for all other circumferential positions) is relatively lower than at 2 m along the pipe. This is unlike the analytical model prediction where the acoustic amplitude is strongest closest to the transmitter, with linear attenuation at increasing distances along the pipe. As noted in Section 3.8.3, the analytical model assumes the acoustic source to be centrally located within the pipe with axisymmetric distribution of acoustic energy around the pipe. The experimental results however show that the same assumption cannot be held for accurately predicting acoustic signal attenuation along the pipe due to the non-axisymmetric location of the acoustic source (ERM vibration motor) along the pipe wall.

The acoustic signal amplitude at each sensor relative to the sensor closest to the acoustic transmitter can further be calculated as

$$Relative\ amplitude\ (dB) = 20 \times log_{10} \frac{A_x}{A_0} \qquad (4.3)$$

Where A_0 (V) and A_x (V) are the acoustic signal amplitudes at 0 and x metres respectively from the acoustic transmitter. Using Equation (4.3), Figure 4.9 shows the relative amplitudes as well as attenuation of the transmitted acoustic signal at 0 degrees around the pipe circumference and at increasing distances along the pipe.

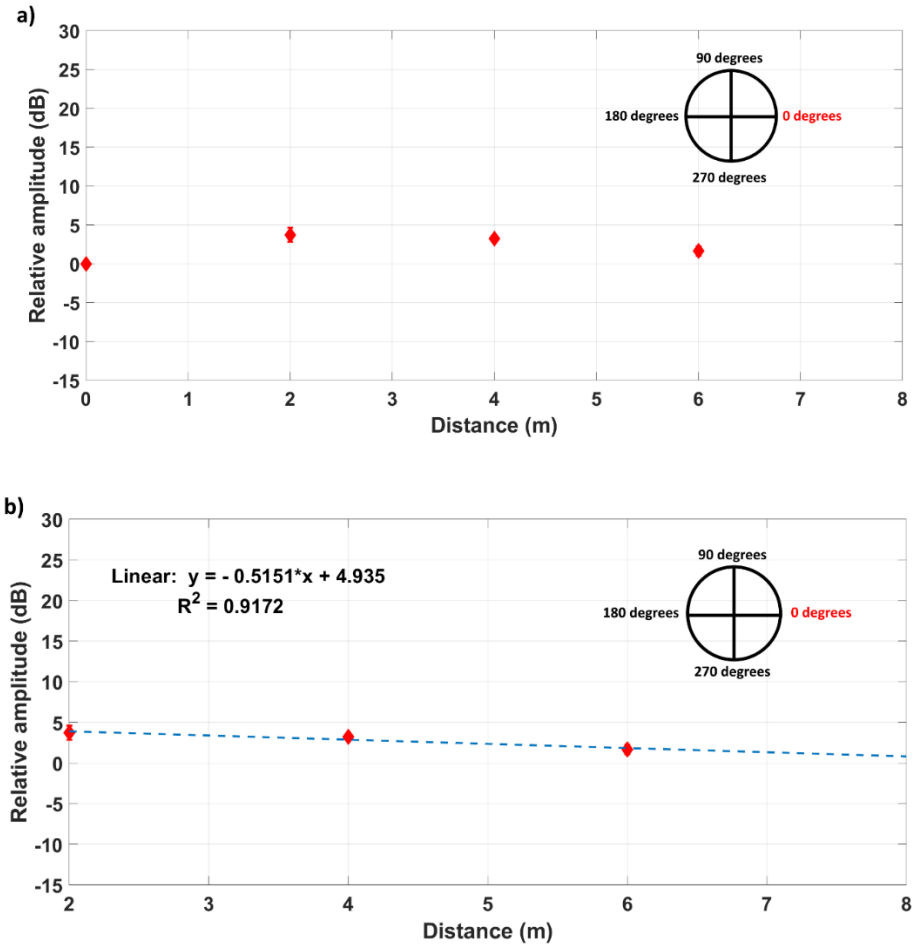

Figure 4.9: Relative acoustic amplitudes and b) attenuation of the acoustic signal along the exposed (empty) MDPE pipe at 0 degrees around the pipe and at increasing distances along the pipe

Figure 4.9a shows the acoustic amplitude distribution at increasing distances along the pipe, relative to the acoustic sensor closest to the transmitter. As expected, an initial increase in acoustic amplitude can be seen between 0 and 2 m (due to the dispersion of high frequency acoustic waves in this region) before a negative trend in the acoustic amplitude beyond 2 m. The region between 0 and 2 m, nominally identifiable as the transmitter near-field, thus featured

a positive gain in low frequency acoustic signal amplitude before gradual attenuation beyond 2 m (or in the region nominally identifiable as the acoustic far-field). As shown in Figure 4.9b, acoustic signal attenuation in the far-field was estimated as 0.5 dB/m while for the other circumferential positions around the pipe, this estimate ranged between 0.2 and 1.1 dB/m as shown in Table 4.7.

Table 4.7: Experimental results for acoustic signal attenuation along the exposed (empty) MDPE pipe

Circumferential position of acoustic receivers	Measured acoustic attenuation (dB/m)
0 degrees	0.5
90 degrees	0.3
180 degrees	0.2
270 degrees	1.1
Average acoustic attenuation	0.5 ± 0.4 dB/m

From Table 4.7, the average acoustic attenuation measured along the pipe wall was estimated at 0.5 ± 0.4 dB/m. One possible reason for the variance in acoustic signal attenuation measurements around the pipe circumference was the curved nature of the pipe along its 40 m length (as opposed to a perfectly straight pipe in theory) due to the flexible nature of the MDPE pipe material especially for that length. The experimentally obtained results however, by distinguishing between near and far-field regions of acoustic signal propagation along the pipe wall, reveal a previously undiscovered feature of low frequency acoustic wave propagation along an MDPE pipe. This finding will be further validated against numerical modelling results in Section 4.3.3.

Using pipe surface temperature readings (Figure 4.10) which were taken over the duration of the acoustic experiments, the average pipe wall temperature was calculated as 12.67 ± 0.67 °C. The corresponding pipe wall elastic modulus for this temperature (according to Equation (4.1)) was further calculated as $(8.36 \pm 0.10) \times 10^8$ N/m^2. Based on this elastic modulus, the analytical model predicted 0.06 dB/m attenuation at 38 Hz along the exposed MDPE pipe, a

lower value than the experimentally obtained average of 0.5 ± 0.4 dB/m. The analytical model result, compared to the experimentally measured average, therefore underestimates acoustic signal attenuation along the exposed MDPE pipe. This is understandable as the analytical model only considers the pipe wall material loss factor as responsible for acoustic attenuation along the pipe. The experimental result on the other hand, due to its higher acoustic attenuation estimate, suggests additional mechanisms by the which the acoustic signal attenuates along the exposed MDPE pipe. Numerical modelling results to validate this hypothesis will be further presented and discussed in Section 4.3.3.

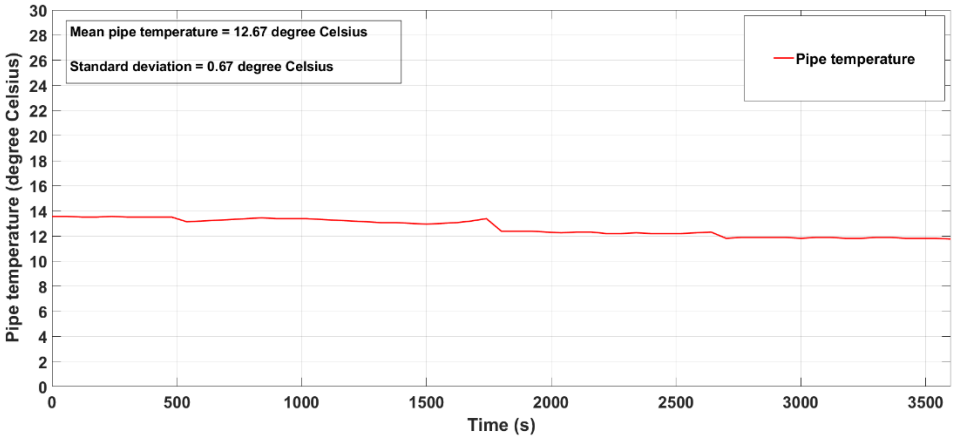

Figure 4.10: Pipe surface temperature readings along the exposed MDPE pipe

For the water-filled MDPE pipe, Table 4.8 and Figure 4.11 show the measured acoustic signal amplitudes at the four circumferential locations around the pipe.

Table 4.8: Peak acoustic signal amplitudes for each circumferential location along the exposed (water-filled) MDPE pipe

Axial distance from acoustic transmitter (m)	Average peak acoustic amplitude at 0 degrees around pipe (V)	Average peak acoustic amplitude at 90 degrees around pipe (V)	Average peak acoustic amplitude at 180 degrees around pipe (V)	Average peak acoustic amplitude at 270 degrees around pipe (V)
0	1.08×10^{-4}	0.98×10^{-4}	1.03×10^{-4}	0.92×10^{-4}
2	1.55×10^{-4}	1.35×10^{-4}	1.20×10^{-4}	1.27×10^{-4}
4	1.10×10^{-4}	1.11×10^{-4}	1.00×10^{-4}	0.88×10^{-4}
6	1.02×10^{-4}	1.05×10^{-4}	1.02×10^{-4}	1.07×10^{-4}

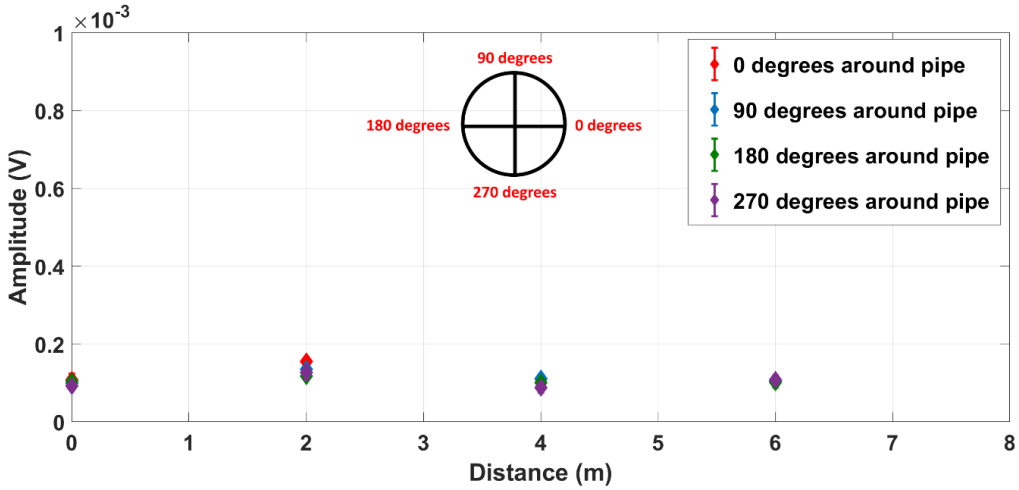

Figure 4.11: Acoustic amplitudes at the four circumferential locations and at increasing distances along the exposed (water-filled) MDPE pipe

Like Figure 4.8, Figure 4.11 also shows the acoustic amplitude closest to the transmitter (i.e., 0 m) to be lower than the acoustic amplitude at 2 m from the acoustic transmitter due to the non-axisymmetric nature of acoustic excitation along the pipe. Compared to Figure 4.8 however, the acoustic signal amplitudes in Figure 4.11 (0.088-0.155 mV) are lower than the amplitudes in Figure 4.8 (0.204-0.332 mV). This is interesting as it suggests additional acoustic energy loss from the pipe wall into the internal fluid medium. The numerical modelling results in Section 4.3.3 further discuss the validity of this finding.

For now, Figure 4.12 shows the relative amplitudes as well as attenuation of the acoustic signal along the water-filled pipe at 0 degrees around the pipe circumference and at increasing distances along the pipe.

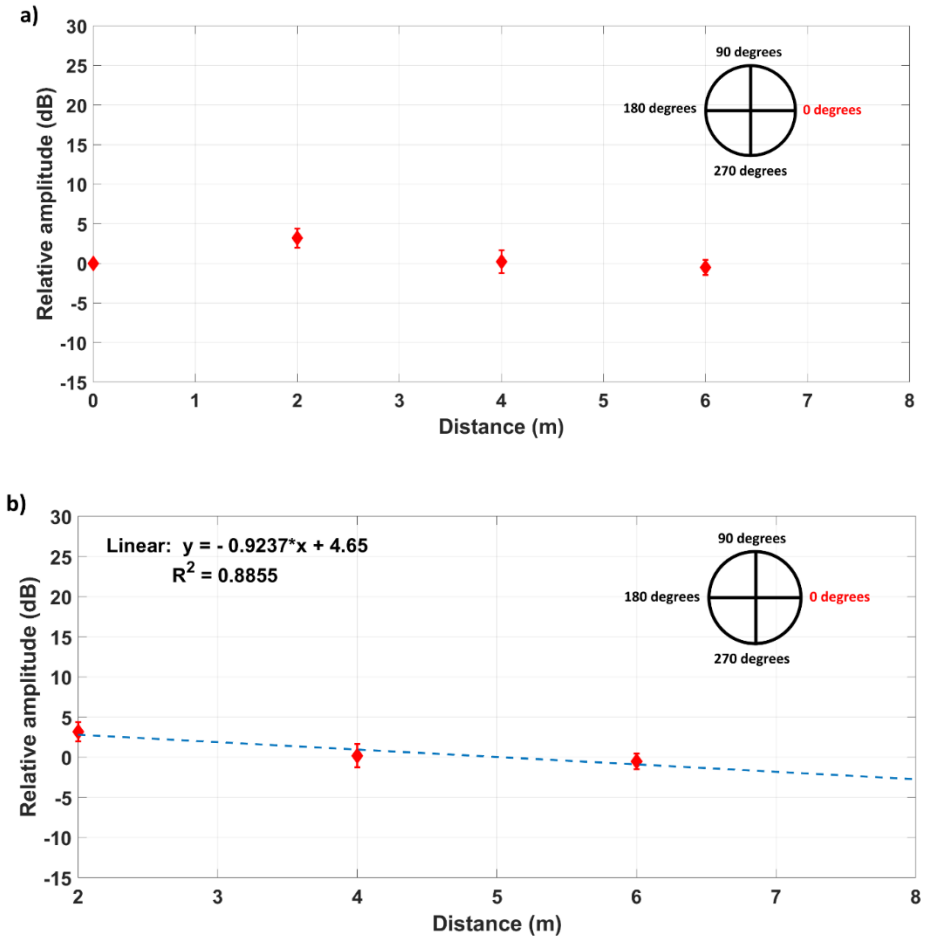

Figure 4.12: Relative acoustic amplitudes and b) attenuation of the acoustic signal along the exposed (water-filled) MDPE pipe at 0 degrees around the pipe and at increasing distances along the pipe

Like the empty pipe (Figure 4.9a), Figure 4.12a also implies the presence of near and far-field acoustic signal propagation along the water-filled pipe. As further shown in Figure 4.12b, far-field acoustic attenuation along the water-filled pipe at 0 degrees around the pipe circumference was calculated as 0.9 dB/m. For the other circumferential positions around the pipe, this estimate ranged between 0.3 and 0.9 dB/m as shown in Table 4.9.

Table 4.9: Experimental results for acoustic signal attenuation along the exposed (water-filled) MDPE pipe

Circumferential position of acoustic receivers	Measured acoustic attenuation (dB/m)
0 degrees	0.9
90 degrees	0.6
180 degrees	0.3
270 degrees	0.4
Average acoustic attenuation	0.6 ± 0.3 dB/m

Compared to acoustic attenuation along the empty pipe (0.5 ± 0.4 dB/m), average acoustic attenuation along the water-filled pipe is slightly higher but nonetheless suggests a minimal impact of the internal fluid medium on acoustic signal attenuation along the pipe. This also broadly agrees with the analytical model results in Figure 4.4 where acoustic attenuation along both empty and water-filled MDPE pipes are approximately the same (especially below 60 Hz).

To further validate the experimental results (for both the empty and water-filled pipes), the next section discusses numerical modelling results for acoustic attenuation along the exposed MDPE pipe.

4.3.3 Numerical model predictions for an exposed water pipe

Using the geometric and material properties of the exposed MDPE pipe and at 38 Hz acoustic excitation (to directly compare with the experiment results), Figures 4.13a, b and c show the time domain acoustic signals at selected distances along the pipe in response to acoustic excitation in the radial and circumferential directions (Figure 3.54 in Section 3.8.3.3). The 38 Hz period (0.026 s) is also shown in each plot.

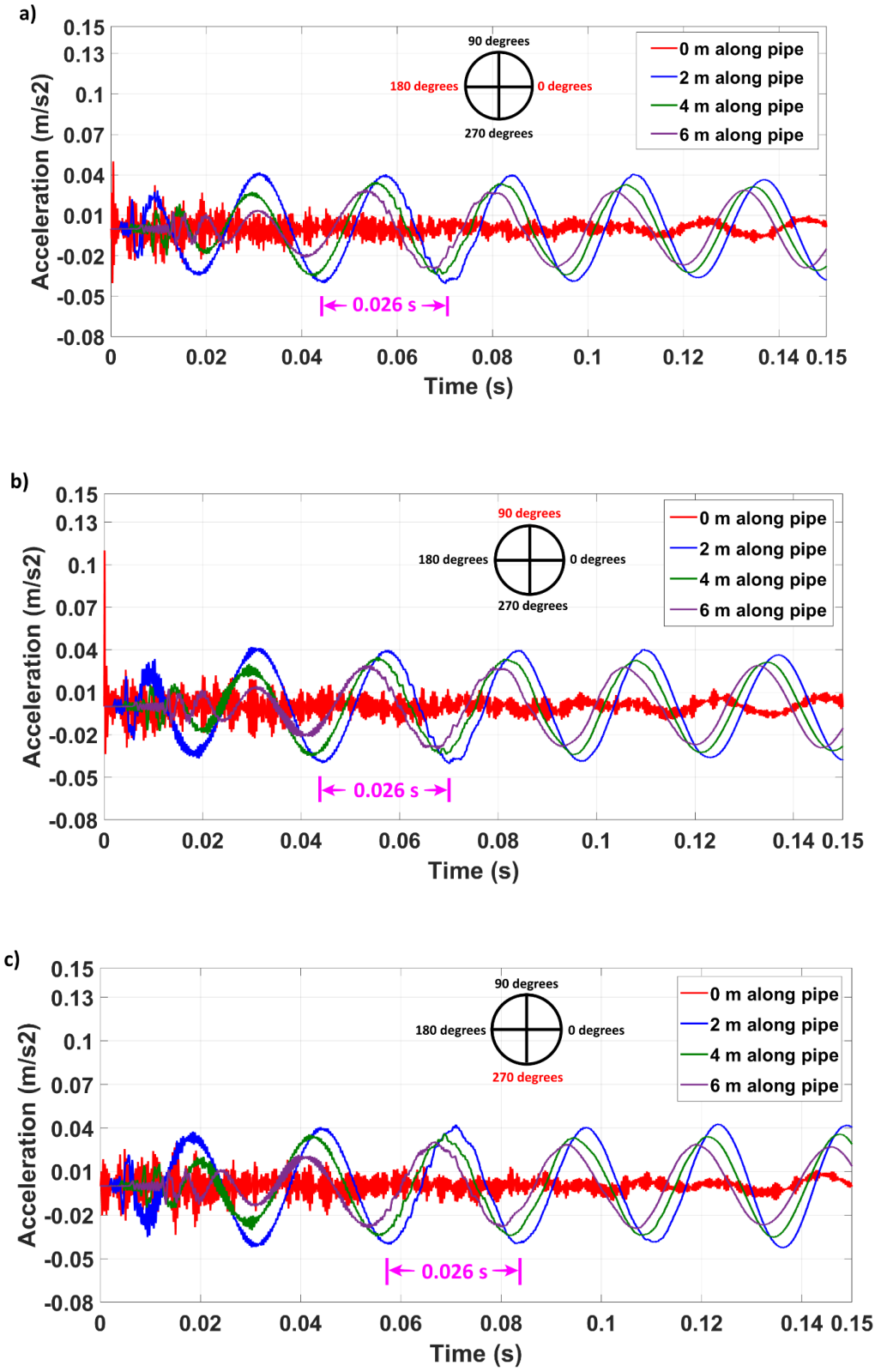

Figure 4.13: Time domain acoustic signals at increasing distances along the exposed MDPE pipe, for radial and circumferential excitation at 38 Hz and with acoustic receivers at a) 0 and 180, b) 90 and c) 270 degrees around the pipe

Figure 4.13 shows the predicted acoustic wave propagation profile along the exposed MDPE pipe, using the numerical model, for acoustic receivers placed at the same circumferential positions and at the same distances as with the experiments. The figures also show the acoustic signal at 0 m from the acoustic transmitter to be significantly weaker than the signals at increased distances along the pipe. This result agrees with the experimental findings regarding the significant presence of high frequency acoustic signals in the immediate vicinity (0-1 m) of the acoustic transmitter (i.e., the acoustic near-field) followed by their diminished presence at further distances along the pipe (where the low frequency, i.e., 38 Hz, acoustic signal dominates the acoustic wave profile).

Figure 4.14 shows the corresponding frequency domain signals of Figure 4.13.

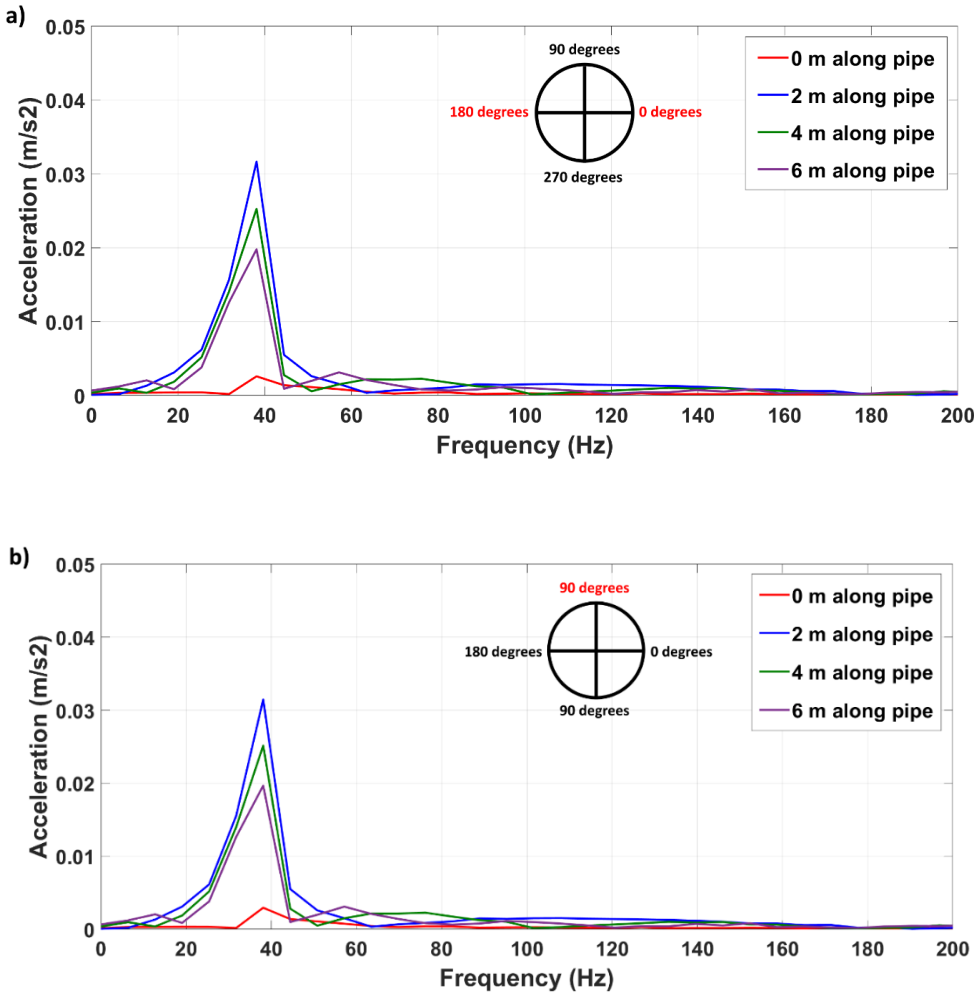

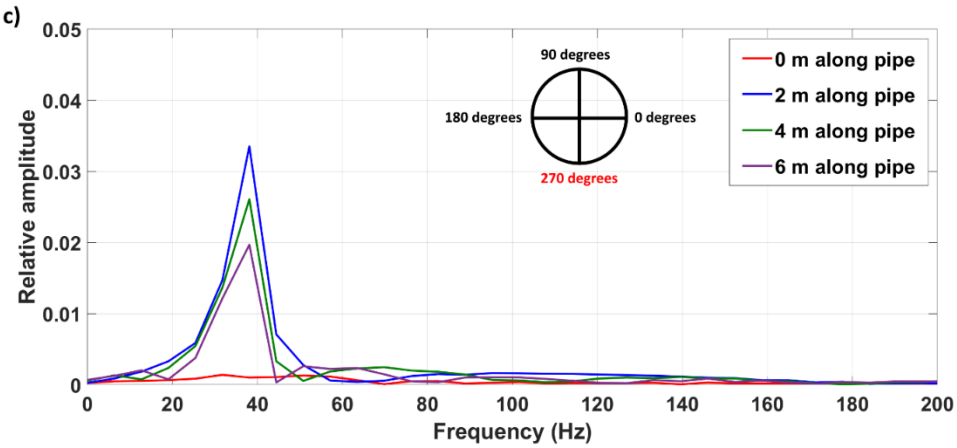

Figure 4.14: Frequency domain acoustic signals at increasing distances along the exposed MDPE pipe, due to radial and circumferential excitation at 38 Hz and for acoustic receivers at a) 0 and 180, b) 90 and c) 270 degrees around the pipe

As shown in Figure 4.14, the acoustic amplitudes are the same across all circumferential positions for each measurement distance, thus confirming the presence of axisymmetric longitudinal wave propagation along the pipe. This acoustic wave mode has been identified as the axisymmetric pipe wall dominated acoustic wave by Muggleton et al. (2002) and also as the longitudinal L(0,1) wave by Long et al. (2003). Figure 4.14 also confirms the weaker acoustic signal amplitude at 0 m, observed in Figure 4.13, compared to the other distances along the MDPE pipe. Using Equation (4.3), Figure 4.15 further shows the far-field acoustic attenuation at finer distance increments of 1 m along the pipe.

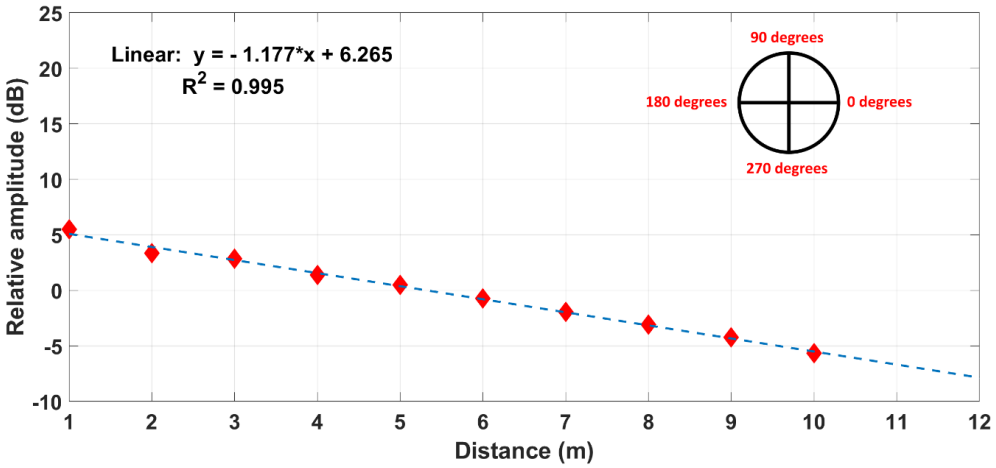

Figure 4.15: Acoustic attenuation at 38 Hz along exposed MDPE pipe, using numerical model, at the four circumferential locations around the pipe

From Figure 4.15, acoustic signal attenuation along the exposed MPDE pipe was calculated as 1.2 dB/m for all circumferential positions around the pipe. Compared to the analytical model prediction of 0.06 dB/m at the same frequency, the numerical model prediction is significantly higher. The reason for this discrepancy can be traced to a fundamental theoretical assumption of the analytical model where the pipe wall is modelled as a thin shell along which a one-dimensional acoustic wave propagates in the axial direction. Acoustic signal attenuation prediction with the analytical model is thus determined solely by the pipe wall material losses. The numerical model, on the other hand, considers the pipe wall as a three-dimensional acoustic propagation medium thereby combining the contribution of acoustic dispersion within the pipe wall, in addition to pipe wall material losses, to the overall acoustic signal attenuation prediction along the pipe.

For a water-filled pipe, Figures 4.16 and 4.17 show the acoustic amplitudes at the same distances used for the experiments as well as the acoustic attenuation (at 1 m distance increments) along the exposed MDPE pipe.

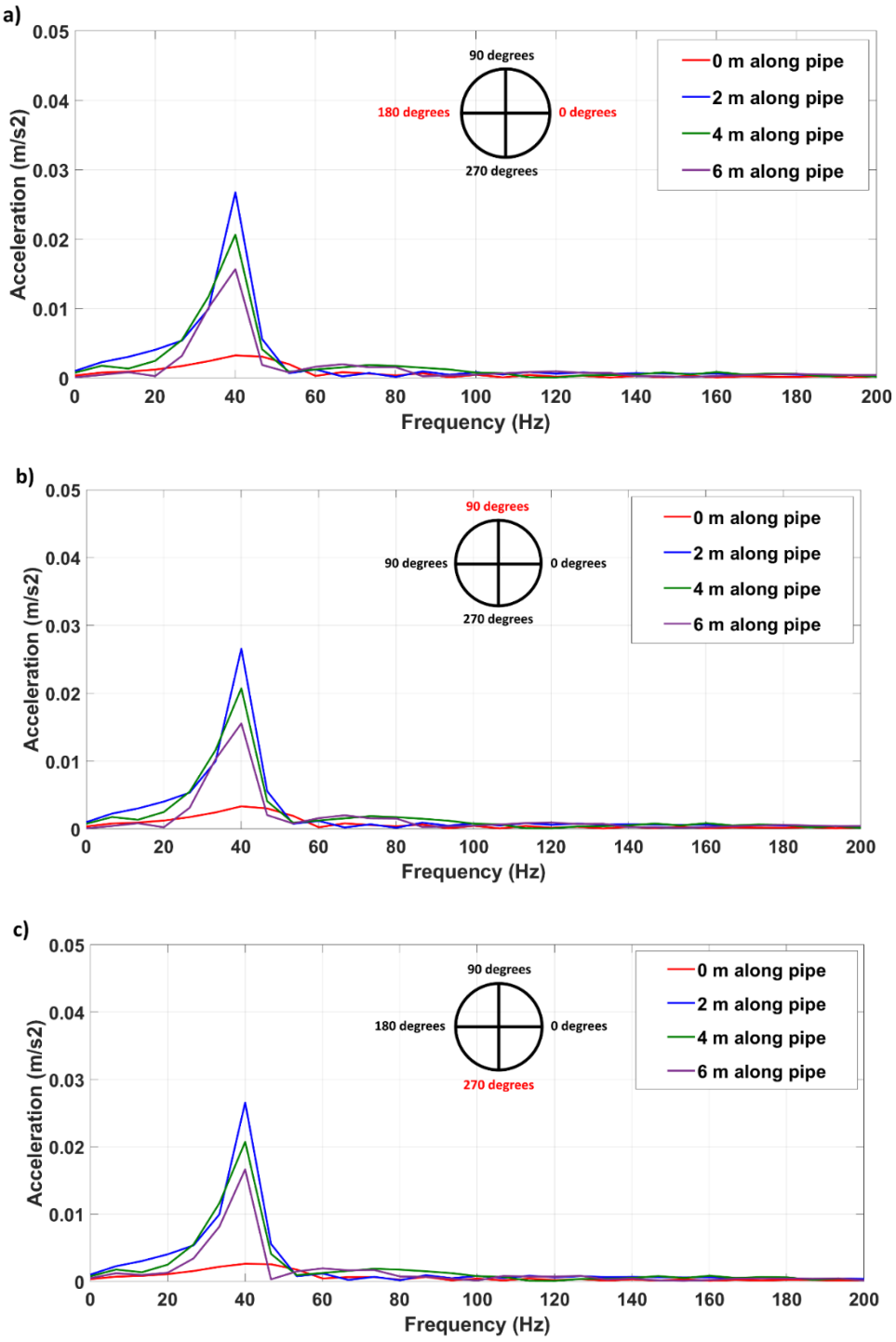

Figure 4.16: Frequency domain acoustic signals at increasing distances along the exposed (water-filled) MDPE pipe, with acoustic receivers at a) 0 and 180, b) 90 and c) 270 degrees around the pipe

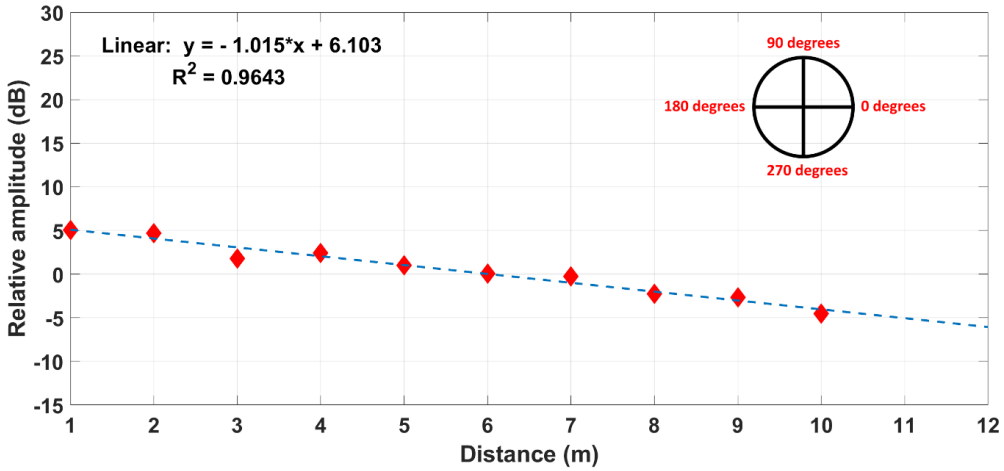

Figure 4.17: Acoustic attenuation at 38 Hz along exposed (water-filled) MDPE pipe, using numerical model, at the four circumferential locations around the pipe

Like Figure 4.14 the acoustic amplitudes are the same across the pipe circumferential positions for each axial distance along the pipe, also confirming the presence of axisymmetric longitudinal wave propagation along the water-filled pipe. Compared to Figure 4.14 however, the acoustic amplitudes at each axial distance along the water-filled pipe are less than the corresponding amplitudes along the empty pipe. This agrees with the experimental findings in Section 4.3.2, where some of the propagating acoustic energy was suspected to couple into the internal fluid medium of the water-filled pipe. A similar observation was made by Long et al. (2002) where, for a buried cast iron pipe, a separate acoustic wave was shown to propagate within the internal fluid medium of the pipe (in addition to the longitudinal acoustic wave along the pipe wall) due to external acoustic excitation of the pipe.

The numerically predicted pipe wall acoustic attenuation for the water-filled pipe was further calculated as 1 dB/m (Figure 4.17). This estimate is slightly less than the corresponding prediction for the empty pipe (1.2 dB/m) suggesting, like the analytical model, the influence of the internal fluid in increasing the pipe wall stiffness thus reducing acoustic attenuation along the pipe.

Like the analytical model, numerical predictions of acoustic attenuation along the exposed MDPE pipe is also frequency dependent as shown in Figure 4.18.

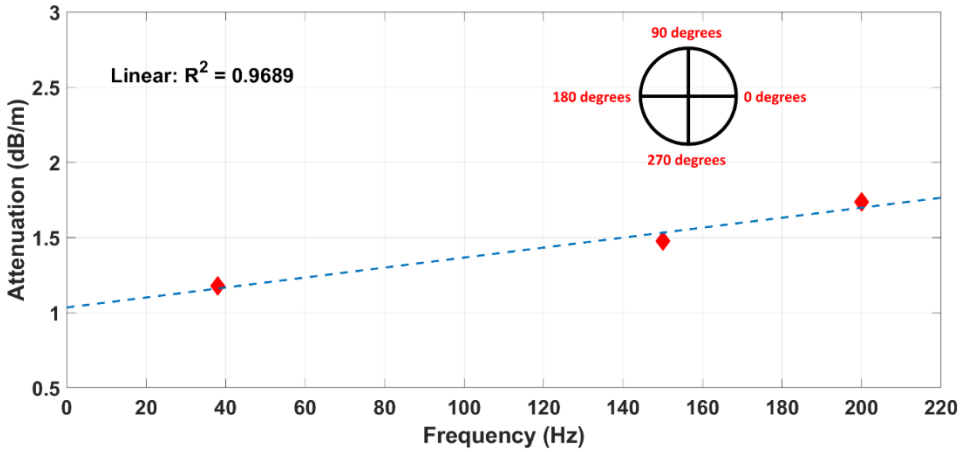

Figure 4.18: Numerical model predictions of acoustic attenuation vs excitation frequency along the exposed MDPE pipe

As shown in Figure 4.18, acoustic attenuation increases linearly along the exposed MDPE pipe with increasing acoustic excitation frequency along the pipe, agreeing with the analytical model prediction of Figure 4.3.

For the separate vibration motor orientations previously described in Section 3.8.3.3, Figures 4.19 and 4.20 show the relative acoustic amplitudes along the exposed MDPE pipe at 150 Hz acoustic excitation.

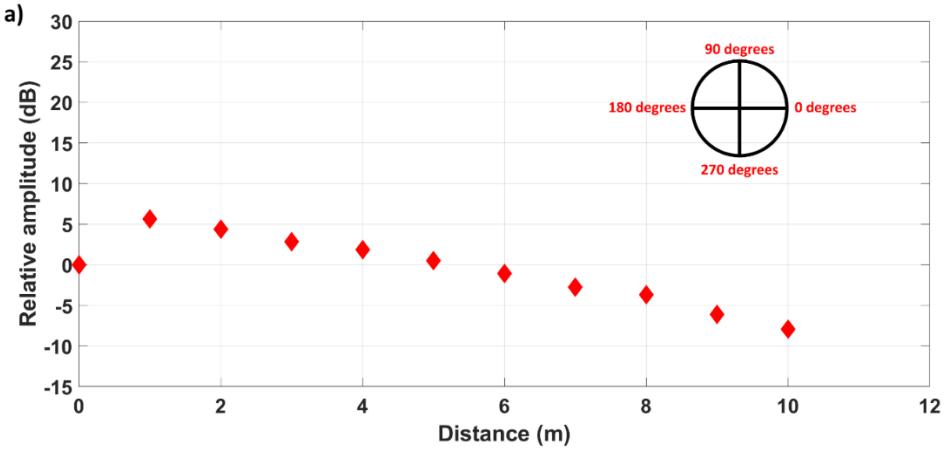

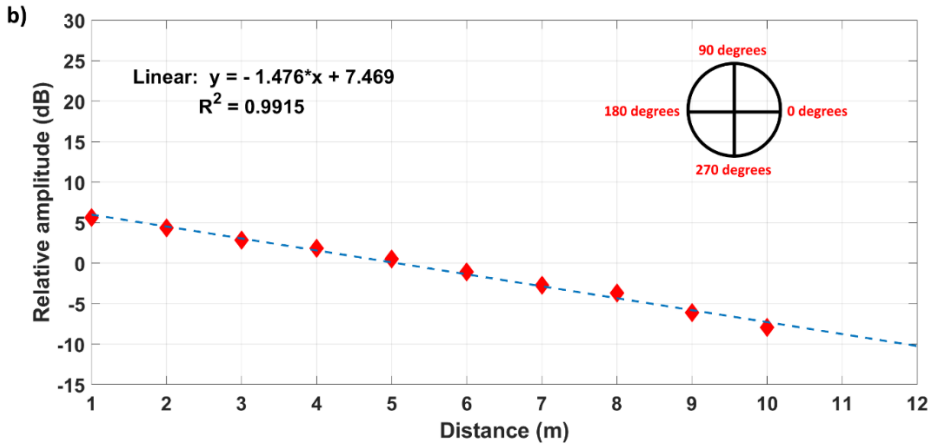

Figure 4.19: Relative acoustic amplitudes and b) acoustic attenuation at the four circumferential locations around the exposed MDPE pipe for 150 Hz acoustic excitation in the radial and circumferential directions

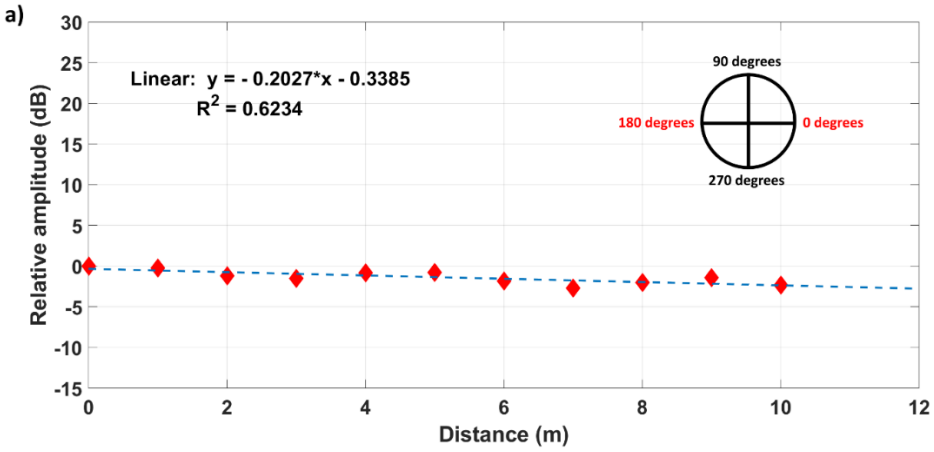

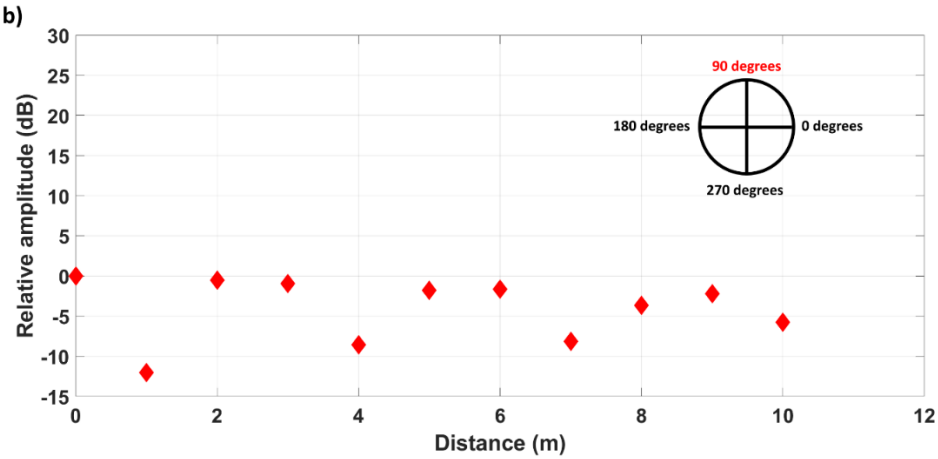

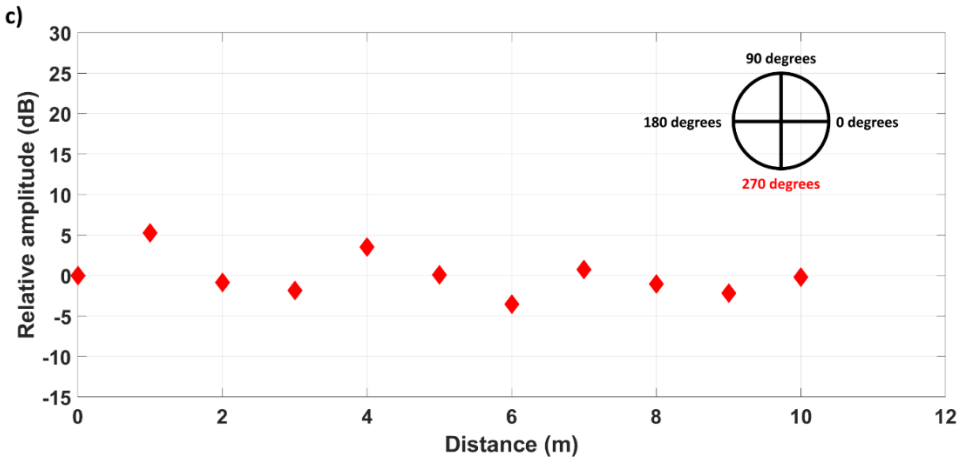

Figure 4.20: Relative acoustic amplitudes at 0 and 180 degrees, b) 90 degrees and c) 270 degrees around the exposed MDPE pipe for 150 Hz acoustic excitation in the radial and axial directions

From Figure 4.19, the relative acoustic amplitudes along the exposed MDPE pipe are the same at the four circumferential locations and with a constant attenuation of 1.5 dB/m at increasing distances along the pipe. This is not the case for the results in Figure 4.20 where acoustic excitation was in the radial and axial directions. In this case, the relative amplitudes at increasing distances along the pipe are particularly non-linear at 90 and 270 degrees around the pipe circumference. The acoustic attenuation (0.2 dB/m) is however relatively linear and predictable at 0 and 180 degrees closely matching the analytical model prediction of 0.18 dB/m at the same frequency. This close similarity can be explained by the axial component of the pipe excitation, which, in the case of the analytical model, is the sole acoustic excitation mechanism along the pipe. For the numerical model however, acoustic amplitude distribution at 90 and 270 degrees around the pipe is non-linear showing a pattern of peaks and throughs (indicative of coherent noise) which tend obscure the transmitted acoustic signal at increasing distances along the pipe. These results, interestingly, therefore show the strong presence of flexural acoustic wave propagation which is non-axisymmetric in nature (this is the F(1,0) acoustic wave mode identified, for example, by Wockel et al. (2015)) and the attenuation of which is relatively unpredictable compared to the longitudinal acoustic wave. Since acoustic

attenuation must be predictable to ensure data communication reliability along the pipe, a key finding from these results is the importance of orienting the vibration motor in such a way as to suppress this flexural acoustic wave propagation along the pipe as much as possible. As shown from the results in Figure 4.19 (as well as the method described in Section 3.8.3.3), this can be achieved by aligning the vibration motor with its shaft parallel to the pipe axis thus exciting the pipe in only the circumferential and radial directions.

Parametric analyses of acoustic signal attenuation along the exposed MDPE pipes using the numerical modelling results for radial and circumferential acoustic excitation of the pipe are further discussed. Like the analytical model, the base case for the parametric analyses are the geometric and material properties of the MDPE pipe in Table 3.6.

To examine the influence of pipe inner radius on acoustic attenuation, Table 4.10 summarises the numerically predicted acoustic attenuation for a range of pipe inner radii.

Table 4.10: Numerically predicted acoustic attenuation along exposed MDPE pipe with respect to change in pipe inner radius

Pipe inner radius (mm)	Acoustic attenuation (dB)
15.8	2.93
36.1	1.48
140.8	1.16

Unlike the analytical model prediction (Table 4.1), Table 4.10 shows that the numerically predicted acoustic signal attenuation along the exposed MDPE pipe decreases with increasing pipe inner radius. Numerical prediction of acoustic attenuation along the MDPE pipe is therefore sensitive to changes in the pipe inner radius. Using the MDPE pipe inner radius in Table 3.6 as a base value, accurate numerical prediction (to within 2 decimal places) of acoustic attenuation along the exposed MDPE pipe (based on a 0.01 dB/m change in acoustic attenuation

per mm change in pipe inner radius) would require a choice of pipe inner radius within $\pm 1\%$ of the base value of the MDPE pipe inner radius in Table 3.6.

For pipe wall thickness variation, Table 4.11 summarises the acoustic attenuation predictions for a range of pipe wall thicknesses.

Table 4.11: Numerically predicted acoustic attenuation along exposed MDPE pipe with respect to change in pipe wall thickness

Pipe wall thickness (mm)	Acoustic attenuation (dB)
9.2	1.48
14.0	1.69
17.0	1.88

From Table 4.11, acoustic attenuation increases with increasing pipe wall thickness thus showing that numerical prediction of acoustic attenuation along the MDPE pipe is sensitive to pipe wall thickness variation. Using the MDPE pipe wall thickness in Table 3.6 as a base value, accurate numerical prediction (to within 2 decimal places) of acoustic attenuation along the exposed MDPE pipe (based on a 0.05 dB/m change in acoustic attenuation per mm change in the pipe wall thickness) would require a choice of pipe wall thickness within $\pm 1\%$ of the base value of the MDPE pipe wall thickness in Table 3.6.

For changes in the pipe wall elastic modulus, Table 4.12 summarises the predicted acoustic attenuation along the exposed MDPE pipe.

Table 4.12: Numerically predicted acoustic attenuation along exposed MDPE pipe with respect to change in pipe wall elastic modulus

Pipe wall elastic modulus (N/m^2)	Acoustic attenuation (dB)
1.6×10^9	1.48
7.3×10^8	1.83
4.3×10^8	2.44

Like the analytical model prediction (Table 4.3), the numerically predicted acoustic attenuation along the exposed MDPE pipe increases with decreasing pipe wall elastic modulus. Using the MDPE pipe wall elastic modulus in Table 3.6 as a base value, accurate numerical prediction (to within 2 decimal places) of acoustic attenuation along the exposed MDPE pipe (based on a 67.4×10^{-11} dB/m change in acoustic attenuation per N/m^2 change in the pipe wall elastic modulus) would require a choice of pipe wall elastic modulus within $\pm 0.4\%$ of the base value of the MDPE pipe wall elastic modulus in Table 3.6.

For changes in the pipe wall Poisson's ratio, Table 4.13 summarises the numerically predicted acoustic attenuation's sensitivity to the pipe wall Poisson's ratio.

Table 4.13: Numerically predicted acoustic attenuation along exposed MDPE pipe with respect to change in pipe wall Poisson's ratio

Pipe wall Poisson's ratio	Acoustic attenuation (dB)
0.16	1.38
0.25	1.39
0.40	1.48

Again, unlike the analytical model results which predicted constant acoustic signal attenuation with respect to change in Poisson's ratio, the numerical model predicted increasing acoustic signal attenuation with increasing pipe wall Poisson's ratio. Using the MDPE pipe wall Poisson's ratio in Table 3.6 as a base value, accurate numerical prediction (to within 2 decimal places) of acoustic attenuation along the exposed MDPE pipe (based on a 0.42 dB/m change in acoustic attenuation per unit change in the pipe wall Poisson's ratio) would require a choice of pipe wall Poisson's ratio within $\pm 0.2\%$ of the base value of the MDPE pipe wall Poisson's ratio in Table 3.6.

Following the treatment of acoustic signal attenuation along an exposed MDPE pipe, the next section presents and discusses analytical and numerical modelling results, in addition to results obtained from field trials, for acoustic attenuation along buried water pipes.

4.4 ACOUSTIC SIGNAL ATTENUATION ALONG A BURIED WATER PIPE

4.4.1 Analytical model predictions for a buried water pipe

In Section 3.8.1.2, it was shown that the attenuation of an acoustic wave along a buried pipe depends the properties of the surrounding soil within which the pipe is buried, particularly the real and imaginary parts of the soil acoustic wave impedance (which in turn depend on a knowledge of the bulk and shear acoustic wave speeds within the soil). In the same section, soil classification tests performed during the communication system field trials showed the soil surrounding the buried pipes to be either well or poorly graded SAND (SP or SW). To determine the acoustic wave speeds in these soils, reference is made to Oelze et al. (2002). In the work, the authors described extensive (a total of 231) experimental evaluations of the acoustic bulk wave speed in six different soil types, as a function of soil moisture content and compaction level. The soil types were specifically chosen to represent a wide range of soil properties expected to influence acoustic wave speed within a soil medium. The soil samples examined by Oelze et al. (2002), closest in particle size distribution to those obtained from the field trials described in Section 3.8.2.2, are summarised in Table 4.14.

Table 4.14: Soil classification results from Oelze et al. (2002)

Soil series	Sample depth (m)	% Sand	% Silt	% Clay
Adrian	0 – 0.2	72	18	10
Plainfield	0 – 0.2	97	1	2

Using 41 different experimental combinations, the soil samples in Oezle et al. (2002) were further prepared for acoustic experiments according to their nominal moisture content, ranging from “air-dry” to “fully saturated”, and compaction levels, classified as either “loose” or

"compact". Results of the acoustic experiments were subsequently presented according to the mean bulk density, mean gravimetric water content, mean porosity, and mean acoustic wave speed for each soil type tested. These results, for the two representative soil samples in Table 4.14, are shown in Table 4.15.

Table 4.15: Soil sample results from Oelze et al. (2002)

Soil series	Mean bulk density (kg/m^3)	Mean gravimetric water content (%)	Mean porosity	Mean Acoustic wave speed (m/s)
Adrian	830	15.9	0.2	89
Plainfield	1450	9.1	0.3	138

As shown Table 4.15, the acoustic wave speeds for Adrian and Plainfield soils were reported by Oelze et al. (2002) as 89 and 138 m/s respectively. Acoustic wave speed can be further expressed in terms of the soil density as (Santamarina, 2001; Head & Jardine, 1992)

$$V_b = \sqrt{\frac{K}{\rho}} \tag{4.4}$$

$$V_s = \sqrt{\frac{G}{\rho}} \tag{4.5}$$

Where V_b (m/s) and V_s (m/s) are the bulk and shear acoustic wave speeds in the surrounding soil, ρ (Kg/m^3) is the density of the surrounding soil and K (N/m^2) and G (N/m^2) are the bulk and shear moduli of the surrounding soil. For the Adrian and Plainfield soils, since the bulk and shear acoustic wave speeds were replaced by mean acoustic wave speeds of 89 and 138 m/s respectively the bulk and shear moduli for a given soil density would be the same.

For the buried steel pipe with material properties in Table 3.7 and surrounding soil properties in Table 3.9, the bulk and shear moduli, using 89 m/s acoustic wave speed, were both calculated as 1.3×10^7 N/m^2. Using the other acoustic wave speed of 138 m/s, the bulk and shear moduli of the soil surrounding the buried steel pipe were calculated as 3.2×10^7 N/m^2. Using this

information, Figure 4.21 shows the predicted acoustic attenuation (for soil acoustic wave speeds of 89 and 138 m/s) along the buried steel pipe, with respect to increasing acoustic excitation frequency.

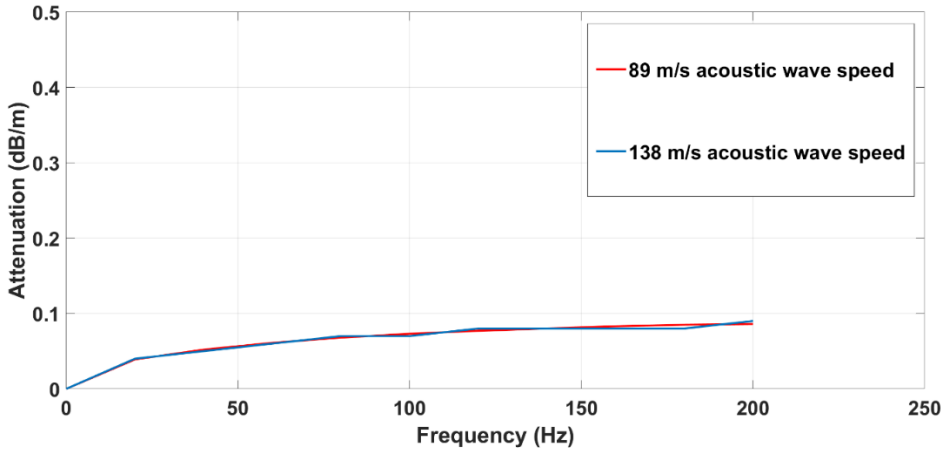

Figure 4.21: Analytical predictions of acoustic attenuation along the buried steel pipes (using acoustic wave speeds of 89 and 138 m/s)

Figure 4.21 shows the analytically predicted acoustic attenuation along the buried steel pipe to be approximately the same for both acoustic wave speeds. This is most likely due to the assumption of a mean soil acoustic wave speeds as opposed separate bulk and shear acoustic wave speeds. Results of acoustic signal attenuation using separate bulk and shear acoustic wave speeds within the soil will be presented later in this section. Another observation from Figure 4.21 is the initially sharp increase in acoustic attenuation, at lower acoustic excitation frequencies (< 50 Hz), before a more gradual increase in acoustic attenuation at increasing acoustic excitation frequencies. As noted in Muggleton et al. (2002), pipe wall losses dominate the analytical prediction of acoustic attenuation along a buried pipe at lower acoustic excitation frequencies while radiation losses dominate acoustic attenuation at higher frequencies. Figure 4.21 therefore suggests that, at relatively higher acoustic excitation frequencies, acoustic energy radiation from the buried steel pipe into the surrounding soil is almost constant regardless of the acoustic excitation frequency.

For the buried MDPE pipe in Trench 1 (and with the surrounding soil properties listed in Table 3.11), Figure 4.22a shows the predicted acoustic attenuation along the pipe (for acoustic wave speeds of 89 and 138 m/s) while Figure 4.22b shows the predicted acoustic attenuation along the buried MDPE pipe in Trench 2 (using the soil properties in Table 3.13) at increasing acoustic excitation frequencies.

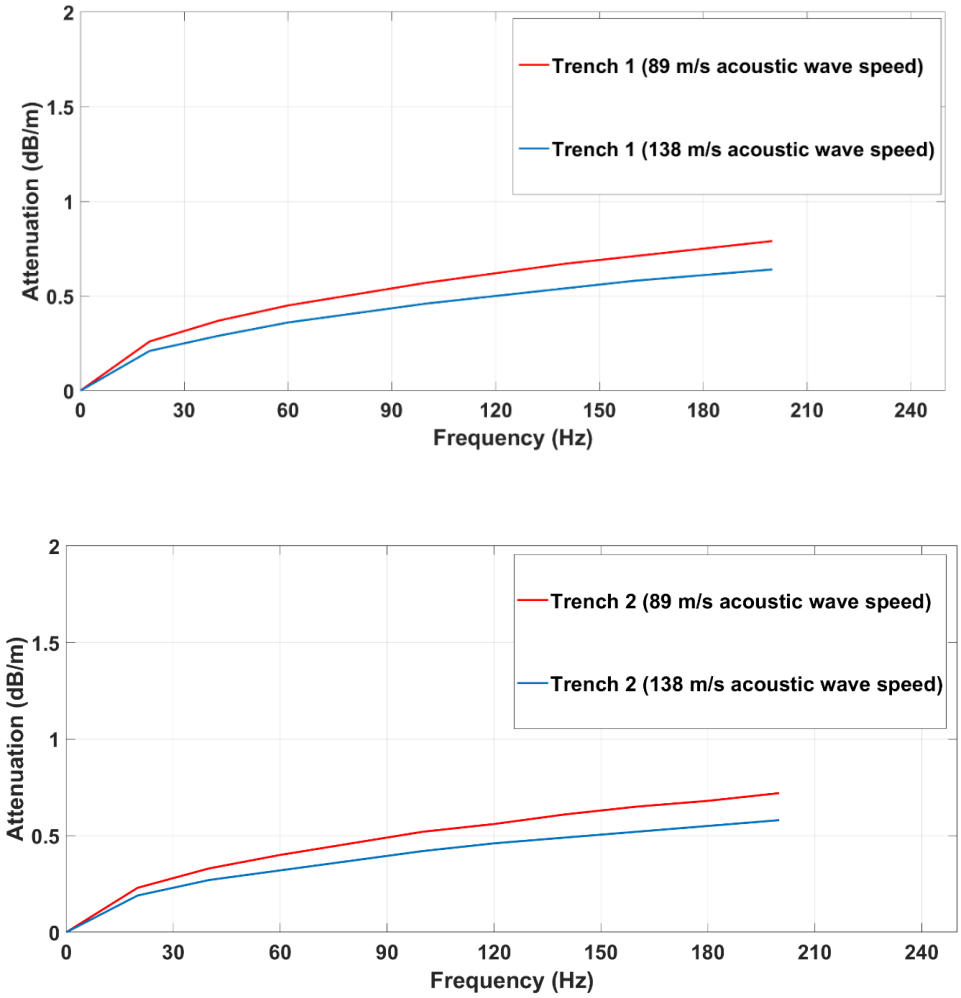

Figure 4.22: Analytical predictions of acoustic attenuation along the buried MDPE pipe (using acoustic wave speeds of 89 and 138 m/s) in a) Trench 1 and b) Trench 2

Figure 4.22 like the exposed MDPE pipe in Figure 4.4, shows increasing acoustic attenuation with increasing acoustic excitation frequency along both pipes in Trenches 1 and 2. Compared to Figure 4.21 however, acoustic attenuation along the buried MDPE pipe is not only greater but also steadily increases with increasing acoustic excitation frequency. Acoustic energy

radiation into the surrounding soil is therefore significantly higher for the buried MDPE pipe (as well as constantly increasing with increasing acoustic excitation frequency) compared to the buried steel pipe.

The higher acoustic attenuation along the buried MDPE compared to the buried steel pipe is understandable considering the specific acoustic impedances of the buried steel and MDPE pipes as well as the surrounding soil which can be expressed as (Santamarina, 2001)

$$Z = \rho c \tag{4.6}$$

Where Z (Pa·s/m) is the specific acoustic impedance of the pipe or soil, ρ (Kg/m^3) is pipe/soil density and c (m/s) is the pipe/soil acoustic wave speed. Using Equation (4.6), the specific acoustic impedances of the buried steel and MDPE pipes are as 4.6×10^7 Pa·s/m and 1.3×10^6 Pa·s/m. Using a soil sample from Table 4.15 (e.g., the "Plainfield" soil sample described by Oezle et al. (2002)), the acoustic impedance of this soil sample was calculated as 2.0×10^5 Pa·s/m. Comparing the acoustic impedance of the soil to each pipe, the acoustic impedance of the MDPE pipe is closer to the soil acoustic impedance (although still higher by a factor of 10) than the acoustic impedance of the steel pipe is to the same soil (which is higher by a factor of 100). Due to a closer acoustic impedance match with the soil, acoustic radiation from the buried MDPE pipe into the soil will therefore be higher than acoustic radiation from the buried steel pipe into the same soil since more acoustic energy will be coupled between the buried MDPE pipe and soil.

Another observation from Figure 4.22 is the reduced acoustic attenuation for both trenches when a higher acoustic wave speed was employed for the analytical computations. Since a higher acoustic wave speed is indicative of higher bulk and shear moduli (Equations 4.4 and 4.5), the results in Figure 4.22 suggest a lower acoustic attenuation for surrounding soil with

higher bulk and shear moduli. Like the case of the water-filled pipe (Figure 4.4) compared to an empty pipe, the surrounding soil stiffens the pipe wall which reduces acoustic wave number along the pipe thus lowering the predicted acoustic attenuation along the buried pipe. A closer observation of Figure 4.22 also shows that the acoustic attenuation prediction for Trench 2 is lower than that of Trench 1. From Tables 3.11 and 3.13, the average soil bulk density measured for Trench 2 (2123 kg/m^3) was greater than the average soil density of Trench 1 (1730 kg/m^3). The results of Figure 4.22 therefore also suggest that a more compact soil reduces acoustic attenuation along the buried MDPE pipe which is understandable as an increased surrounding soil density also stiffens the pipe wall which in turn reduces acoustic signal attenuation along the pipe.

The analytical model predictions so far have assumed equal bulk and shear acoustic wave speeds within the surrounding soil of the buried pipe. According to Equations (4.4) and (4.5), these values depend on the bulk and shear moduli of the soil. Extensive investigation into the determination of these properties for sandy soils can be found in the literature (e.g., Seed et al., 1986; Hardin & Drnevich, 1972; Silver & Seed, 1971; Richart et al., 1962). These experiments however showed that determination of the shear modulus of a given soil sample, for example, depends on the knowledge of the void ratio of the sample, the strain amplitude of motions within the soil sample as well as the confining pressure on the soil sample (which is not a trivial exercise). Typical values of in-situ separate bulk and shear acoustic wave speeds for loose, medium, and dense unsaturated sand can however be found in Head & Jardine (1992) and are summarized in Table 4.16.

Table 4.16: Typical values for in-situ bulk and shear acoustic wave speeds (Head & Jardine, 1992)

Soil material	In-situ acoustic bulk wave speed (m/s)	In-situ acoustic shear wave speed (m/s)
Loose unsaturated sand	185 - 450	100 - 250
Medium unsaturated sand	325 - 650	200 - 350
Dense unsaturated sand	550 - 1300	350 - 700

Using the average acoustic bulk and shear wave speeds for loose, medium, and dense unsaturated sand while focusing on the buried MDPE pipes, Figures 4.23a and b show the acoustic attenuation predictions for the buried MDPE pipes in Trenches 1 and 2.

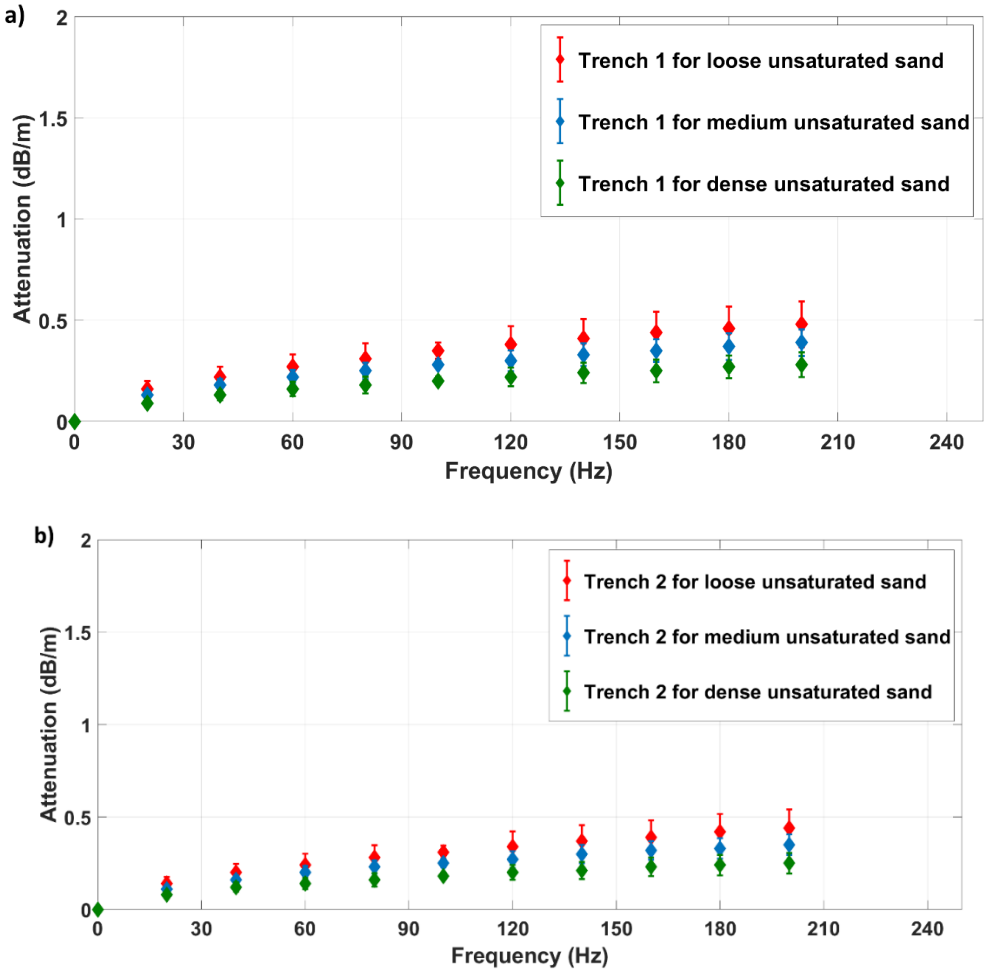

Figure 4.23: Analytical predictions of acoustic attenuation along the buried MDPE pipe (using acoustic separate bulk and shear acoustic wave speeds) in a) Trench 1 and b) Trench 2

Figures 4.23a and b show the acoustic attenuation predictions for the buried MDPE pipe in Trenches 1 and 2 for separate bulk and shear acoustic wave speeds (the error bars in the figure indicate the predicted attenuation at maximum and minimum acoustic wave speeds for each soil type). For both trenches, the average attenuation is even less than the predictions in Figure 4.22 since the average bulk or shear acoustic wave speeds for each soil type in Table 4.15 is higher than 138 m/s. Figures 4.23a and b also show, individually, the reduction of acoustic signal attenuation along the pipe with increasing soil compaction (i.e., from loose to dense unsaturated sand). To compare with these analytical model predictions, the next section further presents the results of field trials which examined acoustic signal attenuation along buried steel and MDPE pipes.

4.4.2 Results of field trials along buried water pipes

Results of field trials examining acoustic signal attenuation along the buried water pipes are presented in this section. For the buried steel pipe in Figure 3.39 of Section 3.7, Figures 4.24a and b show the measured acoustic amplitudes along the pipe as detected by the MFC sensors 1 and 2 m away from the ERM vibration motor during repeated acoustic transmissions.

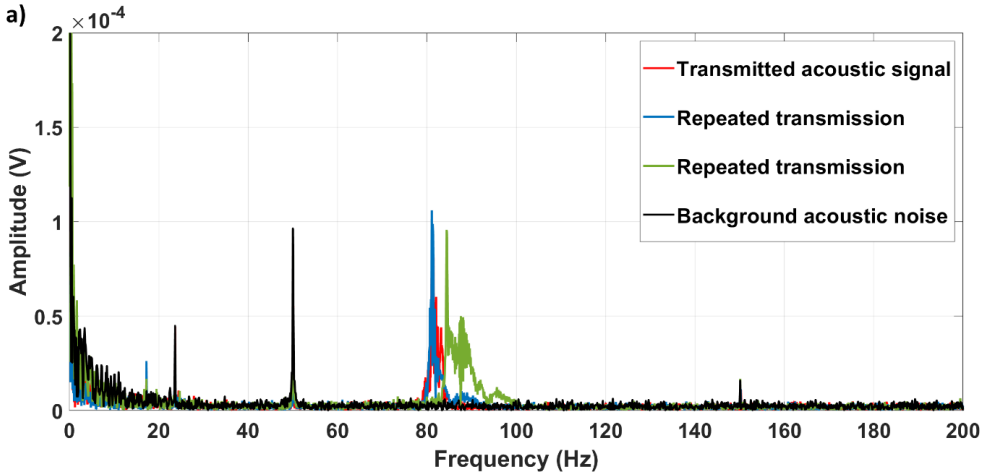

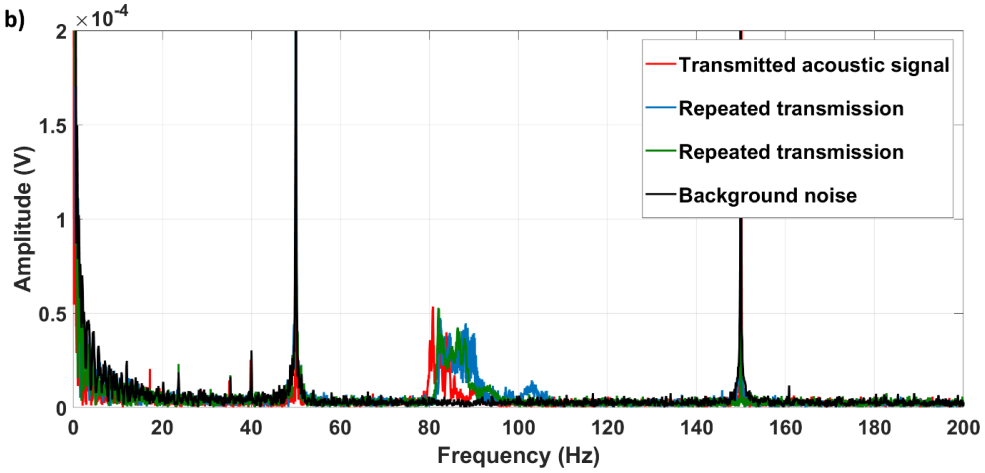

Figure 4.24: Acoustic signals detected along the buried steel pipe at a) 1 m and b) 2 m

From Figure 4.24, the average peak acoustic amplitudes (during acoustic excitation) recorded at each sensor are further summarised in Table 4.17.

Table 4.17: Measured acoustic signal amplitudes along the buried steel pipe

Distance (m)	Average amplitude (V)	Standard deviation (V)
1	1.0×10^{-4}	5.5×10^{-6}
2	0.5×10^{-4}	3.8×10^{-6}

The relative acoustic amplitude between both sensors, from Table 4.17 and using Equation (4.3), was calculated as -5.8 dB. Using the sensor spacing (i.e., 1 m), acoustic attenuation along the buried steel pipe was subsequently calculated as 5.8 dB/m. The analytical model, on the other hand, predicts acoustic signal attenuation along the buried steel pipe (using the acoustic wave speeds in Tables 4.15 and 4.16) according to Table 4.18.

Table 4.18: Analytical predictions of acoustic signal attenuation at 80 Hz along the buried steel pipe

Mean bulk acoustic wave speed (m/s)	Mean shear acoustic wave speed (m/s)	Predicted acoustic attenuation (dB/m)
89.0	89.0	0.07
138.0	138.0	0.06
317.5	175.0	0.04
487.5	275.0	0.03
925.0	525.0	0.02

From Table 4.18, acoustic attenuation prediction along the buried steel pipe is between 0.02 and 0.07 dB/m which is significantly less than the experimental measurement of 5.8 dB/m. It is however worth mentioning that in addition to the limited number of acoustic measurement points along the buried steel pipe, the presence of a valve connection along the pipe (Figure 3.39) also introduced pipe wall discontinuities which presented an avenue for acoustic wave scattering along the pipe and likely contributing to the higher acoustic wave attenuation measurement.

For the buried MDPE pipe, the acoustic signal attenuation experiments were only conducted in Trench 2 due to the unfortunate tampering with the sensor cabling in the other trench by the site contractors during soil backfilling. Figures 4.25a and b show the measured acoustic signal amplitudes along the pipe, using the MFC sensors 3.0 and 5.6 m away from the ERM vibration motor during repeated acoustic transmissions.

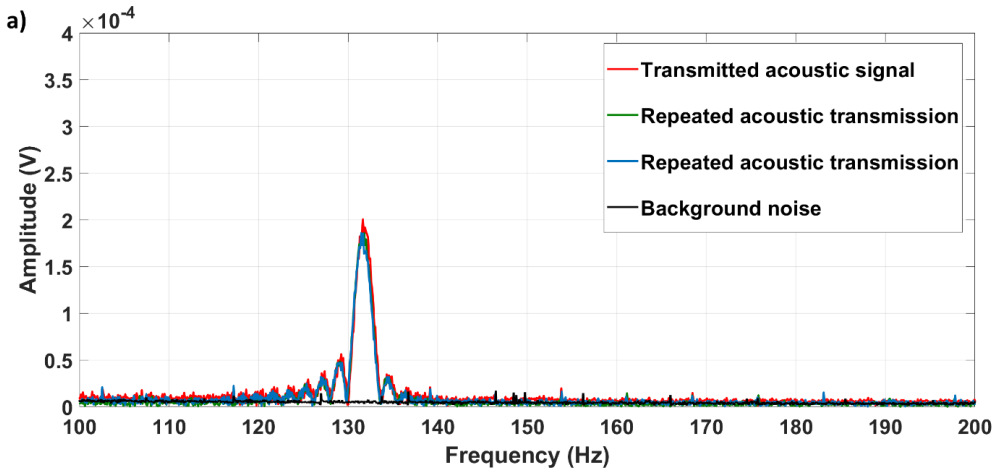

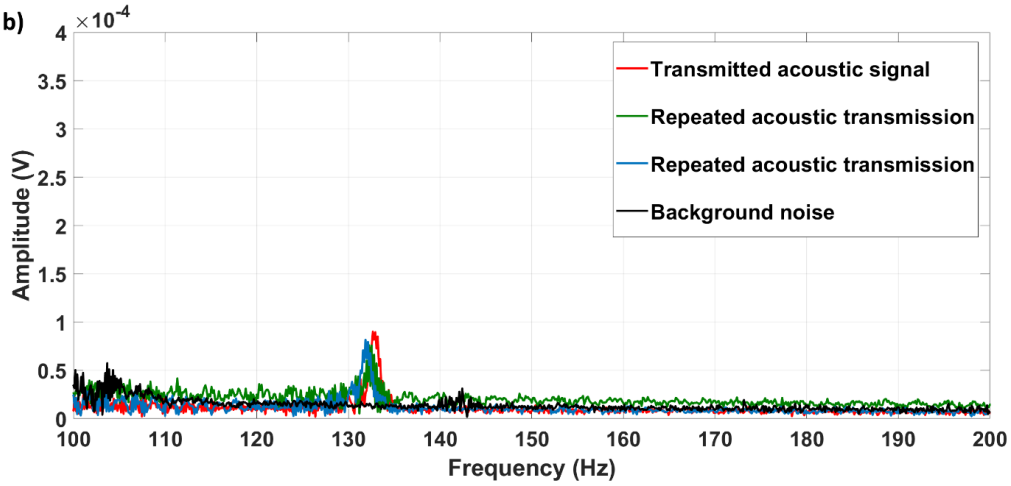

Figure 4.25: Acoustic signals along the buried MDPE pipe at a) 3 m and b) 5.6 m

From Figure 4.25, the average peak acoustic amplitudes recorded at each sensor during acoustic excitation along of buried MDPE pipe are further summarised in Table 4.19.

Table 4.19: Measured acoustic signal amplitudes along the buried MDPE pipe

Distance (m)	Average amplitude (V)	Standard deviation (V)
3.0	1.9×10^{-4}	7.3×10^{-6}
5.6	0.8×10^{-4}	7.1×10^{-6}

From Table 4.19 and using Equation (4.3), the relative acoustic amplitude between both sensors was calculated as -7.5 dB. With the sensor spacing of 2.6 m, acoustic attenuation along the buried MDPE pipe was therefore calculated as 2.9 dB/m. With the analytical model on the other hand, Table 4.20 summarises the acoustic attenuation predictions using the soil acoustic wave speeds in Tables 4.15 and 4.16.

Table 4.20: Analytical predictions of acoustic signal attenuation at 130 Hz along the buried MDPE pipe

Mean bulk acoustic wave speed (m/s)	Mean shear acoustic wave speed (m/s)	Predicted acoustic attenuation (dB/m)
89.0	89.0	0.6
138.0	138.0	0.5
317.5	175.0	0.4
487.5	275.0	0.3
925.0	525.0	0.2

The acoustic attenuation predictions in Table 4.20 are, as expected, higher than the predictions for the buried steel pipe due to a closer acoustic impedance match between the buried MDPE pipe and soil compared to the buried steel pipe and soil. The analytically derived acoustic attenuation predictions (0.2-0.6 dB/m) for the buried MDPE pipe are also significantly less than the experimentally derived acoustic attenuation (i.e., 2.9 dB/m) along the buried MDPE pipe. A likely reason for this discrepancy is the limited prediction accuracy of the analytical model which as previously stated in Section 3.8.3, assumes a centralised acoustic source within the pipe which was not the case for the field trials. The next section further presents numerical modelling results for acoustic attenuation along buried steel and MDPE pipes during non-axisymmetric excitation of the pipes.

4.4.3 Numerical model predictions for a buried water pipe

The numerical modelling results presented in this section, focus on the buried steel pipe as well as the buried MDPE pipe in Trench 2. As previously described in Section 3.8.3.4, the surrounding soil medium of the buried pipe model was acoustic in nature thus supporting only bulk acoustic wave propagation. To generate the numerical modelling results, the average bulk acoustic wave speeds in Table 4.15 for each soil type listed in the table was employed for the FEA by calculating their corresponding bulk moduli (as shown in Tables 4.21 and 4.22) before inputting these values into the FEA model.

Table 4.21: Bulk moduli of the soil surrounding the buried steel pipe in the numerical model

Soil type	Average bulk acoustic wave speed (m/s)	Bulk modulus (N/m^2)
Loose unsaturated sand	317.5	1.7×10^8
Medium unsaturated sand	487.5	4.0×10^8
Dense unsaturated sand	925.0	1.4×10^9

Table 4.22: Bulk moduli of the soil surrounding the buried MDPE pipe in Trench 2 in the numerical model

Soil type	Average bulk acoustic wave speed (m/s)	Bulk modulus (N/m^2)
Loose unsaturated sand	317.5	2.1×10^8
Medium unsaturated sand	487.5	5.0×10^8
Dense unsaturated sand	925.0	1.8×10^9

Using the bulk moduli in Tables 4.21 and 4.22, Figures 4.26a and b show the numerically predicted acoustic signal attenuation along the buried steel and MDPE pipes (at 80 and 130 Hz acoustic excitation respectively) for loose, medium and dense unsaturated sand.

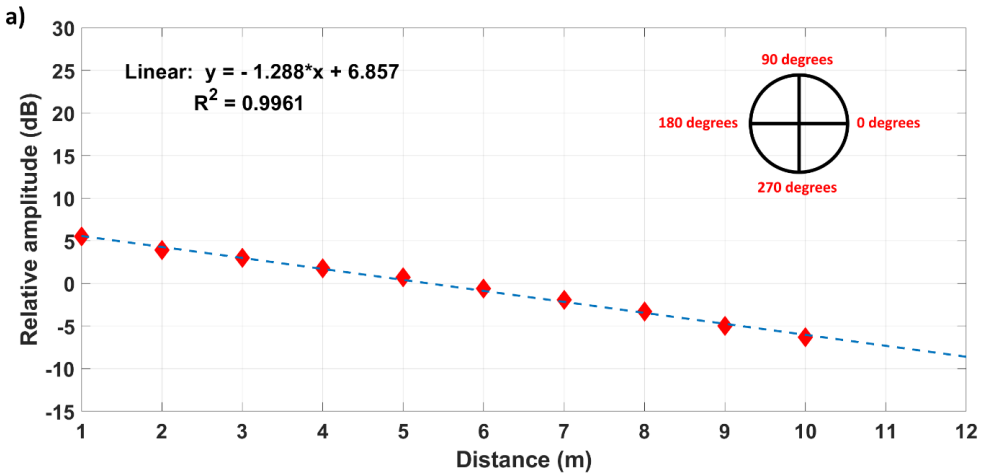

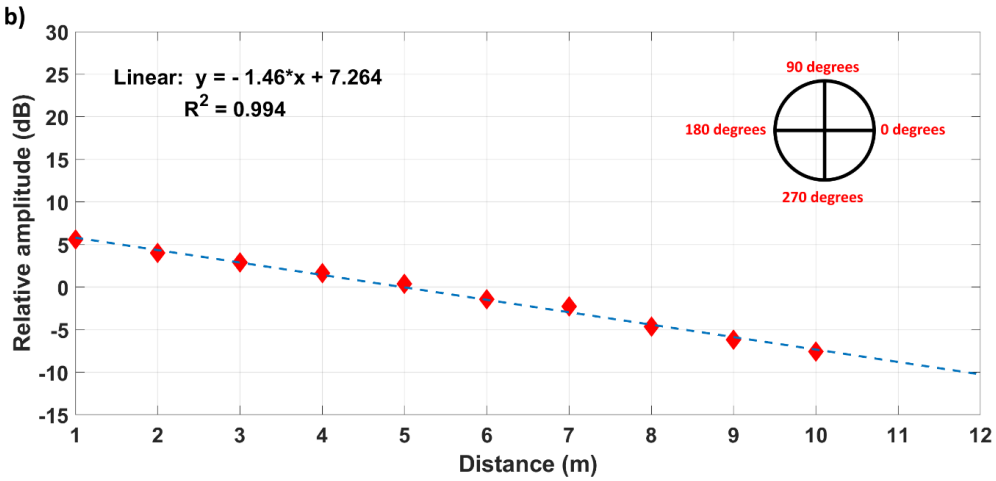

Figure 4.26: Numerical predictions of acoustic attenuation along a) buried steel pipe (acoustic excitation at 80 Hz) and b) buried MDPE pipe (acoustic excitation at 130 Hz)

Figure 4.26 shows that regardless of the surrounding soil type (i.e., loose, medium, or dense unsaturated sand), acoustic attenuation along the buried steel or MDPE pipe is the same. The numerical modelling results therefore suggest that the influence of acoustic signal dispersion along the pipe wall significantly outweighs any contribution of the surrounding soil stiffness on acoustic attenuation along the buried water pipe. For the buried steel pipe, Figure 4.26a shows a significantly higher acoustic attenuation prediction (1.3 dB/m) by the numerical model compared to the corresponding analytical model prediction of 0.02-0.07 dB/m. Like the exposed pipes, this difference in results can be attributed to the contribution of acoustic dispersion along the pipe wall (due to the non-axisymmetric pipe excitation) to the overall acoustic signal attenuation along the pipe. For the same reasons, the numerically predicted acoustic attenuation along the buried MDPE pipe (1.5 dB/m) is significantly greater than the analytically predicted values of 0.2-0.6 dB/m.

Compared to the results from the field trials, the numerical prediction of acoustic attenuation along the buried MDPE pipe is still significantly lower than the measured acoustic attenuation (2.9 dB/m) along the buried MDPE pipe. As described in Section 3.8.3.4, a shorter pipe length (6 m) was also designed in the numerical model to directly compare its acoustic attenuation

predictions with the results from the field trials. Figure 4.27 shows the numerically predicted acoustic attenuation for the 6 m length buried MDPE pipe.

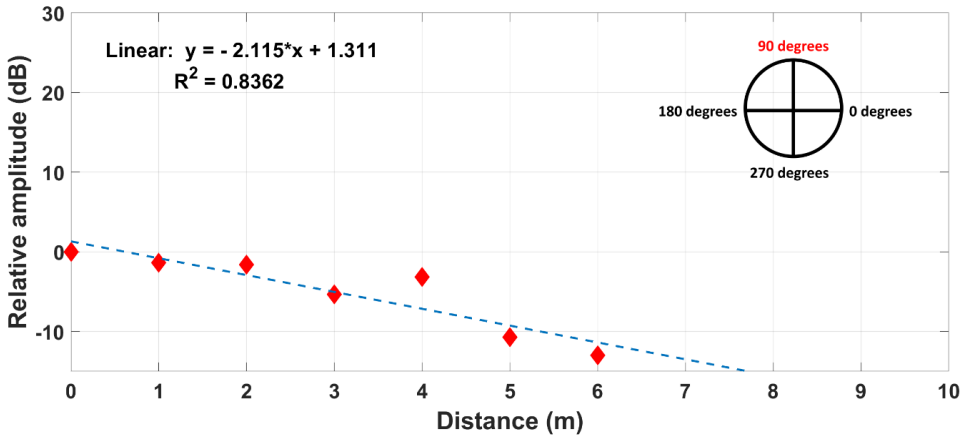

Figure 4.27: Numerical prediction of acoustic attenuation along the 5.6 m length buried MDPE pipe

From Figure 4.27, numerical prediction of acoustic attenuation along the buried MDPE pipe of 6 m length is 2.1 dB/m which is closer to the field trial estimate of 2.9 dB/m thus suggesting the influence of acoustic signal reflection at the pipe wall discontinuities at each pipe end in contributing to increased acoustic attenuation along the pipe.

Based on the acoustic attenuation results for the exposed and buried water pipes presented so far, the next section further discusses the distances at which reliable digital communication can be achieved along the pipes.

4.5 ACOUSTIC DATA COMMUNICATION RELIABILITY ALONG A WATER PIPE

This section analyses data communication reliability along the exposed and buried water pipes and includes predictions of the maximum distances at which reliable digital communication can be achieved along the pipes. Data communication reliability, in this context, refers to the bit error ratio (BER) of a digital information signal during data transmission along the pipe. BER, for the purpose of definition, is the probability of incorrectly decoding a previously transmitted

digital information signal at a digital communication receiver (Mutagi, 2012; Kokossolakis, 2006).

As discussed in Chapter 3, the proposed communication system employed OOK modulation for digital transmission along a pipe. BER, using OOK modulation, can be expressed as (Proakis & Salehi, 2008)

$$BER = \frac{1}{2} erfc\left(\sqrt{{}^{1}/_{2}\, SNR}\right) \tag{4.8}$$

Where BER is the bit error ratio of the digital information signal, SNR is the signal to noise ratio of the digital information signal and $erfc(x)$ is the complementary error function ($erfc(0) = 1$). Equation (4.8) shows that BER depends on the SNR of a transmitted signal (in this case the transmitted acoustic signal along the water pipe). Due to acoustic signal attenuation along the pipe, this SNR will reduce at increasing distances along the pipe. The objective of this section is therefore to use Equation (4.8) to examine data communication reliability along a pipe thus predicting of the maximum distances at which reliable digital communication can be achieved along the exposed and buried water pipes described in Chapter 3.

As described in Section 3.6.1, the front-end of the digital communication receiver featured a signal pre-amplifier followed by a PLL circuit. This PLL circuit, with an input signal threshold of 200 mV (Texas Instruments, 2014), was responsible for converting the incoming acoustic signal into a binary signal before further signal processing operations were carried out at the receiver. Below the PLL input threshold therefore, the incoming acoustic signal would be undetectable at the digital communication receiver. The relative amplitude (in dB) between the signal pre-amplifier output and the input threshold of the PLL can further be expressed as

$$SNR = 20log_{10}\frac{V_{out}}{V_{in}} \tag{4.9}$$

Where SNR (dB) is the relative amplitude between the signal pre-amplifier output and the PLL input threshold, V_{out} (V) is the signal pre-amplifier output voltage and V_{in} (V) is the PLL input threshold. As noted in Section 3.6.1, the maximum output voltage of the signal pre-amplifier is 4 V. Using Equation (4.9) therefore, the maximum SNR between V_{out} and V_{in} was calculated as 26 dB. This can also be considered as the starting SNR for Equation (4.8). It therefore follows that for a constant acoustic transmitter power, this SNR will continue to diminish as the digital communication receiver is moved away from the transmitter due to acoustic attenuation along the pipe. Using this information as well as the theoretically predicted and experimentally measured acoustic attenuation along the exposed and buried water pipes, the next section further discusses the maximum ranges at which reliable digital communication can be achieved along the pipes.

4.5.1 Data communication reliability along an exposed water pipe

This section discusses the data communication reliability along the exposed MDPE pipe described in Section 3.8.2.1, for acoustic excitation at 38 Hz (based on the recorded peak acoustic signals Figure 4.7). With a maximum SNR of 26 dB between the signal pre-amplifier output and the PLL input and with the analytical and numerical predictions (in addition to the experimental measurements) of acoustic attenuation along empty and water-filled MDPE pipes, Figures 4.28 shows the BER predictions along each pipe.

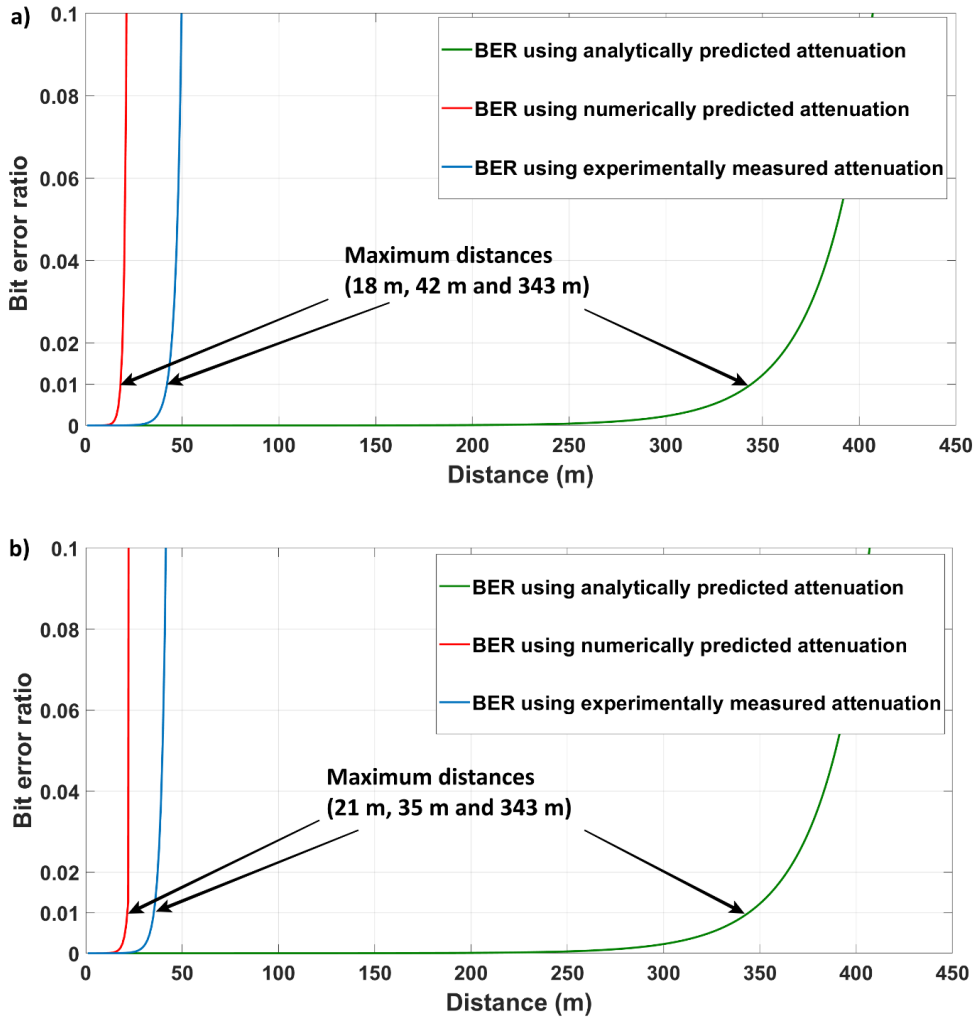

Figure 4.28: Acoustic data communication reliability along a) the exposed (empty) MDPE pipe and b) the exposed (water-filled) MDPE pipe

From Figure 4.28, the maximum distances at which digital communication is theoretically possible along the exposed (empty and water-filled) MDPE pipes vary depending on the acoustic attenuation prediction along the pipe. To predict the maximum distance, a BER of 0.01 (or 1%) is recommended as the minimum threshold below which digital communication can be safely assumed to be reliable. This minimum threshold for reliable digital communication threshold has also been suggested for radio based wireless underground communication by Akyildiz et al. (2009). A BER above 0.01 therefore implies an increasingly unreliable digital communication system. Using this minimum reliability threshold, the maximum digital communication distances in Figures 4.28a and b are similar, since (as previously discussed in

Section 4.3) acoustic attenuation along the empty and water-filled pipes are approximately the same.

It can also be seen in Figure 4.28 that the maximum data communication distance, using the analytically predicted acoustic attenuation along the exposed MDPE pipe, is significantly greater than the maximum digital communication distance with the numerically modelled and experimentally measured results. This can be considered an overestimation of the data communication distance since, as previously discussed in Section 4.3.3, the analytical model does not consider the contribution of pipe wall dispersive losses to acoustic attenuation along the pipe. The numerically predicted and experimentally measured acoustic attenuation-based digital communication reliability calculations thus provide a more realistic projection of the maximum distances at which reliable digital communication can be achieved along the pipe. The next section further discusses digital communication reliability along buried water pipes while focusing on the numerically predicted and experimentally measured acoustic attenuation estimates for the BER calculations.

4.5.2 Data communication reliability along a buried water pipe

Data communication reliability along the buried steel and MDPE pipes (described in Section 3.7) is discussed in this section. For the buried steel pipe, Figure 4.29 shows the expected BER along the pipe.

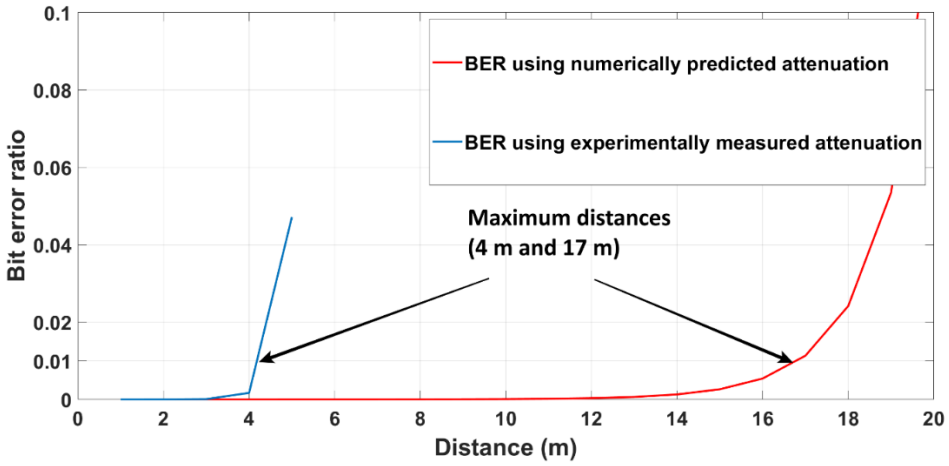

Figure 4.29: Acoustic data communication reliability along the buried steel pipe

From Figure 4.29, the maximum data communication distance (4 m) based on the experimentally measured acoustic attenuation is significantly shorter than the maximum communication distance (17 m) based on the numerically predicted acoustic attenuation. As previously mentioned in Section 4.4.2, the presence of a valve connection between the acoustic measurement points along the buried steel pipe is likely to have contributed to the increased attenuation measured along the pipe. Consequently, the maximum communication distance achievable for such a high acoustic attenuation estimate is significantly shorter than the numerical prediction which does not consider any pipe wall discontinuity. Without the impediment of a valve connection along the pipe, Figure 4.29 nevertheless shows that reliable digital communication can be achieved along the pipe at distances approaching 17 m. This is significant when considering that existing approaches for achieving wireless underground communication for real-time water pipe monitoring such as in Vuran & Silva (2010) and Akyildiz et al. (2009) are limited to less than 3 m. The results presented in Figure 4.29 (in addition to the result presented next) therefore show the possibility of achieving even greater communication distances, using acoustic signal propagation within an underground soil environment, for real-time buried water pipe monitoring. This finding is particularly important

for the cost-effective monitoring of buried water pipes as will be shown in Section 4.6. For now, Figure 4.30 shows the expected BER along the buried MDPE pipe in Trench 2.

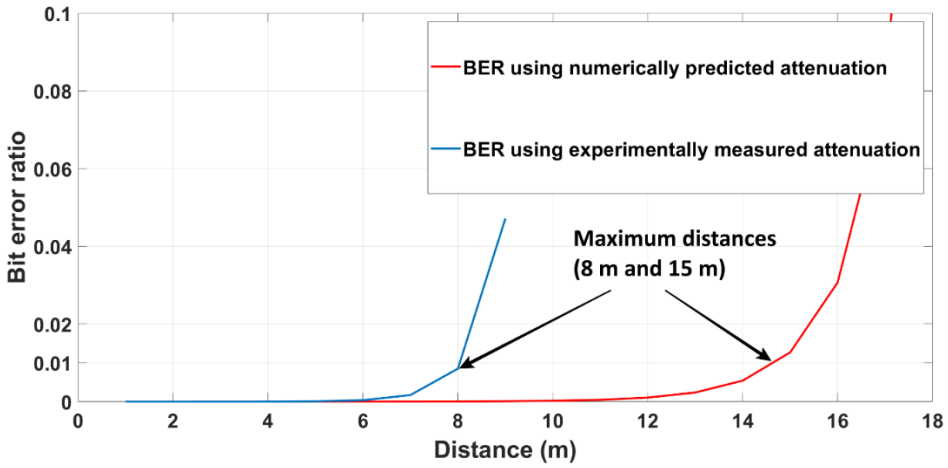

Figure 4.30: Acoustic data communication reliability along the buried MDPE pipe in Trench 2

From Figure 4.30, the maximum communication distances along the buried MDPE pipe, based on the numerically predicted and experimentally measured acoustic attenuation along the pipe, are closer compared to Figure 4.29. This is expected since the numerically predicted acoustic attenuation (i.e., 1.5 dB/m) is closer to the experimentally measured acoustic attenuation (i.e., 2.9 dB/m) along the buried MDPE pipe than it is for the buried steel pipe. As mentioned in Section 4.4.3 however, the numerical model predicted acoustic attenuation along an infinitely long pipe rather than a pipe of finite length (6 m) as used in the field trials. Using the 6 m pipe for the numerical model, Figure 4.31 shows the adjusted BER along the buried MDPE pipe.

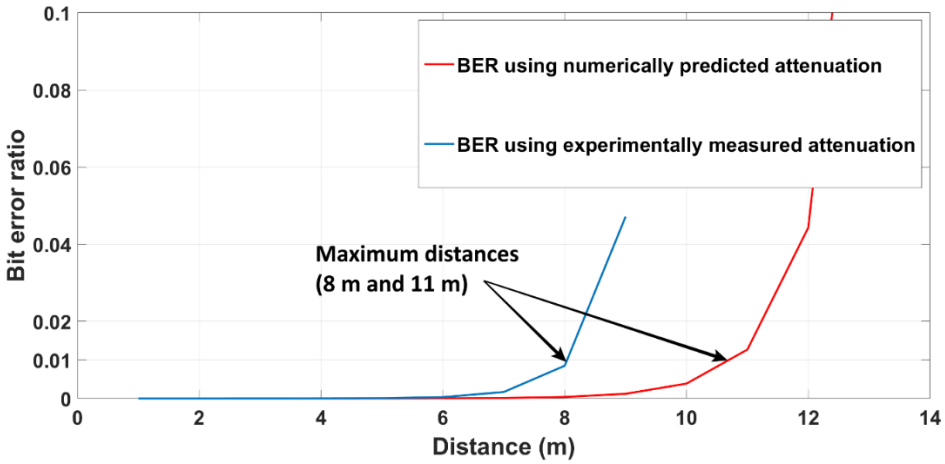

Figure 4.31: Acoustic data communication reliability along the buried MDPE pipe in Trench 2 using adjusted numerical model attenuation

From Figure 4.31, the maximum data communication distance along the buried MDPE pipe, based on the numerically predicted acoustic attenuation, is closer to the maximum distance based on the experimentally measured acoustic attenuation than it is in Figure 4.30. As previously discussed in Section 4.4.3, the numerically predicted acoustic attenuation is higher (i.e., 2.1 dB/m compared to 1.5 dB/m) for the 6 m pipe than it is for the infinitely long pipe due to the influence of acoustic signal reflections at the pipe edges in contributing to an increased acoustic attenuation along the pipe. Figures 4.30 and 4.31 therefore show that for a buried pipe of finite length (i.e., is terminated by pipe wall discontinuities) the maximum data communication distance along such a pipe will be reduced (compared to an infinitely long pipe) due to the influence of acoustic signal reflections at the pipe wall discontinuities.

In addition to the presence of pipe wall discontinuities, the complexity of a buried pipeline network, in terms of material constitution of the individual pipes, will influence the distances at which reliable wireless underground data communication can be achieved using the proposed communication system. As noted by Rogers et al (2012), accurate knowledge of pipe material distribution within water supply networks in the UK is challenging due to variations in type and quality of materials employed over the years since these networks were originally constructed.

As previously mentioned in the literature review (Table 2.1 and Figure 2.1), cast iron pipes are estimated to constitute the majority of buried pipe material distribution in the UK although newer pipe installations for replacing and expanding existing water pipe networks are exclusively plastic in nature. Based on analytical model predictions, acoustic attenuation is theoretically higher along non-metallic compared to metallic pipes (due to increased acoustic energy radiation into the surrounding soil in the case of non-metallic pipes) and so the expected data communication range along buried plastic pipes will be comparatively shorter than metallic pipes of the same pipe diameter and wall thickness. Numerical modelling predictions however suggested only a slight difference in acoustic attenuation (0.2 dB/m difference according to Figure 4.26) and subsequent data communication range (2 m difference according to Figures 4.29 and 4.30) between non-metallic and metallic pipes. The reason for the slight difference in acoustic attenuation along buried metallic and non-metallic pipes according to the numerical model (compared to the analytical model) is the increased influence of acoustic dispersion within the pipe wall in the case of the steel pipe where (due to the high acoustic impedance mismatch between the buried steel pipe and soil) acoustic energy is trapped within the pipe wall thus contributing to the overall acoustic attenuation along the pipe. It is nevertheless advantageous to conservatively deploy wireless underground communication nodes at distances which are based on the predicted data communication range for buried non-metallic pipes (as opposed to their metallic counterparts), which for example, is approximately 10 m for the buried MDPE pipe employed for this research.

The bond between a pipe wall and the surrounding soil is also important since this can couple acoustic energy between the pipe wall and soil by creating an acoustic matching interface between both materials. This is particularly important for buried cast iron pipes where one of the main contributing factors to pipe deterioration is pipe wall corrosion (Rajeev et al., 2014). Cast iron corrosion occurs in soil due to electrochemical reactions resulting in the formation of

pitting, converting metal substrates into oxides, hydroxides, and aqueous salts (Abed et al., 2020). Electrochemical reactions between the cast iron and chemically aggressive soils such as clay will thus create a closer acoustic impedance match between the buried pipe and soil resulting in increased acoustic attenuation along the pipe since greater acoustic energy will be coupled between the pipe wall and the surrounding soil. This is especially relevant for aged cast iron pipes buried in clay soils where, as noted by Abed et al. (2020), electrochemical corrosion of the cast iron pipe alters the chemical composition of the surrounding soil in the immediate vicinity of the pipe by releasing ferrous ions into the soil. The closer acoustic impedance match between the cast iron pipe and the affected soil will thus result in increased acoustic energy radiation into the soil and by implication, acoustic attenuation along the buried pipe. The increased acoustic attenuation will subsequently reduce the acoustic data communication range along the pipe depending on the degree to which acoustic energy is radiated from the buried pipe into the soil (which in turn depends on the strength of chemical bonding between the pipe wall and surrounding soil).

Regarding long term material properties of a buried MDPE pipe, Stewart & Bilgin (2020) noted that the temperature along a buried polyethylene pipe due to seasonal variations in ground temperature fluctuates between -7 °C and 21 °C (representing a 28°C change buried pipe temperature). Based on the parametric analysis of Table 4.12, the expected difference in acoustic attenuation along the buried MDPE pipe due to the impact of ground temperature fluctuations on the pipe wall elastic modulus will be 0.3 dB/m. With the BER calculations of Section 4.5, this implies that the maximum expected data communication range along a buried MDPE pipe would vary between 11-13 m due to the impact of seasonal variations in ground temperature on the pipe wall elastic modulus. For the pipe wall Poisson's ratio, the range of buried MDPE pipe Poisson's ratio for ground temperature variations between -7 °C and 21 °C is between 0.43 and 0.46 (Using Equation (4.2)). Based on the parametric analysis of Table

4.13, the expected difference in acoustic attenuation along the buried MDPE pipe due to the impact of ground temperature fluctuations on the pipe wall Poisson's ratio will be 0.01 dB/m With the BER calculations of Section 4.5, this change in acoustic attenuation due to the impact of ground temperature fluctuations on the pipe wall Poisson's ratio would have minimal effect on the maximum predicted data communication range along the buried MDPE pipe.

The presence of electro-fusion as well as butt fusion joints can also introduce variations in the MDPE pipe wall thickness. For good quality pipe joints, pipe wall pipe thickness variations should not exceed 10% (MAB, 2017) and so with a 9.2 mm pipe wall thickness for example, the maximum variation in pipe wall thickness will be 0.9 mm. Using Table 4.11, this difference in pipe wall thickness translates to an acoustic attenuation difference of 0.05 dB/m which implies a less than 1 m difference in predicted data communication range along the buried MDPE pipe due to pipe wall thickness variation.

Regarding soil bedding material, pipe embedment material should be a coarse-grained soil such as gravel or sand (or a coarse-grained soil containing silt or clay) due to their stiffness thus minimising pipe deflections due to external loading (PPI, 2008). A key objective of underground polyethylene (PE) pipe installation is to limit or control pipe deflection (which is a change in pipe diameter due to external loading) after burial. The stiffer the embedment material therefore, the less pipe deflection occurs. As noted by Yimsiri & Ratananikom (2021), pipe deflection can develop over time due to creep of pipe, backfill soil structure rearrangement and in-situ soil consolidation. Pipe deflection also typically varies along a buried pipe length due to variations in construction technique, soil type and loading with a typical range of $\pm 2\%$ of the pipe diameter (PPI, 2008). For a 90 mm diameter MDPE pipe for example, this represents a deflection of $\pm 1\%$ (0.9 mm) of the pipe wall inner radius. Using Table 4.10, the variation in

acoustic attenuation due to this pipe deflection will be $\pm 9 \times 10^{-3}$ dB/m which has minimal effect on the acoustic data communication range along the buried MDPE pipe.

4.6 POTENTIAL APPLICATION OF THE PROPOSED COMMUNICATION SYSTEM

As mentioned in Chapter 1, the occurrence of leaks and bursts are an inescapable reality for buried water distribution networks and are responsible for significant water loss within such networks if left unattended for long periods. In many instances, the presence of leaks within underground pipe networks often goes unnoticed and in more severe cases, can lead to catastrophic failures such as pipe bursts which impose further economic consequences on the affected communities.

In Chapter 2, a real-time monitoring approach based on wireless sensor networks for buried water pipe monitoring was argued as the way forward in managing pipe leaks. Key to the cost-effective deployment of wireless sensor networks for buried water pipe monitoring is reliable wireless underground communication between sensors deployed (non-invasively) along the pipe. These sensors should also be deployable in a manner that is effective both spatially and temporally (Stioanov et al., 2007). With radio based wireless underground communication, the spatial distribution of wireless underground sensors is limited to less than 3 metres due to the limited range of radio signal propagation within an underground soil environment using commercially available wireless sensor nodes (e.g., Sadeghioon, 2014; Vuran & Akyildiz, 2010; Akyildiz & Stuntebeck, 2006). This high sensor deployment density can become cost prohibitive for a utility owner especially for covering vast areas of buried water distribution networks. The proposed communication system described in this research can potentially overcome the issue of high sensor deployment density by offering an improved wireless underground communication range (beyond 3 m) between a pair of wireless sensor nodes, while

maintaining the low cost (tens of pounds at most), low power supply (in the order of 1 Watt-hour) and small size (centimetre scale) requirements of a typical wireless sensor node.

As an example, the proposed communication system can be employed as part of a continuous leak detection and location scheme using cross-correlation. The cross-correlation technique uses the time difference in arrival of a leak signal between two adjacent acoustic sensors for the detection and subsequent location of a leak (Stoianov et al., 2007; Hunaidi et al., 2000; Hunaidi & Chu, 1999). Moreover, this technique is generally deployed on site only after a problematic section in the network has been initially identified (e.g. Kumar et al. 2020). The communication system developed in this research can facilitate a new approach for continuously monitoring buried water pipes using the cross-correlation technique, where a direct underground communication link is established between low cost, low power and small size wireless sensor nodes which are conveniently deployed at pipe access points (e.g. valves).

For a pair of adjacent acoustic sensors installed along the buried water pipe, the presence of a leak can be determined by detecting an acoustic signature within a specific bandwidth typical of a leak noise (e.g. 200-250 Hz in Stoianov et al. (2007)). To accurately determine the presence of a leak, these acoustic sensors can initially periodically obtain digital samples of background acoustic noise along the buried water pipe during periods of low environmental activity (e.g. the early morning hours of 2.00 to 4.00 am). Since analysis of leaks is not time critical, leak detection and location procedures can be carried out by the wireless sensor network during hours of low background noise for short periods of time (i.e. within minutes) (Stoianov et al., 2007). During the occurrence of a leak, increased energy in the leak signal bandwidth of the acoustic power spectrum (as measured by the acoustic sensors) which exceeds a previously set threshold (below which the acoustic signal is classified as background noise) activates the nearest acoustic sensor to the leak. This acoustic sensor subsequently generates an alarm which,

accompanied by a sensor identifier (in the form of a digitally encoded marker unique to each acoustic sensor), can be further relayed, using the underground communication system to an above ground gateway with direct terrestrial access to a central server (i.e. monitoring station) which is then notified of the suspected presence of a leak.

Once the central server is notified of the suspected presence of a leak, it transmits an instruction to the gateway stipulating the specific time at which the acoustic sensors adjacent to the suspected leak should begin the process of recording the leak signal. This information is subsequently transmitted to the acoustic sensors before the leak recording process is initiated (by acoustic sensors which are adjacent to the suspected leak) at the allocated time. To conserve power, the leak recording process can be limited to within seconds before the recorded leak signal is digitized, compressed (to minimise its bandwidth) and relayed back to the above-ground gateway and eventually the central server. At the central server, cross-correlation of the digitised leak signal can be performed to locate the maximum peak of the cross-correlated signal. If this peak exceeds a prescribed threshold, the location of the leak can be computed using the axial distances (in metres) of its adjacent acoustic sensors, the time lag of the peak of the cross-correlated signal (in seconds) as well as the acoustic propagation velocity of the leak signal (in metres/second). This leak detection and location procedure, using direct underground communication between acoustic sensors, thus represents a potential application of the proposed communication system for buried water pipe monitoring.

4.7 SUMMARY

This chapter began by presenting the results of digital communication along exposed and buried water pipes, using the novel communication system described in this thesis. The results showed, for the first time, that reliable digital communication is possible along an exposed or buried water pipe (of either metallic or non-metallic material) using low frequency (less than 1 kHz)

acoustic propagation along the pipe wall. Regarding acoustic signal propagation along the pipe, results of analytical and numerical modelling in addition to laboratory and field trials for evaluating acoustic signal attenuation along exposed and buried water pipes were presented and discussed. From the results, it was evident that the analytical model, in not considering the contribution of pipe wall acoustic dispersion, underestimates acoustic attenuation along the exposed or buried water pipe. It was also evident from the numerical as well as laboratory results, that acoustic attenuation along the pipe consists of near- and far-field regions due to the non-axisymmetric nature of acoustic excitation along the pipe. While the near-field region (between 0 m and 1 m from the acoustic transmitter) is characterised by a rise in acoustic signal amplitude, the far-field region (beyond 1 m from the acoustic transmitter) is characterised by a linear drop in acoustic signal amplitude along the pipe.

For a buried water pipe, the analytical model showed the effect of the surrounding soil in increasing acoustic attenuation along the pipe (through acoustic wave radiation from the pipe into the soil) compared to its exposed counterpart. The analytical model also interestingly showed the effect of increasing soil bulk and shear moduli as well as density in reducing acoustic attenuation along the buried pipe due to the soil's role in stiffening the pipe wall. With the numerical results no difference was observed in acoustic attenuation along the buried steel or MDPE pipe when the soil bulk or shear moduli was increased suggesting the greater influence of acoustic signal dispersion along the pipe wall (compared to any radiative loss) on the overall acoustic attenuation along the buried pipe. While the acoustic attenuation measurement for the buried steel pipe (5.8 dB/m) showed significant discrepancy with the numerical modelling result (1.3 dB/m), the measured acoustic attenuation along the buried MDPE pipe (2.9 dB/m) was closer to the numerical modelling results of 1.5 dB/m. For a finite pipe length equal to the pipe length employed for the field trials (i.e., 5.6 m), the numerical modelling result for the buried MDPE pipe (i.e., 2.1 dB/m) showed even closer agreement to

the field trial result suggesting the influence of acoustic signal reflection at the pipe extremities in contributing to increased attenuation along the pipe.

Finally, analysis of data communication reliability along exposed and buried pipes showed that reliable digital communication is possible along an exposed MDPE pipe at distances of at least 18 m while for buried steel and MDPE pipes the reliable communication distances ranged from 4 m to 17 m. Compared to the currently achievable range of wireless underground communication for real-time buried water pipeline monitoring, which is less than 3 m, the results presented in this chapter show notable promise. A potential application of the proposed communication system for real-time leak detection and location was also discussed in this chapter, showing the practicality of the communication system deployment for cost-effective and real-time buried water pipe monitoring.

CHAPTER 5

CONCLUSIONS AND RECOMMENDATIONS FOR FURTHER WORK

5.1 INTRODUCTION

This thesis presented the design and development of a novel wireless underground communication system for buried water pipe monitoring, using low frequency (< 1 kHz) acoustic propagation along the pipe. A new data communication algorithm (using an embedded systems approach) was designed and culminated in the development of separate low cost (tens of pounds at most), low power supply requirement (in the order of 1 Watt-hour) and miniature (centimetre scale) working prototypes of a digital communication transmitter and receiver (which also addressed the third research objective in Chapter 1). The digital communication system design focused not only on enabling wireless underground communication at distances beyond 3 m in an underground soil environment, but also on ensuring that such data communication is reliable (i.e., with no bit error). In this regard, results of laboratory and field testing of the prototype communication system showed promise as reliable data communication was achieved at 5.6 m along both exposed and buried MDPE pipes.

Key to predicting the reliability of this communication system was the quantification of acoustic signal attenuation along a water pipe waveguide. To this end, separate analytical, numerical, and experimental models were developed to comparatively examine acoustic signal attenuation along exposed and buried water pipes before using the results to predict the maximum ranges at which reliable digital communication can be achieved using the proposed communication system. The next section further presents the key findings of this research.

5.2 CONCLUSIONS

The key findings of this research are summarised below:

- From the first research objective, based on a review of wireless underground communication techniques for buried water pipe monitoring, it was evident that unlike traditional radio-based communication, low frequency (< 1 kHz) acoustic propagation along a water pipe waveguide can enable digital communication at distances beyond 3 m within an underground soil environment. The literature review also showed that while the subject of acoustic communication along water pipes has traditionally exploited the internal fluid medium for long range (i.e., tens of metres) communication, the use of the pipe wall itself for achieving similar ranges of wireless underground communication remained relatively unexplored. The main contribution of this research is therefore the demonstration of the possibility of achieving reliable wireless underground digital communication along a buried water pipe (especially of non-metallic material) using low frequency acoustic propagation along the pipe wall.
- Based on a thorough review of state-of-the-art commercially available acoustic transducers as well as laboratory-based examination of these transducers (the second objective of this research), this research, for the first time, has shown that a selection of low cost (tens of pounds at most), low power (in the order of 1 W) and miniature (centimetre scale) commercially available acoustic transducers can be employed for acoustic based digital communication along a water pipe. These transducers, discovered among plethora of commercially available options (over 130 different models) through careful selection and laboratory testing, are the ERM vibration motor and the MFC piezoelectric sensor. A new window of opportunity has therefore been opened by this research by applying these traditionally haptic transducers to the area of buried water pipe monitoring through integration within a novel wireless underground communication system for buried water pipe monitoring. Related to this finding are:

- Considering the cost, physical size, and power limitations of a wireless underground communication node, an ERM vibration motor was shown to generate the highest vibration amplitude of any commercially available acoustic transducer for transmitting acoustic waves along a water pipe surface. This is due to its relatively large form factor (enabled by an eccentric rotating mass located outside the motor body) which offered the possibility of an increased acoustic communication range compared to smaller acoustic transducers which, although may have the same operating principle, have a smaller form factor (due to, for example, an internally located eccentric mass within the motor body).
- It is possible to increase the data transmission rate for acoustic communication along a water pipe by rapidly deactivating the ERM vibration motor. Traditionally, this technique has been applied for haptic control applications where the vibration motor is rapidly deactivated to improve haptic feedback. This research has however opened a new avenue for using this active braking technique for acoustic data communication by showing how the technique can be employed for improving acoustic data transmission throughput along an exposed or buried water pipe.
- An active (i.e., generating its own power) commercially available sensor, specifically the MFC piezoelectric sensor, has for the first time been shown to not only detect acoustic waves along a non-metallic (MDPE) pipe by direct attachment to the pipe but also to successfully do so within a low cost, low power, and miniature digital communication receiver.
- For the low cost, low power and miniature acoustic communication receiver, this research has also shown the possibility of integrating a single chip coherent demodulator within the acoustic communication receiver to achieve reliable digital communication along an exposed or buried water pipe. This finding is especially

key to the application of low-cost wireless underground communication nodes for dependable and real-time pipeline monitoring as it shows that reliable digital communication can still be achieved along a buried water pipe while pushing the boundaries of low cost, low power, and smaller size hardware components for wireless underground communication.

- Reliable digital communication (albeit at 1 bps data transmission rate), for the first time, has been shown to be possible along the surface of a metallic (steel) and (especially) non-metallic (MDPE) pipe buried in well or poorly graded SAND (SP or SW). This is in line with the fourth objective of this research. As highlighted in the literature review, other wireless communication techniques for buried pipeline monitoring have individual shortcomings such as limited range (in the case of radio) or the need to install the digital communication transmitter and receiver within the pipe (in the case of underwater acoustic communication). This finding however shows that reliable wireless underground communication, where the acoustic communication transmitter and receiver are non-invasively (i.e., on the outer pipe surface) installed along the buried water pipe (especially a non-metallic pipe), can still be achieved while still offering greater communication distance compared to underground radio communication. Furthermore, the limited data rate of the novel communication system may not be an issue for certain pipeline monitoring applications (e.g., leak monitoring) where data can be collected and transmitted from the pipe at hourly or even daily intervals thus placing less emphasis on the quantity, as opposed to the quality of data transmission.
- Addressing the fifth research objective, separate analytical and numerical models were developed as part of this research for examining acoustic signal attenuation along exposed and buried water pipes. Comparison of the numerical and analytical models for acoustic signal attenuation along the MDPE pipe showed that the numerical model,

unlike the analytical model, predicted a near- and far-field region of acoustic signal attenuation based on the proximity of the acoustic receiver to the transmitter. While the near-field was dominated by non-propagating high frequency (> 1 kHz) acoustic signals, the far-field was dominated by low frequency (< 1 kHz) acoustic signal propagation. This near- and far-field effect was similarly observed in laboratory experiments for acoustic signal attenuation along an exposed MDPE pipe. For the far-field acoustic attenuation, the numerical model also predicted a notably higher acoustic attenuation of 1.2 dB/m compared to the analytical model prediction of 0.06 dB/m at the same acoustic excitation frequency, which indicated that, in addition to pipe wall material losses, acoustic dispersion also contributes to the overall acoustic attenuation along the pipe. Like the analytical model, the numerical model also predicted significantly higher acoustic attenuation (by 2 orders of magnitude) along non-metallic compared to metallic pipes. Related findings for acoustic attenuation along the exposed and buried water pipes include:

- Based on analytical calculations, acoustic attenuation was shown to increase linearly along an exposed MDPE pipe with increasing acoustic excitation frequency between 0 and 200 Hz. Parametric studies of acoustic signal attenuation along the pipe, using the analytical model, also showed that the acoustic attenuation prediction is insensitive to uncertainties/variations in the pipe inner radius, wall thickness or Poisson's ratio (within the limits typical of water distribution pipes) but sensitive to changes in elastic modulus. To accurately predict (to within 2 decimal places) acoustic attenuation along the MDPE pipe using the analytical model therefore, the chosen pipe wall elastic modulus must be within $\pm 2\%$ of the parametric base value for MDPE pipe wall elastic modulus.

- Unlike the analytical model parametric studies, parametric studies for the numerical model results showed that acoustic attenuation (far-field) along the MDPE pipe is sensitive to changes in the pipe inner radius, wall thickness and Poisson's ratio in addition to sensitivity to the pipe wall elastic modulus. To accurately predict (to within 2 decimal places) acoustic attenuation along the MDPE pipe using the numerical model therefore, the chosen values for pipe inner radius, wall thickness, elastic modulus and Poisson's ratio must therefore be within $\pm 1\%$, $\pm 1\%$, $\pm 0.4\%$ and $\pm 2\%$ respectively of their parametric base values.
- To ensure the predictability of acoustic attenuation along the MDPE pipe, it is important to align the ERM vibration motor in such a way as to suppress the generation of flexural acoustic wave propagation in favour of a longitudinal acoustic wave along the pipe. As shown during this research, this can be achieved by aligning the ERM vibration motor shaft parallel (instead of perpendicular) to the pipe axial axis.
- For the buried water pipes, according to the analytical model, acoustic signal attenuation along the buried MDPE pipe is greater compared to acoustic attenuation along the buried steel pipe due to increased acoustic energy radiation between the buried MDPE pipe and the surrounding soil compared to the buried steel pipe. The analytical model findings also indicated that factors such as increasing the bulk or shear acoustic wave speed in soil as well as well as the soil density (which are indicative of a more compact soil) reduce acoustic attenuation along the buried MDPE by further stiffening the pipe wall and lowering the propagating acoustic wave number.
- The numerical modelling results for acoustic signal attenuation along the buried water pipe, unlike the analytical, revealed no difference in the acoustic attenuation

prediction along the buried water pipes for loose, medium, or dense unsaturated sand. The results therefore suggested that the influence of acoustic signal dispersion along the pipe wall significantly outweigh any contribution of the surrounding soil stiffness on acoustic attenuation along the buried water pipe.

- Comparisons between the measured acoustic attenuation along the buried MDPE pipe and the numerical modelling predictions for a pipe of the same length showed reasonably close agreement (i.e., 2.1 dB/m numerical model prediction compared to 2.9 dB/m obtained from the field trials). This is important as the numerical model was able to show increased acoustic attenuation along a buried pipe of limited length (i.e., 6 m) compared to an infinitely long pipe due to acoustic signal reflections at the pipe edges. A key finding from the numerical and experimental results is therefore the significant contribution of pipe wall discontinuities to acoustic attenuation along a buried water pipe.

- According to the final research objective and based on theoretical BER predictions for the communication system, it is estimated that reliable digital communication can realistically be achieved at maximum distances of between 35 m and 42 m for an exposed MDPE pipe and 15 m along a buried MDPE pipe (in the absence of acoustic reflections along the pipe). Even with a significant presence of acoustic reflections which increase acoustic attenuation along the pipe, maximum data communication distances at 11 m can still be achieved along the buried MDPE pipe. Particularly for the buried MDPE pipe, these results are a significant improvement to the currently achievable ranges (less than 3 m) of reliable wireless underground communication (using commercially available radio-based data communication nodes) for real-time buried water pipe monitoring. The solution described in this thesis thus presents a new acoustic-based technique for cost-effective and real-time buried water pipe monitoring

by improving wireless underground communication range at minimum deployment costs to the utility owner.

5.3 RECOMMENDATIONS FOR FURTHER WORK

From the research described in this thesis, some recommendations for further work have been identified.

- While some field trials along buried water pipes were conducted during this research, the findings suggest that there is still some uncertainty with respect to the impact of the surrounding ground on the results indicated by the discrepancies between the analytical and numerical models with the experimental results. Thus, more extensive field trials along buried water pipes are needed to experimentally examine the communication system's performance (in terms of its predicted range).

- Theoretical and experimental work conducted during this research focused on acoustic signal propagation along pipes without discontinuities. While this is an important first step for successful system deployment, more research is needed to analyse the system's performance in the presence of pipe joints and fittings. Such an undertaking can provide valuable information on the achievable ranges of reliable digital communication within a complex water pipe distribution network.

- The influence of the adhesive coupling, between the acoustic transducer and the pipe, on the acoustic signal attenuation should also be further investigated. Examination of the mechanical properties (such as stiffness and damping factor) of a chosen adhesive can reveal the influence of acoustic signal attenuation within the coupling material on the overall signal attenuation along the pipe. Furthermore, such investigation can enable efficient acoustic transducer coupling, which combine versatility along different types

of pipes as well as offering minimal acoustic impedance to the propagating acoustic wave, to be deployed along the pipes potentially enabling even greater distances of acoustic data communication along the pipe.

REFERENCES

Abdorahimi, D. (2014). *Comparison of radio frequency path loss models in soil for wireless underground sensor networks.* MPhil. Thesis. University of Birmingham. Available at: https://etheses.bham.ac.uk/id/eprint/8349/1/Abdorahimi18MPhil.pdf (Accessed: 1 June 2019).

Abed, T.M, Torbaghan, E.M., Hojjati, A., Rogers, C.D. and Chapman, D.N., 2020 'Experimental Investigation into the Effects of Cast-Iron Pipe Corrosion on GPR Detection Performance in Clay Soils', *Journal of Pipeline Systems Engineering and Practice*, 11(4), pp. 04020040-1-04020040-15.

Advanced Engineering Solutions (2019). *Pipeline assessment and integrity services.* Available at: https://www.aesengs.co.uk/ (Accessed: 1 August 2020).

Akyildiz, I.F. and Stuntebeck, E.P. (2006) 'Wireless underground sensor networks: Research challenges', *Ad Hoc Networks*, 4(6), pp. 669-686.

Akyildiz, I. F., Su, W., Sankarasubramaniam, Y. and Cayirci, E. (2002) 'Wireless sensor networks: a survey', *Computer Networks*, 38(4), pp. 393–422.

Akyildiz, I.F., Sun, Z. and Vuran, M.C. (2009) 'Signal propagation techniques for wireless underground communication networks', *Physical Communication*, 2(3), pp. 167-183.

Akyildiz, I.F. and Vuran, M.C. (2010). *Advanced Texts in Communications and Networking: Wireless Sensor Networks.* Hoboken, N.J: Wiley.

Al-Barqawi, H. and Zayed, T. (2006) 'Condition rating model for underground infrastructure sustainable water mains', *Journal of Performance of Constructed Facilities*, 20(2), pp. 126-135.

Analogue Devices (2010). *Small, low power, 3-axis ±3g accelerometer.* Available at: https://www.analog.com/media/en/technical-documentation/data-sheets/ADXL337.pdf (Accessed: 1 October 2019).

Anastasopoulos, A., Kourousis, D. and Bollas, K. (2009) 'Acoustic emission leak detection of liquid filled buried pipeline', *Journal of Acoustic Emission*, 27 (2009), pp. 27-39.

Anguiano, G., Chiang, E., Araujo, M., Strum, S., Medina, V., Waisner, S., Condit, W., Matthews, J. and Stowe, R. (2016). *Innovative acoustic sensor technologies for leak detection in challenging pipe types.* Available at: https://apps.dtic.mil/sti/pdfs/AD1039195.pdf (Accessed: 1 August, 2020).

Ariaratnam, S.T. and Chandrasekaran, M. (2010). *Development of a free-swimming acoustic tool for liquid pipeline leak detection including evaluation for natural gas pipeline applications.* Available at: https://rosap.ntl.bts.gov/view/dot/34534 (Accessed: 30 July 2020).

Bareille, O., Kharrat, M., Zhou, W. and Ichchou, M.N., 2012 'Distributed piezoelectric guided-T-wave generator, design and analysis', *Mechatronics*, 22(5), pp. 544-551.

Battery Station (2021). *GP Lithium 9V PP3 CRV9 Battery | 1 Pack*. Available at: https://www.batterystation.co.uk/gp-lithium-9v-pp3-crv9-battery-1-pack/ (Accessed: 1 April 2021)**.**

BenSaleh, M.S., Qasim, S.M., Obeid, A.M. and Garcia-Ortiz, A. (2013) 'A review on wireless sensor network for water pipeline monitoring applications' *2013 International Conference on Collaboration Technologies and Systems (CTS),* San Diego, CA, USA, 20 to 24 May 2013.

Bilgin, Ö., Stewart, H.E. and O'Rourke, T.D. (2007) 'Thermal and mechanical properties of polyethylene pipes', *Journal of materials in civil engineering*, 19(12), pp.1043-1052.

Bond, A., Mergelas, B. and Jones, C. (2004) 'Pinpointing leaks in water transmission mains', *Pipeline Division Specialty Congress 2004*, San Diego, California, 1 to 4 August 2004.

British Standards Institution (1990) *BS 1377-2: 1990, Methods of test for soils for civil engineering purposes-Part 2: Classification tests*. London UK: British Standard Institution.

Bulusu, N. and Jha, S. (2005). *Wireless sensor networks. A systems perspective.* Norwood MA: Artech House.

Cawley, P. (2002) 'Practical long range guided wave inspection-applications to pipes and rail' *NDE2002 to predict assure improve National seminar of the Indian society for non-destructive testing (ISNT)*, Chennai, India 5 to 7 December 2002.

Chakraborty, S., Saulnier, G.J., Wilt, K.W., Curt, E., Scarton, H.A. and Litman, R.B. (2015), 'Low-power, low-rate ultrasonic communications system transmitting axially along a cylindrical pipe using transverse waves' *IEEE transactions on ultrasonics, ferroelectrics, and frequency control*, 62(10), pp. 1788-1796.

Costello, S.B., Chapman, D.N., Rogers, C.D.F. and Metje, N. (2007) 'Underground asset location and condition assessment technologies', *Tunnelling and Underground Space Technology*, 22(5-6), pp. 524-542.

Dassault Systemes (2011) 'Abaqus 6.11: Abaqus/CAE User's Manual'. Available at: http://130.149.89.49:2080/v6.11/pdf_books/CAE.pdf (Accessed: 1 March 2018).

Datta, S. and Sarkar, S. (2016) 'A review on different pipeline fault detection methods', *Journal of Loss Prevention in the Process Industries*, 41(2016), pp. 97-106.

Demirci, S., Yigit, E., Eskidemir, I.H. and Ozdemir, C. (2012) 'Ground penetrating radar imaging of water leaks from buried pipes based on back-projection method' *Ndt & E International*, *47*(2012), pp. 35-42.

DipTrace (2020). *DipTrace: Schematic and PCB design software.* Available at: https://diptrace.com/diptrace-software/ (Accessed: 1 March 2017).

Drinking Water Inspectorate (2020). *Drinking water 2020 Public water supplies for England and Wales Quarter 1 January – March 2020*. Available at: https://cdn.dwi.gov.uk/wp-content/uploads/2020/11/03133359/CIR_Q1_2020.pdf (Accessed: 1 May 2020).

Drozdz, M.B. (2008) *Efficient finite element modelling of ultrasound waves in elastic media.* Ph.D. Thesis. Imperial College London. Available at: https://spiral.imperial.ac.uk/handle/10044/1/7974 (Accessed: 30 August 2019).

Duran, O., Althoefer, K. and Seneviratne, L.D. (2002) 'Automated sewer pipe inspection through image processing' *Proceedings 2002 IEEE International Conference on Robotics and Automation (Cat. No.02CH37292)*, Washington DC, USA, 11 to 15 May 2002.

Echologics (2020). *Echoshore®-DX platform.* Available at: https://www.echologics.com/services/small-diameter-leak-monitoring/echoshore-dx/ (Accessed: 30 July 2020).

Echologics (2020). *Echowave® Transmission main inspection – A proven acoustic correlation service.* Available at: https://www.echologics.com/services/large-diameter-leak-detection/echowave/ (Accessed: 30 July 2020).

Echologics (2020). *ePulse® Pipeline condition assessment*. Available at: https://www.echologics.com/services/condition-assessment/epulse/ (Accessed: 30 July 2020).

Echologics (2020). *LeakFinder-ST™ Correlator.* Available at: https://www.echologics.com/products/leakfinderst/ (Accessed: 30 July 2020).

Envirosight (2020) *Underground understood.* Available at: https://www.envirosight.com/ (Accessed: 1 August 2020).

Fernandez-Vallejo, M. and Lopez-Amo, M. (2012) 'Optical fiber networks for remote fiber optic sensors', *Sensors*, 12(4), pp. 3929-3951.

Finnveden, S. (1997) 'Simplified equations of motion for the radial–axial vibrations of fluid filled pipes', *Journal of Sound and Vibration*, 208(5), pp. 685–703.

Fletcher, R. and Chandrasekaran, M. (2008) 'SmartBall™: A new approach in pipeline leak detection', *2008 7th International Pipeline Conference*, Calgary, Alberta, Canada, 29 September to 3 October 2008.

Frank (2000). *Understanding smart sensors* (2nd ed.). Norwood, MA: Artech House.

Frings, J. (2011) 'Enhanced pipeline monitoring with fiber optic sensors' *6th Pipeline Technology Conference,* Hannover, Germany, 4 to 5 April 2011.

Garrett, C. and Shatat, A. (2012) 'NDE Techniques for Water and Wastewater Pipe Condition Assessment' *North American Society for Trenchless Technology (NASTT) No-Dig Show 2012,* Nashville, TN, USA, 11 to 15 March 2012.

Hardin, B.O. and Drnevich, V.P. (1972) 'Shear modulus and damping in soils: design equations and curves', *Journal of Soil Mechanics & Foundations,* 98(sm7) pp. 667-692.

Hao, T., Rogers, C.D.F., Metje, N., Chapman, D.N., Muggleton, J.M., Foo, K.Y., Wang, P., Pennock, S.R., Atkins, P.R., Swingler, S.G., Parker, J., Costello, S.B., Burrow, M.P.N., Anspach, J.H., Armitage, R.J., Cohn, A.G., Goddard, K., Lewin, P.L., Orlando, G., Redfern, M.A., Royal, A.C.D., Saul, A.J. (2012) 'Condition assessment of the buried utility service infrastructure', *Tunnelling and Underground Space Technology*, 28 (2012), pp. 331-344.

Head, J.M. and Jardine, F.M. (1992). *Ground-borne vibrations arising from piling*. Japan: Public Works Research Institute.

Horowitz, P. and Winfield, H. (2016) *The Art of Electronics.* Cambridge: Cambridge University Press.

Hunaidi, O. and Chu, W.T. (1999) 'Acoustical characteristics of leak signals in plastic water distribution pipes', *Applied Acoustics*, 58(3), pp.235-254.

Hunaidi, O., Chu, W., Wang, A. and Guan, W. (2000) 'Detecting leaks in plastic

Pipes', *Journal-American Water Works Association*, 92(2), pp. 82-94.

Hunaidi, O. and Giamou, P. (1998) 'Ground-penetrating radar for detection of leaks in buried plastic water distribution pipes' *7th International Conference on Ground Penetrating Radar (GPR'98)*, Lawrence, Kansas, 27 to 28 May 1998.

Inaudi, D. and Glisic, B. (2010) 'Long-range pipeline monitoring by distributed fiber optic sensing', *Journal of pressure vessel technology*, 132(1), pp. 011701-1 – 011701-9.

Jackson, P. (2019) *Guided Wave Testing: Why two modes are better than one.* Available at: https://blog.eddyfi.com/en/guided-wave-testing-why-two-modes-are-better-than-one (Accessed: 1 May 2021).

Jawhar, I., Mohamed, N. and Shuaib, K. (2007) ‘A framework for pipeline infrastructure monitoring using wireless sensor networks’ *2007 Wireless Telecommunications Symposium*, Pomona, CA, USA, 26 to 28 April 2007.

Jin, Y., Ying, Y. and Zhao, D. (2013) ‘Data communications using guided elastic waves by time reversal pulse position modulation: Experimental study’, *Sensors*, 13(7), pp. 8352-8376.

Jo, B.Y., Laven, K. and Jacob, B. (2010) ‘Advances in CCTV technology for in-service water mains’ *Pipelines 2010: Climbing New Peaks to Infrastructure Reliability: Renew, Rehab, and Reinvest*, Keystone, Colorado, USA, 28 August to 1 September 2010.

Johnson, M., Healy, M., Van de Ven, P., Hayes, M.J., Nelson, J., Newe, T. and Lewis, E. (2009) ‘A comparative review of wireless sensor network mote technologies’ *IEEE Sensors 2009 Conference*, Christchurch, CAN, New Zealand, 25-28 October 2009.

Joseph, K.M., Watteyne, T. and Kerkez, B. (2018) ‘Awa: Using water distribution systems to transmit data’, *Transactions on Emerging Telecommunications Technologies*, 29(1), pp. 1-14.

Kantaris, G.S. and Makris, N.A. (2015) ‘Underwater wireless in-pipe communications system’ *2015 IEEE International Conference on Industrial Technology (ICIT)*, Seville, Spain, 17 to 19 March 2015.

Kausel, E. (2005). *Fundamental solutions in elastodynamics: A compendium.* Cambridge: Cambridge University Press.

Keddis, S. and Schwesinger, N. (2016) ‘Powering In-pipe Wireless Sensors Using Flexible Piezoelectric Micro-generators’, *Energy Harvesting and Systems*, *3*(3), pp. 223-228.

Kinsler, L. E., Frey, A.R., Coppens, A.B. and Sanders, J.V. (1999). *Fundamentals of Acoustics (4th Edition).* Hoboken, N.J: Wiley.

Kirkham, R., Kearney, P.D., Rogers, K.J. and Mashford, J. (2000) 'PIRAT-a system for quantitative sewer pipe assessment', *The International Journal of Robotics Research,* 19(11), pp. 1033-1053.

Kokossalakis, G. (2006). *Acoustic data communication system for in-pipe wireless sensor networks.* Ph.D. Thesis. Massachusetts Institute of Technology. Available at: https://dspace.mit.edu/handle/1721.1/34379 (Accessed: 1 July 2014).

Kondis, A. (2005). *Acoustical wave propagation in buried water filled pipes.* MSc. Thesis. Massachusetts Institute of Technology. Available at: https://dspace.mit.edu/handle/1721.1/30199 (Accessed 1 August 2014).

Kumar, S.S., Abraham, D.M., Behbahani, S.S., Matthews, J.C. and Iseley, T. (2020) 'Comparison of Technologies for Condition Assessment of Small-Diameter Ductile Iron Water Pipes', *Journal of Pipeline Systems Engineering and Practice,* 11(4), pp. 04020039-1-10.

Laven, K., Jones, C., Larsen, M. and Payton, R. (2008) 'Inline CCTV Inspections of In-Service Pressurized Water Mains' *Pipelines 2008: Pipeline Asset Management: Maximizing Performance of our Pipeline Infrastructure,* Atlanta, Georgia, USA, 22 to 22 July 2008.

Lee, A. (2017). *Condition assessment technologies for water transmission and sewage conveyance systems.* Available at: https://www.sustain.ubc.ca/sites/default/files/2017-20_Condition%20Assessment%20-

%20Water%20Distribution%20%26%20Sewage%20Conveyance_Lee.pdf (Accessed: 1 June 2020).

Lee, K.B. (2011). *Principles of microelectromechanical systems*. Hoboken, N.J: Wiley.

Lewis (2004). *Smart environments: technologies, protocols and applications.* Edited by D.J. Cook and S.K. Das. New York, N.Y: John Wiley.

Li, L., Vuran, M.C. and Akyildiz, I.F. (2007) 'Characteristics of underground channel for wireless underground sensor networks' *Proc. Med-Hoc-Net,* Corfu, Greece, June 2007.

Linear Technology (1983). *LT1001 precision operational amplifier.* Available at: https://www.analog.com/media/en/technical-documentation/data-sheets/LT1001.pdf (Accessed: 1 February 2017).

Lin, M., Wu, Y. and Wassell, I. (2008). 'Wireless sensor network: Water distribution monitoring system' *2008 IEEE radio and wireless symposium,* Orlando, Fl, USA, 22 to 24 January 2008.

Liu, Z. and Kleiner, Y. (2013) 'State of the art review of inspection technologies for condition assessment of water pipes', *Measurement,* 46(1), pp. 1-15.

Liu, Z., Kleiner, Y., Rajani, B., Wang, L. and Condit, W. (2012). *Condition assessment technologies for water transmission and distribution systems.* Available at: https://cfpub.epa.gov/si/si_public_record_report.cfm?Lab=NRMRL&dirEntryId=241510 (Accessed: 1 September 2016).

Long, R., Cawley, P., and Lowe, M. (2003) 'Acoustic wave propagation in buried iron water pipes', *Proceedings of the Royal Society A: Mathematical, Physical and Engineering Sciences,* 459(2039), pp. 2749–2770.

Lowe, M. J. S., Alleyne, D. N., and Cawley, P. (1998) 'Defect detection in pipes using guided waves', *Ultrasonics*, 36(1-5), pp. 147–154.

Lowe, M. J. S., and Cawley, P. (2006). *Long Range Guided Wave Inspection Usage – Current Commercial Capabilities and Research Directions*. Available at: https://www.imperial.ac.uk/pls/portallive/docs/1/55745699.PDF (Accessed: 1 May 2016).

Lowe, M. and Pavlakovic, M. (1997) 'Disperse: An interactive programme for generating dispersion curves'. Available at: https://www.imperial.ac.uk/media/imperial-college/research-centres-and-groups/non-destructive-evaluation/Disperse-specification-2016-02-08.pdf (Accessed 1 May 2016).

Makar, J. and Chagnon, N. (1999) 'Inspecting systems for leaks, pits, and corrosion', *Journal-American Water Works Association*, 91(7), pp. 36-46.

Makar, J.M., Desnoyers, R. and McDonald, S.E. (2001) 'Failure modes and mechanisms in gray cast iron pipe' *Underground Infrastructure Research: Municipal, Industrial and Environmental Applications, Proceedings,* Kitchener, Ontario, 10 to 13 June 2001.

Makar, J.M. and Kleiner, Y. (2000) 'Maintaining water pipeline integrity' *AWWA Infrastructure Conference and Exhibition*, Baltimore, Maryland, USA, 12 March 2000.

Marlow, D., Heart, S., Burn, S., Urquhart, A., Gould, S., Anderson, M., Cook, S., Ambrose, M., Madin, B., and Fitzgerald, A. (2007). *Condition Assessment Strategies and Protocols for Water and Wastewater Utility Assets*. Available at: https://silo.tips/download/condition-assessment-strategies (Accessed: 1 July 2020).

Martini, A., Troncossi, M. and Rivola, A. (2017) 'Leak detection in water-filled small-diameter polyethylene pipes by means of acoustic emission measurements', *Applied Sciences*, 7(1), pp. 1-13.

Maser, K.R. (1996) 'Condition assessment of transportation infrastructure using ground-penetrating radar', *Journal of infrastructure systems*, 2(2), pp. 94-101.

Maxim Integrated (2019). *DS18B20: Programmable resolution 1-wire digital thermometer.* Available at: https://datasheets.maximintegrated.com/en/ds/DS18B20.pdf (Accessed: 1 October 2019).

Measurement Specialties (no date) 'Piezo Film Sensors'. Available at: https://www.te.com/content/dam/te-com/documents/sensors/global/te-sensor-solutions-catalog-piezo-film-sensors.pdf. (Accessed: 10 March 2016).

Metje, N., Atkins, P. R., Brennan, M. J., Chapman, D. N., Lim, H. M., Machell, J., Muggleton, J.M., Pennock, S., Ratcliffe, J., Redfern, M., Rogers, C.D.F., Saul, A.J., Shan, Q., Swingler, S. and Thomas, A. M. (2007) 'Mapping the Underworld – State-of-the-art review', *Tunnelling and Underground Space Technology*, 22(5-6), pp. 568–586.

Metje, N., Chapman, D.N., Walton, R., Sadeghioon, A.M. and Ward, M. (2012) 'Real time condition monitoring of buried water pipes', *Tunnelling and Underground Space Technology*, 28(2012), pp. 315-320.

Misiunas, D. (2005) *Failure Monitoring and Asset Condition Assessment in Water Supply Systems*. Ph.D. Thesis. Lund University. Available at: https://www.iea.lth.se/publications/Theses/LTH-IEA-1048.pdf (Accessed: 1 July 2016).

Misiunas, D., (2008) 'Failure Monitoring and Asset Condition Assessment in Water Supply Systems' *The 7th International Conference*, Faculty of Environmental Engineering Vilnius Gediminas Technical University, Vilnius, Lithuania, 22nd to 23rd May 2008.

Molisch, A.F. (2011). *Wireless communications* (2nd ed.). Hoboken, N.J.: Wiley

Muggleton, J. M., Brennan, M. J., and Pinnington, R. J. (2002) 'Wavenumber Prediction of Waves in Buried Pipes for Water Leak Detection', *Journal of Sound and Vibration* 249(5), pp. 939-954.

Muggleton, J.M., Brennan, M.J. and Linford, P.W. (2004) 'Axisymmetric wave propagation in fluid-filled pipes: wavenumber measurements in in vacuo and buried pipes', *Journal of Sound and Vibration*, 270(1-2), pp.171-190.

Muggleton, J.M. and Yan, J. (2013) 'Wavenumber prediction and measurement of axisymmetric waves in buried fluid-filled pipes: Inclusion of shear coupling at a lubricated pipe/soil interface', *Journal of Sound and Vibration*, 332(5), pp.1216-1230.

Municipal Advisory Board (2017). *MAB Generic Electrofusion Procedure for Field Joining of 14 Inch to 30 Inch Polyethylene (PE) Pipe.* Available at: https://plasticpipe.org/pdf/mab-02-generic-electrofusionn.pdf (Accessed: 1 June 2021).

Mustafa, H. and Chou, P.H. (2012) 'Embedded damage detection in water pipelines using wireless sensor networks' *2012 IEEE 14th International Conference on High Performance Computing and Communication & 2012 IEEE 9th International Conference on Embedded Software and Systems*, Liverpool, UK, 25 to 27 June 2012.

Mutagi, R.N. (2012) *Digital Communications: Theory, Techniques, and Applications*. Oxford: Oxford University Press.

National Instruments (2009) 'DAQ M Series: NI USB-621x user manual'. Available at: https://www.ni.com/pdf/manuals/371931f.pdf (Accessed: 1 May 2015).

Nestleroth, B., Flamberg, S., Lal, V., Condit, W., Matthews, J., Chen, A. and Wang, L. (2013) *Field demonstration of innovative condition assessment technologies for water mains: Acoustic pipe wall assessment, internal inspection, and external inspection*. Available at: https://cfpub.epa.gov/si/si_public_record_report.cfm?Lab=NRMRL&dirEntryId=283716 (Accessed: 1 August 2020).

Nguyen, H.H. and Shwedyk, E. (2009) *A First Course in Digital Communications*. Cambridge: Cambridge University Press.

NXP (2009) 'Rapid Prototyping for the LPC1768 MCU'. Available at: https://www.sparkfun.com/datasheets/DevTools/ARM/mbed_LPC1768.pdf (Accessed: 1 December 2016).

NXP (2016) 'UM10360. LPC176x/5x User Manual. Rev. 4'. Available at: https://www.nxp.com/docs/en/user-guide/UM10360.pdf (Accessed: 30 January 2017)

Oelze, M.L., O'Brien, W.D. and Darmody, R.G. (2002) 'Measurement of attenuation and speed of sound in soils', *Soil Science Society of America Journal*, 66(3), pp.788-796.

Owojaiye, G., and Sun, Y. (2013), 'Focal design issues affecting the deployment of wireless sensor networks for pipeline monitoring', *Ad Hoc Networks*, 11(3), pp. 1237–1253.

Pal, M. (2008) *Leak detection and location in polyethylene pipes.* Ph.D. Thesis. Loughborough University. Available at: https://ethos.bl.uk/OrderDetails.do?uin=uk.bl.ethos.603092 (Accessed: 1 September 2017).

Pan, X., Forrest, J.A. and Juniper, R.G. (2009) 'Optimal design of a control actuator for sound attenuation in a piping system excited by a positive displacement pump' *Proceedings of ACOUSTICS 2009*, Adelaide, Australia, 23 to 25 November 2009.

Paulson, P., Mascarenhas, R., Bell, G. and Clark, B. (2014). *Acoustic Signal Processing for Pipe Condition Assessment (WaterRF Report 4360).* Available at: https://cfpub.epa.gov/si/si_public_record_report.cfm?Lab=NRMRL&dirEntryId=305970 (Accessed: 30 July 2020).

PCBWay (2019). *PCB prototype the easy way.* Available at: https://www.pcbway.com/ (Accessed: 30 April 2017).

Pelletier, G., Mailhot, A. and Villeneuve, J. (2003) 'Modelling water pipe breaks-three case studies', *Journal of water resources planning and management*, 129(2), pp. 115–123.

Pennock, S.R., Jenks, C.H.J., Orlando, G. and Redfern, M.A. (2012) 'In-pipe GPR configuration and the determination of target depth and ground permittivity' *2012 IEEE International Geoscience and Remote Sensing Symposium (IGARSS)*, Munich, Germany, 21 July to 26 July 2012.

Pennock, S.R., Redfern, M.A. and Shan, Q. (2006) 'Subsurface illumination and propagation in Ground Penetrating Radar' *2006 First European Conference on Antennas and Propagation*, Nice, France, 6 to 10 November 2006.

Physical Acoustics (2020) *World leader in Acoustic emission.* Available at: https://www.physicalacoustics.com/ (Accessed: 30 July 2020).

Physik Instrumente (PI) (2016) 'Piezoelectric Actuators: Components, Technologies, Operation'. Available at:

https://static.piceramic.com/fileadmin/user_upload/pi_ceramic/files/catalog_CAT/PI_CAT128E_R3_Piezoelectric_Actuators.pdf (Accessed: 5 March 2016).

PiezoDrive (no date a) 'BA Series Bender Actuators'. Available at: https://www.piezodrive.com/actuators/ba-series-bender-actuators/ (Accessed: 2 March 2016).

PiezoDrive (no date b) '100 V Piezoelectric Bimorph Bender'. Available at: https://www.piezodrive.com/wp-content/uploads/2016/01/BA4510.pdf. (Accessed: 2 March 2016).

PiezoDrive (no date c) 'Piezoelectric Tube Scanners'. Available at: https://www.piezodrive.com/actuators/piezoelectric-tube-scanners/ (Accessed: 2 March 2016).

PiezoDrive (no date d) 'SB Series 200 V Piezo Stack Actuators'. Available at: https://www.piezodrive.com/actuators/200v-piezo-stack-actuators/ (Accessed: 2 March 2016).

Piezo Systems (no date a) 'Piezoelectric bending actuators (Motors)'. Available at: http://www.piezo.com/prodbm0nav.html (Accessed: 3 March 2016).

Piezo Systems (no date b) 'Piezoelectric bending sensors (Generators)' Available at: http://www.piezo.com/prodbg0nav.html (Accessed: 3 March 2016).

Piezo Systems (no date c) 'Piezoelectric Extension Actuators (Motors)' Available at: http://www.piezo.com/prodexm0nav.html (Accessed: 3 March 2016).

Piezo Systems (no date e) 'Piezoelectric Extension Sensors (Generators)' Available at: http://www.piezo.com/prodexg0nav.html (Accessed: 3 March 2016).

Piezo Systems (no date f) ‘Large Piezo Stack’ Available at: http://www.piezo.com/prodstacks1.html (Accessed: 3 March 2016).

Pinnington, R.J. and Briscoe, A.R. (1994) ‘Externally applied sensor for axisymmetric waves in a fluid filled pipe’, *Journal of Sound and vibration*, 173(4), pp. 503-516.

Piratla, K.R., Yerri, S.R., Yazdekhasti, S., Cho, J., Koo, D. and Matthews, J.C. (2015) ‘Empirical analysis of water-main failure consequences’, *Procedia Engineering*, 118 (2015), pp. 727-734.

Plastic Pipes Institute (2008) ‘Underground Installation of PE Piping’ Available at: https://plasticpipe.org/pdf/chapter07.pdf (Accessed: 1 June 2021).

Pons, J. L. (2005) *Emerging Actuator Technologies: A Micromechatronic Approach*. Hoboken, N.J: Wiley.

Precision Microdrives (no date) ‘AB-014: Mechanical Layout Of Vibration Motors For Typical User-Interfaces And Controls’ Available at: https://www.precisionmicrodrives.com/content/ab-014-mechanical-layout-of-vibration-motors-for-typical-user-interfaces-and-controls/ (Accessed: 1 August 2019).

Precision Microdrives (2015a) ‘Product Data Sheet. Pico Vibe. 8mm Vibration Motor’ Available at: https://www.precisionmicrodrives.com/product/datasheet/308-100-8mm-vibration-motor-3mm-type-datasheet.pdf (Accessed: 30 January 2015).

Precision Microdrives (2015b) ‘Product Data Sheet. Uni Vibe. 8mm Vibration Motor’ Available at: https://www.precisionmicrodrives.com/product/datasheet/308-103-8mm-vibration-motor-20mm-type-datasheet.pdf (Accessed: 30 January 2015).

Proakis, J.G. (2001) *Digital Communications*. 4th edn. New York, N.Y: McGraw-Hill.

Proakis, J.G. & Salehi, M. (2008) *Digital Communications*. 5th edn. New York, N.Y: McGraw-Hill.

Pure Technologies (2020). *PipeDiver®.* Available at: https://puretechltd.com/technology/pipediver-condition-assessment/ (Accessed: 1 July 2020).

Pure Technologies (2020). *SmartBall®*. Available at: https://puretechltd.com/technology/smartball-leak-detection/ (Accessed: 1 July 2020).

Pure Technologies (2020). *Soundprint®*. Available at: https://puretechltd.com/technology/soundprint/ (Accessed: 10 July 2020).

Rajani, B. and Kleiner, Y., (2004) 'Non-destructive Inspection Techniques to Determine Structural Distress Indicators in Water Mains' *Evaluation and Control of Water Loss in Urban Water Networks*, Valencia, Spain, 21 to 25 June 2004.

Rajeev, P., Kodikara, J., Chiu, W.K. and Kuen, T. (2013) 'Distributed optical fibre sensors and their applications in pipeline monitoring', *Key Engineering Materials*, 558(2013), pp. 424-434.

Rajeev, P., Kodikara, J., Robert, D., Zeman, P. and Rajani, B. (2014) 'Factors contributing to large diameter water pipe failure', *Water Asset Management International*, 10(3) pp. 9-14.

Raorane, R. and Patil, M.D. (2014) 'Magnetic Induction-Based Wireless Underground Waveguide Modelling and Its Parameters', *International Journal of Electronics Communication and Computer Technology (IJECCT), 4(3),* pp. 614-618.

RapidView (2019) *Pipeline and manhole inspection and rehabilitation systems.* Available at: https://rapidview.com/ (Accessed: 1 August 2020).

Richardson, A. (2016) ‘Selly Oak sinkhole repairs will take weeks, say Severn Trent’, *Birmingham Live*, 25 November. Available at: http://www.birminghammail.co.uk/news/midlands-news/selly-oak-sinkhole-repairs take-12230604 (Accessed: 5 December 2016).

Richart, F. E., Hall, J. R., and Lysmer, J. (1962). *Study of the propagation and dissipation of ‘elastic’ wave energy in granular soils.* Available at: https://apps.dtic.mil/dtic/tr/fulltext/u2/286075.pdf (Accessed: 1 December 2017).

Rogers, P.D. and Grigg, N.S. (2009) ‘Failure assessment modelling to prioritize water pipe renewal: two case studies’, *Journal of Infrastructure Systems*, *15*(3), pp. 162-171.

Rogers, C.D.F., Hao, T., Costello, S.B., Burrow, M.P.N., Metje, N., Chapman, D.N., Parker, J., Armitage, R.J., Anspach, J.H., Muggleton, J.M., Foo, K.Y., Wang, P., Pennock, S.R., Atkins, P.R., Swingler, S.G., Cohn, A.G., Goddard, K., Lewin, P.L., Orlando, G., Redfern, M.A., Royal, A.C.D. and Saul, A.J. (2012) ‘Condition assessment of the surface and buried infrastructure–A proposal for integration’, *Tunnelling and Underground Space Technology*, 28(1), pp. 202-211.

Rose, J.L. (2014). *Ultrasonic guided waves in solid media*. Cambridge: Cambridge University Press.

Rose, J.L., Mu, J. and Cho, Y. (2008) ‘Recent advances on guided waves in pipe inspection’, *Proceedings of the 17th World Conference on Non-Destructive Testing*, Shanghai, China, 25 to 28 October 2008.

Sadeghioon, A., Metje, N., Chapman, D., and Anthony, C (2014) ‘SmartPipes: Smart Wireless Sensor Networks for Leak Detection in Water Pipelines’, *Journal of Sensor and Actuator Networks*, *3*(1), pp. 64-78.

Sadeghioon, A. (2014) *Design and Development of Wireless Underground Sensor Networks for Pipeline Monitoring*. Ph.D. Thesis. University of Birmingham. Available at: https://etheses.bham.ac.uk/id/eprint/5947/1/MollazadehSadeghioon15PhD.pdf (Accessed: 1 March 2015).

Santamarina, J.C., Klein, K.A. and Fam, M.A. (2001). *Soils and waves*. New York, N.Y.: John Wiley.

Saul, A.J., Unwin, D.M. & Boxall, J.B. (2003) 'Data mining and relationship analysis of water distribution system databases for improved understanding of operations performance' *Proceedings of the International Conference on Computing and Control for the Water Industry - Advances in Water Supply Management*, London, UK, 15 to 17 September 2003.

Seed, H.B., Wong, R.T., Idriss, I.M. and Tokimatsu, K. (1986) 'Moduli and damping factors for dynamic analyses of cohesionless soils', *Journal of Geotechnical Engineering*, 112(11), pp. 1016-1032.

Selvakumar, A., Tuccillo, M.E., Martel, K.D., Matthews, J.C. and Feeney, C. (2014) 'Demonstration and evaluation of state-of-the-art wastewater collection systems condition assessment technologies', *Journal of Pipeline Systems Engineering and Practice*, 5(2), pp. 1-11.

Severn Trent (2019) 'Summary of Charges 2019-2020: A householder's guide to how we calculate your bill'. Available at: https://www.stwater.co.uk/content/dam/stw/my-account/our-charges/stw-summary-of-charges-2019-20.pdf (Accessed: 1 April 2021).

Sharma, A. (2011). 'Wired vs. Wireless Technologies for Communication Networks in Utility Markets', *Utility Products*, 1 April. Available at: https://www.utilityproducts.com/test-

measurement/article/16002788/wired-vs-wireless-technologies-for-communication-networks-in-utility-markets (Accessed: 1 February 2020).

Shinozuka, M., Chou, P.H., Kim, S., Kim, H.R., Yoon, E., Mustafa, H., Karmakar, D. and Pul, S. (2010) 'Nondestructive monitoring of a pipe network using a MEMS-based wireless network' *Nondestructive Characterization for Composite Materials, Aerospace Engineering, Civil Infrastructure, and Homeland Security 2010, 76490P,* San Diego, California, USA, 12 April 2010.

Shukla, H., Desai, H., Sorber, J. and Piratla, K, R. (2018) 'Evaluation of energy harvesting potential in water pipelines to power sustainable monitoring systems' *Construction Research Congress 2018,* New Orleans, LA, 2-4 April 2018.

Silva, A.R. (2010). *Channel characterization for wireless underground sensor networks.* MSc. Thesis. University of Nebraska-Lincoln, Lincoln, Nebraska. Available at: https://digitalcommons.unl.edu/computerscidiss/13/ (Accessed: 1 September 2017).

Silva, A.R. and Vuran, M.C. (2010) 'Development of a testbed for wireless underground sensor networks', *EURASIP Journal on Wireless Communications and Networking,* 2010(620307), pp. 1-14.

Silver, M.L. and Seed, H.B. (1971) 'Deformation characteristics of sands under cyclic loading', *Journal of the Soil Mechanics & Foundations Division 1971,* 97(8), pp.1081-1098.

Sklar, B. (2001). *Digital Communications: Fundamentals and Applications.* 2nd edn. London: Pearson.

Smart Material (2015) ‘Macro Fibre Composite – MFC’. Available at: https://www.smart-material.com/media/Datasheets/MFC_V2.3-Web-full-brochure.pdf (Accessed 10 March 2016).

Sodano, H.A. (2003) *Macro-Fiber Composites for Sensing, Actuation and Power Generation*. MSc. Thesis. Virginia Tech. Available at: http://scholar.lib.vt.edu/theses/available/etd-08012003-105114/ (Accessed: 12 March 2016).

Sparkfun Electronics (no date a) ‘Circular Surface Transducer’. Available at: https://www.proto-pic.co.uk/product/sparkfun-com-10975-surface-transducer-large/ (Accessed: 1 February 2015).

Sparkfun Electronics (no date b) ‘Rectangular Surface Transducer’. Available at: https://www.proto-pic.co.uk/product/sparkfun-com-10917-surface-transducer-small/ (Accessed: 1 February 2015).

Steiner & Martins, Inc. (no date a) ‘Piezo Bimorph’. Available at: https://www.steminc.com/PZT/en/piezo-bimorph (Accessed: 1 March 2016).

Steiner & Martins, Inc. (no date b) ‘Stack Piezo Actuators’. Available at: https://www.steminc.com/PZT/en/stack-piezo-actuators (Accessed: 1 March 2016).

Stewart, H.E. and Bilgin, O. (2020). *Thermal stresses in HDPE water pipes.* Available at: https://plasticpipe.org/pdf/ppi-stewart-and-bilgin-thermal-hdpe-final-report.pdf (Accessed: 1 June, 2021).

Stoianov, I., Nachman, L., Madden, S., Tokmouline, T. and Csail, M. (2007) ‘PIPENET: A Wireless Sensor Network for Pipeline Monitoring’ *2007 6th International Symposium on Information Processing in Sensor Networks*, Cambridge, MA, USA, 25 to 27 April 2007.

Stoianov, I., Nachman, L., Whittle, A., Madden, S. and Kling, R. (2008) 'Sensor networks for monitoring water supply and sewer systems: Lessons from boston' *Eighth Annual Water Distribution Systems Analysis Symposium (WDSA),* Cincinnati, Ohio, USA, 27 to 30 August 2008.

Sun, Z. and Akyildiz, I.F. (2010) 'Magnetic induction communications for wireless underground sensor networks' *IEEE transactions on antennas and propagation*, 58(7), pp. 2426-2435.

Sun, Z., Wang, P., Vuran, M.C., Al-Rodhaan, M.A., Al-Dhelaan, A.M. and Akyildiz, I.F. (2011) 'MISE-PIPE: Magnetic induction-based wireless sensor networks for underground pipeline monitoring', *Ad Hoc Networks*, 9(3), pp. 218-227.

Texas Instruments (2016) 'DRV8662 Piezo Haptics Driver Evaluation Module'. Available at: https://www.ti.com/lit/ug/slou319b/slou319b.pdf?ts=1612549971935&ref_url=https%253A%252F%252Fwww.ti.com%252Ftool%252FDRV8662EVM (Accessed: 1 June 2016).

Texas Instruments (2014) 'LM567x Tone Decoder'. Available at: http://www.ti.com/lit/ds/symlink/lm567c.pdf (Accessed: 1 October 2016).

Texas Instruments (2016) 'Quadruple Half-H Drivers'. Available at: http://www.ti.com/lit/ds/symlink/l293.pdf (Accessed: 1 April 2016).

Thornton, J., Sturm, R. and Kunkel, G. (2008) *Water Loss Control.* 2nd edn. New York, N.Y: McGraw-Hill.

Valvano, J.W. (2012). *Embedded Systems: Real-Time Interfacing to ARM® Cortex™ -M Microcontrollers.* 5th edn. Texas: Valvano.

Vuran, M.C. and Akyildiz, I.F. (2010) ‘Channel model and analysis for wireless underground sensor networks in soil medium’, *Physical Communication*, 3(4), pp. 245-254.

Vuran, M.C. and Silva, A.R. (2009). *Sensor Networks: Where Theory Meets Practice*. Edited by Ferrari, Gianluigi. Berlin: Hiedelberg.

Walton, R., Sadeghioon, A.M., Metje, N., Chapman, C. and Ward, M. (2011) ‘Smart Pipes: The future for proactive asset management’ *International Conference on Pipelines and Trenchless Technology 2011*, Beijing, China, 26-29 October 2011.

Wang, Q.M., Du, X.H., Xu, B. and Cross, L.E. (1999) ‘Electromechanical coupling and output efficiency of piezoelectric bending actuators’, *IEEE transactions on ultrasonics, ferroelectrics, and frequency control*, 46(3), pp. 638-646.

Water UK (2020) ‘Water companies record lowest leakage levels from pipes’. Available at https://www.water.org.uk/news-item/water-companies-record-lowest-leakage-levels-from-pipes/ (Accessed: 1 June 2021).

Weimer, D. (2001) *Water Loss Management and Techniques.* Available at: http://www.geocities.ws/kikory2004/41_German_report_WAter_Loss.pdf (Accessed 1 June 2020).

White, C. (2020) *Sonar Lets Organizations Inspect Pipes with Flow.* Available at: https://redzone.com/nr/sonar-tackles-pipes-with-flow/ (Accessed: 30 September 2020).

Whittle, A.J., Allen, M., Preis, A. and Iqbal, M. (2013) ‘Sensor networks for monitoring and control of water distribution systems’ *6th International Conference on Structural Health Monitoring of Intelligent Infrastructure (SHMII 2013),* Hong Kong, 9 to 11 December 2013.

Williams, R.B., Park, G., Inman, D.J. and Wilkie, W.K. (2002) 'An overview of composite actuators with piezoceramic fibres' *Proceeding of IMAC-XX*, Westin Los Angeles Airport, Bethel, Conn, 4 to 7 February 2002.

Wöckel, S., Steinmann, U. and Arndt, H. (2015) 'Low frequency guided wave transmission in water pipe systems', *Procedia engineering*, 120(2015), pp. 1257-1260.

Yick, J., Mukherjee, B. and Ghosal, D. (2008) 'Wireless sensor network survey. *Computer networks*, *52*(12), pp.2292-2330.

Yimsiri, S. and Ratananikom, W. (2021) 'Long-term response of flexible pipe in sand trench due to consolidation of native clay', *Soils and Foundations* (2021), https://doi.org/10.1016/j.sandf.2021.05.003.

APPENDICES

Appendix A: C programmes

```
//Algorithm for digital transmission of ones and zeros

#include "mbed.h"

Serial in(NC,p10);          //serial connection from the external computer station
DigitalOut enable(p26);     //connection to enable the H-Bridge circuit
DigitalOut forward(p29);    //rotate the DC motor in the forward direction
DigitalOut reverse(p23);    //rotate the DC motor in the reverse direction
DigitalOut myled(LED1);     //LED indicator on the microcontroller prototype board

void run()  //function to rotate the DC motor in the forward direction
{
        forward = 1;
        reverse = 0;
        myled = 1;
}

void back() //function to rotate the DC motor in the reverse direction
{
        reverse = 1;
        myled = 0;
}

int main() //main function of the programme
{
    in.baud(300);   //baud rate of serial connection from the external computer station
    enable = 1;    //enable the H-Bridge circuit

    while(1)
    {
        char data_in = in.getc();   //read input character from external computer station

        if(data_in == '1')          //if input character is "0", begin digital transmission of "ones" and "zeros"
        {
                    myled = 1;
                    run();          //transmit pilot signal
                    wait(1);
            while(1)
            {
                myled = 0;
                back();              //digital tranmsission of "zero"
                wait(1);
                myled = 1;
                run();             //digital transmission of "one"
                wait(1);
            }
        }
    }
}
```

Figure A.1: C programme for binary information transmission at the digital communication transmitter

```
//Algorithm for the digital communication reciever

#include "mbed.h"

Serial out(p28,NC);                 //serial connection to the external computer station
AnalogIn signal(p20);               //analogue input to the LPC1768 microcontroller
InterruptIn signal_prompt(p5);      //interrupt input to the LPC1768 microcontroller
DigitalOut myled(LED1);             //LED indicator on the microcontroller prototype board

void data() //interrupt handler routine for the digital information signal
{
    myled = 1;                     //LED indicator to notify of the presence of a pilot signal
    wait_ms(1500);                 //time delay before the detection of the digital information signal

    while(1)
    {
        if(signal < 2.5)                        //condition for detecting a binary "1"
        {
            myled = 1;
            char dataout = out.putc('1');
        }
        else                                    //condition for detecting a binary "0"
        {
            myled = 0;
            char dataout = out.putc('0');
        }
        wait_ms(1000);                          //wait for the next digital information signal
    }
}

int main()                                      //main function of the programme
{
    out.baud(300);                              //baud rate of serial connection to the external computer station
    signal_prompt.fall(&data);                  //trigger for interrupt handler routine on the detection of a pilot signal

    while(1)
    {
        out.printf(" Waiting for signal...");    //idle state of the digital communication receiver (waiting for signal)
        wait(10);
    }
}
```

Figure A.2: C programme for binary information recovery at the digital communication receiver

```
//Algorithm for formatted data (ASCII format) transmission using the vibration motor

#include "mbed.h"

Serial in(NC,p10);          //serial connection from the external computer station
DigitalOut enable(p26);     //connection to enable the H-Bridge circuit
DigitalOut forward(p29);    //rotate the DC motor in the forward direction
DigitalOut reverse(p23);    //rotate the DC motor in the reverse direction
DigitalOut myled(LED1);     //LED indicator on the microcontroller prototype board

void run()  //function to rotate the DC motor in the forward direction
{
        forward = 1;
        reverse = 0;
        myled = 1;
}

void back() //function to rotate the DC motor in the reverse direction
{
        reverse = 1;
        myled = 0;
}

int main() //main function of the programme
{
    in.baud(300);   //baud rate of serial connection from the external computer station
    enable = 1;    //enable the H-Bridge circuit

    while(1)
    {
        char data_in = in.getc();   //read input character from external computer station
```

```

       if(data_in == 'A')          //if input character is "A", begin digital transmission of binary code for "A"
       {
                  myled = 1;
                  run();           //transmit pilot signal
                  wait(1);

                  myled = 0;       //1st bit
                  back();
                  wait(1);

                  myled = 1;       //2nd bit
                  run();
                  wait(1);

                  myled = 0;       //3rd bit
                  back();
                  wait(1);

                  myled = 0;       //4th bit
                  back();
                  wait(1);

                  myled = 0;       //5th bit
                  back();
                  wait(1);

                  myled = 0;       //6th bit
                  back();
                  wait(1);
```

```
62
63                      myled = 0;      //7th bit
64                      back();
65                      wait(1);
66
67                      myled = 1;      //8th bit
68                      run();
69                      wait(1);
70
71                      myled = 0;      //end transmission
72                      back();
73          }
74      }
75  }
76
```

Figure A.3: C programme for ASCII information transmission at the digital communication transmitter

```
//Algorithm for ASCII formatted data (ASCII format) detection at the digital communication receiver

#include "mbed.h"

Serial out(p28,NC);                 //serial connection to the external computer station
AnalogIn signal(p20);               //analogue input to the LPC1768 microcontroller
InterruptIn signal_prompt(p5);      //interrupt input to the LPC1768 microcontroller
DigitalOut myled(LED1);             //LED indicator on the microcontroller prototype board

void data() //interrupt handler routine for the digital information signal

    {
        int data_byte[8];               //declaration of array to store ASCII data (8 bits)

        myled = 1;                      //LED indicator to notify of the presence of a pilot signal
        wait_ms(1500);                  //time delay before the detection of the digital information signal


        for(int i = 0; i<8; i++)                //populate the array
        {

            if(signal < 2.5)                   //condition for detecting a binary "1"
            {
                myled = 1;
                data_byte[i] = 1;              //populate one bit of the array with the symbol "1"
            }
            else                               //condition for detecting a binary "0"
            {
                myled = 0;
                data_byte[i] = 0;              //populate one bit of the array with the symbol "0"
            }

            wait_ms(1000);                     //wait for the next digital information signal
        }

    //if array = 01000001 then print "A" to the computer screen, else print ""

     if(data_byte[0] == 0 && data_byte[1] == 1 && data_byte[2] == 0 && data_byte[3] == 0 && data_byte[4] == 0 && data_byte[5] == 0 && data_byte[6] == 0 && data_byte[7] == 1)
     {
         out.printf(" A ");
     }
     else


     {
         out.printf("");
     }
     myled = 0;
}

int main()                                      //main function of the programme
{
    out.baud(300);                              //baud rate of serial connection to the external computer station
    signal_prompt.fall(&data);                  //trigger for interrupt handler routine on the detection of a pilot signal

    while(1)
    {
        out.printf(" Waiting for signal...");          //idle state of the digital communication receiver (waiting for signal)
        wait(10);
    }
}
```

Figure A.4: C programme for ASCII information recovery at the digital communication receiver

Appendix B: Matlab programmes

```
%FFT script

dt = time(2)-time(1);

% calculate sampling frequency
fs = 1/dt;

% FFT length
length = length(x);


% calculate FFT of sampled signal
x_fft = fft(x);

% generate single sided FFT spectrum amplitudes
P2 = abs(x_fft/length);
P1 = P2(1:length/2+1);
P1(2:end-1) = 2*P1(2:end-1);

% generate frequency bins for the FFT
f = fs*(0:(length/2))/length;

% plot the single sided FFT
plot(f,P1)

```

Figure B.1: FFT script in Matlab

```
% Matlab programme for analytical computation of acoustic attenuation
% along exposed MDPE pipe

%geometric and material properties of the pipe

poi = 0.4;          %poisson's ratio
poi_sq = poi^2;
h = 0.0092;         %pipe wall thickness
a = 0.0361;         %pipe inner radius
a_sq = a^2;
rho = 900;          %pipe material density
E = 1.77E9;         %pipe wall elastic modulus
loss = 0.06;        %pipe wall material loss factor

bulk  = 2.25E9;     %bulk density of internal fluid (water)

f = 150;            %acoustic excitation frequency
omega = 2*pi*f;
omega_sq = omega^2;


%acoustic wavenumber calculation
kl_sq = (omega_sq*rho*(1-poi_sq))/E*(1 + i*loss);

A = (poi_sq)/(1-poi_sq);
B = (E*(1 + i*loss)*h)/a_sq;
C = ((E*(1+i*loss)*h)/a_sq)-((omega_sq)*h*rho);
k2_sq = kl_sq*(1+(A*(B/C)));
k2 = sqrt(k2_sq);
im_k2 = imag(k2);
k2_a = k2*a;
im_k2_a = imag(k2_a);

%if the pipe is filled with water,
%adjust the wavenumber calculation by recalculating "C" as:

%C = ((E*(1+i*loss)*h)/a_sq) + (2*bulk/a) -((omega_sq)*h*rho);


% acoustic wavespeed calculation

wave_speed = 2*pi*f/(real(k2))


%acoustic attenuation (dB/m) calculation

att = 20*((im_k2)/log(10))
```

Figure B.2: Matlab programme for analytical computation of acoustic signal attenuation along exposed MDPE pipe

```
% Matlab programme for analytical computation of acoustic attenuation
% along exposed MDPE pipe

%geometric and material properties of the pipe

poi = 0.4;                  %poisson's ratio
poi_sq = poi^2;
h = 0.0092;                 %pipe wall thickness
a = 0.0361;                 %pipe inner radius
a_sq = a^2;
rho = 900;                  %pipe material density
E = 1.6E9;                  %pipe wall elastic modulus
loss = 0.06;                %pipe wall material loss factor

bulk  = 2.25E9;     %bulk density of internal fluid (water)

f = 150;            %acoustic excitation frequency
omega = 2*pi*f;
omega_sq = omega^2;

% %soil parameters
bulk_soil = 6574430;        %soil bulk modulus
shear_soil = 6574430;       %soil shear modulus
rho_soil = 830;             %soil bulk density
comp_speed_soil = 89;       %bulk acoustic wave speed in soil
shear_speed_soil = 89;      %shear acoustic wave speed in soil


%acoustic wave number calculation
k_comp_sq =(rho_soil*omega_sq)/(bulk_soil+(2*shear_soil));
k_comp = sqrt(k_comp_sq);
k_shear_sq = (rho_soil*omega_sq)/shear_soil;
k_shear = sqrt(k_shear_sq);

k_comp_a = k_comp*a
k_shear_a = k_shear*a

hankel_comp = 0.9679676712790938472602 +0.6817275966841125448072i;
hankel_comp_drv = -0.1768141293762055437286 -1.9544863101753086685513i;
hankel_ratio_comp = hankel_comp/hankel_comp_drv;

hankel_shear = 0.8924935868369917017225 +0.2302659581566518860416i;
hankel_shear_drv = -0.3144136298290286551281 -1.1539194419739306584l3i;
hankel_ratio_shear = hankel_shear/hankel_shear_drv;

z_comp = -i*rho_soil*comp_speed_soil*hankel_ratio_comp;
z_shear = -i*rho_soil*shear_speed_soil*hankel_ratio_shear;
```

```
48
49 -     z_rad = z_comp + z_shear;
50 -     R_rad = real(z_rad);
51 -     omega_M_rad = imag(z_rad);
52 -     M_rad = omega_M_rad/omega;
53
54
55 -     A = (poi_sq)/(1-poi_sq);
56 -     B = (E*h)/(a_sq)*(1+i*loss);
57 -     C = (E*h)/(a_sq);
58 -     D = (2*bulk_f)/a;
59 -     E = omega_sq*(rho*h + M_rad);
60 -     F = i*(omega*R_rad + (loss*E*h)/a_sq);
61
62 -     kl_sq = (omega_sq*rho*(1-poi_sq))/E*(1 + li*loss);
63
64 -     k2_sq_new = kl_sq*(1+(B/(C+D-E+F)));
65 -     k2_new = sqrt(k2_sq_new)
66
67 -     im_k2 = imag(k2_new);
68
69
70      %acoustic attenuation (dB/m) calculation
71 -     att = 20*((im_k2)/log(10))
72
```

Figure B.3: Matlab programme for analytical computation of acoustic signal attenuation along buried MDPE pipe

Appendix C: Circuit diagrams

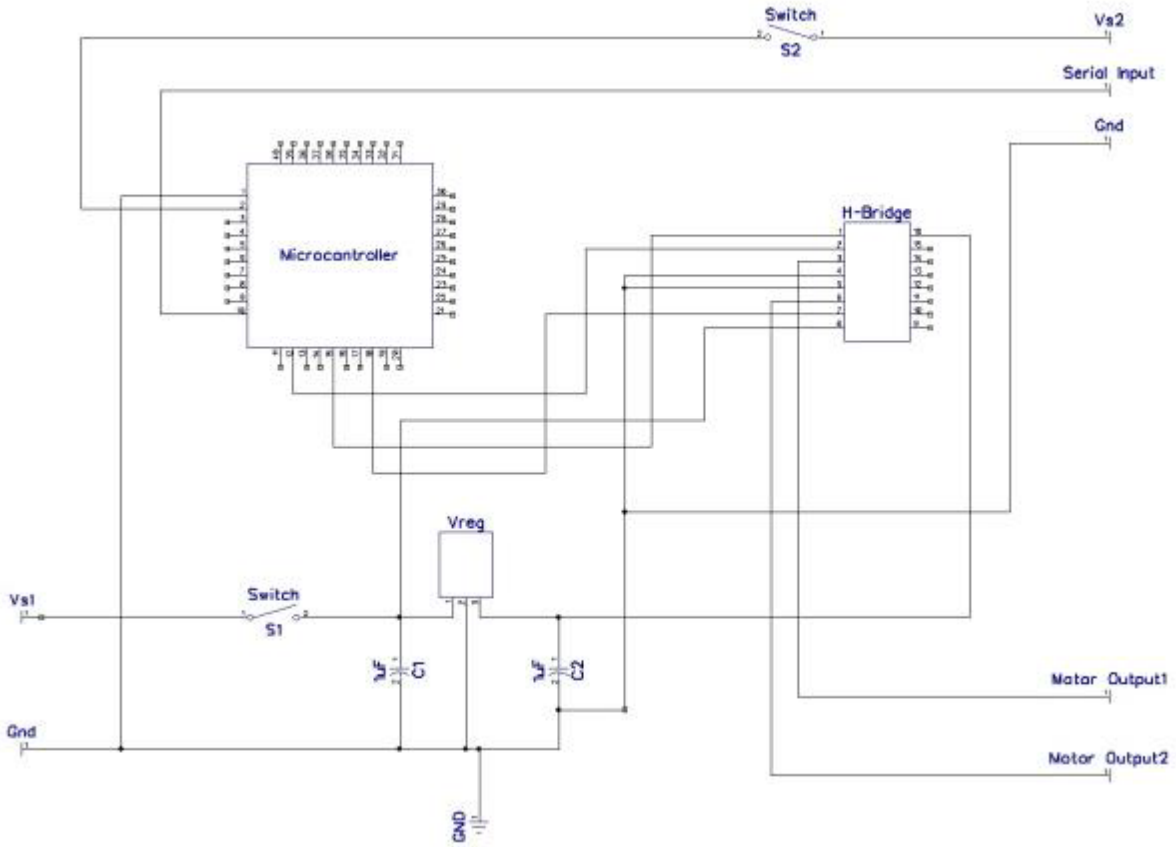

Figure C.1: Digital communication transmitter circuit layout

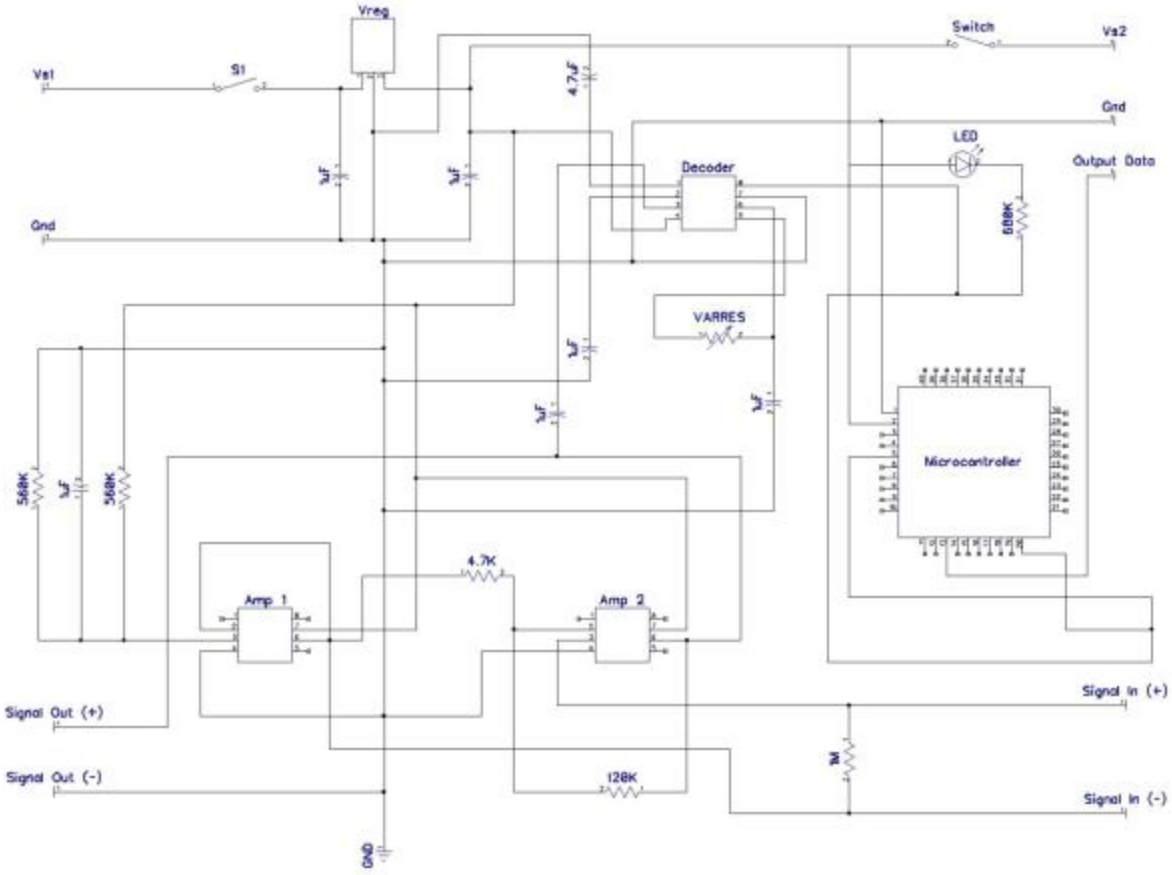

Figure C.2: Digital communication receiver circuit layout